This electronic thesis or dissertation has been downloaded from Explore Bristol Research, http://research-information.bristol.ac.uk

Author:
Marsili, Emanuele

Title:
Leveraging computational chemistry to model photochemical reactions and calculate experimental observables

General rights
Access to the thesis is subject to the Creative Commons Attribution - NonCommercial-No Derivatives 4.0 International Public License. A copy of this may be found at https://creativecommons.org/licenses/by-nc-nd/4.0/legalcode This license sets out your rights and the restrictions that apply to your access to the thesis so it is important you read this before proceeding.

Take down policy
Some pages of this thesis may have been removed for copyright restrictions prior to having it been deposited in Explore Bristol Research. However, if you have discovered material within the thesis that you consider to be unlawful e.g. breaches of copyright (either yours or that of a third party) or any other law, including but not limited to those relating to patent, trademark, confidentiality, data protection, obscenity, defamation, libel, then please contact collections-metadata@bristol.ac.uk and include the following information in your message:

- Your contact details
- Bibliographic details for the item, including a URL
- An outline nature of the complaint

Your claim will be investigated and, where appropriate, the item in question will be removed from public view as soon as possible.

Leveraging computational chemistry to model photochemical reactions and calculate experimental observables

By

Emanuele Marsili

School of Chemistry
University of Bristol

A dissertation submitted to the University of Bristol in accordance with the requirements of the degree of Doctor of Philosophy in the Faculty of Chemistry.

April 2023

Abstract

Predictive atmospheric models are essential to inform political and social decisions regarding the behavior of chemicals and pollutants in the atmosphere. However, experimental studies investigating the photochemistry of some key volatile organic compounds, which play a crucial role in atmospheric chemical reactions, can be extremely challenging or even impossible to conduct due to their short lifetimes. This is even more true when considering the photochemistry of transient species whose reactivity is often inferred based on proxy molecules or simply neglected in current atmospheric models. To address this issue, this thesis proposes a theoretical protocol for calculating the photolysis rate constant, a critical experimental observable for atmospheric models, *in silico*. Using the developed protocol, we demonstrated its effectiveness in studying the photochemistry of one exponent of the α-hydroperoxycarbonyls and its implications in atmospheric chemistry. Our research not only provided new insights into the significance of studying the photochemistry of volatile organic compounds but also brought attention to certain shortcomings of commonly used theoretical methods. Specifically, we uncovered a novel flaw in the algebraic diagrammatic construction at the second order – a promising candidate for studying volatile organic compounds. Finally, our developed protocol was utilized to explore the photodissociation of Lewis adducts, with ammonia borane being the initial focus of our investigation. Despite being an excellent material for hydrogen storage, its photochemistry had not been studied before. Our investigation revealed new insights into the unique electronic properties of the dative bond driving the photolysis of Lewis adducts. In particular, we offered a comprehensive study of the mechanisms underlying the photodissociation of Lewis adducts, paving the way for exciting and innovative applications of these molecules.

Dedication and acknowledgements

To Dr. Basile F. E. Curchod, whose guidance and expertise have been invaluable throughout my academic journey. Your dedication to the pursuit of science is truly admirable but, beyond your scientific achievements, I am grateful for the person you are. Despite the difficulties that I have been through I have always found in you a supportive, sincere, and helpful person and I could never thank you enough for this. It is an honor to have had you as my mentor.

To my family, whose support and love have been the cornerstone of my life. Without them, I would not be the light-hearted person I am today.

I would like to express my heartfelt gratitude to my colleagues, whose encouragement, motivation, and stimulating discussions have enriched both my personal and professional life. I am particularly grateful to my group members – Yorick Lassmann, Antonio Prlj, Lea-Maria Ibele, Lewis Hutton, Daniel Hollas, Jack Taylor, Dasha Shchepanovska, and Harry Stroud – for their invaluable contributions and unwavering support. I would like to express my appreciation to all the people I have had the privilege of meeting during this journey, as they have played a significant role in both my personal and scientific development.

To my friends, whose support and encouragement have been a source of strength and inspiration throughout my life.

I am of the opinion that true happiness can only be achieved by discovering our passions in life. Pursuing these passions consistently can be difficult, and the Covid pandemic served as a sorrowful instance for me. Hence, I am grateful to all people who have supported and encouraged me in pursuing my ambitions. To them, I owe my happiness.

Author's declaration

I declare that the work in this dissertation was carried out in accordance with the requirements of the University's Regulations and Code of Practice for Research Degree Programmes and that it has not been submitted for any other academic award. Except where indicated by specific reference in the text, the work is the candidate's own work. Work done in collaboration with, or with the assistance of, others, is indicated as such. Any views expressed in the dissertation are those of the author.

SIGNED: Emanuele Marsili DATE: 21 April 2023

Table of Contents

List of Tables

Tables **Page**

List of Figures

Figures **Page**

Acronyms

2-HPP 2-hydroperoxy-propanal

ADC(2) Algebraic Diagrammatic Construction at the second order

AIMD Ab Initio Molecular Dynamics

AIMS Ab Initio Multiple Spawning

BH Born-Huang

BOA Born-Oppenheimer Approximation

CAS Complete Active Space

CC2 Coupled Cluster at the second order

CI Conical Intersection

CIS Configuration Interaction Singles

CISD Configuration Interaction Singles and Doubles

CP Crossing Point

CSF Configuration State Functions

DBOC Diagonal Born-Oppenheimer correction

DDM Difference Density Matrix

DF Density Fitting

DFT Density Functional Theory

EDC Energy Decoherence Correction

EOM Equation Of Motion

FC Franck-Condon

FCHT Franck-Condon-Herzberg-Teller

FCI Full Configuration Interaction

FMS Full Multiple Spawning

HF Hartree–Fock

HPALD Hydroperoxyaldehydes

IC Internal Conversion

IS Intermediate State

ISC Intersystem Crossing

ISR Intermediate State Representation

KEO Kinetic Energy Operator

LIIC Linear Interpolation in Internal Coordinates

LR Linear-Response

LR-TDDFT Linear-Response Time-Dependent Density Functional Theory

MCM Master Chemical Mechanism

MCSCF Multiconfigurational Self Consistent Field

MD Molecular Dynamics

MECI Minimum Energy Conical Intersection

MM Molecular Mechanics

MO Molecular Orbitals

MP Møller-Plesset

MPPT Møller-Plesset Perturbation Theory

MS-CASPT2 Multi-State Complete Active Space Perturbation Theory at the second order

MS-MR Multi-State, Multi-Reference

NAC Nonadiabatic Couplings

NEA Nuclear Ensemble Approach

NRCI Non Reactive Conical Intersection

PAH Polycyclic Aromatic Hydrocarbon

PECT Proton-Coupled Electron Transfer

PES Potential Energy Surface

QT Quantum Thermostat

RI Resolution of Identity

SA State Average

SA-CASSCF State-Average Complete Active Space Self Consistent Field

SAR Structure-Activity Relationship

SCS Spin-Component-Scaled

SOC Spin-Orbit Coupling

SPA0 Saddle-Point Approximation at the zero order

SS-SR Single-State, Single-Reference

TBF Trajectory Basis Function

TDA Tamm-Dancoff Approximation

TDM Transition Density Matrix

TDSE Time-Dependent Schrödiger Equation

TISE Time-Independent Schrödiger Equation

TS Transition State

TSH Trajectory Surface Hopping

VOC Volatile Organic Compound

XMS-CASPT2 Extended Multi-State Complete Active Space Perturbation Theory at the second order

Chapter 1

Introduction

1.1 The early age of quantum mechanics

The beginning of the twentieth century was the cradle for one of the most important discoveries in physics: the theory of quantum mechanics. The origins of quantum mechanics can be traced back to the early 1900s when physicists realized that ordinary laws of classical mechanics were not applicable to systems of small size, comparable to atoms and elementary particles. In classical mechanics, particle motion is dictated by Hamilton's equations that trace a trajectory in phase space, unique for each distinct initial condition. However, when the matter wavelength – associated with a moving particle – becomes comparable to the trajectory (or orbits) lengths then a wave-like propagation has to be assumed for the mechanical system. Before starting my introduction, I would like to highlight a quote taken from a work by Einstein regarding the theory of quantum mechanics that, at that time, was still in its infancy. "*It seems as though we must use sometimes the one theory and sometimes the other, while at times we may use either. We are faced with a new kind of difficulty. We have two contradictory pictures of reality; separately neither of them fully explains the phenomena of light, but together they do.*" [8] We hope that the confusion that transpires from Einstein's words will console the reader unaccustomed to the quantum mechanical theory.

The quest to understand the wave nature of matter started with the observation of black-body radiation. In 1900, Planck proposed that energy was emitted and absorbed in discrete packets, or quanta, rather than continuously as described by the classical Maxwell equations. This revolutionary idea, known as the quantum hypothesis, marked the beginning of the development of quantum theory.[9] Based on the quantum hypothesis, Niels Bohr proposed in 1913 a model of the atom in which the electrons are confined to specific energy levels and can only jump between these levels by absorbing or emitting a specific amount of energy.[10] A few years later, Louis de Broglie proposed the concept of wave-particle duality, which states that all particles exhibit both wave-like and particle-like behaviour.[11] De Broglie's ideas become the foundation of the work of Erwin Schrödinger who, in 1925, postulated the celebrated equation published a year later. This equation resulted in Schrödinger Nobel Prize in Physics in 1933 and now bears his name.[12] The Schrödinger equation is a partial differential equation that governs the non-relativistic (*i.e.*, the masses of the particles are independent of their velocities) wave propagation of quantum particles such as electrons and nuclei described by a wavefunction. The wave-like behaviour of matter brings intriguing effects that are negligible in classical mechanics such as (i) interference (waves are combined depending on their phase and amplitude), (ii) decoherence (the quantum system lost its quantum nature when interacting with an environment), (iii) tunnelling (particles can tunnel through barriers that are impenetrable according to classical mechanics), (iv) superposition (a particle can exist in multiple states simultaneously), (v) entanglement (two or more particles become correlated). All these effects are naturally taken into account in the Schrödinger equation that will be – without surprise – the guiding star of our narrative. However, I note in passing that the interpretation of Schrödinger is not unique and different formulations were developed to describe quantum mechanical systems such as the Heisenberg mechanics, the "new dynamics" – now called Bohmian dynamics – postulated by De Broglie[11, 13] and completed in 1952 by Bohm,[14–16] or even the path integral approach derived by Feynman.[17]

Quantum mechanics has been successful in explaining a wide range of phenomena, including the behaviour of atoms and molecules, the properties of solids and liquids, and the nature of chemical bonds and chemical reactions. It paved the way for the first simulations of atomic and small molecular systems and provided an opportunity to understand the absorption and emission of light by atoms and molecules. It also serves as the launching pad for a new era of physics, started with the seminal work of Enrico Fermi in quantum electrodynamics,[18] then refined by means of re-normalization procedure by Feynman[17] that also introduced the standard way of representing perturbation series using diagrams.[19]

1.2 Quantum mechanics and molecules

Quantum mechanics acted as a real scientific revolution. However, from the very beginning, scientists realized that the new insights that this revolution was providing were coming with a cost. In fact, the description of chemical systems using an exact theoretical treatment was impossible (or I shall say extremely challenging) due to the complexity of solving the Schrödinger equation. On this topic, Dirac wrote in his evergreen paper of 1929[20]: "*The underlying physical laws necessary for the mathematical theory of a large part of physics and the whole of chemistry are thus completely known, and the difficulty is only that the exact application of these laws leads to equations much too complicated to be soluble. It, therefore, becomes desirable that approximate* *practical methods of applying quantum mechanics should be developed, which can lead to an explanation of the main features of complex atomic systems without too much computation*". A new field of chemistry – which now is defined as theoretical chemistry – was born with the idea of developing approximated methods to solve the many-body Schrödinger equation efficiently while retaining the quantum nature of the particles composing the molecular system.

The first milestone towards the current quantum theory for molecules was proposed in 1927 by Max Born and J. Robert Oppenheimer.[21] Born and Oppenheimer proposed to partition the molecular system into an electronic and nuclear part allowing for a convenient simplification: the electronic motion – which is much faster than the nuclear motion – can be disentangled from the nuclear motion. In other words, the two subsystems (nuclei and electrons) can be treated separately. This approximation led to the concept of potential energy surfaces (PESs) that describe the electronic energy as a function of the positions of the nuclei, *i.e.*, the energy of the electronic subsystem for a particular configuration of the nuclei. The concept of PESs is now general knowledge for chemists and physicists and it is the cornerstone to understanding the behavior of molecules such as their stability and reactivity.

Born and Oppenheimer placed the first brick in building modern computational chemistry but not long after, Douglas Hartree and Vladimir Fock developed the first method to approximate the many-body interactions in a molecular system, enabling the computation of the energy of the electronic subsystem efficiently.[22, 23] The Hartree–Fock (HF) method led to a frenetic development of more accurate methods (post-HF) that are nowadays the core of *ab initio* computational chemistry. Post-HF methods build upon the HF ansatz and improve its accuracy by providing a better description of the many-body interactions, *i.e.*, electron correlation. Some of these methodologies, such as the Møller-Plesset perturbation theory (MPPT), will be explained further in chapter 2. Others like density functional theory (DFT) will be used throughout this thesis but they will be not discussed in detail.

1.3 Theoretical and computational photochemistry

Photochemistry is an extremely active field of research that has found a wide range of applications. In the last few decades, the development of experimental techniques, able to probe molecular excited-state dynamics,[24, 25] have fostered a coequal growth in the field of theoretical and computational chemistry. Computational studies are now routine in materials discovery,[26–28] materials science,[26, 29, 30] molecular biology,[31–33] organic,[34–36] and inorganic chemistry[37, 38] to investigate the photochemical and photophysical properties of such systems.[39–42] Let us first investigate the different steps of a photochemical reaction, depicted in Fig. 1.1.

In a ground-state reaction, the reactant – the blue Gaussian symbolizes the nuclear wavefunction in a given electronic state – evolves solely in the ground state (S_0) and can reach a transition state (TS). The TS acts as a saddle point for the molecule to funnel to another minimum which is the product of the reaction. Within this picture, only the S_0 PES has to be taken into account to describe the whole chemical process, and the overall reactivity is characterized by the energy differences between the minima and TSs. When we allow the molecule to absorb light, the picture becomes more convoluted.

① The electronic transition, depicted by a purple arrow in Fig. 1.1, allows the molecule to access the manifold of excited electronic states. In the scheme, I represent the excitation as the “rigid translation” of the molecules into a higher excited state. This way of picturing the excitation resonates with the aforementioned Born-Oppenheimer approximation. Upon light absorption, the electrons rearrange rapidly in comparison with the slow nuclei. The electronic transition (in this case $S_0 \rightarrow S_1$) modifies the bond pattern and provokes the nuclei to adjust to the new electronic distribution. Therefore, the excited molecule evolves in configuration space following the excited-state PES – exploring regions that may not be accessible within a ground-state reaction – and ultimately branching into multiple components. The branching is determined by the topology of the PESs that may have local minima (S_1min) or energy barriers (S_1TS). ② The nuclear population can also be transferred to other accessible excited states (such as S_2) but ultimately decays onto the ground state. The exchange of population between different electronic states in a nonradiative process is called internal conversion (IC). IC processes are particularly efficient in regions of the configuration space where the electronic states become close in energy or even degenerate and configurations at which two electronic states are degenerate are called conical intersections (CIs). CIs play a crucial role in determining the photochemical pathways of a molecule and they will be discussed more in detail in chapter 2.

If ICs processes are not easily accessible, the molecule may reach a minimum in the excited state (S_1min) and remain “trapped” in the excited state for long enough to relax through fluorescence. ③ Fluorescence is a radiative process in which the molecule relaxes to its ground state from an excited state with the same spin-multiplicity by emitting light. The energy of the photon emitted is usually lower than the energy of the light that was absorbed. This so-called Stokes shift – defined as the energy difference between the 0-0 emission and absorption bands – is caused by the solvent reorganization and energy redistribution that occurs in the excited state before emission.

What happens if the molecule can access electronic states with a different spin multiplicity? ④ The change of spin-multiplicity following photo-excitation is called intersystem crossing (ISC). ISC is particularly efficient in metal complexes or organic molecules counting one or more heavy atoms and will be further detailed in chapter 2. Upon ISC, the molecule can suffer the IC process, with the formation of photoproducts or ⑤ relax to the S_0 state via a radiative mechanism called phosphorescence, which, in contrast with fluorescence, involves a change in the electron spin.

The scheme presented in Fig. 1.1 provides the framework to understand a number of

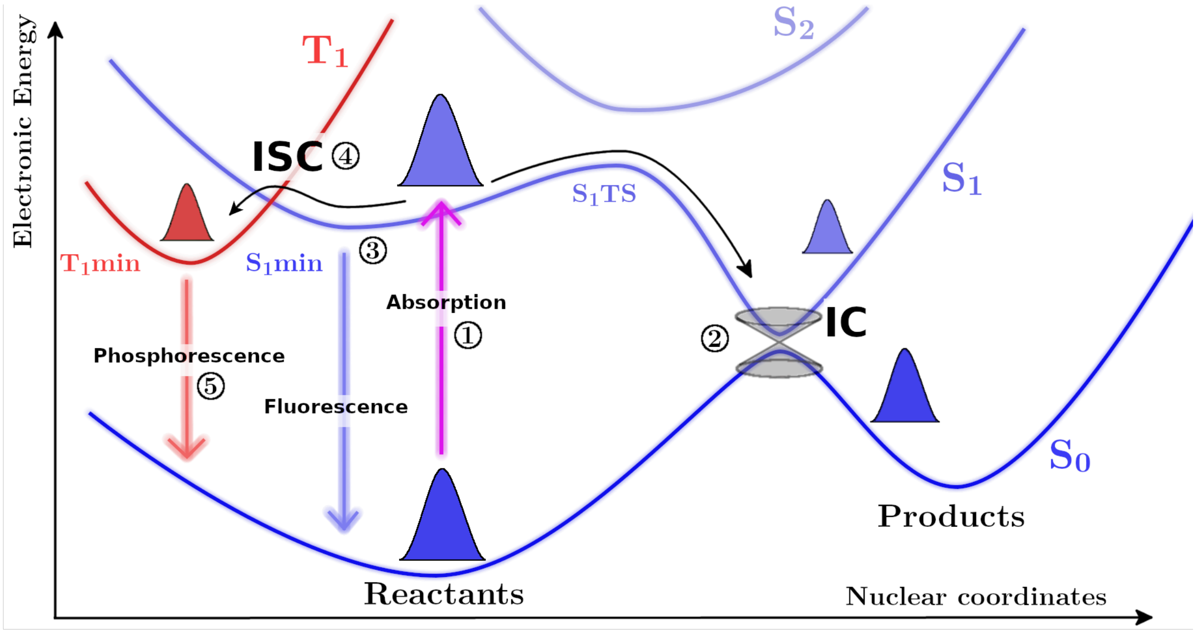

Figure 1.1: Schematic representation of photochemical and photophysical reactions. The absorption of light promotes the ground state molecule (dark blue Gaussian) to a higher excited state (S_1). From the excited state, the molecule can suffer internal conversion towards the ground state (S_0) or intersystem crossing toward a state with different spin-multiplicities. Additionally, we can observe radiative decay by the emission of photons. If the emission occurs from a state with the same spin-multiplicity as the ground state, the process is called fluorescence, otherwise, it is termed phosphorescence.

photochemical processes, including some key steps of oxygenic photosynthesis as light absorption, exciton formation, and charge separation. The first photosynthetic organisms (primitive cyanobacteria) appeared around 3.5 billion years ago[43] and their early presence on Earth is confirmed by stromatolites such as the one in the Shark Bay (Australia)[44–46] – one of the oldest fossils on Earth. Photosynthesis is accomplished by a series of reactions catalyzed by two separate photosystems, PSI and PSII. Both PSI and PSII operate with extremely high quantum yield, unmatched by any biological or chemical system (1.0 for PSI and 0.85 for PSII).[47, 48] PSII – which is responsible for the oxidization of H_2O liberating H^+ and O_2 through the absorption of four photons – have been extensively studied to understand the architecture and the mechanistic steps that allow its functionality.[49, 50] To accomplish this goal, computational and theoretical chemistry has provided tremendous help. Not only simulations have supported the modelling of the natural light-harvesting complexes and unrevealing their reaction mechanisms,[51–54] but they have also played a fundamental role to artificially mimic photosynthesis using synthetic materials.[55, 56] One of the first developments in artificial photosynthesis, inspired by the seminal work of Fujishima and Honda in 1972,[57] used semiconductor materials[58–60] as a replacement for natural photosynthetic pigments. More recently, bio-mimetic metal complexes have been developed as miniaturized catalytic centres for water splitting[61, 62] or to activate and reduce CO_2[62, 63] and facilitate its conversion into useful chemicals, such as methanol[64] or formic acid.[65]

Alongside photosynthesis, vision is another intriguing photochemical process that has benefited incredibly from the advancement of computational chemistry. The vision process occurs in the retina of the eye where light is absorbed by photoreceptors in the rods and cones.[66] The pigment that absorbs light, also called rhodopsin, is composed of a protein (opsin) and a small molecule called retinal covalently linked to the opsin.[66, 67] When light hits rhodopsin, it causes the photoisomerization of the retinal that, in animal rhodopsins, isomerize from the 11-*cis* to the all-*trans* configuration.[68–70] The process of vision is a perfect example of how nature transforms light into mechanical energy. Another fascinating example comes from the bacteria rhodopsin which was first discovered in 1971.[71] The wild-type protein serves as a light-driven ion pump (see Fig. 1.2) – one of the best-used neural silencers in optogenetics[72] – but, upon mutations, shows fluorescence with efficient quantum yield.[73] Computational studies have provided a robust framework to understand how mutations affect the photochemical and photophysical properties of rhodopsins such as their absorption,[74] fluorescence[75] or even enabled the design of artificial ones.[76]

More details on computational methods for photochemistry will be provided in chapter 2 of this thesis.

1.3.1 Atmospheric photochemistry

The overarching need to understand the process of photosynthesis and vision has served as a fertile playground for computational and theoretical chemistry. However, the last decades have also seen a growing interest in environmental issues with particular attention to global warming effects and air pollution. Population growth, in combination with the rising demand for energy per capita, led to the increasing consumption of coal, oil, and natural gas[77] and the emissions produced by their combustion – in the form of sulfur oxides, nitrogen oxides, carbon oxides, and volatile organic compounds (VOCs) – are an increasing concern. Examples of the interplay between the bi-products formed by the combustion of hydrocarbons and light date back to the half of the 20^{th} century when Haagen-Smit identified the hydrocarbons and nitrogen oxides cocktail as the precursor of photochemical smog.[78, 79] The nitrogen dioxide released by vehicle circulation quickly photodissociates into oxygen and nitrogen oxide radicals under intense solar irradiation. The formation of oxygen radical species triggers the tropospheric formation of ozone which – in combination with oxidized hydrocarbons – led to the production of peroxyacyl nitrates,[80, 81] a highly phytotoxic and eye irritants compounds.[82, 83]

Photochemical smog is typical of densely inhabited urban areas. However, other fascinating chemical processes also occur in forestal and rural areas where anthropogenic emissions are limited. In fact, VOCs such as terpenoids (aka isoprenoids), alcohols, and carbonyls are abundantly released by biogenic sources encompassing plants and microorganisms.[84] Although

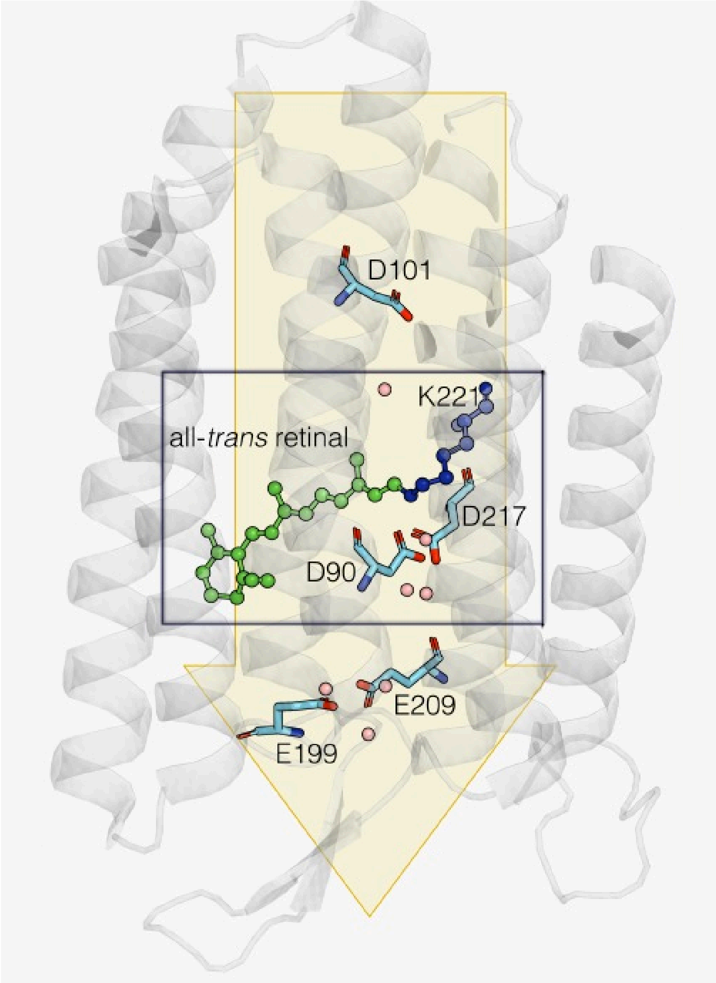

Figure 1.2: Archaerhodopsin-3 (Arch3) rhodopsin. Arch3 is a proton pump, used in optogenetics to silence the synaptic transmission by hyperpolarizing the membrane potential of targeted neurons. The proton pump activity of Arch3 involves multi-step reaction processes triggered by the isomerization of the retinal.

atmospheric chemistry is not restricted to the oxidation of VOCs, the plethora of reactions that characterize VOCs oxidation makes their investigations challenging and an unprecedented collective effort from the scientific community has been devoted to inspect their reactivity. This demanding yet rewarding task has already provided the basis to build up atmospheric models, such as the master chemical mechanism (MCM).[85, 86] The MCM – armed with the kinetic rate constants of the oxidation reactions of atmospherically-relevant VOCs – can predict the time-evolution of chemicals in the atmosphere. Atmospheric models of this kind have been particularly useful in shaping political and societal decisions on a worldwide scale to control air pollution.

Examining all oxidation reactions that take place in the atmosphere and quantifying their kinetic rate is a Homeric work due to the myriad of VOCs involved. Further exacerbating the issue, oxidation reactions are often mediated by radical species which are transient species, hardly characterizable experimentally. This limitation is even more striking when we consider the photochemistry of these transient VOCs, which may contain one or more chromophoric groups and are expected to absorb light.[87, 88] Surprisingly, the photochemistry of transient VOCs is often completely neglected in atmospheric models or sometimes deduced by qualitative methodology such as structure-activity relationships (SARs).[6, 89] Using SARs, the rate of a reaction can be deduced by a proxy molecule or – in multi-functional compounds – estimated by the mono-functional parents. Although SARs are extremely popular in atmospheric chemistry and on some occasions are also accurate, their applicability to processes showing several branching pathways (as in the case of photochemical processes) can be less appealing.[90]

For computational chemists, the photochemistry of transient VOCs is instead an exciting playground where protocols developed by theoretical chemistry can be used to determine the kinetic rates *in silico*. But is computational and theoretical chemistry mature enough to face this challenge? This thesis will address this question.

1.3.2 The photochemistry of Lewis adducts

Another field of photochemistry with limited experimental data and a circumscribed understanding is the photochemistry of Lewis adducts. Lewis adducts are named after the American physical chemist Gilbert N. Lewis, who introduced the concept of the Lewis acid and Lewis base in 1923.[91] In response to the definition proposed by Brønsted[92] and Lowry[93], he wrote "*It seems to me that with complete generality we may say that a basic substance is one which has a lone pair of electrons which may be used to complete the stable group of another atom and that an acid substance is one which can employ a lone pair from another molecule in completing the stable group of one of its own atoms. In other words, the basic substance furnishes a pair of electrons for a chemical bond; the acid substance accepts such a pair.*"[91] The early studies on Lewis adducts laid the foundation for the field of coordination chemistry and the investigation of Lewis adducts in various chemical reactions and processes.[94, 95] During the following years, the field of coordination chemistry experienced significant growth, with the discovery of new coordination compounds[96] and the growth in the understanding of their physical and chemical properties.[97, 98]

Today, the chemistry of Lewis adducts continues to be an active area of research, and these molecules found applications in a variety of different fields of chemistry. Lewis pairs have played an important role in many chemical reactions, including organic synthesis,[99, 100] catalysis,[101–103] production of new types of dyes for solar cells[104] and polymers.[105, 106] The main feature that distinguishes Lewis adducts and that makes them so appealing for a variety of applications is the peculiarities of the dative bond. The dative bond is usually weaker with respect to both covalent and ionic compounds, which in turn is reflected in lower melting and boiling points. Another peculiar feature is their dissociative behaviour that occurs in a heterolytic fashion. In fact, in the ground state, Lewis adducts generally dissociate into their parent Lewis acid and base and this dissociation is usually reversible. Things become more interesting when we consider their reactivity in an excited state. The photochemistry of Lewis adducts includes isomerization[107], photo-rearrangement[108, 109], and photo-dissociation leading to the breaking of the dative bond between the Lewis acid and base,[7, 110] but almost nothing is known about the mechanistic details of these photochemical reactions.

1.4 Aims of the thesis

In the introduction, I have presented four topics of photochemistry that have attracted the attention of scientists for a long time and that, despite increasing efforts, continue to reveal surprises and leave the community with questions to be answered. However, there is a key difference between the four topics. While in photosynthesis and vision, theoretical and computational chemistry have already strong roots and solid protocols to study the underlined process, the same can not be said for the photochemistry of VOCs and Lewis adducts perhaps due to the more complex nature of these photochemical processes. Theoretical and computational chemistry allowed huge progress in the field of photosynthesis and vision and I believe that its contribution would be determinant in studying the photochemistry of VOCs and Lewis adducts, where simulations are still in their infancy.

The first issue I have highlighted is that current atmospheric models do not include photochemical processes related to transient VOCs. Since these processes are extremely challenging to study experimentally, this thesis will aim to lay the foundations of determining *in silico* the photolysis rate constant of transient VOCs – the first-order kinetic rate for a specific photolysis process. To do so, I break down the problem in the calculations of two observables that are (i) the photoabsorption cross-section and (ii) the wavelength-dependent quantum yield.

The simulation of the absorption cross-section and the wavelength-dependent quantum yield is not easy for transient VOCs. This difficulty arises from the high flexibility and the complex nature of the electronic states that drive their photochemistry. Hence, an informed choice of theoretical approaches is required. Given the lack of data in the literature, I will provide a first scrutiny and benchmark for the available theoretical methods in the study of VOCs, highlighting issues that were still undisclosed, and proposing a protocol to determine photolysis observables. Finally, I use our developed protocol to investigate the photochemistry of a few exemplary transient VOCs of high interest in atmospheric chemistry, fully characterizing their photochemical pathways as well as quantifying their photolysis rate constant under atmospheric conditions.

Building upon this protocol I will investigate the photochemistry of Lewis adducts. Despite the vast body of literature on the use of photochemistry with Lewis adducts, very little is known about the mechanistic details that drive their photodissociation, and, due to their prime role in basically all fields of chemistry, the understanding of their photodissociation is a top priority. Although it has been pointed out that the photodissociation behaviour of these systems strongly depends on the Lewis basicity of the adduct, a clear understanding of the role of the substituents is still unclear.[7, 111] Armed with the protocols developed for VOCs I will show how the computational photochemistry toolbox can be used to investigate the photochemistry of Lewis adducts providing a better understanding of the role of substituent and clarifying their photodissociation behaviour.

1.5 Outline of the thesis

In the first part of this thesis, I will present some of the cutting-edge methods that are strings to the bow of computational chemists to study molecular photochemistry. In doing so, I give lustre to both electronic structure and dynamic strategies which are used to determine static properties and to capture dynamical effects triggered by the photo-excitation of molecules.

Chapter 2 presents the heart of theoretical chemistry by discussing the approximations to solve the molecular Schrödinger equation. In this chapter I will focus on the time-dependent molecular Schrödinger equation and build up a hierarchy of approximations that constitute the backbone of computational photochemistry. I will highlight the main features characterizing trajectory surface hopping and *ab initio* multiple spawning – somewhat state-of-the-art in theoretical photochemistry. To conclude, I will illustrate a few of the more noteworthy computational strategies to compute electronic quantities by solving the time-independent version of the electronic Schrödinger equation.

Chapter 3 aims to illustrate a theoretical protocol to calculate the two crucial observables required to estimate the photolysis rate constant of volatile VOCs, namely the photoabsorption cross-section and the wavelength-dependent quantum yield. I will investigate in detail the current approaches available to compute the photoabsorption cross-sections of VOCs paying particular attention to the nuclear ensemble approach.

In chapter 4, I highlight an artefact of the algebraic diagrammatic construction at the second order – a popular electronic structure method within the computational photochemistry community – which could have been a great candidate to simulate the photochemistry of transient VOCs. This method produces artificial IC pathways leading to ultra-fast relaxation to the ground state when used for carbonyl-containing molecules, a common motif of VOCs.

In chapter 5 I investigate the photochemistry of a crucial transient VOC, namely 2-hydroperoxypropanal. This transient VOC is formed during the degradation of isoprene in the atmosphere and its photolysis is thought to be a factor in determining the oxidation power of the atmosphere. Since experimental data is not available for either the photoabsorption cross-section or the wavelength-dependent quantum yield, I use the computational chemistry toolbox to predict *in silico* its photolysis rate constant.

Chapter 6 will illustrate the photochemistry of Lewis adducts. Using three exemplary molecules, I will uncover the mechanistic details that drive the photodissociation of B−N dative bond. Using a molecular engineering approach to fine-tune the properties of adducts, I will provide unprecedented insights into the IC process featuring photoexcited Lewis adducts. Despite this work being preliminary, I believe that it will serve as a launch pad for further research in the field to provide a better understanding of the photochemistry of Lewis adducts which is surprisingly uncharted.

CHAPTER 2

A theoretical approach to photochemistry

2.1 A brief survey of molecular dynamics

Solving the equations of motion for the particles that constitute a molecular system is paramount to gaining important insights into molecular reactivity and chemical properties. However, computational chemists have to find their way between Scylla and Charybdis in order to simulate properties with accurate but efficient methodologies. Generally, the first assumption in molecular dynamics (MD) arises from the inherent nature of nuclei and electrons which evolves in two very different time/energy scales. Electrons are light particles and their dynamics are governed by quantum mechanics. On the other hand, nuclei are heavier particles whose dynamics can be described, in some instances, by the simpler Newton's law.

Being able to simulate the simpler classical equation of motion for the nuclei, without worrying about electrons, is an extreme approximation but it is still popular in the field of computational chemistry. In this framework, the effects of electrons on nuclear dynamics are parameterized using simple mathematical expressions called force fields. These mathematical expressions mimic the electron-nuclear interaction energies for a specific nuclear configuration on the basis of geometric variables such as bond lengths, angles, and dihedrals. Force fields also include long-range interactions such as van der Waals forces – to describe electronically neutral atom centres and electrostatic effects between partially charged atom centres. These effects are the results of (instantaneous or permanent) depletion or accumulation of electron densities that, however, figure in the force field as parametrized values and not as the outcome of a cumbersome electronic structure calculation. The sum of all interaction energies in the force field constitutes a potential energy that depends on the nuclear coordinates and is employed to propagate (classically) the nuclear equations of motion.[112, 113] This procedure, dubbed molecular mechanics (MM), yields efficient computational scaling which is highly desirable for molecular systems of the size of proteins and biological aggregates. On the other hand, it sufferers critical drawbacks that prevent its applicability for general molecular reactions. Firstly, (i) the transferability of the force fields to predict a wide range of molecules and molecular environments is challenging. An additional aspect (ii) is the lack of information about the electronic structure, *i.e.*, and the ability to describe different bonding patterns.

In stark contrast with MM, *ab initio* molecular dynamics (AIMD) takes fully into account the quantum nature of the electrons through the solution of the time-independent electronic Schrödiger equation (TISE). For each nuclear configuration, solving the TISE yields the electronic energy (which is coined potential energy surface, PES, for varying nuclear conformations) and its gradient with respect to the nuclear coordinates which are the two ingredients required to propagate the classical nuclear dynamics. The first AIMD simulation was already conducted in the 1970s,[114] but it was with the seminal paper of Roberto Car and Michele Parrinello, in the mid-1980s,[115] that the popularity of AIMD has exponentially grown over the last 15 years. The major drawback of using AIMD instead of MM is the increase in computational efforts required to obtain the PES on which the nuclei evolve. Nevertheless, AIMD constitutes a practical way to describe chemical processes without any prior knowledge of the system in consideration. AIMD can be safely used to study a large variety of chemical reactions that occur wholly in a single electronic state and its accuracy mainly depends on the method used to solve the TISE. Accurate electronic-structure methods describe in a balanced way the different regions of the PES, yielding consistent and reliable outcomes for energy and gradients, and as a result, producing accurate nuclear dynamics.

However, the accurate description of the energy and gradients is not sufficient – even though necessary – when multiple electronic states are involved in the chemical process. In this case, another important effect must be accounted for: the influence that the nuclear motion exerts on the electron motion. This coupling is the typical process that one expects when we wish to simulate photochemical and photophysical phenomena where the electronic and nuclear dynamics become entangled. As we will see in this chapter, this type of dynamics is challenging and for this reason, a variety of computational methods have been developed to fulfil this goal, gathered under the name of nonadiabatic AIMD. It would be a Homeric work to describe all categories of nonadiabatic AIMD and I will focus our attention now on the most important mixed quantum-classical schemes. One of the simplest mixed quantum-classical methods is trajectory surface hopping (TSH),[116–120] which is based on the Born-Hung expansion of the molecular wavefunction. It represents an optimal starting point to describe the excited state dynamics of complex molecular systems due to its simplicity and computational efficiency. Possible alternatives to TSH, not discussed in this thesis, are the Ehrenfest dynamics – derived from a mean-field ansatz,[119–123] or the coupled trajectory mixed quantum-classical – derived from the exact factorization of the molecular wavefunction.[124–126] As the name suggests, in quantum-classical methods the electronic and nuclear motions are treated on two different footings: the electrons quantum mechanically and the nuclei classically. To propagate the nuclear dynamics the electronic properties are computed on-the-fly which means that only a local and limited number of electronic structure calculations (the bottleneck of dynamical propagation) are required.

Despite the reasonable efficiency, many quantum mechanical phenomena cannot be captured such as decoherence, wavepacket interference, and tunneling. One possible way to overcome these drawbacks is to fully incorporate the quantum nature of the nuclei, and this can be achieved in a multitude of ways. An interesting example is full multiple spawning (FMS)[127–129] which proposes to represent the nuclear wavefunction with Gaussians and to evolve the Gaussians classically. Other methods which exploit Gaussian basis functions to describe the nuclear wavepackets are then multiconfigurational Ehrenfest[130–132] or variational multiconfigurational Gaussian.[133–135] Finally, the crowning event of our discussion terminates with the solution of the time-dependent Schrödinger equation (TDSE) for the full molecular wavefunction, expanded on a grid using time-dependent single particle basis functions – such as multiconfigurational time-dependent Hartree[136–138] – or with predefined time-independent basis functions. While these latter approaches are (in the non-relativistic limit) the most accurate way to describe molecular dynamics, their usage is extremely limited due to the prohibitive computational costs. In fact, in stark contrast with on-the-fly methodologies, full quantum dynamics require the knowledge of the electronic PESs for a broad portion of the configuration space which becomes quickly unfeasible when the molecular system has more than a few degrees of freedom.

In section 2.2, I will introduce the theoretical background to understand nonadiabatic AIMD. Starting from the TDSE, I will present one of the most popular ways to decompose the total molecular wavefunction, namely the Born-Huang (BH) expansion (section 2.2.1). In section 2.2.2, I will derive the ubiquitous Born-Oppenheimer approximation (BOA) that is the cornerstone of AIMD in which we neglect the coupling between electronic and nuclear motion such that the nuclear dynamics evolves on a single electronic PES.

In section 2.3, I will describe the differences between adiabatic and diabatic electronic states and how these two different representations can help theoretical chemists gain important chemical insights from the molecular dynamics simulation.

Section 2.4 will present an overview of the most important nonadiabatic AIMD method which can be generally applied to realistic molecular systems. Starting from the BH expansion will explain the most important equations featuring TSH and the main concepts behind *ab initio* multiple spawning (AIMS) in section 2.4.1 and 2.4.2, respectively.

Finally, section 2.5 focuses the attention on methods to solve the TISE, a prerequisite to solve the nuclear equation of motion. In section 2.5.2, I will introduce the concept of Slater determinant (SD) and how to calculate excited state properties from a linear combination of SD using the so-called configuration interaction expansion. A similar concept will be used in section 2.5.3 to describe the state-average complete active space self-consistent field method that is one of the most popular ways to compute excited state properties. To conclude, in section 2.5.4 I will illustrate the algebraic diagrammatic construction at the second order scheme, a newcomer in the field of nonadiabatic AIMD that has already shown promising results in terms of accuracy and computational performance.

2.2 The time-dependent molecular Schrödinger equation

The state of all particles in a molecular system, *i.e.*, electrons and nuclei, is completely described by a multi-dimensional wavefunction $\Psi(\mathbf{r},\mathbf{R},t)$. $\Psi(\mathbf{r},\mathbf{R},t)$ depends on the nuclear coordinates $\mathbf{R}$, the electronic coordinates $\mathbf{r}$ and time t and it spans $3\times(N_n+N_e)+1$ dimensions where N_n and N_e are the number of nuclei and electrons, respectively. The wavefunction encodes all information about the molecular system. It describes both electrons and nuclei as quantum mechanical particles and it accounts for the exact coupling between them. The time evolution of $\Psi(\mathbf{r},\mathbf{R},t)$ – in the non-relativistic limit – is governed by the TDSE[12] that reads

$$i\hbar\frac{\partial\Psi(\mathbf{r},\mathbf{R},t)}{\partial t}=\hat{H}(\mathbf{r},\mathbf{R})\Psi(\mathbf{r},\mathbf{R},t)\,, \tag{2.1}$$

where $\hat{H}(\mathbf{r},\mathbf{R})$ is the molecular Hamiltonian defined in atomic units (but retaining $\hbar$) as

$$\begin{aligned}\hat{H}(\mathbf{r},\mathbf{R})&=-\sum_{\alpha}^{N_n}\frac{\hbar^2}{2M_\alpha}\nabla_\alpha^2-\sum_{i}^{N_e}\frac{\hbar^2}{2}\nabla_i^2+\sum_{i,j<i}^{N_e,N_e}\frac{1}{|\mathbf{r}_i-\mathbf{r}_j|}-\sum_{\alpha,i}^{N_n,N_e}\frac{z_\alpha}{|\mathbf{R}_\alpha-\mathbf{r}_i|}+\sum_{\alpha,\beta<\alpha}^{N_n,N_n}\frac{z_\alpha z_\beta}{|\mathbf{R}_\alpha-\mathbf{R}_\beta|}\\&=\hat{T}_n(\mathbf{R})+\hat{H}^{el}(\mathbf{r},\mathbf{R})\,.\end{aligned} \tag{2.2}$$

$\hat{T}_n(\mathbf{R})=-\sum_\alpha^{N_n}\frac{\hbar^2}{2M_\alpha}\nabla_\alpha^2$ is the nuclear kinetic energy operator (KEO) and $\hat{H}^{el}(\mathbf{r},\mathbf{R})$ is the electronic Hamiltonian which incorporates the electronic kinetic energy, the electron-electron repulsion, the nuclear-electron Coulomb attraction, and the nuclear-nuclear repulsion terms. The letters $\{i,j\}$ label the electrons and $\{\alpha,\beta\}$ the nuclei. M_α and z_α are the mass and the atomic number of the α-th nucleus. It is worth noticing that in Eq. (2.2) we have not included any external field. $\hat{H}^{el}(\mathbf{r},\mathbf{R})$ depends on $\mathbf{R}$ through the electron-nuclear attraction and the nuclear-nuclear repulsion term. In the limit that the nuclei are immobile ($\hat{T}_n(\mathbf{R})\to 0$), we can map the spectrum of $\hat{H}^{el}(\mathbf{r},\mathbf{R})$ at each fixed position $\{\mathbf{R}\}$ of the nuclei. The eigenfunctions of $\hat{H}^{el}(\mathbf{r},\mathbf{R})$, called adiabatic states $\{\Phi_j(\mathbf{r};\mathbf{R})\}$, and its eigenvalues, denoted as electronic energies $E_j^{el}(\mathbf{R})$, satisfy the TISE equation

$$\hat{H}^{el}(\mathbf{r},\mathbf{R})\Phi_j(\mathbf{r};\mathbf{R})=E_j^{el}(\mathbf{R})\Phi_j(\mathbf{r};\mathbf{R})\,. \tag{2.3}$$

Importantly, the adiabatic states form a complete orthonormal basis

$$\int d\mathbf{r}\;\Phi_i(\mathbf{r};\mathbf{R})\Phi_j(\mathbf{r};\mathbf{R})=\delta_{ij}\,. \tag{2.4}$$

The concept of complete basis will be useful in the following sections and it guarantees that any function belonging to a Hilbert space can be expressed through a unique expansion in terms of the complete basis.

The adiabatic states are a ubiquitous concept in computational chemistry and they will be our starting point to decompose $\Psi(\mathbf{r}, \mathbf{R}, t)$ in the BH expansion.

2.2.1 Born-Huang expansion

The BH expansion was first introduced in 1951 for the time-independent problem.[139] It expands $\Psi(\mathbf{r}, \mathbf{R}, t)$ – without introducing any approximation – in terms of the adiabatic states

$$\Psi(\mathbf{r}, \mathbf{R}, t) = \sum_j^{\infty} \chi_j(\mathbf{R}, t)\Phi_j(\mathbf{r}; \mathbf{R})\,. \tag{2.5}$$

The $\chi_j(\mathbf{R}, t)$ can be viewed as time-dependent expansion coefficients (nuclear factors) and they account for the full time-dependency of the molecular wavefunction. Inserting the BH expansion into the TDSE (Eq. (2.1)) leads to

$$\begin{aligned} i\hbar\sum_j^{\infty} \Phi_j(\mathbf{r}; \mathbf{R})\frac{\partial \chi_j(\mathbf{R}, t)}{\partial t} &= \sum_j^{\infty} \Big\{\chi_j(\mathbf{R}, t)\Phi_j(\mathbf{r}; \mathbf{R})E^{el}(\mathbf{R}) - \sum_{\alpha}^{N_n} \frac{\hbar^2}{2M_\alpha}\Big[\chi_j(\mathbf{R}, t)\nabla_\alpha^2\Phi_j(\mathbf{r}; \mathbf{R}) + \\ &\qquad \Phi_j(\mathbf{r}; \mathbf{R})\nabla_\alpha^2\chi_j(\mathbf{R}, t) + 2\nabla_\alpha\Phi_j(\mathbf{r}; \mathbf{R})\nabla_\alpha\chi_j(\mathbf{R}, t)\Big]\Big\}\,. \end{aligned} \tag{2.6}$$

Multiplying this expression by $\Phi_i^*(\mathbf{r}; \mathbf{R})$, integrating over the electronic coordinates, and noting that $\chi_j(\mathbf{R}, t)$ does not depend on the integration variable $d\mathbf{r}$, we obtain the equations of motion for the nuclear factors:

$$i\hbar\frac{\partial \chi_i(\mathbf{R}, t)}{\partial t} = \Big[-\sum_{\alpha}^{N_n} \frac{\hbar^2}{2M_\alpha}\nabla_\alpha^2 + E_i^{el}(\mathbf{R})\Big]\chi_i(\mathbf{R}, t) - \sum_j^{\infty} C_{ij}(\mathbf{R})\chi_j(\mathbf{R}, t)\,, \tag{2.7}$$

where the $C_{ij}(\mathbf{R})$ are the exact nonadiabatic coupling matrix elements:

$$C_{ij}(\mathbf{R}) = \sum_{\alpha}^{N_n} \frac{\hbar^2}{2M_\alpha}\int d\mathbf{r}\,\Phi_i^*(\mathbf{r}; \mathbf{R})\nabla_\alpha^2\Phi_j(\mathbf{r}; \mathbf{R}) + \sum_{\alpha}^{N_n} \frac{\hbar^2}{M_\alpha}\Big(\int d\mathbf{r}\,\Phi_i^*(\mathbf{r}; \mathbf{R})\nabla_\alpha\Phi_j(\mathbf{r}; \mathbf{R})\Big)\cdot\nabla_\alpha\,. \tag{2.8}$$

The first term in the right-hand side of Eq. (2.8) is a matrix element of the KEO – second-order nonadiabatic couplings – whereas the second depends on their momenta – first-order nonadiabatic couplings (NAC). The $C_{ij}(\mathbf{R})$ are responsible for the coupling between electronic states and the nuclear motion and therefore represent the feedback that the electronic motion exerts on the nuclear motion. They are partitioned as inter-state couplings ($i \neq j$) and intra-state coupling ($i = j$). In the latter case, the quantity $\int d\mathbf{r}\,\Phi_j^*(\mathbf{r}; \mathbf{R})\nabla_\alpha\Phi_j(\mathbf{r}; \mathbf{R})$ vanishes (for real electronic wavefunction), and only the first term on the right-hand-side of Eq. (2.8) survives.

2.2.2 Born-Oppenheimer approximation

Looking at Eq. (2.7) we notice that amplitude transfer between two different adiabatic states is possible only when we include the intra-state couplings that are the off-diagonal coupling matrix elements (C_{ij} terms). In the Born-Oppenheimer approximation (BOA)[21] these off-diagonal terms are neglected and, therefore, the nuclear amplitude transfer between two different adiabatic states is not possible. Within this approximation, the molecular wavefunction assumes the simple form of a single product between nuclear and electron terms: $\Psi(\mathbf{r}, \mathbf{R}, t) = \chi_i(\mathbf{R}, t)\Phi_i(\mathbf{r}; \mathbf{R})$ and Eq. (2.7) reduces to

$$i\hbar \frac{\partial \chi_i(\mathbf{R}, t)}{\partial t} = \Big[-\sum_{\alpha}^{N_n} \frac{\hbar^2}{2M_\alpha} \nabla_\alpha^2 + E_i^{el}(\mathbf{R}) - \sum_{\alpha}^{N_n} \frac{\hbar^2}{2M_\alpha} \int d\mathbf{r}\, \Phi_i^*(\mathbf{r}; \mathbf{R}) \nabla_\alpha^2 \Phi_i(\mathbf{r}; \mathbf{R}) \Big] \chi_i(\mathbf{R}, t)\,. \tag{2.9}$$

The equation of motion for the nuclei now takes the form of a TDSE where the $\chi_i(\mathbf{R}, t)$ is the nuclear wavefunction satisfying the continuity equation. The term $\int d\mathbf{r}\, \Phi_i^*(\mathbf{r}; \mathbf{R}) \nabla_\alpha^2 \Phi_i(\mathbf{r}; \mathbf{R})$ is the diagonal Born-Oppenheimer correction (DBOC), a “potential-like” term that can be regarded as a second-order correction in $\hbar$ to the electronic PES. On a first approximation, it is reasonable to neglect this term which is usually very small. However, the DBOC diverges in the proximity of the crossing of two (or more) adiabatic states, drastically modifying the shape of the electronic PESs. Mixed quantum-classical methods usually do not include the DBOC that can actually produce detrimental effects.[140, 141] Neglecting also the DBOC term in Eq. (2.9) leads to the standard adiabatic BOA reading

$$i\hbar \frac{\partial \chi_i(\mathbf{R}, t)}{\partial t} = \Big[-\sum_{\alpha}^{N_n} \frac{\hbar^2}{2M_\alpha} \nabla_\alpha^2 + E_i^{el}(\mathbf{R}) \Big] \chi_i(\mathbf{R}, t)\,. \tag{2.10}$$

Since this chapter is focused on mixed quantum-classical dynamics, it is instructive at this point to derive a classical equation of motion for the nuclei from Eq. (2.10). In doing so, we remind the reader that we are starting from the adiabatic BOA, in which the coupling between the nuclear and electronic motions is neglected, and the nuclear dynamics is restricted to a single electronic PES.

2.2.3 Taking the classical limit of the adiabatic Born-Oppenheimer approximation

A well-known route to re-write quantum mechanical equation – without introducing approximation – is by invoking the polar representation for the wavefunction[142, 143]:

$$\chi_i(\mathbf{R}, t) = A_i(\mathbf{R}, t) e^{iS_i(\mathbf{R}, t)/\hbar}\,, \tag{2.11}$$

where $A_i(\mathbf{R}, t)$ and $S_i(\mathbf{R}, t)/\hbar$ are real functions that correspond to an amplitude and a phase, respectively. Inserting Eq. (2.11) into Eq. (2.10) and separating the result into real and imaginary parts, we obtain two coupled equations for the time-evolution of the amplitudes and the phases:

$$\frac{\partial S_i(\mathbf{R},t)}{\partial t} = -E_i^{el}(\mathbf{R}) + \sum_\alpha^{N_n} \frac{\hbar^2}{2M_\alpha}\left[\frac{\nabla_\alpha^2 A_i(\mathbf{R},t)}{A_i(\mathbf{R},t)} - \frac{1}{\hbar^2}\Big(\nabla_\alpha S_i(\mathbf{R},t)\Big)^2\right], \tag{2.12}$$

$$\frac{\partial A_i(\mathbf{R},t)}{\partial t} = -\sum_\alpha^{N_n} \frac{1}{2M_\alpha}\Big[2\nabla_\alpha A_i(\mathbf{R},t)\cdot\nabla_\alpha S_i(\mathbf{R},t) - A_i(\mathbf{R},t)\nabla_\alpha^2 S_i(\mathbf{R},t)\Big]. \tag{2.13}$$

Eq. (2.13) can be re-written, after multiplying on the left by $2\,A_i(\mathbf{R},t)$, as

$$\frac{\partial A_i(\mathbf{R},t)^2}{\partial t} + \sum_\alpha^{N_n}\frac{1}{M_\alpha}\nabla_\alpha\Big(A_i(\mathbf{R},t)^2\nabla_\alpha S_i(\mathbf{R},t)\Big) = 0, \tag{2.14}$$

which is equivalent to

$$\frac{\partial \rho_i(\mathbf{R},t)}{\partial t} + \sum_\alpha^{N_n}\nabla_\alpha\,\mathbf{J}_{i,\alpha}(\mathbf{R},t) = 0. \tag{2.15}$$

Eq. (2.15) is the continuity equation for the given electronic state i; where we have identified the nuclear probability density as $\rho_i(\mathbf{R},t) = |\chi_i(\mathbf{R},t)|^2 = A_i(\mathbf{R},t)^2$ from Eq. (2.11), and the associated current density as $\mathbf{J}_{i,\alpha}(\mathbf{R},t) = A_i(\mathbf{R},t)^2\left(\nabla_\alpha S_i(\mathbf{R},t)\right)/M_\alpha$.

Eq. (2.12) describes the time evolution of the nuclear phase on the electronic state i. Its classical limit is imposed by $\hbar \to 0$,

$$\frac{\partial S_i(\mathbf{R},t)}{\partial t} + E_i^{el}(\mathbf{R}) + \sum_\alpha^{N_n}\frac{1}{2M_\alpha}\Big(\nabla_\alpha S_i(\mathbf{R},t)\Big)^2 = 0, \tag{2.16}$$

yielding a first-order partial differential equation in ($3N_n + 1$ variables) completely equivalent to the Hamilton-Jacobi equation[144]

$$\frac{\partial S_i(\mathbf{R},t)}{\partial t} + H_i(\mathbf{R},\nabla S_i(\mathbf{R},t),t) = 0, \tag{2.17}$$

where $S_i(\mathbf{R},t)$ is the Hamilton's principal function with conjugate momenta $\mathbf{P}_i = \nabla S_i(\mathbf{R},t)$. Within this classical approximation, the nuclear dynamics reduce to a fluid of trajectories moving on the vector field generated by the Hamilton equations of motion. The use of the Lagrangian frame, *i.e.*, the moving grid represented by a set of nuclear trajectories ($\mathbf{R} \to \mathbf{R}(t)$ and $\mathbf{P} \to \mathbf{P}(t)$), has found tremendous popularity due the simplicity and effectiveness in the depiction of molecular reactivity. In such a framework, an initial condition $(\mathbf{R}(t_0), \mathbf{P}(t_0))$ on selected state i evolves via the classical Newtonian equation of motion.

To derive Newton's equation we apply the operator ∇ from the left to Eq. (2.16), obtaining

$$\frac{\partial}{\partial t}\nabla S_i(\mathbf{R},t) + \nabla E_i^{el}(\mathbf{R}) + \sum_\alpha^{N_n}\frac{1}{M_\alpha}\nabla_\alpha S_i(\mathbf{R},t)\cdot\nabla\left(\nabla_\alpha S_i(\mathbf{R},t)\right) = 0, \tag{2.18}$$

where we have used Schwarz's theorem to re-write $\nabla\frac{\partial S_i(\mathbf{R},t)}{\partial t} = \frac{\partial}{\partial t}\nabla S_i(\mathbf{R},t)$. Given the chain rule in vector form

$$\frac{d}{dt}\nabla S_i(\mathbf{R},t) = \frac{\partial}{\partial t}\nabla S_i(\mathbf{R},t) + \sum_\alpha^{N_n}\frac{d\mathbf{R}_\alpha}{dt}\cdot\nabla\left(\nabla_\alpha S_i(\mathbf{R},t)\right), \tag{2.19}$$

and noting that $M_\alpha \frac{d\mathbf{R}_\alpha}{dt} = (\mathbf{P}_i)_\alpha = \nabla_\alpha S_i(\mathbf{R}, t)$, we derive the relation

$$\frac{d}{dt}\nabla S_i(\mathbf{R}, t) = \frac{\partial}{\partial t}\nabla S_i(\mathbf{R}, t) + \sum_{\alpha}^{N_n} \frac{1}{M_\alpha}\nabla_\alpha S_i(\mathbf{R}, t) \cdot \nabla \left(\nabla_\alpha S_i(\mathbf{R}, t)\right) . \tag{2.20}$$

The substitution of Eq. (2.20) into Eq. (2.18) and the adoption of the Lagrangian frame, yields the familiar Newton's law

$$\frac{d\mathbf{P}_i(t)}{dt} = \mathbf{F}_i(t) = -\nabla E_i^{el}(\mathbf{R}) . \tag{2.21}$$

Eq. (2.21) provides an efficient way of propagating the nuclear dynamics within the BO molecular dynamics. Given the energy $E_i^{el}(\mathbf{R})$ – solution of the TISE – we compute the forces acting on the nuclei at time t ($\mathbf{F}_i(t)$). The new positions and momenta for at time $t + \Delta t$ (Δt = time step) are determined from Eq. (2.21) and the process is iterated until a certain propagation time is achieved.

2.3 Representations of the electronic states

2.3.1 Adiabatic states

In the previous section, we have introduced the adiabatic states as the electronic wavefunction for which $\hat{H}^{el}(\mathbf{r}, \mathbf{R})$ is diagonal. This definition causes the adiabatic states to be the natural choice to describe electronic PES. In addition, energies and associated quantities are available from any quantum chemistry packages – which solve Eq. (2.3) – constituting a convenient base to work with. Despite their popularity, adiabatic states are not always the best option to perform nonadiabatic AIMD. When two or more electronic states approach each other, the PESs of two adiabatic states (i, j) become degenerate for some values of $\mathbf{R}$, namely $E_j^{el} - E_i^{el} = 0$. At the CIs we also have that the derivatives of the PESs with respect to $\mathbf{R}$ are not continuous and the first-order NACs (Eq. (2.8)) diverge as made explicit by the relation:

$$\mathbf{d}_{ji} = \int d\mathbf{r}\, \Phi_j^*(\mathbf{r}; \mathbf{R}) \nabla \Phi_i(\mathbf{r}; \mathbf{R}) = \frac{1}{E_j^{el}(\mathbf{R}) - E_i^{el}(\mathbf{R})} \int d\mathbf{r}\, \Phi_j^*(\mathbf{r}; \mathbf{R}) \nabla \hat{H}^{el}(\mathbf{r}, \mathbf{R}) \Phi_i(\mathbf{r}; \mathbf{R}) . \tag{2.22}$$

Furthermore, the adiabatic states suffer another intriguing issue. Adiabatic electronic states are real and by construction are defined up to a phase. This definition of adiabatic states implies that they pick up an additional non-dynamical (*i.e.*, geometrical) phase – the so-called Berry's phase – when we perform a loop in configuration space that encircles a CI.[145–148] Interestingly, it is, in general, possible to include phase factors ($\Phi_i(\mathbf{r}; \mathbf{R}) \rightarrow \Phi_i(\mathbf{r}; \mathbf{R}) e^{i\theta(\mathbf{R})}$) such that the electronic states become single-valued at the price of including a vector potential-like term in the molecular Hamiltonian. This Berry's phase phenomenon closely resembles its counterpart in magnetism described by Aharonov and Bohm[149] for which a charged particle acquires a phase if it follows a path enclosing a magnetic flux, even if the magnetic field itself is zero everywhere along the path. Similarly to the Aharonov and Bohm effect, a quantum mechanical particle picks up an additional phase when following a path enclosing the (pseudo) magnetic field – which is the curl of the vector potential. Since the total molecular wavefunction must be unique and independent of Berry's phase, the nuclear wavefunction acquires a geometric phase that must be taken into account to describe nuclear wavefunction dynamics in the adiabatic representation.[150]

Without further digging into the Berry phase and its role in quantum and quantum-classical dynamics we would like to present an alternative to adiabatic states, the so-called diabatic states ($\{\Phi_i^{dia}(\mathbf{r};\mathbf{R})\}$), that do not suffer from the geometrical phase ambiguity and solve the divergence of the first-order NACs.

2.3.2 Diabatic states

The diabatic states are defined as the unitary transformation, *i.e.*, a linear combination of the adiabatic states, that minimize the first-order NACs, such as

$$\Phi_i^{dia}(\mathbf{r};\mathbf{R}) = \sum_j^{\infty} W_{ji}(\mathbf{R})\Phi_j(\mathbf{r};\mathbf{R})\,, \tag{2.23}$$

where W_{ij} are the expansion coefficients of the linear combination, and

$$\mathbf{d}_{ij}^{dia} = \sum_{kl}(\mathbf{W}^T)_{ik}\,\mathbf{d}_{kl}\,(\mathbf{W})_{lj} + \sum_k(\mathbf{W}^T)_{ik}\,\nabla\,(\mathbf{W})_{kj} \to 0\,. \tag{2.24}$$

In Eq. (2.24), $\mathbf{W}$ is the matrix notation for the expansion coefficients, and $\mathbf{d}^{dia}$ and $\mathbf{d}$ are the matrix notation for the first-order NACs in the diabatic and adiabatic representations, respectively. Due to the change of basis, the electronic Hamiltonian is not diagonal in the diabatic representation. It can be decomposed as diagonal components – that are the diabatic states – and off-diagonal matrix elements – the electronic couplings. In other words, via the adiabatic-diabatic transformation, we shift the complexity of the problem by transforming the "kinetic" coupling terms (first-order NAC) into "potential-like" coupling terms (electronic couplings).

Eq. (2.24) indicates that the mixing of the diabatic state is as small as possible which in turn means that the diabatic states preserve their "electronic character" in every region of the configuration space. Unfortunately, since the first-order NACs diverge at the crossing of two (or more) adiabatic states, Eq. (2.24) is hard to implement practically. In addition, a rigorous definition is no longer possible for polyatomic molecules.[151–153] In fact, for polyatomic molecules, the only choice of the diabatic states that satisfies Eq. (2.24) is trivially the set of diabatic states that do not depend on the nuclear coordinates. Choosing the diabatic states as constant functions requires taking into account an infinite number of adiabatic states in Eq. (2.23), which is again not practical.[152, 154] Other procedures have been developed to retrieve smooth functions – approximating the true diabatic states – using the orbital overlap scheme[155] or by maximizing the overlap between the electronic wavefunction.[156] These schemes endeavour to preserve the "electronic character" of each diabatic state in proximate regions of the configuration space which usually leads to the conventional diabatic states. From a chemical perspective, the diabatic states are extremely useful since they encode precious properties (*i.e.*, oscillator strength) and key information regarding molecular reactivity to comprehend nonadiabatic dynamics.

2.3.3 Differences between diabatic and adiabatic states

To clarify the difference between diabatic and adiabatic electronic states I show them side-by-side on panel A of Fig. 2.1. In the diabatic representation, each state is labelled by its electronic character – using the orbitals that contribute to the excitation – and spin multiplicity. For instance, the ^{1}nπ^* state corresponds to a singlet state characterized by a n$\rightarrow$ π^* excitation and it is a typical case of carbonyl-containing molecules. Interestingly, understanding the electronic character of an excited state allows us to extract important information regarding the photophysics and photochemistry of the molecule under investigation. It is well known that ^{1}nπ^* states are relatively dark states due to the spatial symmetry of the n and π^* orbitals resulting in a vanishing transition dipole moment. In contrast, we expect a stronger oscillator strength for the $^1\pi\pi^*$ (*i.e.*, the state is bright) due to the sizable overlap between the π and π^* orbitals. Finally, from the nature of the excitations, we expect that the two excited states may show minima – with structured vibronic transitions – which are not present in dissociative states.

If we look now at the shape of the PESs in the diabatic states we notice that they are always smooth and slowly varying with respect to the nuclear coordinates and their coupling is small, delocalized, and never diverges. The situation changes when we turn our attention to the adiabatic representation. In particular, the adiabatic PESs are altered in the regions of the configuration space when two diabatic states come close in energy. Upon the crossing of two diabatic states, we can observe an avoided crossing, occurring between S_0 and S_1, or a CI, between S_1 and S_2 that are degenerate at the crossing point. The difference between avoided crossing and CI is reflected in the NAC which is finite in the former but diverges in the latter.

We finally investigate the topology of the PESs in the diabatic and adiabatic representation at the CI. To do so, we use a simple 2 states/2 modes model as presented in panel B Fig. 2.1. The inspection of this point in the diabatic representation (shown on the left of panel B) corroborates our previous finding for which the PESs crossing occurs smoothly. Here, only one coordinate is responsible for lifting the degeneracy between the states leading to a crossing seam (dashed black line) along which the diabatic states degenerate. The inspection of the right of panel B reveals that the PESs in the adiabatic representation change dramatically. Here, the two states are only degenerate at the CI and both coordinates lift the degeneracy between the adiabatic states – we shall refer to these two coordinates as the gradient difference vector and the derivative coupling vector. The remaining $3N_n$-8, or $3N_n$-7 for linear molecule, coordinates

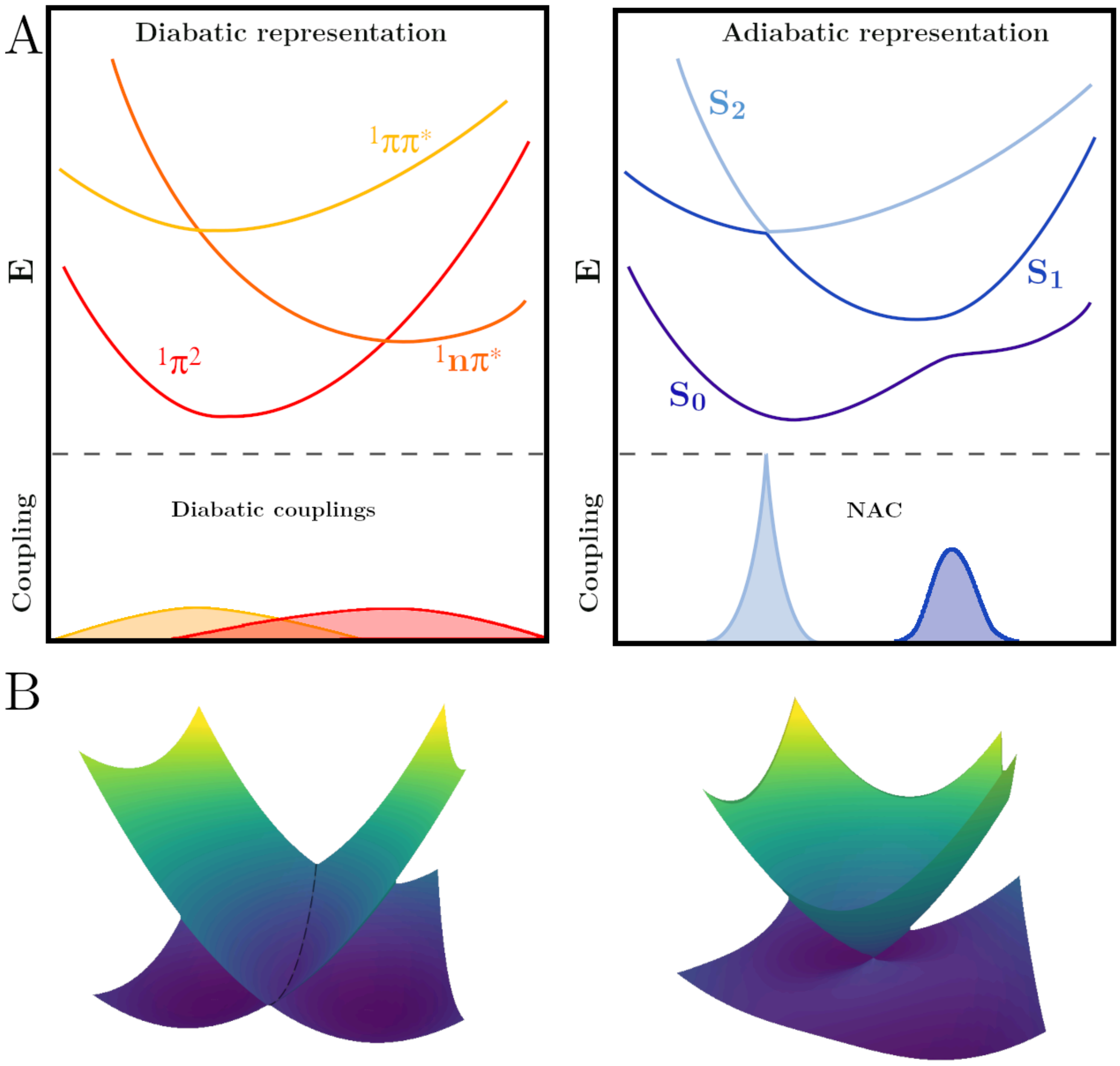

Figure 2.1: Panel A: schematic representation of the diabatic states (left) and adiabatic states (right). The PESs of three singlet states are shown together with their interstate couplings. Panel B: we report the PESs topology at the crossing point between $^1n\pi^*/^1\pi\pi^*$ (S_1/S_2) states using a 2 states/2 modes model in the diabatic (left) and adiabatic (right) representation. In the diabatic representation, the states are smooth along the nuclear coordinates and they cross via a seam of points (dashed line). In the diabatic representation, the seam is lifted and the states are degenerate only at the CI.

leave the degeneracy intact. In this model, the avoided crossing will be all points belonging to the diabatic seam but the CI.

2.3.4 Inclusion of spin-orbit coupling

Up to this point, I have considered states with the same spin-multiplicities. Once I consider the interplay between states with different spin-multiplicities, such as singlets and triplets states, I have to take into account another form of coupling: the spin-orbit couplings (SOCs). The SOC is derived within the relativistic quantum chemistry formalism and it arises from the interaction of the magnetic field induced by the orbital momentum of an electron and the magnetic dipole related to the electron spin. Since the orbital momentum depends on the nuclear charges, SOC is stronger in molecules containing one or more heavy atoms.[157, 158] Naively, one might assume that SOC needs to be taken into account only if heavy elements are involved, however, when two electronic states of different multiplicity are close in energy a small coupling still suffices to induce a transition between the states. Although such a change of spin state occurs rarely in electronic ground-state reactions, it corresponds to a common situation in molecular processes involving electronically excited states.

When the SOC is considered, the total Hamiltonian becomes

$$\hat{H}^{tot}(\mathbf{x},\mathbf{R}) = \hat{H}(\mathbf{r},\mathbf{R}) + \hat{H}^{SOC}(\mathbf{x},\mathbf{R})\,, \tag{2.25}$$

where $\hat{H}^{tot}(\mathbf{x},\mathbf{R})$ is the total Hamiltonian of the system, $\hat{H}(\mathbf{r},\mathbf{R})$ is the molecular Hamiltonian of in Eq. (2.2), the $\hat{H}^{SOC}(\mathbf{x},\mathbf{R})$ is the SOC operator accounting for the coupling between states with different multiplicities, and $\mathbf{x}$ groups the electronic spatial and spin coordinates. For multi-body systems, the explicit calculation of $\hat{H}^{SOC}(\mathbf{x},\mathbf{R})$ can be done via several approximated methods. Some of the most popular one and two-electron operators are the Breit-Pauli or the Douglas–Kroll–Hess Hamiltonians.[159, 160] Alternatively, also one-electron operators within the mean-field approximation are used to describe the SOC interplay in heavy elements, where the one-electron terms dominates.[158, 161]

The explicit evaluation of the SOC can be computationally cumbersome. However, there exists a number of qualitative rules – such as El-Sayed's rule – that can help us discern which states are more likely to have sizable SOC. El-Sayed's rule states that if the two states have the same "electronic character" – *i.e.*, the radiationless transition does not involve a change in orbital type – I expect a small SOC because the change in spin angular momentum is not counterbalanced by a change in the spatial angular momentum and the total angular momentum is not conserved.[158] On one hand, since the SOC magnitude is directly related to the ISC rate, El-Sayed's rule predicts that the ISC rate will be faster for a $^1\pi\pi^* \rightarrow ^3\mathrm{n}\pi^*$ than a $^1\pi\pi^* \rightarrow ^3 \pi\pi^*$ transition. On the other hand, the ISC rate does not depend only on the magnitude of the SOC but it is also related to the density of states and the location and accessibility of crossing regions between singlets and triplets. This makes any prior assessment of ISC rates challenging and experiments have found that ISC rates can occur on very different time scales that are not necessarily correlated with the magnitude of SOCs.

For a relatively slow ISC process – typical of a small organic molecule that has relatively small SOCs and a substantial energy difference between the spin-diabatic states (*i.e.*, they do not cross) – several methods have been used to compute the ISC rate without making use of expensive nonadiabatic molecular dynamics simulation such as Landau-Zener theory[162] or Fermi's golden rule.[163, 164] However, for systems that are highly harmonic and show ultrafast

ISC processes, the magnitude of the SOC is not sufficient anymore and a dynamical treatment has to be embraced. Here, the representation chosen to propagate the electronic and nuclear equation of motions is crucial. In fact, in a purely quantum-mechanical treatment of nuclear motion, the choice of representation does not influence the results. However, in the realm of quantum-classical methods the choice of the electronic basis matters.[165] A first choice is the so-called spin-diabatic representation. In this representation, I use the electronic states that are the solution of Eq. (2.3), eigenfunctions of the electronic Hamiltonian and of the $\hat{S}^2$ and $\hat{S}_z$ operators. The states with different multiplicities are coupled by means of SOC and they freely cross similarly with what was noted for the diabatic representation, see the left-hand-side of Fig. 2.2. Since the $\hat{H}^{SOC}(\mathbf{x}, \mathbf{R})$ matrix – as well as the $\hat{H}^{tot}(\mathbf{x}, \mathbf{R})$ – is not diagonal, I may diagonalize via unitary transformation of the total Hamiltonian. This procedure leads to the spin-adiabatic representation, as shown in the right-hand side of Fig. 2.2. Here, the states with different spin multiplicity mix so that only the total angular momentum is used to label the different electronic states while the spin multiplicity is not a good quantum number anymore. All the coupling between diagonal states derives from the nonadiabatic couplings that are localized and become large when two PES are close to each other. In addition, none of the states cross although they might touch at the CI. Finally, as a result of the different coupling experienced with the singlet state, the multiplets of the triplet state are split and are not degenerate as in the spin-diabatic representation.

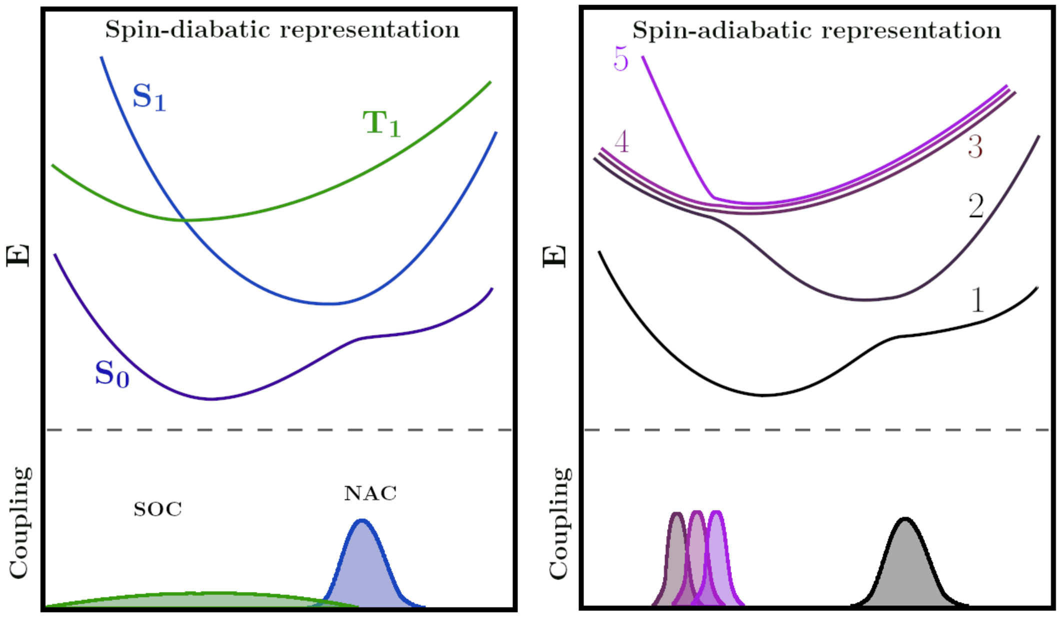

Figure 2.2: Scheme illustrating spin-diabatic states (left) and the spin-adiabatic states (right). In the spin-diabatic, we show the PESs of two singlets and one triplet state together with their interstate couplings. The diagonalization of the total Hamiltonian leads to the spin-adiabatic representation where the triplet multiplets are split accordingly to SOC.

Since our goal is to perform nonadiabatic molecular dynamics the representation chosen to propagate the electronic and nuclear equation of motion is crucial. In quantum-classical methods is desirable to have localized coupling which makes the spin-adiabatic states a natural choice. However, quantum chemistry mostly offers electronic structure quantities in the spin-diabatic representation. To overcome this limitation, several schemes have been conceived[166–168] to transform spin-diabatic quantities in the diabatic[169] or spin-adiabatic quantities.[165, 168] In the following section, I am not going to discuss in detail such propagation schemes but rather I will provide a rather comprehensive overview of the more common methods that can be readily implemented in the spin-diabatic representation and the reader may wish to use to perform nonadiabatic molecular dynamics.

2.4 Solving the time-dependent Schrödinger equation within the Born-Huang expansion

Eq. (2.1) sets challenging constraints for the methodologies that can be realistically used to simulate molecular systems. In particular, to describe multi-body systems one has to efficiently propagate the nuclear dynamics without sacrificing the quality and accuracy of the nuclear propagation. In this chapter, I will present two methodologies based on the BH expansion that have found tremendous popularity in the computational chemistry field. In section 2.4.1, I will detail the TSH method.[117] TSH is the most popular method within the nonadiabatic molecular dynamics community and represents the typical choice due to its simplicity and time efficiency. However, TSH is not derived from first principles and its accuracy should not be assumed.[117, 170, 171] From a heuristic standpoint, it has been proven that TSH provides surprisingly accurate results in the vast majority of molecular cases, but it can fail catastrophically in specific circumstances.[171, 172] In these instances, more accurate strategies have to be invoked. In section 2.4.2 I will present AIMS which shows excellent performances at the expense of inflated algorithm complexity and computational cost. This limitation did not prevent the quick spreading of AIMS within the computational-chemistry community which surely deserves a quick overview within this chapter.

2.4.1 Trajectory surface hopping

In TSH, the motion of the nuclear wavepacket is reproduced by a swarm of independent classical trajectories ($\{I\}$) evolving adiabatically on a set of BOA states. Briefly, the nuclear motion is treated classically (see Eq. (2.21)) and the only quantum effects accounted for is the transfer of "nuclear amplitude" between different electronic states, following the results of Eq. (2.8). In TSH, the population transfer between electronic states is accomplished through hops of the classical trajectories. The hopping probability – related to the magnitude of the first-order NAC vectors – is then compared with a stochastic number to evaluate whether the hop occurs or not.

If the hop occurs, the kinetic energy of the trajectory is re-scaled to enforce the conservation of the classical total energy and also momentum (if NAC available) for each trajectory.

Let us investigate the key equation of the TSH scheme.[117, 119, 120] Firstly, I construct the electronic wavefunction associated with the I-th trajectory,

$$\Psi^{[I]}\left(\mathbf{r},t;\mathbf{R}(t)\right)=\sum_{j}^{\infty}C_{j}^{[I]}\left(t\right)\Phi_{j}^{[I]}\left(\mathbf{r};\mathbf{R}(t)\right)\,, \tag{2.26}$$

where each term of the expansion is attached to a particular nuclear trajectory-$[I]$. Notice that I have made explicit the time-dependency of the nuclear coordinates. Inserting Eq. (2.26) into the time-dependent electronic Schrödinger equation, multiplying for $\Phi_{i}^{[I]\,*}\left(\mathbf{r};\mathbf{R}(t)\right)$ and integrating over $\mathbf{r}$ I obtain:

$$i\hbar\,\dot{C}_{i}^{[I]}\left(t\right)=C_{i}^{[I]}\left(t\right)\;E_{i}^{el}\left(\mathbf{R}^{[I]}\right)-i\hbar\sum_{j}^{\infty}C_{j}^{[I]}\left(t\right)\sum_{\alpha}^{N_n}\mathbf{d}_{ij,\alpha}\left(\mathbf{R}^{[I]}\right)\cdot\dot{\mathbf{R}}_{\alpha}^{[I]}\,, \tag{2.27}$$

that constitutes a set of differential equations governing the time-dependent coefficients. To derive Eq. (2.27) I have made use of the chain rule for partial differentiation:

$$\frac{\partial}{\partial t}\Phi_{j}^{[I]}\left(\mathbf{r};\mathbf{R}(t)\right)=\sum_{\alpha}^{N_n}\nabla_{\alpha}\,\Phi_{j}^{[I]}\left(\mathbf{r};\mathbf{R}(t)\right)\cdot\dot{\mathbf{R}}_{\alpha}^{[I]}\,. \tag{2.28}$$

In Eq. (2.27) I notice that $\sum_{\alpha}^{N_n}\mathbf{d}_{ij,\alpha}\left(\mathbf{R}^{[I]}\right)\cdot\dot{\mathbf{R}}_{\alpha}^{[I]}$ (time-derivative nonadiabatic couplings) is the only term responsible for the amplitude transfer between the j-th and i-th electronic states. This term is the scalar product between the nuclear velocities – $\dot{\mathbf{R}}_{\alpha}^{[I]}$ – and the first-order NAC – $\mathbf{d}_{ij}(\mathbf{R}^{[I]})=\int d\mathbf{r}\,\Phi_{i}^{[I]\,*}\left(\mathbf{r};\mathbf{R}(t)\right)\,\nabla\,\Phi_{j}^{[I]}\left(\mathbf{r};\mathbf{R}(t)\right)$. Eq. (2.27) can be rearranged in the density matrix notation as

$$\begin{aligned}i\hbar\frac{d}{dt}\left(\rho_{ij}^{[I]}\left(t\right)\right)=\rho_{ij}^{[I]}\left(t\right)E_{i}^{el}\left(\mathbf{R}^{[I]}\right)-i\hbar\sum_{l}^{\infty}\rho_{lj}^{[I]}\left(t\right)\sum_{\alpha}^{N_n}\mathbf{d}_{il,\alpha}\left(\mathbf{R}^{[I]}\right)\cdot\dot{\mathbf{R}}_{\alpha}^{[I]}\\-\rho_{ij}^{[I]}\left(t\right)E_{j}^{el}\left(\mathbf{R}^{[I]}\right)+i\hbar\sum_{l}^{\infty}\rho_{il}^{[I]}\left(t\right)\sum_{\alpha}^{N_n}\mathbf{d}_{lj,\alpha}\left(\mathbf{R}^{[I]}\right)\cdot\dot{\mathbf{R}}_{\alpha}^{[I]}\,.\end{aligned} \tag{2.29}$$

We have introduced the density matrix elements $\rho_{ij}^{[I]}\left(t\right)=C_{i}^{[I]}\left(t\right)C_{j}^{[I]\,*}\left(t\right)$ and make use of the relation $\mathbf{d}_{jl}^{*}=-\mathbf{d}_{lj}$ stemming from the anti-Hermitian nature of the operator ∇ when acting on orthogonal states. In Eq. (2.29), the diagonal terms of the time-dependent density matrix are the electronic populations and they satisfy the equation

$$\frac{d}{dt}\left(\rho_{ii}^{[I]}\left(t\right)\right)=-\sum_{l}^{\infty}2\Re\left[\rho_{li}^{[I]}\left(t\right)\sum_{\alpha}^{N_n}\mathbf{d}_{il,\alpha}\left(\mathbf{R}^{[I]}\right)\cdot\dot{\mathbf{R}}_{\alpha}^{[I]}\right]=\sum_{l}^{\infty}\Xi_{il}^{[I]}(t)\,, \tag{2.30}$$

while the off-diagonal terms are the coherence. If the state of the system is pure – *i.e.*, described by a single normal state vector – Eq. (2.29) is equivalent to Eq. (2.27). Although all cases treated here will be pure states, the former leaves open the possibility of treating "ensembles" of pure states (mixed states) and, therefore, is more general.

A natural question arising here is: how the distribution of trajectories running on different electronic states can be related to Eq. (2.30)? Our simulation starts by distributing a fraction of trajectories onto the different electronic states to mirror the initial electronic populations. During the dynamics propagation, a trajectory will hop, changing electronic states, such that the fractional change of trajectories will reflect the variation of the electronic population given by Eq. (2.30). To enforce this constraint, the probability of one trajectory to hop from state i to another state l must be

$$P_{i \to l} = \frac{\Delta t \, \Xi_{il}^{[I]}(t)}{\rho_{ii}^{[I]}(t)} \,, \tag{2.31}$$

that is the number trajectories hopping from the state i to l ($\Delta t \, \Xi_{il}^{[I]}(t) \times N_{tot}$, where N_{tot} is the total number of trajectories) divided for the number of trajectories on the state i ($\rho_{ii}^{[I]}(t) \times N_{tot}$). Δt is the chosen time step to propagate the time-dependent coefficients. It is worth noticing that the total probability of switching electronic state (*i.e.*, the integration of Eq. (2.31)) is, as expected, independent from the time step chosen to perform the numerical integration. At each time step of the propagation, a uniform random number $0 \leq \zeta \leq 1$ is selected and the hop from state i to l will occur if $\sum_k^{l-1} P_{i \to k} < \zeta < \sum_k^{l} P_{i \to k}$. If the hop occurs, the trajectory will start evolving on the l-th electronic states, and, in order to preserve the total energy, the kinetic energy is adjusted to make up for the difference in the potential energy ($E_i^{el}\left(\mathbf{R}^{[I]}\right) - E_j^{el}\left(\mathbf{R}^{[I]}\right)$) at the hopping time. The component of the velocities can be re-scaled along the first-order NAC, as justified by semi-classical reasoning,[173] or more straightforwardly, in an isotropic manner along each degree of freedom.[174] Since the solution of Eq. (2.30) requires only the evaluation of the time-derivative nonadiabatic couplings,[118, 175] an explicit calculation of the first-order NACs is not needed in TSH. Therefore, the scaling along the momentum vector is usually the method of choice.

2.4.1.1 Issues of trajectory surface hopping

Despite the great advantages offered by TSH, this method suffers from several internal inconsistencies. The underlying algorithm should lead to a match between the fraction of trajectory running in a given state and the quantum probability, however, this is usually not the case.[176] One of the reasons for this discrepancy regards the constraint applied to the hop algorithm which has to guarantee total energy conservation. In particular, hops to higher excited states are "frustrated" (discarded) if the kinetic energy of the trajectory cannot make up for the potential energy difference.[177] Another and even more important source of internal inconsistency stems from the intrinsic over-coherence nature of TSH. The molecular wavefunction is reduced to a single point in the nuclear phase space (a trajectory). Therefore, the coefficients of the electronic states are constrained to follow such a trajectory not allowing the branching of the wavepackets.

Several ad-hoc strategies have been developed to introduce decoherence in TSH; amongst them, the energy-based decoherence correction (EDC) is the most used. The EDC was first introduced by Truhlar[178] and then applied to TSH by Granucci and Persico.[177] The main idea of the EDC is to "dump" the expansion coefficients of Eq.(2.27) associated with all the states (k) but the running state (r), therefore mimicking the effect of quantum decoherence. The EDC adopted by Granucci and Persico reads

$$C_r^{\prime[I]}(t) = C_r^{[I]}(t)\left[\frac{1-\sum_{i\neq r}^{\infty}|C_i^{\prime[I]}(t)|^2}{|C_r^{[I]}(t)|^2}\right], \tag{2.32}$$

$$C_k^{\prime[I]}(t) = C_k^{[I]}(t)\, e^{-\frac{\Delta t}{\tau_{kr}}} \qquad \forall k \neq r\,, \tag{2.33}$$

$$\tau_{kr} = \frac{\hbar}{E_k - E_r}\left(1+\frac{\eta}{K}\right), \tag{2.34}$$

where the prime coefficients indicate the EDC coefficients. The decoherence time (τ_{kr}) between the state k and r is inversely proportional to their energy difference ($E_k - E_r$) and the trajectory kinetic energy (K). When the ($E_k - E_r$) $\rightarrow 0$ or $K \rightarrow 0$ (the trajectory does not move in the configuration space) then $\tau_{kr} \rightarrow \infty$ and the system do not decohere. η is a parameter that is usually set to be 0.1 a.u.

In general, TSH is an excellent starting point to perform nonadiabatic molecular dynamics in a full atomistic fashion. In addition, TSH yields excellent results for molecular systems where internal consistency flaws are less relevant than in reduced dimensionality models.[179, 180] However, there are still a few cases where multiple re-crossing can occur in a short period of time leading to quantitative discrepancies between TSH and exact quantum dynamics.[117, 171, 181] Here, the decoherence issue creates artifacts in the hopping probability which deteriorates the quality of the dynamics. Without invoking the full quantum dynamics, it would be recommended to explore the dynamics of these molecular systems with a more accurate method able to treat correctly nuclear quantum dynamics, still maintaining the benefits of a trajectories-based formalism. In the next chapter, I will outline the main feature of AIMS which shows these desirable features and it is now one of the most promising competitors of TSH for nonadiabatic molecular dynamics.

2.4.2 Ab initio multiple spawning

A possible route to overcome the intrinsic limitation affecting the performance of TSH is to expand the nuclear terms appearing in the BH expansion (Eq. (2.5)) using trajectory basis functions (TBFs). In the case of FMS, the TBFs correspond to frozen multidimensional Gaussians. The coefficient of each TBF obeys the TDSE while the centre of the Gaussian evolves according to classical equations of motion. In addition, I allow the number of TBFs to change over time, augmenting the basis over which the nuclear terms are expanded. If a TBF (parent) encounters a region where the NACs are large, it spawns a new TBF (child) onto the state that couples with the running state. During the dynamics the parent and child TBFs exchange populations under the effect of the NACs. In stark contrast with TSH, FMS is in principle exact,[182–186] however, for full atomistic simulations, one often resorts to several approximations that lead to the AIMS method. Without exploring AIMS in depth I will present a few key points which are particularly appealing in nonadiabatic molecular dynamics and allow AIMS to gain reliability within the computational chemistry community.[183, 187–189]

The key ingredient of AIMS is the expansion of the nuclear terms in Eq. (2.5) in terms of multi-dimensional Gaussian function. The i-th nuclear amplitude is expanded as

$$\chi_i(\mathbf{R},t) = \sum_{K}^{N_i(t)} C_i^K(t)\, g_i^K(\mathbf{R}, \overline{\mathbf{R}}_i^K(t), \overline{\mathbf{P}}_i^K(t), \overline{\gamma}_i^K(t), \boldsymbol{\eta})\,. \tag{2.35}$$

Each K-th Gaussian in the electronic state i is described by a frozen (time-independent) width ($\boldsymbol{\eta}$), its center is located at $\overline{\mathbf{R}}_i^K(t)$ and it has a momentum $\overline{\mathbf{P}}_i^K(t)$. In addition, each Gaussian carries a dynamical nuclear phase ($\overline{\gamma}_i^K(t)$), *i.e.*, its value depends on the path of the trajectory. Finally, the number of Gaussian basis functions is denoted by $N_i(t)$ which is time-dependent. Each multidimensional Gaussian is given by a product of monodimensional Gaussians

$$g_i^K(\mathbf{R}, \overline{\mathbf{R}}_i^K(t), \overline{\mathbf{P}}_i^K(t), \overline{\gamma}_i^K(t), \boldsymbol{\eta}) = e^{i\,\overline{\gamma}_K(t)} \prod_{\alpha=1}^{3N_n} \left(\frac{2\,\eta_\alpha}{\pi}\right)^{1/4} e^{-\eta_\alpha \left(R_\alpha - \overline{R}_{i\,\alpha}^K(t)\right)^2 + i\,\overline{P}_{i\,\alpha}^K(t)\left(R_\alpha - \overline{R}_{i\,\alpha}^K(t)\right)}\,. \tag{2.36}$$

Plugging the Eq. (2.35) into the BH expansion (Eq. (2.5)) I obtain the ansatz of the molecular wavefunction in AIMS:

$$\Psi(\mathbf{r},\mathbf{R},t) = \sum_{i}^{\infty} \sum_{K}^{N_i(t)} C_i^K(t)\, g_i^K(\mathbf{R}, \overline{\mathbf{R}}_i^K(t), \overline{\mathbf{P}}_i^K(t), \overline{\gamma}_i^K(t), \boldsymbol{\eta})\, \Phi_i(\mathbf{r};\mathbf{R})\,. \tag{2.37}$$

At this point, I want to derive an equation of motion for the coefficients $C_i^K(t)$ that satisfies the TDSE. To do so, I insert Eq. (2.37) into the TDSE (Eq. (2.1)), I multiply from the left by $g_j^{K\,*}(\mathbf{R}, \overline{\mathbf{R}}_j^K(t), \overline{\mathbf{P}}_j^K(t), \overline{\gamma}_j^K(t), \boldsymbol{\eta})\Phi_j^*(\mathbf{r};\mathbf{R})$ and I integrate over nuclear and electronic coordinates. In matrix notation and atomic units, it reads

$$\dot{\mathbf{C}}_j(t) = -i\,\mathbf{S}_{jj}^{-1}\left[\left(\mathbf{H}_{jj} - i\dot{\mathbf{S}}_{jj}\right)\mathbf{C}_j + \sum_{i\neq j}^{\infty} \mathbf{H}_{ji}\mathbf{C}_i\right]. \tag{2.38}$$

$\mathbf{C}_j$ and $\dot{\mathbf{C}}_j$ are column vectors of length $N_j(t)$ containing the coefficients and the time derivative of the coefficients for each TBF on the adiabatic state j, respectively while the matrices $\mathbf{S}_{jj}$ and $\dot{\mathbf{S}}_{jj}$ are $N_j(t) \times N_j(t)$ square matrices representing different overlap terms between the TBFs. We direct the interested reader to the excellent existing literature[182–186] to have a detailed overview. Finally, the matrix $\mathbf{H}_{ji}$ arises from the action of the molecular Hamiltonian onto the adiabatic states and the TBFs. Its matrix elements read

$$\begin{aligned} H_{ji}^{LK} &= \left\langle g_j^L \middle| \hat{T}_n + E_i^{el} \middle| g_i^K \right\rangle_{\mathbf{R}} \delta_{ji} \\ &\quad - \sum_{\alpha=1}^{3N_n} \frac{1}{2M_\alpha}\left[\left\langle g_j^L \middle| \left\langle \Phi_j \middle| \nabla_\alpha^2 \middle| \Phi_i \right\rangle_{\mathbf{r}} \middle| g_i^K \right\rangle_{\mathbf{R}} + 2\left\langle g_j^L \middle| \left\langle \Phi_j \middle| \nabla_\alpha \middle| \Phi_i \right\rangle_{\mathbf{r}} \nabla_\alpha \middle| g_i^K \right\rangle_{\mathbf{R}}\right], \end{aligned} \tag{2.39}$$

where the subscripts $\langle ... \rangle_{\mathbf{R}}$ and $\langle ... \rangle_{\mathbf{r}}$ denote the integration over the nuclear and electronic degrees of freedom, respectively. The first and second terms on the right-hand side are responsible for the interaction between TBFs evolving on the same electronic state ($i = j$). In contrast, the first-order and the second NAC account for the exchange in population between the TBFs. An analytical solution for these matrix elements is beyond the computational capability when simulating realistic molecules because they require the knowledge of the electronic energies and coupling over the whole configuration space covered by the TBFs. In AIMS, this problem is overcome by computing the integrals approximately by using the so-called saddle-point approximation at zero order (SPA0). In addition, the second-order NACs (which are usually small) are neglected.[190] Although neglecting these terms would lead to a non-hermitian molecular Hamiltonian,[191] the hermiticity is retained by using the SPA0. These approximations allow the calculation of $\mathbf{H}$ matrix on-the-fly which is an essential requirement to perform nonadiabatic dynamics of molecular systems. When a certain parent TBF reaches a region of nonadiabaticity (*i.e.*, the first-order NAC exceeds a certain threshold), it spawns a new child TBF on the state that couples with the running state of the parent TBF. The spawning is performed such that the total energy is conserved while maximizing the overlap between the parent and the child TBFs at the spawning time.[192]

Despite the algorithm of AIMS is far more complicated than TSH and computationally more expensive, it is particularly appealing because it naturally incorporates nuclear quantum effects that are missing in the TSH method. Furthermore, recent developments of AIMS have led to a massive streamlining of the computational costs via the elimination of superfluous TBF coupling terms, which is the bottleneck of the algorithm. For example in AIMSWISS, the TBFs are stochastically selected and only an informative subset is kept during the propagation.[193] I believe that AIMS is an excellent playground to develop an efficient yet accurate method for nonadiabatic molecular dynamics: a step forward to glimpse the nuclear quantum effect in molecular dynamics.

2.5 Solving the electronic structure problem with wavefunction-based methods

In chapter 2.4, I have analyzed different methods to solve the TDSE. However, I have left unsolved a pressing issue: the solution of the TDSE requires the adiabatic electronic state and energies as well as NAC and first-order properties such as gradients. But how I can solve the TISE? Like almost everything in quantum chemistry, the real challenge is to find a compromise between accuracy and computational efficiency. As already alluded to in chapter 2.4, this choice depends on the system considered and a simple and unique solution should not be expected. More often than not, an informed choice of an electronic structure method requires multiple tests and an exhaustive benchmark is always the first priority. In this chapter, I will highlight some of the key concepts of the most popular electronic structure methods used to solve – approximately – Eq. (2.3). In section 2.5.2 I will give an overview of the configuration interaction expansion starting from the SD expressed in terms of molecular orbitals (MOs). The concepts behind the configuration interaction are the cornerstone upon which other electronic structure methods took root. In section 2.5.3 I will briefly describe a multi-configurational method, *i.e.*, based on more than one SD, that is the state-average complete active space self-consistent field (SA-CASSCF). SA-CASSCF and in particular the multi-state complete active space perturbation theory at the second order (MS-CASPT2) are seen as the ultimate goal for nonadiabatic molecular dynamics because they provide a balanced description of the PESs which is beyond the capabilities of single-reference methods based on a unique SD. To conclude, in section 2.5.4, I will present one example of a single-reference method which is the algebraic diagrammatic construction in the second order (ADC(2)). Despite underlying limitations, ADC(2) applications boomed in the past decade thanks to its excellent accuracy, black-box formalism, and affordable computational cost. The esteem for this method in the computational chemistry community has grown exponentially making ADC(2) one of the first choices to describe excited state PESs, however, I shall see that popular and widely accepted methods can deliver some unexpected surprises.

2.5.1 General consideration when solving the electronic structure problem

The TISE can be solved exactly only for hydrogen-like atoms such as the H atom, He^+, or 3-bodies molecular systems with elliptical symmetry such as ${H_2}^+$. In the more general cases, the exact electronic wavefunction can not be computed for the molecular system and the goal of an electronic structure method becomes to find a close approximation via a trial wavefunction. The trial wavefunction is usually constructed allowing for multiple parameters which, in turn, can be optimized to get as close as possible to the exact solution. There is a multitude of ansatze for the functional form of the electronic wavefunction that can be utilized for molecular systems. The most approximated electronic structure methods usually rely on the simple form of the electronic wavefunction with a limited number of optimization parameters. On the other hand, more parameters imply a more complex wavefunction to be optimized with the advantage of getting closer to the exact solution.

A first point to keep in mind for the optimization of our trial wavefunction is the *variational principle*: the expectation value of the electronic Hamiltonian of any trial wavefunction will be always higher than the exact solution. In other words, the lower bound of the energy is only reached when the exact wavefunction is obtained. In contrast, when the energy is not computed as an expectation value of the electronic Hamiltonian, this lower bound is not guaranteed as for the case of MPPT.[194]

A second point to keep in mind is the nature of the particles that the wavefunction describes. The wavefunction must be invariant under the exchange of identical particles, which requires symmetrization of the wavefunction of bosonic particles or the antisymmetrization of the wavefunction for fermionic particles. Electrons are particles with half-integer spin and are therefore fermions which means that the many-electron wavefunction must be antisymmetric with respect to the permutation of any two electrons. The antisymmetrization of the molecular wavefunction leads to the *Pauli exclusion principle*, formulated by Wolfgang Pauli in 1925,[195] ensuring that only one electron can occupy a given quantum state. A natural choice to incorporate the correct symmetry of fermionic wavefunction is via a determinantal form – that has the desirable property of changing sign via a single permutation of two rows or two columns – as proposed by Dirac in 1926[196]: "*The antisymmetrical [wavefunction] may be written in the determinantal form [...]. An antisymmetrical eigenfunction vanishes identically when two of the electrons are in the same orbit. This means that in the solution of the problem with antisymmetrical eigenfunctions there can be no stationary states with two or more electrons in the same orbit, which is just Pauli's exclusion principle*".

A simple way to construct such a determinant is via expanding the multi-body wavefunction in terms of a set of single-particle wavefunctions. These single-particle (one electron) wavefunctions are the so-called MOs, also known as spinorbitals, which are a product of a spatial orbital, depending on the spatial coordinates of an electron, and a spin function. The MOs can be considered as one of the fundamental ingredients used by chemists and physicists to reduce the complexity of the electronic structure problem by decomposing the many-body wavefunction into a linear combination (determinantal form) of single-particle wavefunctions. The MOs are chosen to be orthonormal

$$\int d\mathbf{x}\, \varphi_i^*(\mathbf{x};\mathbf{R})\varphi_j(\mathbf{x};\mathbf{R}) = \delta_{ij}\,, \tag{2.40}$$

where $\varphi_j(\mathbf{x};\mathbf{R})$ is the j-th spinorbital depending on the electronic coordinates and the spin coordinate $(\mathbf{x})$. Since only two spin states are allowed for a fermion (↑ or ↓), up to two electrons can be located in the same spatial orbital. The determinantal form of the many-body wavefunction describing N_e electrons in terms of N_e occupied spin-orbitals takes the form of an SD:

$$\varphi^{SD}(\mathbf{x};\mathbf{R}) = \frac{1}{\sqrt{N_e!}} \begin{vmatrix} \varphi_1(\mathbf{x}_1;\mathbf{R}) & \varphi_2(\mathbf{x}_1;\mathbf{R}) & \dots & \varphi_{N_e}(\mathbf{x}_1;\mathbf{R}) \\ \varphi_1(\mathbf{x}_2;\mathbf{R}) & \varphi_2(\mathbf{x}_2;\mathbf{R}) & \dots & \varphi_{N_e}(\mathbf{x}_2;\mathbf{R}) \\ \vdots & \vdots & \ddots & \vdots \\ \varphi_1(\mathbf{x}_{N_e};\mathbf{R}) & \varphi_2(\mathbf{x}_{N_e};\mathbf{R}) & \dots & \varphi_{N_e}(\mathbf{x}_{N_e};\mathbf{R}) \end{vmatrix}\,, \tag{2.41}$$

where $\frac{1}{\sqrt{N_e!}}$ is a normalization constant such that the wavefunction satisfies the Eq. (2.4). Eq. (2.41) is the minimal form of the wavefunction that guarantees the Pauli exclusion principle. The ansatz of the trial wavefunction as a single SD implies that the electron-electron interactions are considered only in an average fashion and it is the cornerstone of the HF method.[22, 23] A single SD is not the only ansatz that we can think of. On one hand, a simpler form of the wavefunction can be constructed as a product of the spin-orbitals (Hartree product):

$$\varphi(\mathbf{x};\mathbf{R})^{HP} = \varphi_1(\mathbf{x}_1;\mathbf{R})\varphi_2(\mathbf{x}_2;\mathbf{R})\ldots\varphi_{N_e}(\mathbf{x}_{N_e};\mathbf{R})\,. \tag{2.42}$$

Clearly, this Hartree product is not antisymmetric with respect to the permutation of two electronic coordinates. As such, the Hartree wavefunction is a truly independent-electron wavefunction since

$$\left|\varphi(\mathbf{x};\mathbf{R})^{HP}\right|^2 d\mathbf{x} = \left|\varphi_1(\mathbf{x}_1;\mathbf{R})\right|^2 d\mathbf{x}_1 \left|\varphi_2(\mathbf{x}_2;\mathbf{R})\right|^2 d\mathbf{x}_2 \ldots \left|\varphi_{N_e}(\mathbf{x}_{N_e};\mathbf{R})\right|^2 d\mathbf{x}_{N_e}\,. \tag{2.43}$$

In contrast, a single SD is somewhat correlated since it incorporates the exchange-correlation, *i.e.*, the motion of two electrons with parallel spins is correlated. On the other hand, a more accurate solution can be obtained by constructing our many-body wavefunction as a linear combination of SDs. We explore this last proposition more in detail in the following section.

2.5.2 Configuration interaction

A single SD is able to account for up to 99% of the total energy of some molecular systems,[197] which is surprisingly good when considering that the electron-electron interactions are treated within a mean-field approach. On the other hand, this result is still not satisfactory if I want to describe chemical reactions since the remaining 1% of the total energy (correlation energy) is often crucial to calculate the relative energies of the various critical points in a balanced way of the PESs. In fact, what is usually interesting is the relative energies between minima, transition states, and, eventually, CIs which drive chemical reactivity. In addition, a single SD is often not sufficient to describe multiple electronic states, as required in the simulation of photochemical reactions. To include both energy correlation and treat excited states I can express the many-body wavefunction in terms of a linear combination of SDs such as

$$\Phi_j^{CI}(\mathbf{x};\mathbf{R}) = \sum_i c_{ji}(\mathbf{R})\,\varphi_i^{SD}(\mathbf{x};\mathbf{R})\,, \tag{2.44}$$

where $\Phi_j^{CI}(\mathbf{x};\mathbf{R})$ is the configuration interaction wavefunction and $\varphi_i^{SD}(\mathbf{x};\mathbf{R})$ are the SDs used to expand the many-body wavefunction. The $c_{ji}(\mathbf{R})$ are expansion coefficients for which normalization condition $\sum_i c_{ji}(\mathbf{R})^2 = 1$ is imposed. The choice of how many and which SDs have to be chosen in the configuration interaction expansion leads to different levels and flavours of the quantum chemistry methods.

Let us first investigate a simple way to generate SDs starting from the definition presented in Eq. (2.41). In the HF method, I variationally optimized a single SD from N_e electrons and N_{MO} spinorbitals such that N_e spinorbitals are occupied and $N_{MO} - N_e$ are unoccupied (virtual orbitals). By replacing spinorbitals that are occupied in the HF determinant with spinorbitals that are virtual, I can generate determinants that are higher in energy with respect to the HF solution and, depending on how many replacements I perform, I will call them singly, doubly, etc. excited determinants. A simple example of excited determinants is presented in Fig. 2.3. The lowest energy SD is the HF solution ①, while the remaining determinants are singly configurations (③ - ⑥) or doubly excited configurations (②) with respect to the reference. Substituting Eq. (2.44) into the TISE (Eq. (2.3)), multiplying from the left for $\varphi_k^{*SD}(\mathbf{x};\mathbf{R})$ and integrating over the electronic coordinates, I obtain the respective eigenvalue problem

$$\sum_i c_{ji}(\mathbf{R})\langle\varphi_k^{SD}|\hat{H}^{el}|\varphi_i^{SD}\rangle = E_j(\mathbf{R})c_{jk}(\mathbf{R})\,, \tag{2.45}$$

where I have assumed the orthonormality of the basis (Eq. (2.40)). Finding the solution to this eigenvalue problem is equivalent to diagonalizing the Hamiltonian matrix and finding the eigenvectors (that are the configuration interaction coefficients) and eigenvalues (the associated energies).[198, 199] In molecular cases, the Eq. (2.44) may include millions of determinants and a direct diagonalization of the Hamiltonian matrix using, for instance, the Jacobi methods is not possible.[200] However, a complete diagonalization is not required since we are typically interested in only a few of its lowest eigenvalues. Selected eigenvalues of the Hamiltonian can be determined by iterative methods such as the Davidson algorithm where only the action of the matrix over a trial vector is required.[200, 201]

Since the orbitals are kept frozen in the solution of Eq. (2.45), the Hamiltonian matrix elements between the HF SD and any single excited determinant vanishes (Brillouins theorem). In fact, the associated matrix element is completely analogous to the energy gradient of the reference SD with respect to the mixing of the occupied-virtual orbital pair featuring the single excited determinant. Since the reference SD is the HF wavefunction – that is a minimum in the energy and for which the gradient with respect to occupied-virtual orbital mixing vanishes – all single excited determinants do not contribute to the ground state energy.[202]

2.5.2.1 Configuration state functions

Using directly the SD as the basis for the diagonalization of the Hamiltonian leads, in general, to spin contamination of the configuration expansion solutions, and thus does not retain a pure spin character. In fact, the SDs are eigenfunctions of the z-components of the spin operator but they are not necessarily eigenfunctions of the total spin operator. For two electrons system, the matrix $\mathbf{S}_{z-tot} = \mathbf{S}_{z,1} \otimes \mathbf{I}_2 + \mathbf{I}_2 \otimes \mathbf{S}_{z,2}$ is diagonal but $\mathbf{S}^2_{tot} = \mathbf{S}^2_{x-tot} + \mathbf{S}^2_{y-tot} + \mathbf{S}^2_{y-tot}$ is not. Here, $\mathbf{S}_{i-tot}$ is the total spin of the product state along the i-th direction, $\mathbf{S}_{z,1}$ and $\mathbf{S}_{z,2}$ are the Pauili's matrices for the two particles along the z-direction, $\otimes$ is the Kronecker product and $\mathbf{I}_2$ is the identity matrix of dimension 2.

The Fig. 2.3 illustrates a simple example of this kind with four spinorbitals and two electrons. The first two determinants (① and ②) are *closed-shell* determinants and are pure spin functions: the first one is the reference determinant while the second is a doubled excited determinant. The remaining four are singly excited and *open-shell* determinants where the two electrons are localized on two distinct spatial orbitals. For these SD I can find a set of configuration state

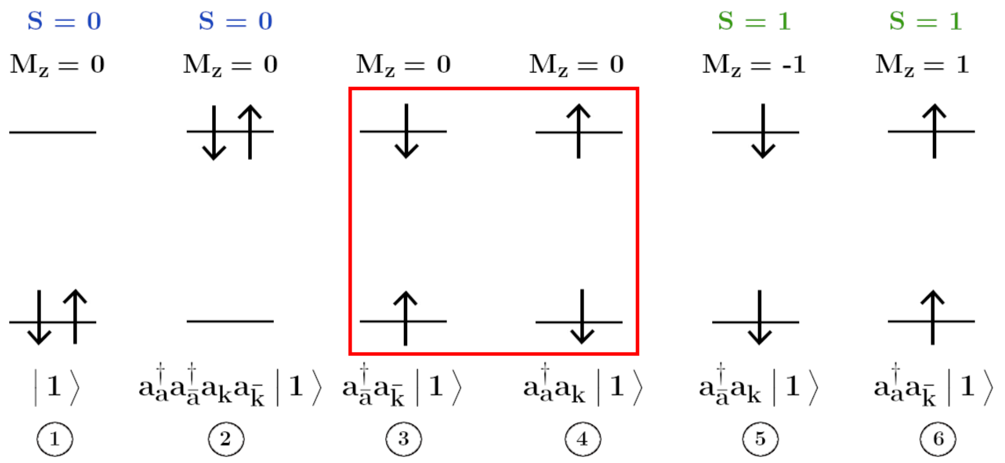

Figure 2.3: We represent all SD generated by distributing two electrons in four spin-orbitals. The excited SD generated are usually not eigenfunctions of the total spin operator as is the case for the framed determinants. To prevent spin contamination I use the CSFs – a linear combination of the SD excited determinants – that are eigenfunctions of the total spin operator. Below I report the string of annihilation and creation operators acting on the spinorbitals of the reference state ($|1\rangle$) to generate a hole (h) in a previously empty orbital (a, $\bar{a}$) or a particle (p) in a previously occupied orbital (k, $\bar{k}$).

functions (CSFs) by the diagonalization of the matrix $\mathbf{S}^2_{tot}$. The last two determinants (⑤ and ⑥) are already eigenfunctions of the total spin operator and they are associated with the two triplet components (S= 1 with $M_z = \pm 1$). However, I need to take an appropriate linear combination of the framed determinants (③ and ④) to obtain a spin-pure CSF. In the present case, the linear combination $3 - 4$ is a singlet (S= 0) CSF while $3 + 4$ is a triplet (S= 1) CSF with both $M_z = 0$.

2.5.2.2 Truncated configuration interaction expansions

In Fig. 2.3 I have generated all possible determinants by distributing all electrons (two) in the available MO space. A configuration interaction calculation of this sort is called full configuration interaction (FCI) and, in the limit of using a complete basis set, it leads to the exact solution of the non-relativistic TISE. In contrast with the HF method, which is invariant with respect to occupied-occupied and virtual-virtual orbital rotation, the FCI is independent of *any* orbital rotation since all possible excitations are generated. Due to the exponential scaling of FCI with respect to the number of orbitals and electrons, FCI calculations are attainable only for small molecular systems. Therefore, to develop a tractable model the number of excited determinants included in the expansion is usually truncated at some order of excitation. When only singly excited state determinants are included I obtain the configuration interaction singles (CIS).[1, 203] CIS ground state is equivalent to the HF reference due to the Brillouins theorem while the remaining states can be used to approximate the excited states. An improvement to

CIS is the configuration interaction with singles and doubles (CISD) that comprehends both single and double-excited determinants. Further excitation terms are usually impossible to include in medium size molecules with a relatively large basis set.[1, 203]

Truncated configuration expansion-based methods are popular in computational chemistry but they also suffer some important drawbacks. For instance, for molecular clusters, higher-order excitations (*i.e.*, triple, quadruple,... excitations) become more important with larger molecular clusters.[203] Thus, although CISD gives a reasonable description of a molecule in regions where the wavefunction is dominated by the HF wavefunction, they do not provide an accurate description of large systems where higher order excitations become important. Furthermore, in contrast to FCI, truncated configuration interaction expansions incorporate only partially the electron correlation, and, as a result, they are not size-extensive – although they can be partially corrected by adding the Davidson correction.[204]

2.5.3 State-average complete active space self consistent field

In the previous section, I discussed the configuration interaction expansion from the HF reference as a possible route to generate an excited state electronic wavefunction. The configuration interaction is then a single reference method, in the sense that the orbitals of a single SD (the HF reference) are used to construct the correlated wavefunctions. There are many cases where a single reference describes well the molecular system considered such as closed-shell organic molecules. However, in many metal complexes or organics radicals, the electronic wavefunction is often dominated by more than one electronic configuration, *i.e.*, multi-configurational. An obvious solution to the multiconfigurational problem is to carry out a configuration interaction calculation where the orbitals are variationally optimized simultaneously with the coefficients of the electronic configurations. This procedure ensures that the orbitals employed in the wave function are optimal for the problem at hand and do not introduce a bias towards a particular configuration. This approach is referred to as the multiconfigurational self-consistent field (MCSCF) method.[205, 206]

Similarly to configuration interaction, the MCSCF wave function is expanded in terms of SD

$$\Phi_j^{MCSCF}(\mathbf{x};\mathbf{R}) = \hat{U}(\mathbf{R}) \sum_i c_{ji}(\mathbf{R})\, \varphi_i^{SD}(\mathbf{x};\mathbf{R})\,, \tag{2.46}$$

where the only difference with Eq. (2.44) is the presence of the unitary orbital-rotation operator $\hat{U}(\mathbf{R})$. The operator $\hat{U}$ – that has the form $\hat{U} = e^{\mathbf{k}}$, where $\mathbf{k}$ is an anti-Hermitian matrix – allows tailoring the orbitals for each configuration by optimizing them variationally together with the coefficients $c_{ji}(\mathbf{R})$.

In practice, the simultaneous optimization of orbitals and coefficients is a cumbersome nonlinear problem leading to a potentially large number of local solutions.[207, 208] The nonlinear nature of the MCSCF optimization imposes a restriction on the number of SDs that can be used in the expansion and the way of selecting the configurations to be included is a crucial question.

2.5.3.1 Selecting the proper configurations

At the dawn of MCSCF approaches, the configurations were selected manually based on physical insights and chemical intuition with a propensity to lead to biased and not reproducible results. Nowadays, there exists a more systematic manner to select the configurations based on the partitioning of the orbital space into subspaces, characterized by certain restrictions with respect to the occupations of the configurations entering the MCSCF wavefunction.

In complete active space (CAS) calculations, the total orbital space is partitioned into a set of (i) inactive orbitals, a set of (ii) active orbitals, and a set of (iii) virtual orbitals.[209–211] In the resulting CASSCF wavefunction, the inactive orbitals are doubly occupied in all configurations, the active orbitals have no restriction in their occupancy while the virtual orbitals are always unoccupied. With this ansatz, all configurations are generated by distributing N active electrons into N_o active orbitals in an FCI fashion (yielding factorial growth with respect to N and N_o). The optimized wavefunction will be invariant within any interspace orbital rotation but will not be for any intraspace rotation.

Similarly to configuration interaction, MCSCF allows to access the wavefunctions of excited electronic states. Since the orbitals must be optimized alongside the configuration interaction coefficients, a popular approach is to use a common orbital basis for all electronic states of interest. In this approach, the orbitals are optimized to minimize the averaged energy of all states expressed as an energy function to which each electronic state contributes with a weight factor:

$$E^{SA} = \sum_i w_i(\mathbf{R}) E_i(\mathbf{R}) = \sum_i^{N_s} w_i(\mathbf{R}) \langle \Phi_i^{MCSCF} | \hat{H}^{el} | \Phi_i^{MCSCF} \rangle \,. \tag{2.47}$$

Here, $w_i(\mathbf{R})$ is the weight factor – usually the same for all N_s electronic states – and $E_i(\mathbf{R})$ is the energy of the i-th electronic state. Although the final set of orbitals is not optimal for each state separately, the state average (SA) provides directly a set of orthonormal electronic states. Hereafter, I will always use the SA formalism for CASSCF calculation identified with the shorthand notation: SA(N_s)-CASSCF(N_o/N).

In contrast to single-reference methods, MCSCF is not a black-box method and cannot easily be applied by nonspecialists. In fact, the choice of the orbitals requires prior knowledge of the excited states involved in the dynamics and the expected molecular reactivity, which is almost never a trivial task. Nevertheless, the MCSCF model is highly flexible and it still constitutes the only approach that, in a balanced manner, can describe bond breakings and molecular dissociation processes, where an unbiased treatment of several electronic configurations is required. In addition, they also provide an accurate description of CIs and their branching space. However, the small number of active orbitals that can be treated in MCSCF theory makes it suitable to describe only the static correlation – arising from the presence of degenerate or nearly degenerate electronic configurations such that few configurations contribute substantially to the electronic wavefunction. In contrast, MCSCF is not tailored to treat dynamical correlation arising from a large number of configurations with a small contribution – the proper description of the Coulomb cusp converges slowly in terms of an orbital expansion. Despite this limitation, MCSCF wave functions may serve as a "zero-order" wavefunction of the electronic system, from which the dynamical correlation can be included by means of configuration-interaction theory, yielding multiconfiguration configuration interaction[212] or perturbation theory such as in MS-CASPT2 or extended multi-state complete active space second-order perturbation theory (XMS-CASPT2).[213–217]

The first requirement to devise an MCSCF wavefunction is the knowledge of the active space and the SA. To do so, it is often necessary to probe the excited state dynamics with an affordable, yet accurate, black-box in order to gain insight into the photochemistry of a molecule. Truncated configuration expansion is a method that is usually far from optimal. On one hand, CIS yields excited states of very poor quality that are not always representative of the expected excited state dynamics. On the other hand, CISD is usually too expensive for exploratory dynamics. A black-box method that has found immense popularity within the computational chemistry community in the past year is the ADC(2) which will be described in the following section.

2.5.4 Algebraic diagrammatic construction

The algebraic diagrammatic construction refers to a formalism to compute algebraically the terms appearing from Green's function, *i.e.*, propagators, via a diagrammatic representation.[218–222] Each type of propagator treated at the ADC level is linked with a different property: the polarization propagator[223] yields the excitation energy while the electron or hole propagators are related to the electron affinity or ionization potential. To avoid the problems associated with propagators and diagrammatic expansion – which is probably not a string in every chemist's bow – I will present a recent formalism that has quickly supplanted the original formulation in favour of a more clean derivation, namely the intermediate state representation (ISR).[222, 224, 225] The ISR not only offers a much simpler derivation with respect to the standard ADC but also guarantees an explicit representation of the excited state wavefunctions which is essential to perform nonadiabatic dynamics.

2.5.4.1 Intermediate-state representation

The set of electronic states – satisfying the TISE (Eq. (2.3)) – are constructed in terms of a complete set of intermediate states (IS)

$$\Phi_j(\mathbf{x};\mathbf{R}) = \sum_i x_{ji}(\mathbf{R})\, \Phi_j^{IS}(\mathbf{x};\mathbf{R}) \,, \tag{2.48}$$

where $x_{ji}(\mathbf{R})$ are the expansion coefficients and $\{\Phi_j^{IS}(\mathbf{x};\mathbf{R})\}$ are the set of ISs used to expand the electronic states. Before deriving an expression for the ISs, I need to consider the set of "correlated excited states" ($|\Phi_i^{CS}\rangle$). The correlated excited states are generated by applying a "physical" excitation operator ($\hat{\tau}_i$) to the reference wavefunction ($|\Phi_0\rangle$)

$$|\Phi_i^{CS}\rangle = \hat{\tau}_i \, |\Phi_0\rangle \,, \tag{2.49}$$

$$\tau_i = \{\hat{a}_a^\dagger \, \hat{a}_k \; ; \; \hat{a}_a^\dagger \, \hat{a}_b^\dagger \, \hat{a}_k \, \hat{a}_l \;\; a < b, k < l ; \; ...\} \,. \tag{2.50}$$

The excitation operator in Eq. (2.50) spans the manifold of all possible excitation and comprises single excitation pairs (first term: 1p-1h), two excitation pairs (second term: 2p-2h), and so on. The correlated intermediate state of Eq. (2.49) are, in general, not orthogonal, and thus they must be orthonormalized with respect to the reference state as well as the other correlated states. Let us investigate the example of an intermediate state belonging to the single excitation class (1p-1h block). The orthogonalization by the Gram-Schmidt algorithm is the correlated state minus the projection of the state onto the reference state so that

$$|\Phi_{ak}^{CS}\rangle = \hat{a}_a^\dagger \, \hat{a}_k |\Phi_0\rangle - |\Phi_0\rangle\langle\Phi_0|\hat{a}_a^\dagger \, \hat{a}_k|\Phi_0\rangle \,. \tag{2.51}$$

The overlap between this correlated state and another correlated state belonging to the single excitation class is

$$S_{ak\,bl} = \langle\Phi_0|\hat{a}_k^\dagger \, \hat{a}_a \, \hat{a}_b^\dagger \, \hat{a}_l|\Phi_0\rangle - \langle\Phi_0|\hat{a}_k^\dagger \, \hat{a}_a|\Phi_0\rangle\langle\Phi_0|\hat{a}_b^\dagger \, \hat{a}_l|\Phi_0\rangle \,, \tag{2.52}$$

and the orthonormal intermediate state becomes

$$|\Phi_{ak}^{IS}\rangle = \sum_{bl} |\Phi_{bl}^{CS}\rangle(\mathbf{S}^{-1/2})_{ak\,bl} \,. \tag{2.53}$$

Once the ISs for the 1p-1h block are generated, a similar procedure – generalized as excitation class orthogonalization – can be applied to the higher excitation class until a complete set of orthonormal states is obtained.

Now that I have the ISs I can proceed to compute the excitation energies. To do so, I make use of a slightly modified TISE where the electronic Hamiltonian operator is now shifted by the ground state energy (E_0). In the basis formed by the intermediate state, the shifted electronic Hamiltonian matrix reads

$$(\mathbf{M})_{ij} = \langle\Phi_i^{IS}|\hat{H}^{el} - E_0|\Phi_j^{IS}\rangle \,. \tag{2.54}$$

Upon diagonalization of Hermitian matrix $\mathbf{M}$ I obtain the excitation energies (eigenvalues) and the electronic states (eigenvectors) corresponding to the expansion coefficients of Eq. (2.48). Explicitly, this secular equation reads

$$\mathbf{M}\mathbf{x} = \mathbf{x}\boldsymbol{\omega} \,, \qquad \mathbf{x}^\dagger\mathbf{x} = \mathbf{1} \,, \tag{2.55}$$

where $\boldsymbol{\omega}$ denotes the diagonal matrix of eigenvalues ω_i and $\mathbf{x}$ are the matrix of eigenvectors.

In addition to the excitation energies, also the properties of the excited states can be obtained in terms of the ISs. Determining the probability of an electronic transition from the ground state to the *i*-th electronic state requires the transition dipole moment ($t_i(\mathbf{R})$) that reads

$$t_i(\mathbf{R}) = \sum_j x_{ij}(\mathbf{R})\, t_j^{IS}(\mathbf{R})\,, \tag{2.56}$$

where $t_j^{IS}(\mathbf{R})$ is the intermediate state transition moments (*i.e.*, the contribution of each IS to the dipole moment). $t_j^{IS}(\mathbf{R})$ can be further expanded in terms of the single-particle contributions ($d_{rs}(\mathbf{R})$) and IS transition amplitudes ($f_{j,rs}(\mathbf{R})$)

$$t_j^{IS}(\mathbf{R}) = \sum_{rs} f_{j,rs}(\mathbf{R})\, d_{rs}(\mathbf{R})\,. \tag{2.57}$$

The IS transition amplitudes are

$$f_{j,rs} = \langle \Phi_j^{IS} | \hat{a}_r^\dagger\, \hat{a}_s | \Phi_0 \rangle\,, \tag{2.58}$$

while the one-particle contribution to the dipole moments reads

$$d_{rs} = \langle \varphi_r |\, \hat{d}\, | \varphi_s \rangle\,. \tag{2.59}$$

The same formalism is not limited to the dipole operator and can easily be extended to other first-order properties. At this point, the reader may wonder what has been gained with respect to an FCI calculation since all excitation classes have been considered until now. Clearly, the complexity of the problem remains the same, and in fact, it leads to an exact solution if the exact ground state is used as the reference state.

However, approximations can be obtained by using an approximated ground state as well as truncating the configuration space (*i.e.*, the excitation class) and the perturbation expansion of the **M** matrix. Although formal proof has not been given yet,[222] the original ADC algebraic expressions can be recovered by using as reference the Møller-Plesset (MP)[226, 227] ground state and the order n of the ADC(n) scheme corresponds to the order of the MPn ground state. Using the MP1 ground state the ADC(1) excitation energies are obtained corresponding to the CIS results. Only when the MP2 ground state is used I obtain correlated excited states at the ADC(2) quality.[225, 228, 229] The resulting **M** matrix, presented in terms of the excitation classes, is depicted in Fig. 2.4. We report the order at which each block is approximated, so that the (p–h/p–h) block is exact up to the second order, the (p–h/2p-2h) and (2p-2h/p–h) coupling blocks up to first order, and the (2p-2h/2p-2h) block only up to zeroth order. Therefore, the ADC(2) matrix has the same dimension as the CISD matrix where both singly-excited and doubly-excited states (even though approximated at the zeroth order) are included.

2.5.4.2 Transition density matrices

The ISR brings another advantage when I want to analyze the transition density of the electronic states. The transition density matrices are one of the most useful tools to bridge the spin-diabatic

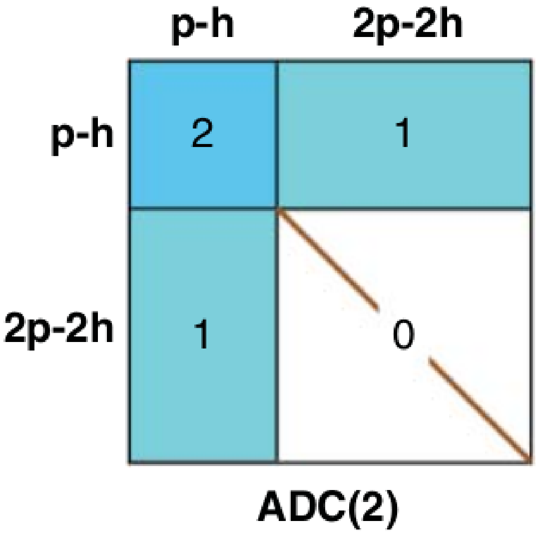

Figure 2.4: Structure of the ADC(2) matrix. The number in the corresponding block refers to the order of perturbation theory to which the matrix elements of the block are exact. Figure reproduced from Ref. 1.

properties computed with the underlined electronic structure and the diabatic representation of the electronic states. In fact, they can be utilized to visualize the nature of the electronic transition and estimate the more prominent "electronic character" of the underlined excited state. The one-electron transition density matrix (1-TDM) is defined as

$$(\mathbf{T}^{0j})_{rs} = \langle \Phi_0 | \hat{a}_r^\dagger \hat{a}_s | \Phi_j \rangle \tag{2.60}$$

The 1-TDM is in general not diagonal in the space of the MOs but it can be factorized via singular value decomposition. Each eigenvector defines the natural transition orbital (NTO)[230] in terms of the MOs while its eigenvalue quantifies the contribution of the NTO to the $0 \to j$ transitions. For some exciting states, only a single pair of NTO is necessary to describe the electronic excitation while, for others, it may be required multiple NTO pairs (multi-configurational excited state). The 1-TDM is related to the electron-hole amplitude, defined as[231, 232]

$$\Upsilon^{0j}(\mathbf{r}_e, \mathbf{r}_h) = \sum_{rs}^{N_e} T_{rs}^{0j}(\mathbf{R})\, \varphi_r^*(\mathbf{r}_h; \mathbf{R}) \varphi_s(\mathbf{r}_e; \mathbf{R})\,, \tag{2.61}$$

where $\mathbf{r}_e$ and $\mathbf{r}_h$ are the vectors specifying the electron and the hole (spin and spatial coordinates). Υ can be interpreted as an exciton wave function associated with the electronic excitation. To compute the respective densities I integrate over the complementary space such that

$$\rho_h(\mathbf{r}_h) = \int d\,\mathbf{r}_e \Big| \Upsilon^{0j}(\mathbf{r}_e, \mathbf{r}_h) \Big|^2 , \tag{2.62}$$

and

$$\rho_e(\mathbf{r}_p) = \int d\,\mathbf{r}_h \Big| \Upsilon^{0j}(\mathbf{r}_e, \mathbf{r}_h) \Big|^2 , \tag{2.63}$$

where $\rho_h(\mathbf{r}_h)$ and $\rho_e(\mathbf{r}_e)$ are the hole and particle densities. A complementary approach to analyzing electronic transitions comes from one-electron difference matrices (1-DDM) or the closely related detachment/attachment densities. We refer the interested reader to the excellent literature for further details.[231, 232]

2.5.4.3 Advantages and limitations of the ADC scheme

The ADC formalism leads to a Hermitian eigenvalues problem (Eq. (2.55)) and it is equivalent to a diagonalization procedure from which a single set of eigenvectors is obtained – in contrast with other formalisms such as equation-of-motion (EOM) and linear response (LR) formalisms. Furthermore, in contrast with truncated configuration interaction schemes, ADC energies are size-extensive and it is more compact (*i.e.*, spans a smaller configuration space) with respect to both configuration interaction or coupled cluster (CC) methods.[225]

However, since ADC excitation energies are based on an MP reference – by virtue of the ISR – their accuracy critically depends on the quality of the MP reference. In fact, the situations where MP fails to describe the ground electronic state are detrimental to the description of the excited states. Since MP reference is based on the single SD, the ADC is not reliable in describing bond-breaking or radical species. Nevertheless, ADC(2) appears to be accurate for single-reference systems showing a relatively low mean error of around 0.2 eV for the excitation energies of singlet and triplet excited states.[225] Although ADC(2) does not properly describe the topology of conical intersections between the ground (S_0) and the first excited (S_1) singlet state,[233] Plasser et al.[234] found that ADC(2) is an excellent compromise between accuracy and stability for nonadiabatic excited state dynamics. Following these reports, the community has gained considerable confidence in ADC(2) to study mid-sized to large molecular systems,[235–245] For these systems ADC(2) is an ideal compromise between accuracy and computational efficiency.

CHAPTER 3

A protocol to compute the photolysis rate constant of volatile organic compounds

In accordance with the University of Bristol guidance on the integration of publications as chapters within a dissertation, I declare that this chapter was adapted from the publications in ACS Earth Space Chemistry[2] and, to a lesser extent, from The Journal of Physical Chemistry Letters[246] My role in the Ref. 2 was to run all the calculations associated with the 2-hydroperoxypropanal, collect and analyze the data, write the associated section and review the overall manuscript. Antonio Prlj, Lewis Hutton, and Basile F. E. Curchod collected, analyzed the data, and wrote the respective sections for the methylhydroperoxide, acrolein, and pyruvic acid. Antonio Prlj and Basile F. E. Curchod wrote the introduction and supervised the project. Daniel Hollas, Darya Shchepanovska, David R. Glowacki, and Petr Slavíček reviewed the manuscript. My role in the Ref. 246 was to contribute to the electronic structure calculations and review the manuscript. Antonio Prlj collected and analyzed the data and wrote the article. Basile F. E. Curchod wrote the article and supervised the overall project. Lea M. Ibele ran the calculation for AIMS.

3.1 Introduction

In chapter 2, I discussed some of the key theoretical methods used to calculate the electronic energies of molecules and simulate their excited-state dynamics beyond the BOA. In this chapter, I will introduce a protocol that will connect computational methodologies with the determination of photolysis quantities of direct interest in atmospheric chemistry. This protocol will lay the cornerstone for the "*in silico*" investigation of the photochemistry of transient VOCs, offering a systematic approach to supplement or even replace experimental studies.

3.2 The photolysis rate constant

Following photoexcitation, a VOC can undergo different photolysis processes, leading to distinct photoproducts. For the general photolytic process

$$\mathrm{A} \xrightarrow{h\nu} \mathrm{B} + \mathrm{C}\,,$$

the reaction rate is

$$-\frac{d\,[A]}{dt} = J\,[A]\,. \tag{3.1}$$

The first-order decay constant (J) depends on the intensity of solar radiation and the photophysical properties of the chemical A. J is calculated as

$$J = \int_{\lambda_{\mathrm{min}}}^{\lambda_{\mathrm{max}}} F(\lambda)\,\sigma(\lambda)\,\phi(\lambda)\,d\lambda\,, \tag{3.2}$$

where λ represents the wavelength while λ_{min} and λ_{max} define the spectral range of interest. $F(\lambda)$ is the flux of the irradiation source (for example, the solar actinic flux) while $\sigma(\lambda)$ and $\phi(\lambda)$ are the photoabsorption cross-section and the photolysis quantum yield, respectively. Eq. (3.2) tells us that to know the rate of a given reaction (J), we need to be informed about the flux of photon $F(\lambda)$ with energy $E = \frac{hc}{\lambda}$ that can excite the molecule, the probability that the molecule will absorb one of these photons (σ) and the yield of the photolysis process of interest (ϕ) once the photon is absorbed. If different photolysis pathways are possible for a given VOC, each dissociation channel is assigned a different $\phi(\lambda)$, and therefore a different J.

In Eq. (3.2), $F(\lambda)$ is a known experimental quantity or, if we are seeking a photolysis process occurring in the atmosphere, it is simply the solar actinic flux which is well documented for different atmospheric conditions.[247] To compute J the only two observables that remain to be determined are $\sigma(\lambda)$ and $\phi(\lambda)$. Their experimental values for some atmospheric relevant molecules can be found in online databases[5] and scientific literature.[248] Nevertheless, this is not always the case for transient VOCs. More often than not, $\sigma(\lambda)$ of transient VOCs is deduced using SARs based on molecules containing the same chromophoric groups. In a similar fashion, $\phi(\lambda)$ is estimated by the value known for a proxy molecule, while its wavelength-dependence is often ignored, *i.e.*, $\phi(\lambda) \approx \phi$.

From a computational chemistry perspective, Eq. (3.2) appears as an exciting playground where our theoretical toolkit can be used to determine, *in silico*, $\sigma(\lambda)$ and $\phi(\lambda)$ of hitherto un(der)explored molecules.

3.3 Calculating photoabsorption cross-sections

The theoretical calculation of the photoabsorption cross-section can be approached in two different ways. One approach is time-dependent, where the photoabsorption spectra are obtained from quantum dynamics using the Fourier transform of the nuclear wavepacket autocorrelation function.[137, 249] Namely,

$$\sigma(E) \propto E \int_{-\infty}^{+\infty} dt\, e^{i(E+E_0)t} \left\langle \chi(\mathbf{R},0) | \chi(\mathbf{R},t) \right\rangle , \tag{3.3}$$

where E is the photon energy, $\chi(\mathbf{R},0)$ is the vibrational wavefunction generated upon the excitation to a specific electronic state, $\chi(\mathbf{R},t)$ is the resulting wavepacket at time t, and E_0 is the energy of the initial state. Fig. 3.1a illustrates the procedure. The black Gaussian on S_0 represents the ground-state wavefunction of a molecule. Upon excitation, a wavepacket is formed that is a coherent linear combination of the vibrational wavefunctions in the excited state of interest. This corresponds to $\chi(\mathbf{R},0)$ and it is represented by the grey Gaussian wavefunction located on S_1. To compute $\sigma(E)$, we allow the wavepacket to evolve in the excited electronic state ($\chi(\mathbf{R},t)$, represented by the evolving black nuclear wavefunction on S_1), and we compute the overlap of $\chi(\mathbf{R},t)$ with $\chi(\mathbf{R},0)$. The Fourier transform of the overlap signal encodes the vibronic details of the photoabsorption spectrum. Although this method is theoretically rigorous, it can be computationally demanding and often requires simplifying assumptions such as reducing the dimensionality of the molecular system.

Alternatively, one can use time-independent approaches based on the calculation of Franck-Condon (FC) integrals[250] between the ground and excited-state vibronic wavefunctions (black and grey Gaussian in S_1, Fig. 3.1b). In these methods, we evaluate the vibronically-resolved absorption spectra based on the probability amplitude for the transition dipole moment. To go beyond the Condon approximation and account for the dependence of transition dipole moments on nuclear coordinates, Herzberg-Teller corrections are often added leading to the Franck-Condon-Herzberg-Teller (FCHT) method.[251] The FCHT method is based on the harmonic approximation, where both the ground and excited electronic states are represented by multidimensional harmonic potentials displaced from each other. However, this method can be inaccurate in molecules with pronounced anharmonicity or dissociative character of the excited states as is the case for many VOCs.

Vibronic features in photoabsorption spectra are not needed for applications that require only the centres, intensities, and widths of absorption bands, rather than their precise structure. In these cases, the simplest method to evaluate photoabsorption cross-sections is to calculate excitation energies and oscillator strengths at the optimized ground state geometry (the black circle in S_0, Fig. 3.1c) and produce a stick spectrum (Fig. 3.1c). This method is easy to implement and the transitions can be further broadened by Gaussian or Lorentzian functions.

A consistent improvement to this simplified method is the nuclear ensemble approach (NEA).[252] The idea behind the NEA is to sample a large number of molecular geometries (black dots in S_0, Fig. 3.1d) from a probability density constructed for the ground electronic and vibrational state of the molecule of interest, and then to project each of these geometries onto the desired excited electronic states. By combining all the calculated transition energies

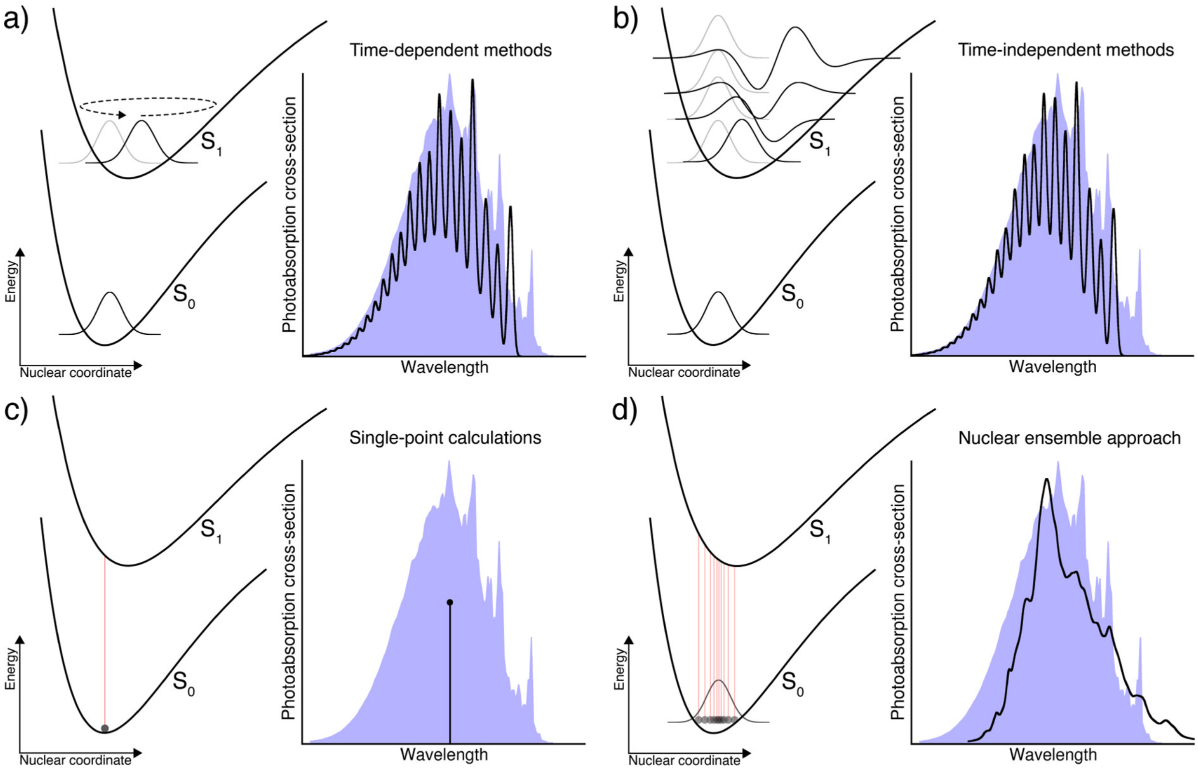

Figure 3.1: Schematic representation of the different main families of methods to determine photoabsorption cross-sections. For each method, a scheme of the key elements of the simulation is presented on the left, with the potential energy curve for the ground (S_0) and first excited (S_1) electronic state. The expected shape of a photoabsorption cross-section is shown on the right (black line), together with a reference experimental spectrum (blue area). a) Time-dependent methods: the ground-state nuclear wavefunction (black Gaussian in S_0) is promoted to S_1 and propagated on this state. b) Time-independent methods: the overlaps between the initial state of the system (black Gaussian in S_0 symbolizing the ground electronic and vibrational state of the system) and all the vibrational wavefunctions in S_1 (black curves in S_1) are calculated. c) Single-point calculations: the minimum-energy structure in S_0 is located (black circle on S_0), and the vertical excitation energy to S_1 is computed for this nuclear configuration only (the vertical red line between S_0 and S_1). d) Nuclear ensemble approach: this method approximates a quantum distribution representative of the ground-state nuclear wavefunction (grey Gaussian in S_0). From this distribution, different nuclear configurations are sampled randomly (black dots in S_0), and for each of them, a vertical transition to S_1 is calculated (as done in (c)). The resulting spectrum is obtained by averaging over all these (broadened) vertical transitions. Figure reproduced from Ref. 2

and oscillator strengths, one can reconstruct a photoabsorption cross-section by convoluting each transition with phenomenological broadening functions, such as Gaussians or Lorentzians. The width of the line shapes is typically chosen to be much narrower than the overall widths of the absorption bands so that it does not affect the simulated band shapes.[252, 253] As such, the NEA can predict accurate widths, heights, and positions of absorption bands. The NEA accounts for non-Condon effects, as it correctly captures the dependence of transition dipole moments on molecular geometry. On the other hand, it completely lacks the description of vibronic structures, as no information about the nuclear wavefunction(s) in the excited states is required (right part of Fig. 3.1d). A formal derivation and justification of the NEA have been already presented[252, 254] and the method has been successfully employed for a broad variety of molecular systems (*e.g.*, Refs. 255–264). Furthermore, an optimal sampling strategy from a statistical perspective has been discussed recently.[265]

One key question remains with the NEA: how we can obtain the best approximation for the ground-state distribution? One possible strategy is to sample the geometries from a Wigner distribution. Wigner distribution offers a way to map quantum nuclear densities to the classical phase space, and its combination with the NEA provides superior photoabsorption cross-sections as compared to thermal sampling.[266] Since the exact Wigner distribution is formally impossible to obtain for multidimensional molecules, one often resorts in practice to the harmonic approximation with uncoupled normal modes of the ground-state potential energy surface. For molecules that are not too anharmonic and for which a proper level of electronic structure theory can be selected, the NEA combined with Wigner sampling reproduces reasonably well the positions of the different bands forming a photoabsorption cross-section, as well as their shape and corresponding intensity.[2] However, its underlying approximations may limit its performance for molecules like VOCs. From this perspective, sampling the molecular geometries from MD still appears to be more beneficial for anharmonic, large, and flexible molecular systems. On one hand, classical MD is a computationally affordable way to sample the ground state following the Boltzmann distribution taking into account the anharmonicity of the PES. On the other hand, it does not recover the zero-point vibrational motion and, as a result, the photoabsorption spectra obtained from such distribution may lead to bands with qualitatively wrong widths.[266] An alternative approximate method that includes zero-point energy is the quantum thermostat (QT).[267, 268] In this approach, classical non-equilibrium dynamics is performed with a generalized Langevin equation that acts as a thermostat to maintain different normal modes at different frequency-dependent temperatures. A QT simulation is exact for a system of uncoupled harmonic oscillators but performs well also for anharmonic molecules. It can accurately sample both high-frequency modes, where quantum effects dominate, and low-frequency modes, where anharmonic and temperature effects are more important.[269]

To evaluate the performance of the NEA when combined with a Wigner or QT sampling we show the absorption cross-sections computed for two exemplary oxygenated VOC molecules of great interest in atmospheric photochemistry: methylhydroperoxide and 2-hydroperoxy-propanal (2-HPP).

3.3.1 Computational details

3.3.1.1 Electronic structure

Except where stated otherwise, we employed the same level of theory for all three molecules, and all electronic-structure calculations were performed with Gaussian 09 revision D.01.[270] Ground-state (S_0) minima and vibrational frequencies were obtained with DFT using the PBE0[271] functional and the 6-311G* basis set. The same level of theory was utilized for the AIMD simulations using the QT approach as detailed below. Excited-state energies and oscillator strengths were calculated with linear-response time-dependent DFT (LR-TDDFT)[272–274] using the Tamm-Dancoff approximation (TDA),[275] at the PBE0/6-311G* level. For methylhydroperoxide, the 6-311+G* basis set was employed since diffuse basis functions are needed to describe the valence-Rydberg mixing in peroxide excited states.[246]

3.3.1.2 Ground-state sampling

Wigner sampling of the vibrational ground state within the harmonic approximation was used as implemented in the Newton-X 2.0 package.[166] AIMD with QT was performed with the ABIN code,[276] coupled to the TeraChem v1.9 package for the electronic structure,[277, 278] using the same ground-state electronic structure level as elsewhere (PBE0/6-311G*). Parameters for the thermostat were taken from the GLE4MD webpage,[279] using a target temperature T = 296 K and parameters: Ns = 6, $\hbar\omega/kT = 20$, strong coupling. The molecular dynamics time step was $\sim$ 0.5 fs. The equilibration time was determined by monitoring the convergence of the average kinetic energy temperature. For molecules with multiple conformers, independent trajectories starting from a given minimum geometry were performed for each conformer. Conversion between conformers was only observed in the simulations of 2-HPP and taken into account for the overall sampling.

3.3.1.3 Spectra calculation

Photoabsorption cross-sections from the NEA were computed with the Newton-X 2.0[166] package interfaced to Gaussian 09 revision D.01 using the equation[252]

$$\sigma(E) = \frac{\pi e^2 \hbar}{2 m_e c \epsilon_0 E} \sum_{J=1}^{N_s} \frac{1}{N_p} \sum_{n}^{N_p} \Delta E_{0J}(\mathbf{R}_n) f_{0J}(\mathbf{R}_n) \omega_s [E - \Delta E_{0J}(\mathbf{R}_n), \delta] \,, \tag{3.4}$$

where E is the photon energy, e the electron charge, m_e the electron mass, ϵ_0 the vacuum permitivity, and c the speed of light. $\Delta E_{0J}(\mathbf{R}_n)$ corresponds to the vertical excitation energy between the ground state 0 and the excited electronic state J, for the n-th sampled molecular geometry with corresponding nuclear configuration $\mathbf{R}_n$. $f_{0J}(\mathbf{R}_n)$ is the corresponding oscillator strength at nuclear configuration $\mathbf{R}_n$. $\omega_s[E - \Delta E_{0J}(\mathbf{R}_n), \delta]$ is a normalized line shape centred at energy $\Delta E_{0J}(\mathbf{R}_n)$ and with a phenomenological width δ. In our calculations, we used a Lorentzian shape for ω_s with a phenomenological broadening of 0.05 eV (default in Newton-X, discussed in Ref. 252). The first sum runs over N_s electronic states. The second sum runs over all the N_p sampled nuclear geometries. N_p is set to 500 for both Wigner and QT sampling, for each conformer. 500 initial conditions are sufficient to converge the positions and the intensities of the absorption bands. The overall spectra were evaluated by scaling the contributions of each conformer with their Boltzmann factors – one conformer for methylhydroperoxide and eight conformers for 2-HPP. For each molecule, the calculated spectra account solely for the $S_0 \rightarrow S_1$ transition, which is well separated from the other transitions at higher energy, except for methylhydroperoxide where the lowest five singlet excited states needed to be considered.

3.3.2 Results and discussion

3.3.2.1 Methylhydroperoxide – limitations of the harmonic approximation

Our first example focuses on methylhydroperoxide, the simplest organic hydroperoxide. Alkylperoxides undergo photolysis which involves the dissociation of OH, H, and O radicals.[246] This is due to the dissociative nature of their low-lying excited states, primarily of $n\sigma^*$ character, where the σ^* orbital is anti-bonding with respect to O−O or O−H bond.[246] The dissociative nature of the excited states excludes the applicability of the FCHT method for the absorption spectrum since the excited states do not possess a minimum. This limitation is not shared by the NEA, which can be applied also in the case of unbound excited states.

Fig. 3.2 offers a comparison between the photoabsorption cross-sections of methylhydroperoxide predicted by the NEA, with both Wigner and QT sampling, and the experimental reference. In contrast with the result of acrolein, the NEA results based on a Wigner or a QT sampling show noticeable differences. Only the cross-section obtained from a QT sampling exhibits a good agreement with experimental data. The NEA using Wigner sampling predicts transitions with a higher oscillator strength in the low-energy range of the spectrum, appearing as sharp features on the photoabsorption cross-section. While such sharp features could be averaged out in the NEA spectrum by increasing the number of sampled geometries or adjusting the line broadening, the problem would persist – the absorption intensity would simply be too high in comparison to the experimental spectrum.

The issues experienced by Wigner sampling for methylhydroperoxide are disclosed by analyzing the distributions of bond lengths. Fig. 3.3 shows histograms of O−O and O−H bond lengths in the Wigner and QT sampling. The distributions of O−O bond lengths are very similar in the two types of sampling, as might be expected from a rather harmonic bond. However, the Wigner and QT distributions are surprisingly different when it comes to the O−H bond.

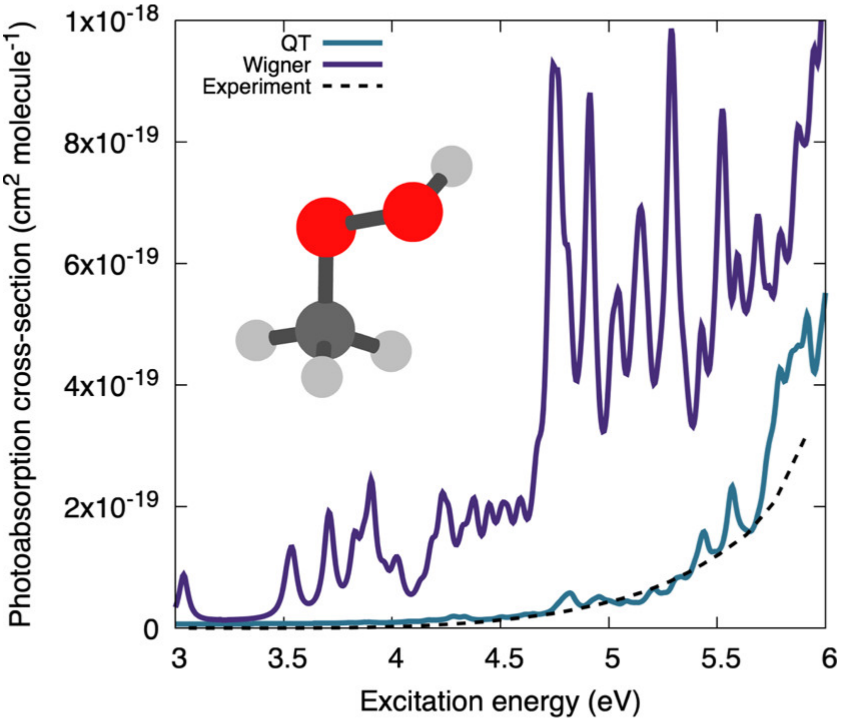

Figure 3.2: Calculated and experimental photoabsorption cross-sections of methylhydroperoxide. The experimental spectrum was obtained by combining data from Refs. 3 and 4, as recommended in the MPI-Mainz UV/Vis Spectral Atlas.[5]

The QT sampling predicts O−H bond lengths between 0.8 and 1.2 Å, while the distribution is much broader with Wigner sampling, extending up to 1.6 Å.

Wigner sampling in its practical implementations for molecules – describing a molecule as a set of uncoupled harmonic oscillators using normal modes described in Cartesian coordinates – has an inherent problem with sampling soft low-frequency modes.[280, 281] In particular, rectilinear normal modes used for the Wigner sampling constitute a bad representation of torsions, as atoms are displaced along the normal mode vectors, *i.e.*, along straight lines, being sheared instead of rotated.[269, 280, 282, 283] For light atoms such as hydrogen, this causes too large interatomic displacements. In the particular case of methylhydroperoxide, the O−H stretching mode itself is well described, but the issue emerges when the low-energy −C−O−O−H torsion mode is sampled. The poor sampling of this torsional mode leads to an artificial stretching of the O−H bond with no energy penalty.

But how does this biased O−H distribution end up affecting the photoabsorption cross-section then? Looking back at the results presented in Fig. 3.2, we can analyze the electronic characters of the transitions resulting in the peaks with a high oscillator strength in the NEA/Wigner spectrum. This analysis reveals that these high peaks correspond to transitions with a $n\sigma^*$ character, where the σ^* orbital is anti-bonding with respect to the O−H bond. This character corresponds to an $S_0 \rightarrow S_2$ transition at the minimum-energy geometry, but

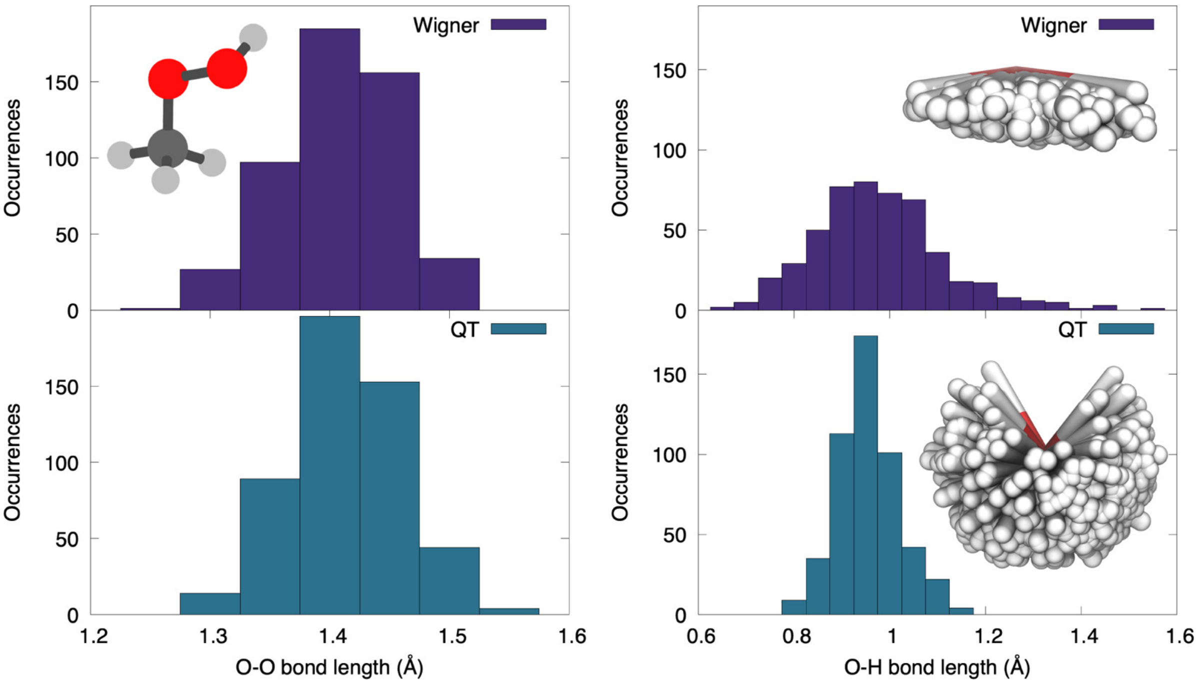

Figure 3.3: Distribution of O−O (left) and O−H bond lengths (right) in methylhydroperoxide for a sampling obtained from a Wigner distribution (upper panels) or a QT dynamics (lower panels). The insets show the spatial distribution of hydrogen atoms from the OH group in the 500 geometries obtained from the two types of sampling.

the energy of this transition decreases sharply when the O−H bond is elongated. In addition, the $n\sigma^*$ (O−H) transition is characterized by a larger oscillator strength than the (O−O) $n\sigma^*$. Hence, the artificial elongation of the O−H bond caused by the Wigner sampling leads to the appearance of artificial high-intensity of the $n\sigma^*$ (O−H) transitions in the lower spectral range that contaminates the overall cross-sections. The QT removes this artefact as the dynamics *per se* do naturally account for the couplings between the different normal modes, proving a more reliable sampling procedure for this molecule.

3.3.2.2 2-hydroperoxy-propanal — on the use of SARs for photoabsorption cross-sections

Unlike methylhydroperoxide, the photophysics and photochemistry of most atmospheric VOCs have not been characterized experimentally. For such compounds, other strategies were proposed to estimate their photoabsorption cross-sections such as SARs, where molecular properties are inferred based on chemically similar compounds for which accurate measurements are available. For instance, the photoabsorption cross-section of a multifunctional molecule may be estimated based on smaller monofunctional fragments, each containing one of the functional groups of the parent multifunctional molecule (for example, see Refs. 87 and 284). Peeters et al. used this strategy in their study of the photolysis of α-hydroperoxy-carbonyls — molecules that contain both a peroxide and a carbonyl moiety.[6] The composite photoabsorption cross-section of 2-HPP (the left structure in Fig. 3.4) was estimated from the sum of photoabsorption cross-sections of methylhydroperoxide and propanal (right structures of Fig. 3.4). Due to possible intramolecular interactions (*e.g.*, H-bonding) between the two functional groups in 2-HPP, the total composite photoabsorption cross-section was multiplied with an enhancement factor that was estimated from the data of chemically similar β-hydroperoxy-carbonyls.[6]

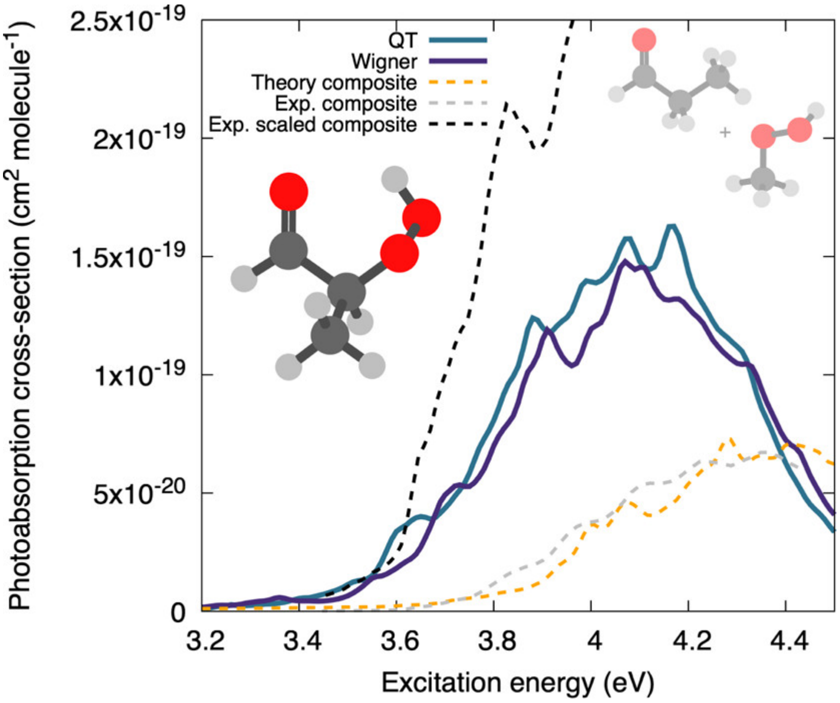

Figure 3.4: Calculated and experimental photoabsorption cross-sections of 2-HPP. The theoretical composite spectrum was obtained by combining the calculated photoabsorption cross-sections of methylhydroperoxide and propanal, depicted on the right inset (see text for additional details). The experimental composite spectra were digitized from Ref. 6.

The experimental composite and scaled composite spectra of 2-HPP are shown in Fig. 3.4 (dashed lines). To validate our approach, we first reproduced the unscaled experimental composite spectra fully by theory, combining the NEA photoabsorption cross-sections of propanal and methylhydroperoxide (as calculated in Fig. 3.2). For methylhydroperoxide, we took our best result based on QT sampling, while the propanal cross-section was calculated using Wigner sampling. Overall, the theoretical and experimental composite spectra agree very closely. However, the theoretical approaches described in this work allow us to study the original 2-HPP molecule itself, bypassing the use of SARs. The photoabsorption cross-section of 2-HPP was calculated with the NEA using two sampling procedures – Wigner and QT – accounting for the eight low-energy conformers of the molecule. Note that the flexibility of 2-HPP and its numerous conformers in the ground and excited (S_1) state complicates the use of the FCHT method – the harmonic approximation not being reliable for several of the nuclear-wavefunction overlaps calculated, we omitted the results of this approach. The NEA results from a QT or Wigner sampling (Fig. 3.4) are in good agreement in this example. More importantly, these results clearly indicate that there is a sizable increase in absorption intensity as compared to the theoretical composite spectra, but the enhancement is significantly smaller than the one predicted by scaling reported in earlier work. This result is corroborated by the analysis of the photoabsorption cross-section of the main conformers as shown in Fig. 3.5. The spectra for the conformers 1c and 1d – which do not have an intramolecular H-bond between the carbonyl group and the hydrogen of the peroxide moiety – are on the order of 1×10^{-19} cm^2 molecule^{-1}, consistent with a $n\pi^*$ transition. In contrast, the conformers 1a and 1b – with intramolecular H-bond – have a larger photoabsorption cross-section than the others due to the perturbation that the H-bond exerts on the n and π^* orbitals involved in the electronic transition. This shows that using SARs bears a risk of over- or underestimating the photoabsorption cross-sections, but this risk can be assessed by using the theoretical approaches described here.

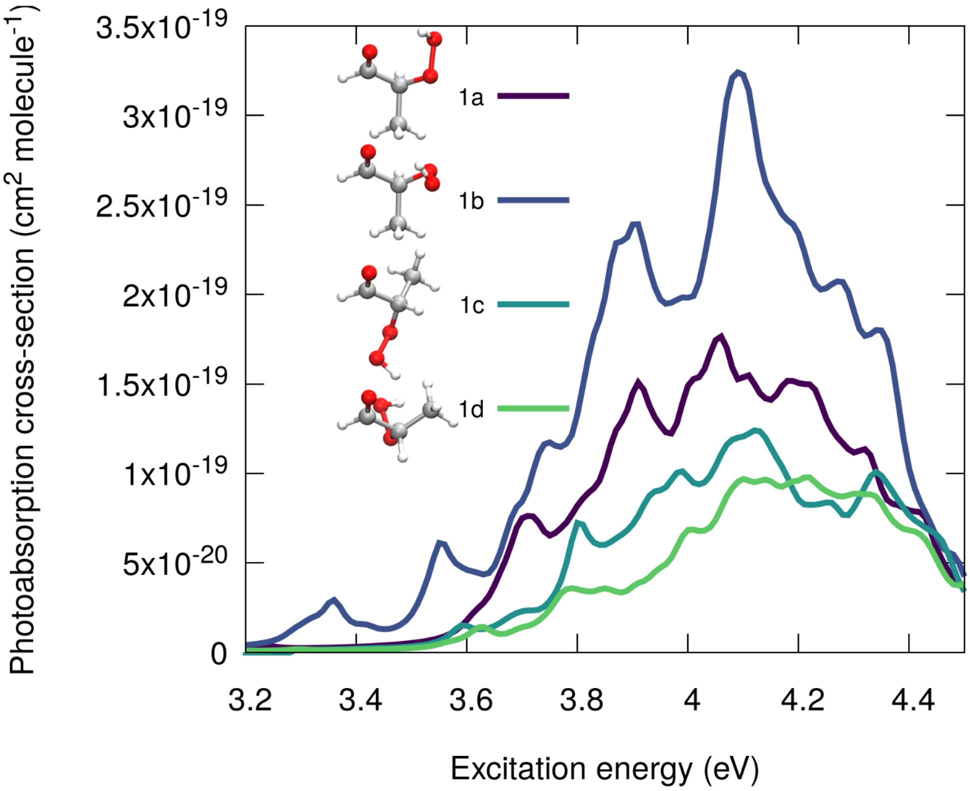

Figure 3.5: Calculated photoabsorption cross-sections of 2-HPP conformers exhibiting different intramolecular interactions. The conformers labelled 1a and 1b have intramolecular H-bonds and exhibit a larger spectral enhancement as compared to conformers 1c and 1d that does not have intramolecular H-bonds.

Having detailed the methodologies to compute $\sigma(\lambda)$ for VOCs we can now turn our attention to the second observable required to compute J following Eq. (3.2), namely $\phi(\lambda)$.

3.4 Calculating the wavelength-dependent quantum yield

The wavelength-dependent quantum yield, $\phi(\lambda)$, can be predicted by using nonadiabatic molecular dynamics simulations, which allow us to investigate the products formed after photoexcitation and their respective yields. For molecular systems in their full dimensionality, methods like the AIMS[183, 185] or TSH would be preferred.[253] The wavelength dependence of the quantum yield can be recovered by carefully selecting the initial conditions for the nonadiabatic dynamics. From the ground-state sampling – Wigner or QT – we obtain, in addition to the nuclear geometries, a set of nuclear momenta. The combination of a nuclear geometry plus nuclear momenta constitutes a given initial condition for the nonadiabatic dynamics. Hence, by dividing the calculated $\sigma(\lambda)$ in different excitation windows, we can select for each window a set of initial conditions for the nonadiabatic dynamics. Once the excited-state dynamics for each of these initial conditions have been performed, one can monitor the formed photoproducts and assign, for each wavelength window, a ratio of photoproducts – a proxy for a quantum yield at this given wavelength. Combining all the windows will therefore provide an estimation of the wavelength-dependent quantum yield for each photolysis product. This strategy was tested in Ref. 246 for the tert-butyl hydroperoxide and will be applied for the 2-HPP in chapter 5.

3.5 Conclusions

In this chapter, we have illustrated the protocol to calculate *in silico* the photolysis rate constant (J) for VOCs. For transient VOCs, where experimental studies are extremely scarce and the results are usually estimated using SARs based on proxy molecules, this theoretical protocol provides a systematic tool to supplement or even supersede experimental results. In particular, two key observables are required to solve Eq. (3.2), namely the photoabsorption cross-section ($\sigma(\lambda)$) and photolysis quantum yield ($\phi(\lambda)$).

The calculation of the photoabsorption cross-section of VOCs can be approached using several computational methodologies. The FCHT technique is a valuable tool if such molecules are rather rigid, exhibit bound excited electronic states, and only one conformer is predominant. However, VOCs often do not follow these prescriptions and the NEA constitutes an excellent alternative. The NEA can predict the correct widths, heights, and positions of absorption bands, which is sufficient for most atmospheric applications, such as the evaluation of J. However, one should be extremely cautious about the sampling of ensemble configurations when using the NEA. Due to the limitation of thermal sampling, we have investigated and compared here the performance of two quantum sampling approaches for VOCs – Wigner and QT. We showed that QT sampling appears superior to the simple Wigner distribution in situations where low-frequency anharmonic modes may affect the computed photoabsorption cross-sections. Such situations are not uncommon, as shown in this work for the example of methylhydroperoxide but are less important in molecules such as 2-HPP due to the nature of their excited state. Despite this advantage, QT sampling is significantly more computationally expensive than using the simple Wigner approach.

Once the photoabsorption cross-section is calculated, one can select the initial conditions based on their excitation energy. Each selected initial condition provides the starting point for a nonadiabatic dynamics simulation which allows us to investigate the photoproducts and their respective yields. More details about the wavelength-dependent will be given in chapter 5 where we will examine the photolysis of the 2-HPP.

CHAPTER 4

Caveat when using ADC(2) for studying the photochemistry of carbonyl-containing molecules

In accordance with the University of Bristol guidance on the integration of publications as chapters within a dissertation, I declare this chapter was previously published in Physical Chemistry Chemical Physics.[285] My role in this study, as the first author of the publication, was to devise the methodology, run the calculations, collect and analyze the data, and write the paper. Antonio Prlj and Basile F. E Curchod wrote and reviewed the paper and supervised the overall project.

4.1 Introduction

In chapter 3, I have shown how computational chemistry simulations can help predict experimental observables, specifically in calculating the photolysis rate constant of VOCs. To do this, two main ingredients are required: the photoabsorption cross-section and the photolysis quantum yield. Although I illustrated that theory is capable of accessing these components, we didn't clarify the role of electronic-structure methods in this procedure. As we discussed in chapter 2, the solution of the TISE gives us access to the energies and properties of electronic states. This provides us with excitation energies and oscillator strengths necessary to compute the photoabsorption cross-section. Additionally, electronic-structure methods allow us to calculate adiabatic forces and non-adiabatic coupling terms, required to determine the wavelength-dependent quantum yield.

To calculate the photoabsorption cross-section using the NEA method, we need to sample the ground-state nuclear wavefunction. The regions of the configuration space that need to be sampled are those around the different ground-state minimums. In most cases, the ground state of VOCs is well represented by a single electronic configuration, which makes single-reference methods a practical choice. Then, the problem of computing the photoabsorption cross-section is reduced to the accuracy at which the excitation energies and oscillator strengths are determined. LR-TDDFT is a widely used method for this purpose due to its low computational cost, which allows the treatment of large molecules with hundreds or thousands of atoms. A competitor to LR-TDDFT is the ADC(2). Despite not being as computationally affordable as LR-TDDFT, it is generally more accurate[225] and also not as computationally cumbersome as multireference approaches.

When we turn our attention to the photolysis quantum yield, choosing the appropriate electronic-structure method becomes more troublesome. Upon photoexcitation, the molecule experiences a different electronic potential which may lead the system to explore regions of the configuration space far from the ground state minimum. For instance, during a homolytic bond breaking – a typical case of the photolysis of VOCs, the ground state acquires a multi-configurational character since the σ and σ^* orbitals become degenerate. In these cases, one is almost always forced to fall back towards multireference methods. However, more subtle situations can occur during the excited state dynamics where the quality of the electronic properties computed with single-reference methods decreases dramatically even without a bond cleavage. Over the years, different failures of LR-TDDFT have been documented for certain types of excited states (*e.g.*, charge-transfer states and doubly-excited states) as well as the situations where DFT ground state reference itself is not well described by a single closed shell configuration.[286] Importantly, gaining knowledge on the failures of LR-TDDFT approximations has also contributed to the better use of this electronic-structure method.

Interestingly, the same awareness is instead not fully mature for ADC(2), and the possible flaws that may affect the reliability of ADC(2) are still not fully explored. Here, we highlight what appears to be a systematic issue of ADC(2) in describing some electronic states of molecules bearing a carbonyl group, which concerns a large class of molecules like chromophores, nucleobases, or atmospheric VOCs. Such systems possess characteristic low-lying singlet excited state of n(O)π^*(C=O) character (shortened by nπ^* in the following), where n(O) is the lone pair orbital associated with the oxygen of the carbonyl group and π^*(C=O) refers here to an unoccupied π-type orbital localized either fully on the carbonyl functional group or partially when delocalization is possible. We start our investigation by examining the ADC(2) excited-state dynamics of small molecules bearing carbonyl moiety. Fig. 4.1 shows the time evolution of the ground (full) and excited (dashed) state electronic energies following the molecular dynamics initiated by a nπ^* photoexcitation. The electronic states were computed with the spin-component-scaled (SCS) variant of MP2/ADC(2), which was recently shown to improve the potential energy surfaces,[287] combined with an SVP basis set – in the following, we will note SCS-MP2/ADC(2) to denote the combination of SCS-MP2 for S_0 and SCS-ADC(2) for the excited states. Inspecting the time trace of the electronic energies for five different carbonyl-containing molecules, namely formaldehyde, (anti-)acrolein, pyrone, 2-hydroperoxy-propanal (2-HPP), and oxalyl fluoride, reveals a common feature: all the systems appear to possess an easily accessible nonradiative decay channel via an S_1/S_0 crossing, achieved by ultrafast elongation of the C=O bond.

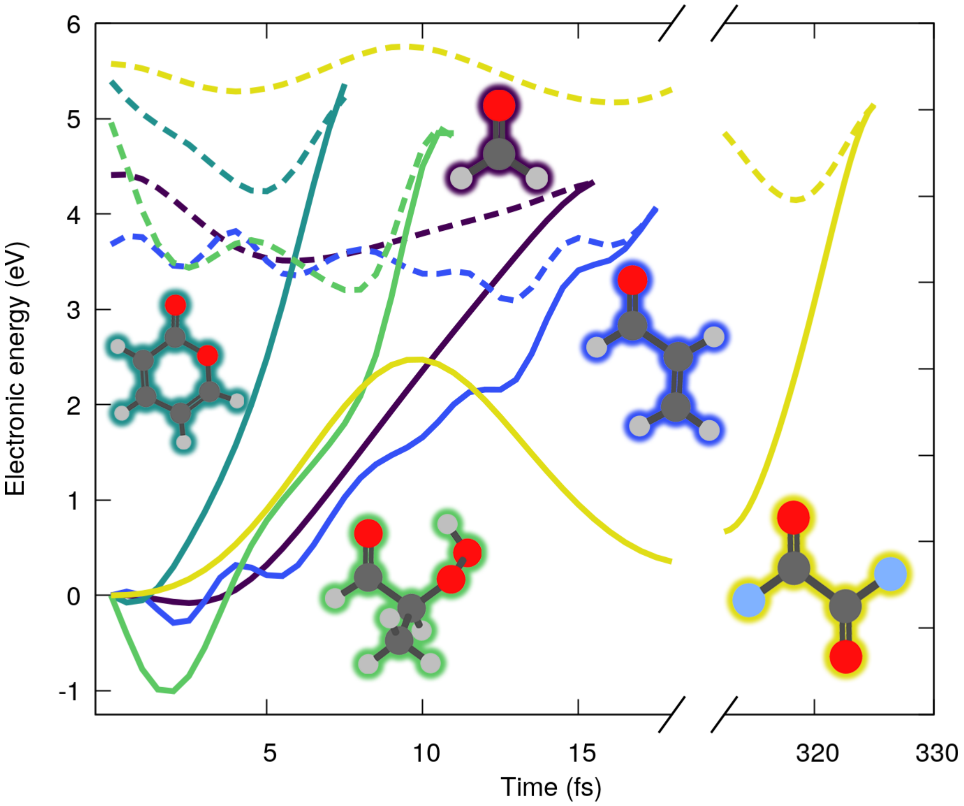

Figure 4.1: Time evolution of the electronic energies of the excited (dashed) and S_0 (solid) states of formaldehyde (purple), acrolein (blue), pyrone (dark green), 2-HPP (light green) and oxalyl fluoride (yellow), following an excited-state molecular dynamics initiated in a $n\pi^*$ electronic state (SCS-MP2/ADC(2)).

Interestingly, a similar nonradiative pathway showed up in the excited-state dynamics of the nucleobase thymine, accounting for 61% of radiationless decay in the gas phase,[288] and 54% in water.[236] The decay channel associated with C=O elongation was also identified in a guanine derivative,[289] though it was argued that other deactivation mechanisms would prevail. Interestingly, all these studies employed ADC(2) method. As such, a nonradiative decay channel mediated by the C=O elongation appears to be a general and well-established feature in the excited-state dynamics of carbonyl-containing molecules. Can it really be the case? In fact, more systematic studies of cytosine[123, 290] and guanine[291] derivatives photophysics cast some doubt on these observations. In these studies, ADC(2) predictions were compared to the results from a high-level multireference method, finding some conspicuous discrepancies. What does that mean for the molecules shown in Fig. 4.1? We will show in the following that such an easily accessible deactivation pathway is an artefact of the MP2/ADC(2) method that end users should be aware of.

4.2 Computational details

The following electronic-structure methods were used in this work: MP2,[226] (strict) ADC(2) and SCS-ADC(2),[225, 228, 229] CC at the second order (CC2)[229, 292] and SCS-CC2,[293], DFT[294, 295] and LR-TDDFT,[272, 274], SA-CASSCF,[203], XMS-CASPT2,[213, 215] in its Single-State, Single-Reference (SS-SR, used if not stated otherwise) and Multi-State, Multi-Reference (MS-MR) versions,[214], and multi-reference CISD (MR-CISD).[212] The calculations were performed with Gaussian09[270] (DFT and LR-TDDFT), Turbomole 7.3[296] (MP2, ADC(2), SCS-ADC(2), CC2 and SCS-CC2), BAGEL 1.2[297] (SA-CASSCF, SS-SR-XMS-CASPT2), and MOLPRO 2012.1[298] (SA-CASSCF, MS-MR-XMS-CASPT2, and MR-CISD) program packages.

The PBE0 exchange-correlation functional was used for all DFT and LR-TDDFT calculations,[271] within the TDA. MP2, ADC(2), SCS-ADC(2), CC2, and SCS-CC2 were performed with frozen core and the resolution of the identity (RI).[299] The standard scaling factors were used for SCS-ADC(2) and SCS-CC2. BAGEL calculations were performed using Density Fitting (DF) and frozen core. DF and frozen core approximations were not utilized in MOLPRO calculations. All XMS-CASPT2 calculations employed a real vertical shift of 0.5 Hartree. The Karlsruhe basis sets def2-SVP and def2-TZVP were employed[300–302] – a def2-SVP basis set should be assumed if not stated otherwise.

For each molecule studied in this work, a linear interpolation in the internal coordinates (LIIC) pathway was calculated between the Franck-Condon geometry (minimum on the S_0 potential energy surface, optimized at SCS-MP2/def2-SVP level of theory) and the S_1/S_0 crossing points (SCS-MP2/def2-SVP for S_0 and SCS-ADC(2)/def2-SVP for S_1). The minimum-energy crossing points close to the Franck-Condon region were located with CIOpt.[303] We note that while the CIOpt code in principle returns minimum-energy conical intersections (MECI), we prefer to coin the geometries obtained in this work "crossing points" (CPs) given that ADC(2) does not describe adequately the branching space of S_0/S_1 conical intersections.[233]

Trajectory surface hopping dynamics employed Tully's fewest switches algorithm and were performed with Newton-X version 2.0[166] using the Turbomole interface and the ADC(2) implementation discussed in Ref. 234. The initial conditions were randomly selected from a Wigner distribution for uncoupled harmonic oscillators, generated from a ground-state optimized geometry and corresponding vibrational frequencies obtained at the SCS-MP2/def2-SVP level of theory. The excited-state dynamics were initiated in a $n\pi^*$ state for all molecules and employed a time step of 0.5 fs. Trajectories were stopped whenever they reached a region of configuration space where the S_1/S_0 energy gap was smaller than 0.01 eV. The default parameters of Newton-X were employed for all dynamics.

4.2.1 Active spaces for multireference methods

To describe accurately the molecular reactivity with multireference methods is crucial to identify a meaningful set of configurations. For carbonyl-containing molecules considered in this work, at the FC point, the S_0 electronic state is a closed-shell configuration while the S_1 electronic state can be identified as a nπ^* excited state. Then, these two electronic states are described by the n(O) and π^*(C=O) orbitals which provide a small, yet sufficient, active space. To have a better description of the electronic structure of the molecule along the C=O stretching we augment this minimal active space. Fig. 4.2 presents the natural orbitals used as reference for the following calculations: XMS(2)-CASPT2(6/5) for formaldehyde, XMS(2)-CASPT2(6/5) for acrolein, XMS(3)-CASPT2(6/5) for pyrone, XMS(4)-CASPT2(12/9) for 2-HPP, and XMS(3)-CASPT2(8/6) for oxalyl-fluoride.

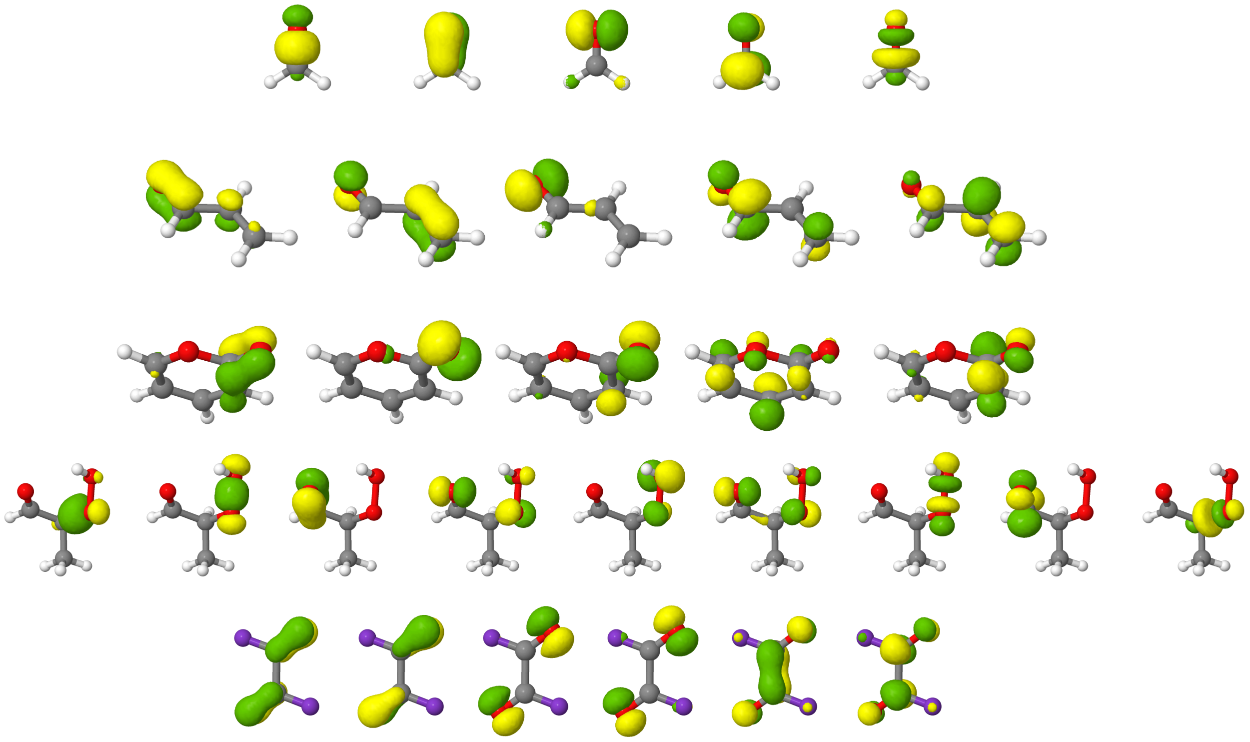

Figure 4.2: SA-CASSCF natural orbitals (isovalue of 0.1) employed as reference for the XMS-CASPT2 calculations. Top to bottom: formaldehyde, acrolein, pyrone, 2-HPP, and oxalyl fluoride.

For formaldehyde, we have added the π(C=O), σ(C=O) and σ^*(C=O) orbitals. For acrolein and pyrone, we have augmented the minimal active space with the additional π(C=O), π', and π'^* orbitals. For 2-HPP we have included the π(C=O) orbital, two σ and σ^* pairs located on the C−O and O−O moieties, and two n orbitals of O−O moiety. Finally, for the oxalyl fluoride, we use minimal active with the additional π(C=O) orbital. Taking into account the symmetry of the molecules it results in eight electrons and six orbitals.

4.3 Results and discussion

To highlight the artificial nature of these nonradiative pathways, we optimized the S_0 minimum geometry – the FC point – with SCS-MP2/def2-SVP and the S_1/S_0 crossing point (S_1/S_0 CP) with SCS-MP2/ADC(2)/def2-SVP. In Fig. 4.3, we then interpolated geometries in internal coordinates between these two critical points and computed electronic energies both with SCS-MP2/ADC(2) and XMS-CASPT2/def2-SVP. Surprisingly, XMS-CASPT2 shows an entirely different behaviour when the C=O bond is extended beyond 1.4 Å. The intersection observed between S_0 and S_1 ($n\pi^*$) at the SCS-MP2/ADC(2) level is not present at the XMS-CASPT2 for all molecules. Any attempt to locate the crossing at the XMS-CASPT2 level did not lead to a structure resembling the S_1/S_0 CP of SCS-MP2/ADC(2). In other words, SCS-MP2/ADC(2) suggests the presence of an easily accessible S_1/S_0 CP, while XMS-CASPT2 strongly indicates that the crossing is not easily accessible – whether it is much higher in energy or does not exist at all. Importantly, such a discrepancy between the two methods is systematic for all five molecules.

Let us now focus on the case of formaldehyde to gain deeper insights into this issue. Fig. 4.4 shows the same electronic-energy profiles as in Fig. 4.3 but now for five different methods: TDA-PBE0/def2-SVP (grey), SCS-ADC(2)/def2-SVP (black), XMS(2)-CASPT2(2/2)/def2-SVP (red), XMS(2)-CASPT2(4/3)/def2-SVP (blue) and MR-CISD(4/3)/def2-SVP (green). The high-level methods XMS(2)-CASPT2(4/3) and MR-CISD both agree on the absence of an intersection at the SCS-MP2/ADC(2) S_1/S_0 CP geometry. The D_1 diagnostic (dashed orange) measures the degree of multiconfigurational character for the MP2 ground state. The quick D_1 surge beyond the recommended limit value of 0.04[304] (and even the less conservative value of 0.1 proposed by others[305]) indicates that the S_0 state acquires a multiconfigurational character along the pathway. In other words, the single-reference wavefunction that serves as a reference for perturbation theory is no longer adequate for large D_1 values. Interestingly, the PBE0 ground state appears to have an incorrect shape in comparison to high-level methods, but as the S_1 electronic energies are also raising steeply along the profile, the S_1/S_0 CP is (fortuitously) avoided.

The artificial S_1/S_0 CP of SCS-MP2/ADC(2) can be explained as the combination of two recurring factors for all molecules bearing a carbonyl group: (*i*) the MP2 ground state is not adequate and overestimates the S_0 energy when stretching the C=O bond and (*ii*) the curvature of the n→ π^* state along the CO stretching coordinate is too small. The poor description of S_1 can be correlated with an increasing contribution of doubly-excited configurations along the

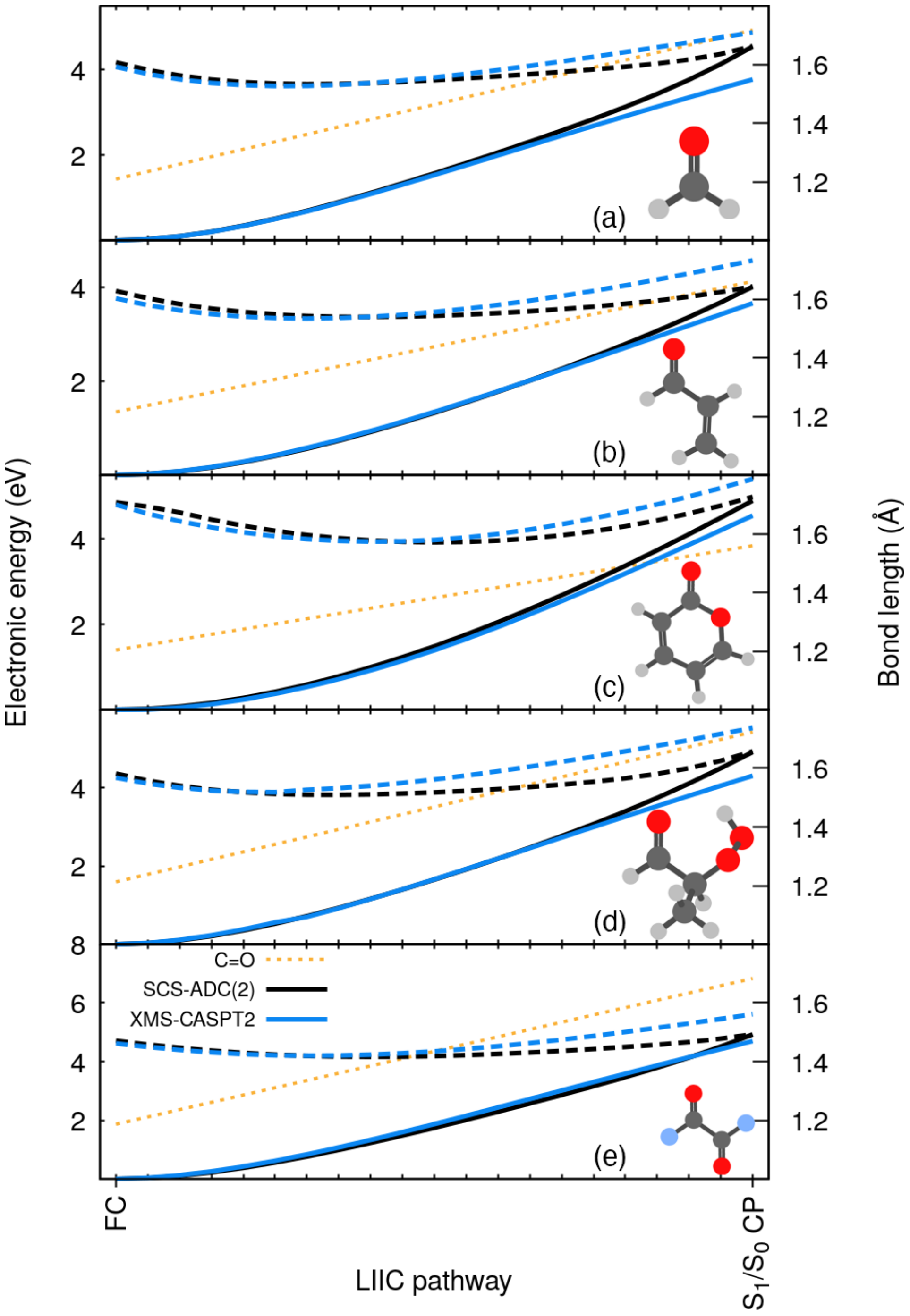

Figure 4.3: Electronic energies along a LIIC between the FC and the S_1/S_0 CP for: (a) formaldehyde, (b) acrolein, (c) pyrone, (d) 2-HPP, and (e) oxalyl fluoride, as obtained with SCS-MP2/ADC(2)/def2-SVP (black) and XMS-CASPT2/def2-SVP (blue). A solid (dashed) line is used for S_0 (S_1), and a dotted orange line for the C=O bond length.

interpolation pathway, highlighted by the increasing %T_2 in Fig. 4.5. Such contributions cannot be optimally described by ADC(2) since the treatment of double excitations in ADC(2) is very

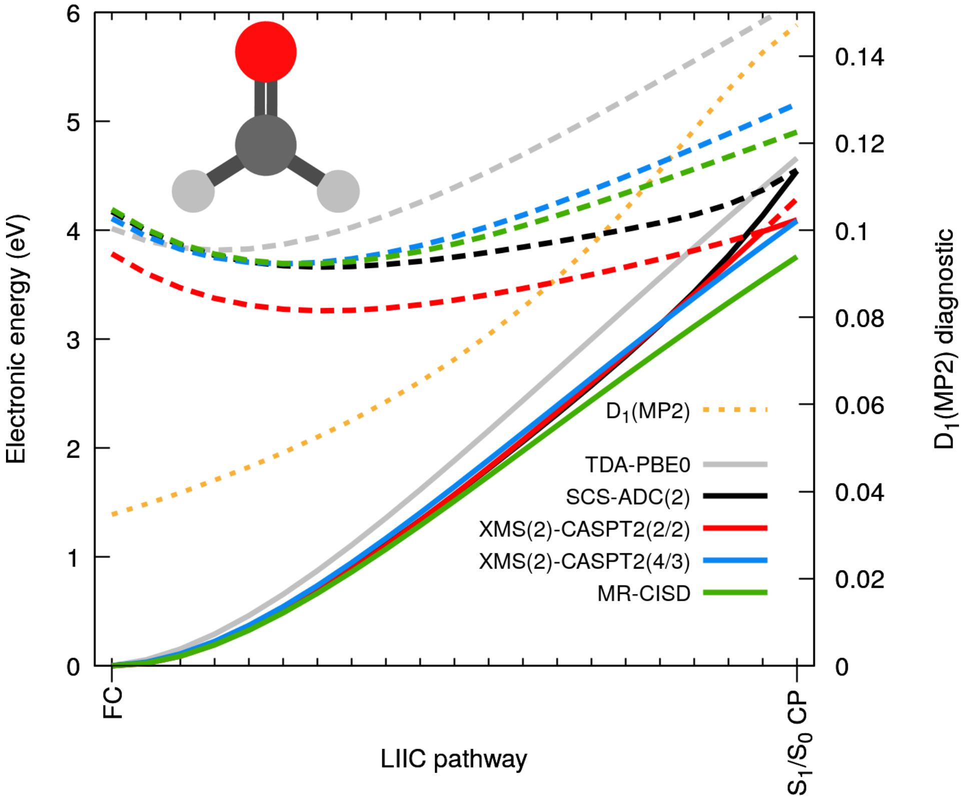

Figure 4.4: Electronic energies along a linear interpolation in internal coordinates between the FC and the S_1/S_0 CP for formaldehyde as obtained with SCS-ADC(2) (black), TDA-PBE0 (grey), XMS(2)-CASPT2(2/2) (red), XMS(2)-CASPT2(4/3) (blue) and MR-CISD (green). A solid (dashed) line is used for S_0 (S_1), and a dotted orange line for the D_1 diagnostic.

limited.[225] Finally, the point (*ii*) resonates with earlier findings that ADC(2) was inaccurate in describing the $n\pi^*$ state of cytosine,[287] (even if SCS-ADC(2) was shown to perform better), while it has been pointed out that ADC(2) performs less accurately when describing $n\pi^*$ transition, yielding too low frequencies associated with the carbonyl stretching.[229] Another study also showed that ADC(2) already overestimate the C=O bond length of formaldehyde at its S_1 minimum.[306]

Based on the considerations above, we could reproduce the S_1/S_0 CP using XMS-CASPT2 by employing the minimal active space constituted only by two electrons in n(O) and the π^*(C=O) (XMS(2)-CASPT2(2/2) in Fig. 4.4). Such a small active space does not include the π orbital, which is a key contributor to the multiconfigurational character of the S_0 along the pathway when the closed-shell configuration starts to strongly mix with a $\pi\pi^*$ contribution as highlighted in the top panel of Fig. 4.5. As a result, XMS(2)-CASPT2(2/2) leads, as for MP2, to a poor description of the ground-state reference wavefunction on which perturbation theory is applied, ultimately leading to a failure of the method when reaching the S_1/S_0 CP region (in stark contrast with XMS(2)-CASPT2(4/3) and MR-CISD, both including the π orbital).

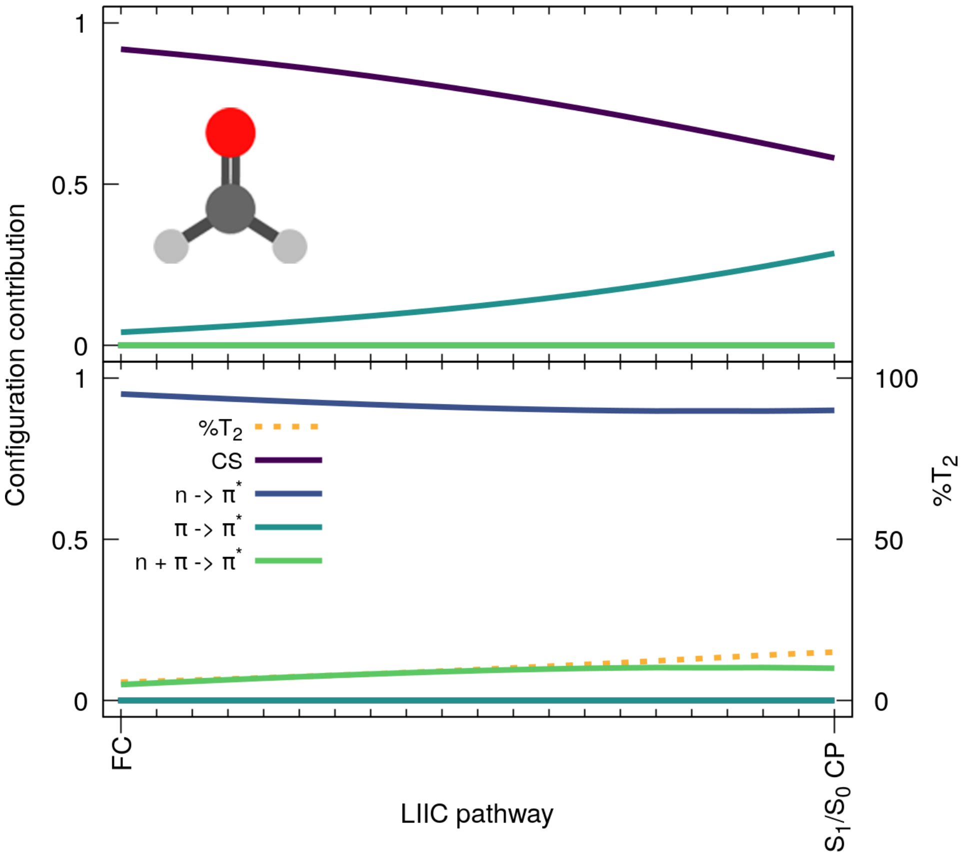

Figure 4.5: Contributing configurations to the MS-MR-XMS(2)-CASPT2(4/3)/def2-SVP wavefunctions along the formaldehyde LIIC pathway: closed shell (CS) configuration, singly-excited configurations nπ^* and $\pi\pi^*$, and doubly-excited configuration obtained from the promotion of a n and a π electron to the π^* orbital (n+$\pi \rightarrow \pi^*$). These configurations are plotted along the LIIC for the ground-state (upper panel) and first excited-state (lower panel) wavefunctions. The %T_2, computed at the SCS-ADC(2)/def2-SVP level of theory, is shown for S_1 with an orange dotted line.

Therefore, the failure of XMS-CASPT2 caused by the small active space appears to mimic that of SCS-ADC(2).

The very same trends are systematically reproduced for the other four compounds, as depicted in Fig. 4.6. Hence, our observations point towards (*i*) a too shallow S_1(nπ^*) along the elongation of the CO bond combined with (*ii*) a bad reference for MP2 destabilizing too rapidly the ground state to explain the fast and artificial decay observed in the excited-state dynamics. We note that the point (*ii*) resonates with earlier findings that ADC(2) tends to have energy gaps between S_1 and S_0 closing too rapidly even still far from the crossing region (*e.g.*, Refs. 307, 308).

Finally, in Fig. 4.7, we investigated the case of the aforementioned thymine nucleobase. Our rational explanation for the failure of both ADC(2) and XMS(2)-CASPT2(2/2) is clearly confirmed for this additional molecule: both ADC(2) and XMS(2)-CASPT2(2/2) predict an

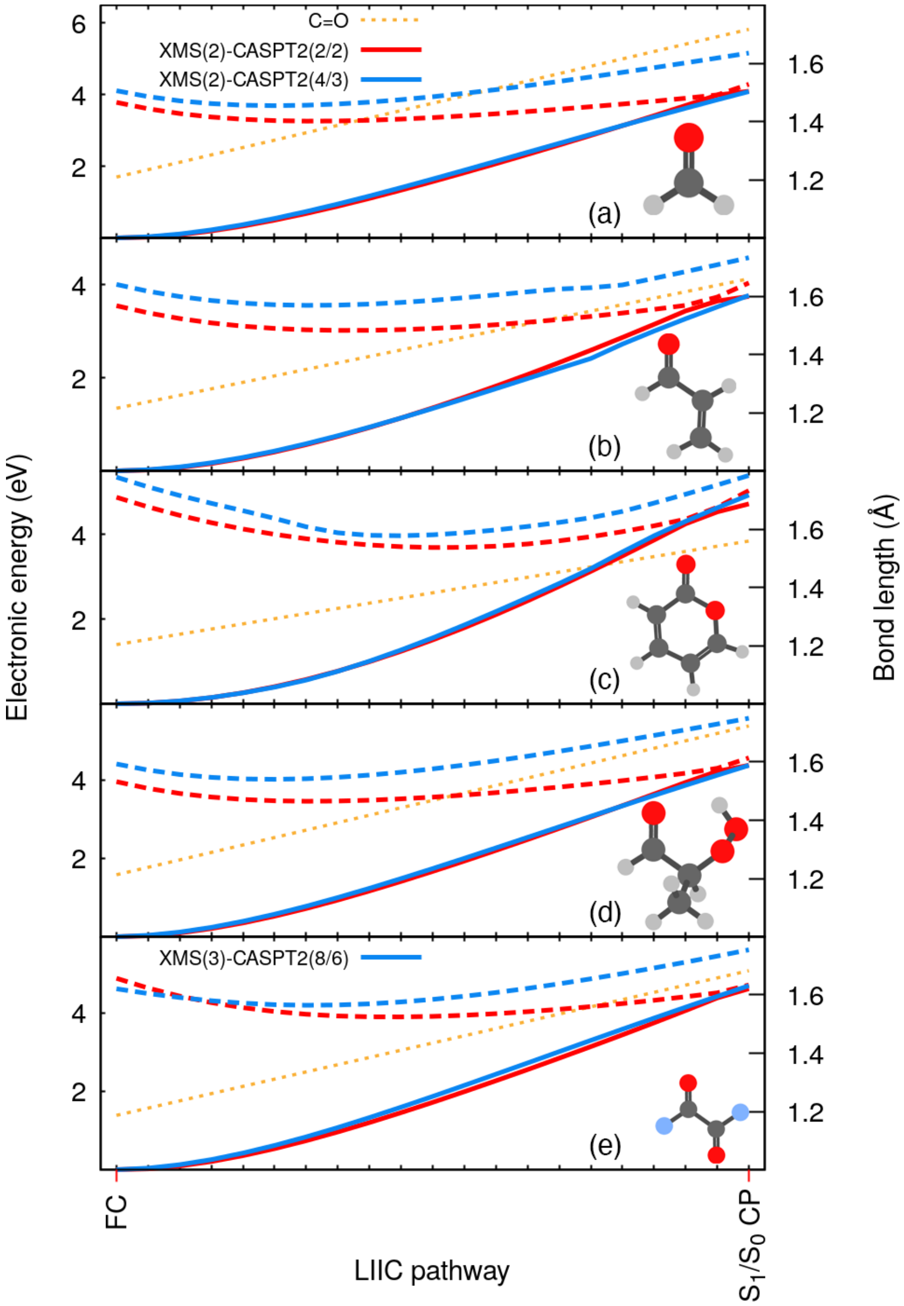

Figure 4.6: Electronic energies along the LIIC pathway for formaldehyde as obtained with XMS-CASPT2(2/2)/def2-SVP (red) and XMS-CASPT2(4/3)/def2-SVP (blue) for (a) formaldehyde, (b) acrolein, (c) pyrone, (d) 2-HPP, and (e) oxalyl fluoride. We note that for oxalyl fluoride, the (4/3) active space was unstable and had to be replaced by an (8/6). A solid line is used for S_0 and a dashed line for S_1. The C=O bond length is given by an orange dotted line.

artificial S_1/S_0 crossing, which is verily avoided when using a suitably high level of theory (XMS(5)-CASPT2(12/9)).

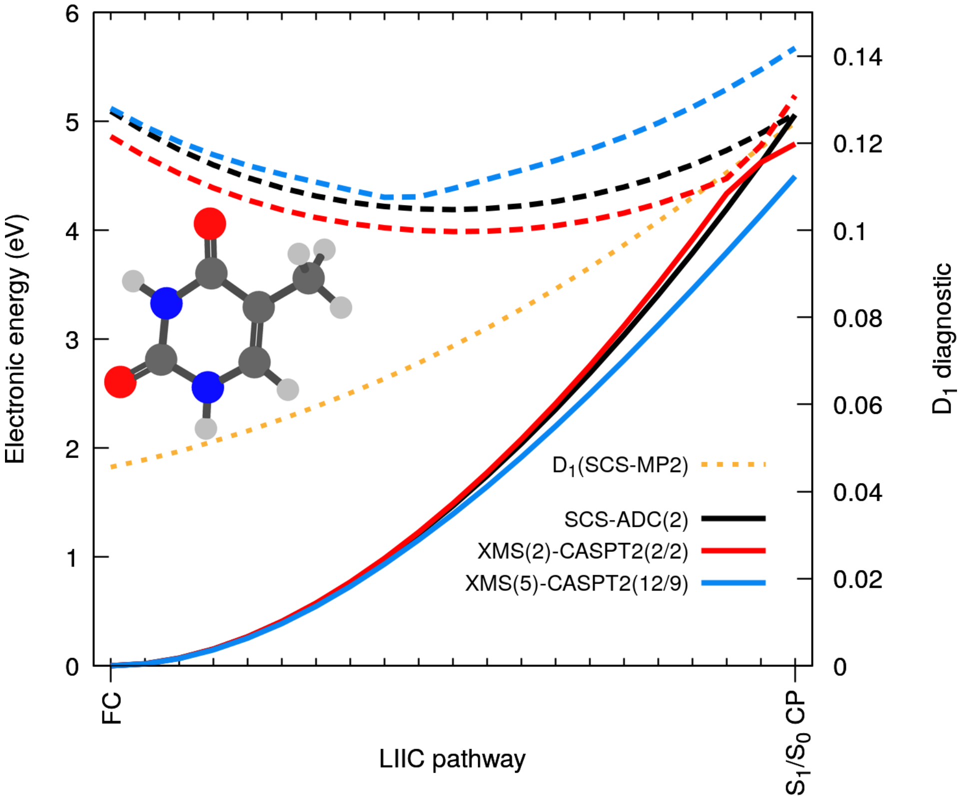

Figure 4.7: Electronic energies along the LIIC pathway for thymine as obtained with SCS-ADC(2)/SVP (black), XMS(2)-CASPT2(2/2)/SVP (red) and XMS(5)-CASPT2(12/9)/SVP (blue). A solid line is used for S_0 and dashed line for S_1. The D_1 diagnostic for the SCS-MP2 ground state is shown with a dotted orange line.

4.4 Conclusions

The electronic-structure method ADC(2) is gaining prominence in describing the photochemistry and photophysics of organic molecules, but its pitfalls still need to be fully uncovered. The unexpected failures of ADC(2) for carbonyl-containing compounds were discussed in several case studies but the systematic nature of these errors in the context of S_1/S_0 crossing points has not been widely recognized. The recurrence of artificial S_1/S_0 crossings upon C=O elongation closely resembles the predictions from multireference methods with an inadequate active space, which prevents the proper description of both ground and excited state, and leads to the unphysical nonradiative decay channels in molecular dynamics. Similar issues are expected for molecules bearing a C=S group, based on the results presented in Ref. 309. Considering the omnipresence of C=O functional group and the increasing interest in using ADC(2) to study photochemical deactivation pathways, our current findings should serve as a warning bell for future research in the field.

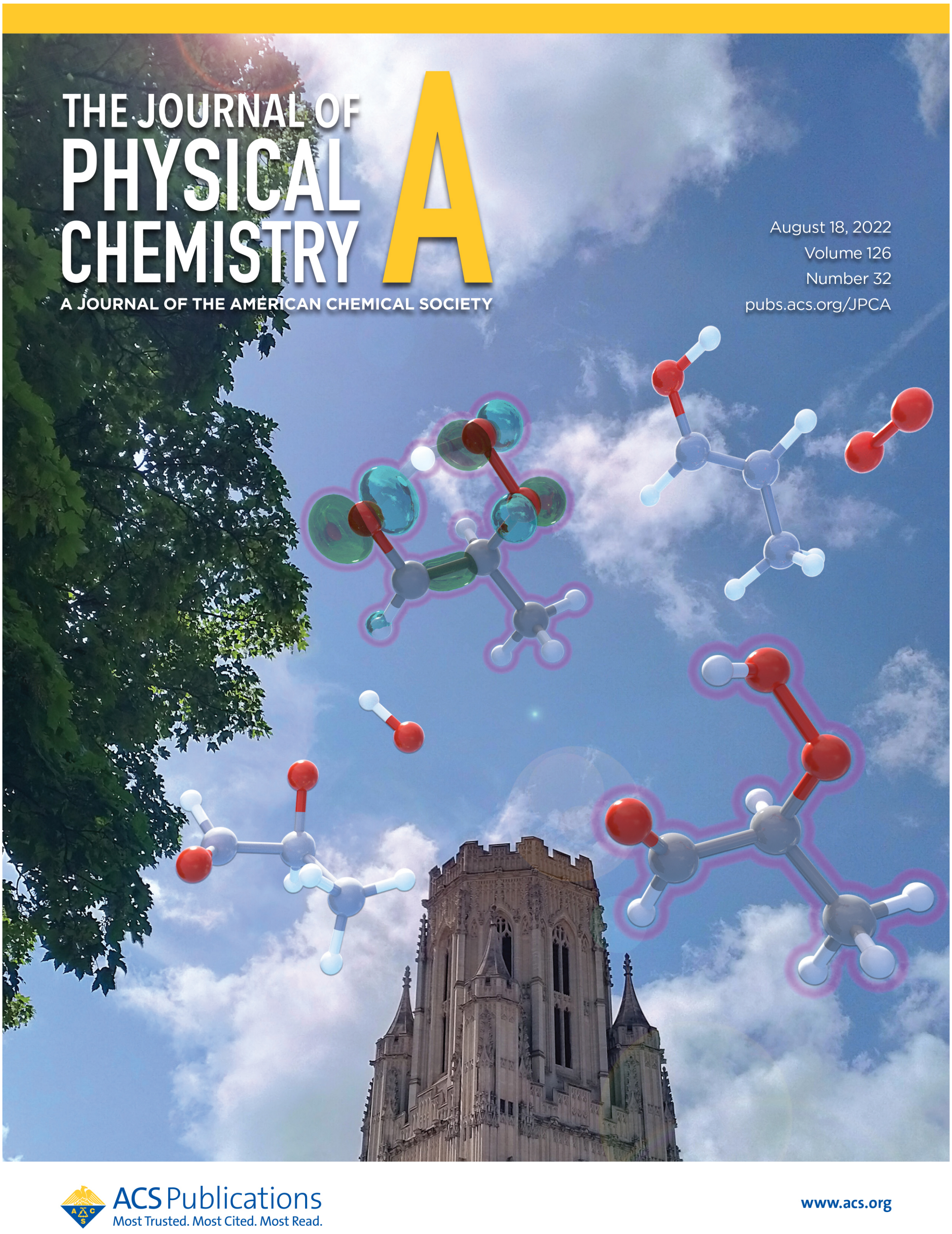

THE JOURNAL OF
PHYSICAL
CHEMISTRY A
A JOURNAL OF THE AMERICAN CHEMICAL SOCIETY

August 18, 2022
Volume 126
Number 32
pubs.acs.org/JPCA

ACS Publications
Most Trusted. Most Cited. Most Read.

www.acs.org

This illustration represents the transient atmospheric volatile organic compound 2-hydroperoxypropanal, which, upon sunlight absorption, releases either singlet O_2 or an OH radical.

CHAPTER 5

A theoretical perspective on the actinic photochemistry of 2-hydroperoxypropanal

In accordance with the University of Bristol guidance on the integration of publications as chapters within a dissertation, I declare this chapter was previously published in the Journal of Physical Chemistry A.[310] My role in this study, as the first author of the publication, was to devise the methodology, run the calculations, collect and analyze the data and write the the paper. Antonio Prlj and Basile F. E Curchod have written and reviewed the paper and supervised the overall project. On the previous page, we report our cover art published on the front page of the Journal of Physical Chemistry A.

5.1 Introduction

The carbonyl functional group can be found in a wide range of atmospheric VOCs, and the examples presented in the preceding chapter are merely a limited selection of the many diverse molecules that may contain this group. Another relevant class of carbonyl-containing molecules are the hydroperoxyaldehydes (HPALDs). HPALDs, which have a structure similar to acrolein and are produced from atmospheric degradation of isoprene, have become a focus of extensive research due to their link to a newly discovered mechanism that results in OH recycling. As OH radical is an essential component of daytime oxidative reactions, it is imperative to accurately model its formation and depletion mechanisms to develop reliable atmospheric models like the MCM.

In the troposphere, HPALDs are mainly formed via 1,6 H-shifts of the isoprenyl-peroxy radicals[311, 312] and, upon formation, they promptly photolyze to regenerate OH.[87, 88, 313] Interestingly, this newly discovered mechanism partially explain the discrepancies between the unexpectedly high OH concentration registered over the Amazon forest in comparison with the predictions of atmospheric models.[314] Research on the HPALDs has provided a prime example of how the photolysis of VOCs can influence the atmospheric balance, emphasizing the critical need for a thorough investigation of VOC photochemistry.

Another class of VOCs structurally similar to HPALDs are the α-hydroperoxycarbonyls. They are formed through isoprene oxidation[315, 316] or as intermediates in the ozonolysis of ethylene.[317] In analogy with HPALD, the photochemistry of α-hydroperoxycarbonyls requires a thorough investigation, as their photolysis can serve as a potential OH recycling channel. Nevertheless, the photochemistry of multi-chromophoric VOC molecules like α-hydroperoxycarbonyls is tremendously challenging to investigate experimentally. Consequently, photolysis rate constants are not directly available for most relevant α-hydroperoxycarbonyls. Recent work has experimentally estimated a sizable photolysis rate constant for 3-hydroperoxy-4-hydroxybutan-2-one, a molecule from the family of α-hydroperoxycarbonyls, hypothesizing that it would release OH upon light absorption.[318] In addition, theoretical and computational photochemistry, aided by SARs, was used to unravel the photodissociation mechanism of simple α-hydroperoxycarbonyls, identifying a 1,5 H-shift followed by the elimination of O_2 as a primary photolytic pathway and estimating the corresponding J values. Photolysis via internal conversion was predicted to be faster than the processes involving ISC based on SAR considerations.

In the following, we make use of the protocol designated in chapter 3 to study the photochemistry of α-hydroperoxycarbonyls. As an instructive model system, we examine the 2-HPP – one of the smallest molecules discussed in Ref. 6. The fully *in silico* protocol – based on quantum-chemical calculations and excited/ground-state dynamics simulations – gives us direct access to experimental observables connected to the photolysis of 2-HPP and offers insights into the mechanisms underlying each of the possible photochemical pathways, both in the excited and ground electronic state.

5.2 Computational details

5.2.1 Photoabsorption cross-section and initial conditions

The twelve conformers identified in Ref. 6 were optimized with SCS-MP2 and a def2-SVP basis set.[300–302] Harmonic vibrational frequencies at the ground-state minima and the thermochemistry were evaluated employing the same level of theory. Based on the calculated free energies, the seven conformers within 10 kJ/mol from the global minimum (conformer 1a – see Fig. 5.1) have been selected and their photoabsorption cross-section calculated using the NEA/Wigner approach.

For each conformer, a Wigner distribution for uncoupled harmonic oscillators was constructed and used to sample 500 geometries. For each geometry, vertical transitions and oscillator

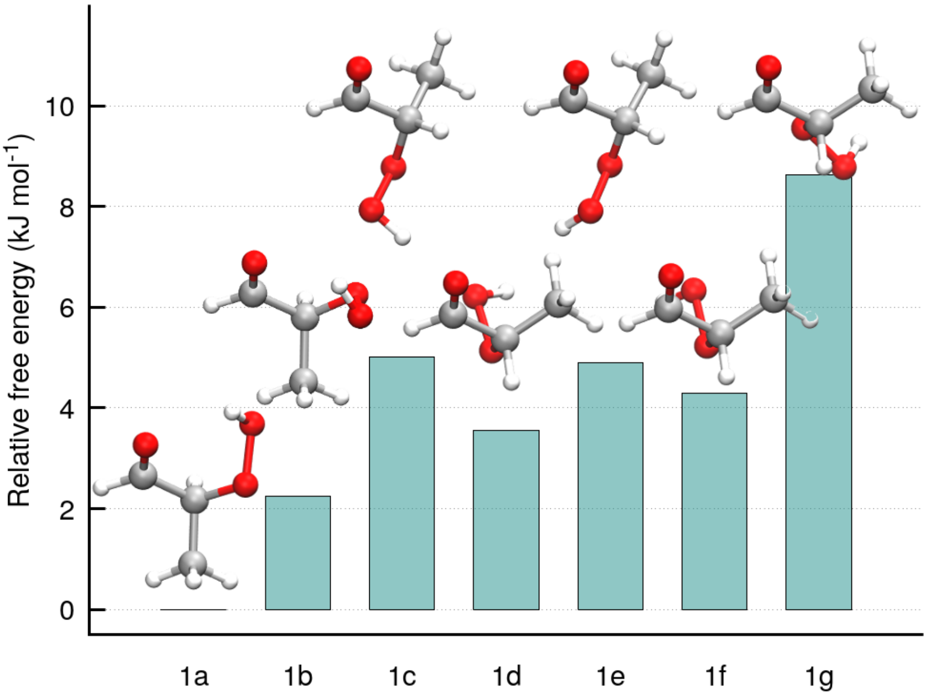

Figure 5.1: Geometries of the seven rotational isomers of 2-HPP and the corresponding relative free energies computed at SCS-MP2/def2-SVP.

strengths were evaluated with SCS-ADC(2)/def2-SVP. All spectral transitions were broadened with Lorentzians using a phenomenological broadening of 0.05 eV. The resulting photoabsorption cross-section for each conformer was obtained by averaging the contribution of all 500 geometries using the NEA. The total photoabsorption cross-section for 2-HPP was then calculated by adding the contribution from each conformer, scaled by the appropriate Boltzmann factor. The NEA and the spectrum were calculated with Newton-X version 2.0.[166]

All SCS-MP2 and SCS-ADC(2)[225] calculations were performed with frozen core and the RI[299] using Turbomole 7.3.[296] D_1 diagnostic was employed as an approximate measure of the multireference character of MP2 ground state.[305]

5.2.2 Critical points on potential energy surfaces and linear interpolation in internal coordinates

For the lowest-energy conformer (1a), different critical points on the potential energy surfaces of 2-HPP were located. The FC point, *i.e.*, the ground-state minimum energy geometry, the S_1 minimum, and a transition state towards a proton-coupled electron transfer in S_1 were obtained with SCS-ADC(2)/def2-SVP. MECIs, the biradical ground-state minimum, and the transition state were located with XMS(3)-CASPT2(12/9) with a cc-pVDZ[319] basis set using BAGEL

1.2.[297] All XMS-CASPT2 calculations reported in this work used DF, the SS-SR contraction scheme, and a real vertical shift of 0.5 Hartree. LIIC pathways were generated to connect the different critical points. The active space for XMS-CASPT2 calculations was designed to ensure a proper description of the potential energy surfaces for the proton-coupled electron transfer, the $^1O_2$ release, the OH and OOH photodissociation, as well as the conservation of total energy during the excited-state and ground-state dynamics. The orbitals included are depicted in Fig. 4.2.

5.2.3 Excited-state dynamics and quantum yields

The excited-state (nonadiabatic) dynamics simulations were performed with the TSH algorithm.[117] The nonadiabatic couplings were obtained by using the wavefunction overlap scheme, and the kinetic energy was adjusted by rescaling the nuclear velocity vector following a successful hop. The electronic populations were corrected to prevent overcoherence using the energy-based decoherence correction of Granucci and Persico.[177]

All TSH trajectories were initiated in the first excited electronic state S_1, starting from initial conditions sampled randomly from a harmonic Wigner distribution for conformer 1a (and 1c). In total, 166 (conformer 1a) and 80 (conformer 1c) trajectories were propagated. All TSH dynamics were performed using SCS-ADC(2)/def2-SVP for the electronic structure, with a time step of 0.5 fs using Newton-X coupled with Turbomole.[234] The TSH trajectories were propagated for a maximum of 100 ps. Since 2-HPP contains a carbonyl moiety it is affected by the artificial non-reactive conical intersection described in chapter 4. All trajectories exhibiting this S_1/S_0 non-reactive conical intersection (NRCI) were discarded (their statistics are discussed in Sec. 5.3.3).

A special treatment was required for those trajectories approaching the S_1/S_0 following proton-coupled electron transfer in S_1 due to enhanced biradical character of the ground electronic state and the need for an adequate description of the intersection seam and nonadiabatic transitions (see Sec. 5.3.1 for a full discussion). In this particular case, a TSH trajectory using SCS-ADC(2)/def2-SVP would be terminated when the S_1/S_0 energy gap gets lower than 0.01 eV. One would then backtrack the trajectory up until 15 fs, monitoring the value of the D_1(MP2) diagnostic to determine the last time along the SCS-ADC(2) TSH trajectory that can be trusted, that is when the D_1 diagnostic is less than 0.075 following the recommendation of Ref. 305 (note that large D_1 values indicate an increased multireference character of the ground state). The nuclear coordinates and velocities at this specific time then serve as a restart for the TSH dynamics now employing multireference XMS(3)-CASPT2(12/9)/cc-pVDZ electronic structure, using a time step of 0.25 fs (the reduced time step is necessary due to the high kinetic energy of the trajectories when transferring back to S_0). We ensure that, at the restarting point, we retrieve the correct set of orbitals. While this is usually the case, when the set of active space orbitals is not recovered, we chose the closest point for which we can optimize the correct active space orbitals and electronic state characters. The validity of this switch between methods is further discussed in Sec. 5.3.1. In total, four trajectories (one for 1a, three for 1c) have been discarded due to the impossibility of recovering the proper active space for XMS(3)-CASPT2(12/9) within the 15 fs preceding the crossing point.

For the trajectories leading to the $^1O_2$ release, the strong destabilisation of the closed-shell character can lead to instabilities in the XMS(3)-CASPT2(12/9) calculations. We closely monitored the variation of the total energy along these trajectories: for each trajectory, if more than four discontinuities of more than 0.05 eV each (but less than 0.25 eV – only three trajectories for 1a and none for 1c have a discontinuity of more than 0.2 eV) in the total energy were observed, the trajectory was stopped and restarted before the first discontinuity occurred, using XMS(2)-CASPT2(12/9). Here, only the two lowest states with biradical character are included in the state average allowing for consistent total energy conservation. All TSH dynamics employing XMS-CASPT2 were performed with the SHARC 2.1 code.[168, 320]

5.2.4 Spin-orbit coupling matrix elements

Spin-orbit coupling matrix elements were calculated with SA(3S,3T)-CASSCF(12/9)/cc-pVDZ using Molpro 2012.1,[298] using the same active space as for all XMS-CASPT2 calculations. For each matrix element calculated, we ensured that the electronic character of the states considered matched between SA-CASSCF and SCS-ADC(2). The magnitude of the spin-orbit coupling between the singlet S_1 and triplet T_n electronic state is calculated as $\mathrm{SOC}_{S_1/T_1} = \sqrt{\sum_{M_S=-1}^{1} |H_{SOC}^{S_1/T_n^{M_S}}|^2}$, where M_S= -1,0,1 are the triplet sublevels of T_n and $H_{SOC}^{S_1/T_n^{M_S}}$ the (complex) spin-orbit coupling matrix element between the singlet electronic state S_1 and the spin sublevel M_S of the triplet electronic state T_n.

5.3 Results and discussion

In this section, we first highlight the possible photochemical pathways that 2-HPP can follow after photoexcitation (section 5.3.1) and use these different pathways as a way to benchmark the levels of theory and computational strategies that will be employed for the excited-state dynamics simulations. We then focus on the simulation of the photoabsorption cross-section $\sigma(\lambda)$ of 2-HPP (section 5.3.2), comparing our theoretical results to earlier work employing SARs. Using the calculated photoabsorption cross-section, we performed excited-state dynamics simulations at different excitation wavelengths, resulting in the generation of theoretical wavelength-dependent quantum yields ($\phi(\lambda)$) for the formed photoproducts and the identification of interesting dynamical processes in the excited electronic states (section 5.3.3). In section 5.3.4, we discuss the importance of intersystem crossing processes in light of our simulations.

5.3.1 Potential photochemical pathways

We focus here on the main reaction channels of 2-HPP when photoexcited to S_1 and without intersystem crossing, namely a proton-coupled electron transfer followed by $^1O_2$ release, OH photodissociation, and OOH photodissociation. This section will not only present pathways and scans characterizing these processes but also a stringent benchmark of the level of electronic structure theory prior to any excited-state dynamics. In the particular case of 2-HPP, we will compare SCS-MP2/ADC(2) and XMS-CASPT2 – the two methods that will be used throughout this work.

5.3.1.1 Excited-state proton-coupled electron transfer and $^1O_2$ release

First, we analyze the possible photochemical pathways of 2-HPP with an excited-state proton-coupled electron transfer. This process, taking place exclusively on the first excited singlet state S_1, is related to the mechanism described in Ref. 6 as 1,5-H shift. Our choice of nomenclature will be explained soon. The characterization of this process begins by localizing the minimum (S_1 min, having a n(O) $\rightarrow \pi^*$(CO) character) and transition state (S_1 TS) in S_1 using SCS-ADC(2)/def2-SVP (Fig. 5.2). Interestingly, the electronic character of the S_1 state at the S_1 TS structure (inset of Fig. 5.2) corresponds to a $(n(\mathrm{O}) + n'(\mathrm{OO})) \rightarrow \pi^*(\mathrm{CO})$ transition, highlighting that the transfer of a proton from the hydroperoxide to the carbonyl takes place with the simultaneous displacement of the part of electron density in the same direction. This observation prompts us to call this process an excited-state proton-coupled electron transfer (PECT), as an H-atom transfer would imply that the electron would be localized on the proton during the transfer. Proton following its path towards the carbonyl group implies the location of a MECI between S_1 and the ground state S_0. This critical geometry was localized with XMS(3)-CASPT2(12/9)/cc-pVDZ due to its inherent multireference character.

The electronic energies at the critical geometries discussed up to now can be connected by performing a linear interpolation between the structures using internal coordinates and calculating electronic energies for each intermediate geometry. Such LIIC pathways highlight important features of the potential energy surfaces between critical points, but should not be confused with minimum-energy pathways. LIICs are represented by lines in Fig. 5.2 – dashed lines are electronic energies calculated with SCS-MP2/ADC(2)/def2-SVP and plain lines with XMS(3)-CASPT2(12/9)/cc-pVDZ. The electronic energy difference between S_1 TS and the S_1 min is 0.20 eV, while the FC point lies 0.72 eV above the S_1 min. The LIIC pathways highlight the sharp decrease of S_1 energy from the S_1 to the MECI. Importantly, SCS-ADC(2)/MP2 appears to reproduce qualitatively well the shape of the XMS-CASPT2 potential energy curves when approaching the MECI.

From the MECI point, the molecule can funnel back towards the S_0 minimum of the original molecule with a back-transfer of the proton to the peroxide. Proceeding towards the release of $^1O_2$ after passage through the MECI, though, requires a biradical, multiconfigurational character

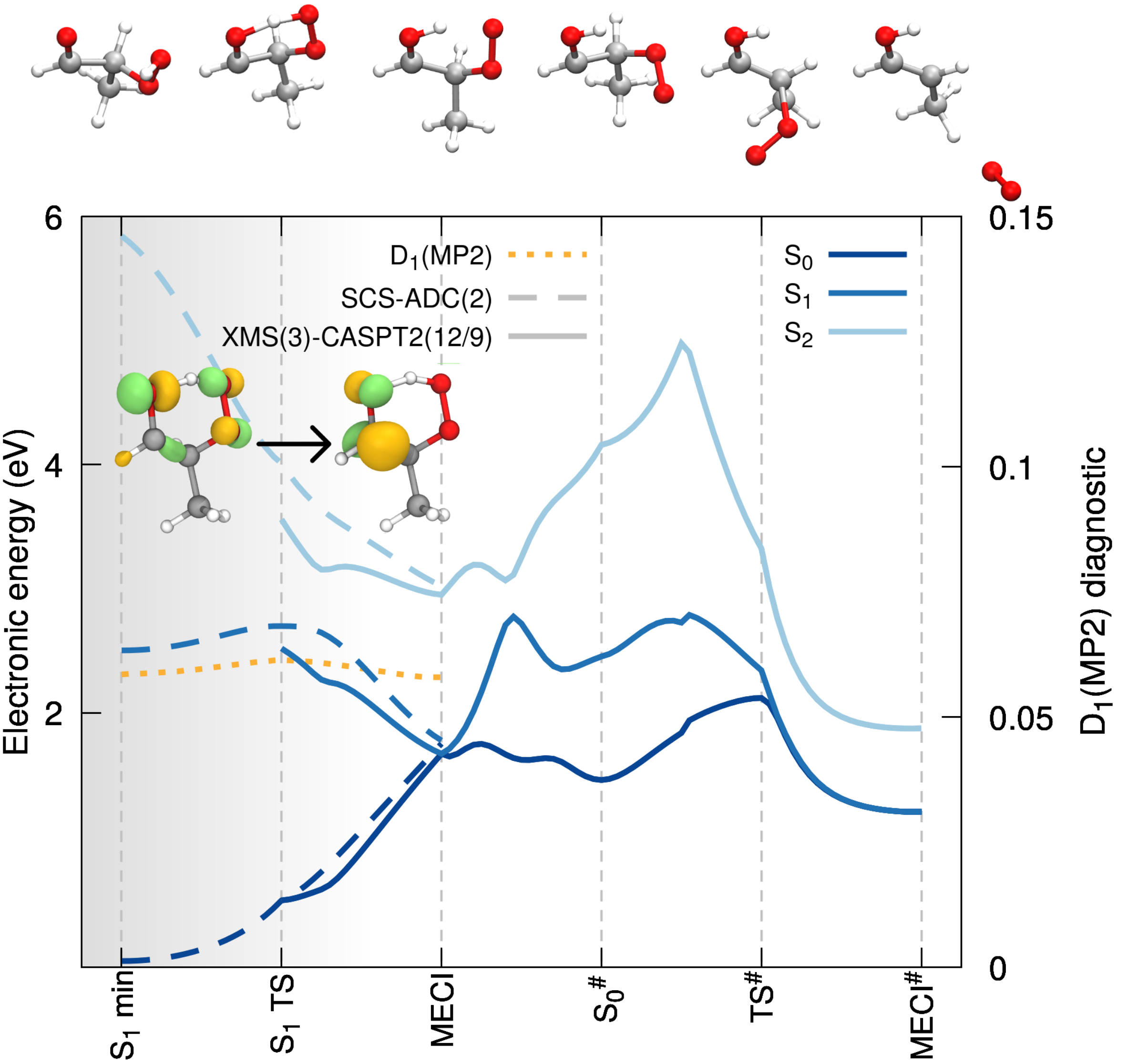

Figure 5.2: LIIC pathways for the excited-state proton-coupled electron transfer and $^1O_2$ release. Comparison of the electronic energies obtained with SCS-ADC(2)/def2-SVP (dashed lines) and XMS(3)-CASPT2(12/9)/cc-pVDZ (solid lines) for the three lowest electronic states, S_0 (dark blue), S_1 (blue), and S_2 (light blue). The S_1 minimum and S_1 TS geometries were obtained at the SCS-ADC(2)/def2-SVP level of theory, while the critical geometries for the S_0/S_1 MECI, biradical S_0 minimum ($S_0^\#$), biradical S_0 TS$^\#$, and O_2 dissociation MECI (MECI$^\#$) were optimized with XMS(3)-CASPT2(12/9)/cc-pVDZ. The inset shows the NTOs characterizing the electronic character of S_1 at the S_1 TS geometry. The upper panel shows the molecular structure corresponding to each critical point located. The D_1 diagnostic along the pathway for the SCS-MP2 ground state is given with a dotted orange line. The shaded area highlights the region of the LIIC where SCS-MP2/ADC(2) could be trusted.

of the molecule in the ground electronic state. The corresponding ground-state minimum ($S_0^\#$) was optimized with XMS(3)-CASPT2(12/9)/cc-pVDZ and preserves the proton on the original carbonyl group (see the upper panel of Fig. 5.2). Focusing on the LIIC pathways between MECI and $S_0^{\#}$, one can observe a steep rise in energy of the S_1 electronic energy, which, from the MECI point, picked up a closed-shell character that is highly destabilized. The closed-shell character later even transferred to S_2 (avoided crossing mid-way between MECI and $S_0^{\#}$). The release of $^1O_2$ requires the passage through a transition state in the biradical ground state ($TS^{\#}$), which eventually leads to a MECI with S_1 ($MECI^{\#}$), where the dissociation takes place. At the $TS^{\#}$ structure, the carbon bearing the original hydroperoxide group displays a significant sp^2 character (see structure in the upper panel of Fig. 5.2), while its bond with the OO group is strongly elongated (1.78 Å).

As attested by Fig. 5.2, the release of $^1O_2$ implies a rather complex series of events on the S_1 and S_0 potential energy surfaces. From an electronic structure perspective, the appearance of a strong biradical character in the ground electronic state following the proton-coupled electron transfer hampers the use of SCS-MP2/ADC(2) from just before the region of the first MECI. SCS-MP2/ADC(2) can, however, be safely used from the FC region until just after the S_1 TS is passed. From a dynamics perspective, reaching the S_1 TS could take several picoseconds, a timescale that prohibits the use of XMS(3)-CASPT2(12/9) due to its high computational cost, in contrast to the computationally affordable SCS-ADC(2). Hence, we are forced to adopt a combination of two methods. The excited-state dynamics of 2-HPP will be conducted with SCS-ADC(2) up until it approaches the S_1/S_0 intersection seam following a proton-coupled electron transfer. We then rewind the trajectory by up to 15 fs and restart the S_1 dynamics with XMS(3)-CASPT2(12/9) from there – making sure that the restart point is far enough from the S_1/S_0 intersection in terms of energy and that the correct active space is recovered. The close agreement between SCS-ADC(2) and XMS-CASPT2 discussed above before the MECI region comforts us in this switch of methods. The dynamics can proceed and describe adequately the nonadiabatic transitions between S_1 and S_0 and the subsequent S_0 and S_1 dynamics with a biradical reference up until the O_2 dissociation. We note that the return to the FC region of 2-HPP can also be described by this strategy. While not being perfectly satisfactory, the blended approach proposed here is a compromise to simulate the entire nonradiative decay of 2-HPP leading to the formation of $^1O_2$ (the shaded area in Fig. 5.2 highlights when SCS-MP2/ADC(2) can be trusted).

5.3.1.2 OH and OOH photodissociation

The photodissociation of OH in the first excited electronic state can be envisioned if a change of electronic character for S_1 can occur, moving from a $n(O) \rightarrow \pi^*(CO)$ character in the FC and S_1 min region to a $n'(OO) \rightarrow \sigma^*(OO)$ dissociative character. To investigate the interplay between the electronic states in such a process, one can start from the S_1 min geometry and stretch the O−O of the hydroperoxide group without relaxing the molecular geometry. The electronic energies obtained from this rigid scan are presented in Fig. 5.3.

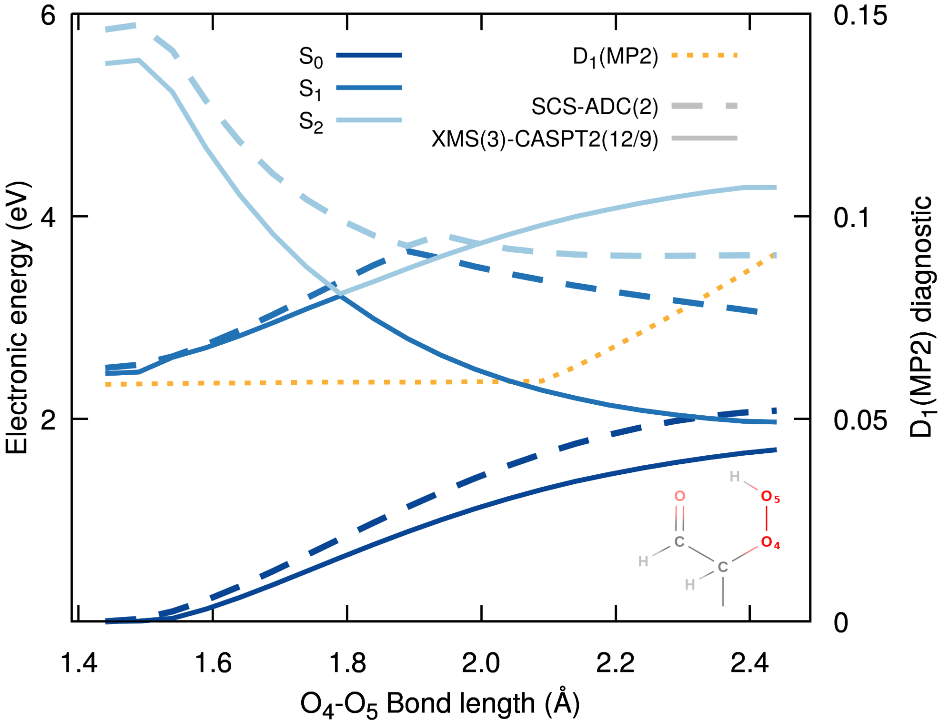

Figure 5.3: OH release in the excited state. Rigid scan along the $O_4{-}O_5$ bond of 2-HPP (see inset) starting from the S_1 min geometry obtained at SCS-ADC(2)/def2-SVP level of theory. Comparison of the electronic energies obtained with SCS-ADC(2)/def2-SVP (dashed lines) and XMS(3)-CASPT2(12/9)/cc-pVDZ (solid lines) for the three lowest electronic states, S_0 (dark blue), S_1 (blue), and S_2 (light blue). The D_1 diagnostic along the scan for the SCS-MP2 ground state is given with a dotted orange line.

The S_1 state is clearly destabilized at the beginning of the stretch as a result of its $n(O) \to \pi^*(CO)$ character, in stark contrast with S_2 which exhibits a $n'(OO) \to \sigma^*(OO)$ nature. At the XMS-CASPT2 level of theory (solid lines in Fig. 5.3), the change of character for the S_1 state occurs at a O−O bond length just under 1.8 Å. After this point, the S_1 electronic state gains a $n'(OO) \to \sigma^*(OO)$ character and would lead to the photodissociation of an OH radical. While this process may appear simple enough to proceed efficiently, earlier dynamical studies on a C_6-HPALD revealed that the very weak diabatic coupling between the two electronic-state characters protects the molecule from dissociation by forcing it to follow the same electronic character, that is, by a nonadiabatic transition to S_2.[321] Only a certain approach of the intersection seam may allow for the release of OH radicals. More information on this process coined diabatic trapping, is provided in Sec. 5.3.3. The description of the OH photodissociation pathway provided by SCS-ADC(2) (dashed lines in Fig. 5.3) presents the same qualitative features as with XMS-CASPT2. A switch of electronic character is observed but at a bond length closer to 1.9 Å. The electronic-character exchange also takes place at a higher S_1

electronic energy from the S_1 min along this rigid scan in comparison to XMS-CASPT2. The D_1(MP2) diagnostic increases sharply when the O−O bond is stretched beyond 2.0 Å, revealing an emerging multiconfigurational nature of the ground electronic state. In addition, the photodissociation of OH from a hydroperoxide group leads to the appearance of low-lying electronic states with a dominant doubly-excited character – a type of electronic state that ADC(2) only approximates to zeroth order.[225, 246] In summary, SCS-ADC(2) is likely able to describe the switching between n→ π^* and n→ σ^* characters fairly well, but, as expected, it does not properly describe the OH dissociation limit.

The OOH release from S_1 can be investigated by using a similar strategy, namely a rigid scan from the S_1 min structure along the C−O bond of the hydroperoxide group (Fig. 5.4). The electronic energies obtained with XMS-CASPT2 and SCS-ADC(2) along this scan are in qualitative agreement, showing a crossing between S_1 and S_2 at just under 2.10 Å for SCS-ADC(2) and around 2.15 Å for XMS-CASPT2. The D_1 diagnostic however increases dramatically after 2.0 Å. While care has to be taken in the analysis of rigid scans, the two methods appear to indicate that the OOH dissociation would be a far more energetically demanding process than the OH release.

5.3.2 Photoabsorption cross-section of 2-HPP

As detailed in chapter 3, the photoabsorption cross-section $\sigma(\lambda)$ is one of the components required to characterize photolytic processes. We calculated the photoabsorption cross-section for the lowest conformers of 2-HPP (see Fig. 5.1) employing the NEA with the optimized S_0 geometry and corresponding vibrational frequencies obtained with the SCS-MP2/def2-SVP and transition energies and oscillator strengths calculated with SCS-ADC(2)/def2-SVP. The total photoabsorption cross-section (black line in Fig. 5.5) was generated by adding together the individual cross-sections for each conformer, weighted by the appropriate Boltzmann factor to represent their theoretical population. The observed band in the actinic region stretches from 3.5 eV up to 5 eV with a centre at 4.25 eV and is characterized by a very small cross-section. Decomposing the total cross-section into its electronic transitions (dashed lines in Fig. 5.5) highlights the dominant contribution of the $S_0 \rightarrow S_1$ excitation to the main band in the actinic region. This transition exhibits a n(O) $\rightarrow$ π^*(CO) character located on the carbonyl moiety of 2-HPP, as expected from the minute cross-section in this region. Interestingly, the $S_0 \rightarrow S_2$ contribution to the total cross-section (light-green dashed line in Fig. 5.5), which exhibits a n′(OO) $\rightarrow$ σ^*(OO) character and is therefore prone to trigger direct OH photodissociation, only appears to contribute for photon energies higher than 4.5 eV.

The experimental photoabsorption cross-section of 2-HPP is unfortunately unknown. Nevertheless, the theoretical photoabsorption cross-section obtained at the SCS-ADC(2) level of theory can be compared to earlier predictions based on SARs.[6] 2-HPP is composed of a hydroperoxide moiety and an aldehyde functional group. Hence, earlier work has proposed

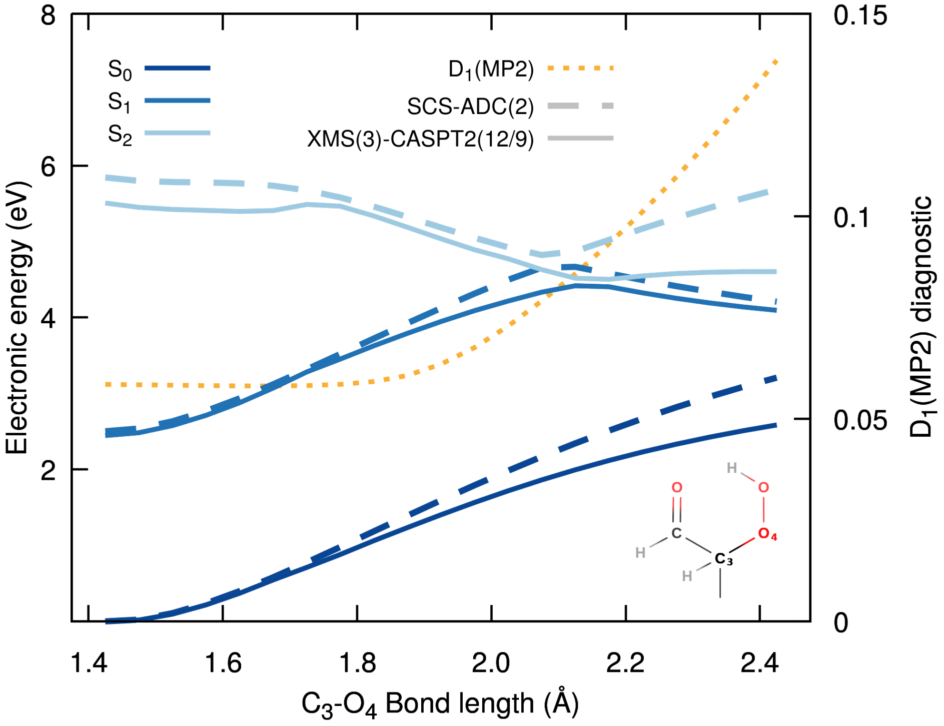

Figure 5.4: OOH release in the excited state. Rigid scan along the $C_3{-}O_4$ bond of 2-HPP (see inset) starting from the S_1 min geometry obtained at SCS-ADC(2)/def2-SVP level of theory. Comparison of the electronic energies obtained with SCS-ADC(2)/def2-SVP (dashed lines) and XMS(3)-CASPT2(12/9)/cc-pVDZ (solid lines) for the three lowest electronic states, S_0 (dark blue), S_1 (blue), and S_2 (light blue). The D_1 diagnostic along the scan for the SCS-MP2 ground state is given with a dotted orange line.

to predict its photoabsorption cross-section by combining the experimental photoabsorption cross-section of methylhydroperoxide and propanal.[6] The resulting composite cross-section is given as a light-grey solid line in Fig. 5.5 and matches the theoretical prediction both from the location of the maximum of the low-energy band and its absolute cross-section. One possible shortcoming of the decomposition of 2-HPP in its functional group is the absence of possible intramolecular interaction – we have seen earlier that two of the low-energy conformers of 2-HPP possess an intramolecular H-bond between the hydroperoxide and carbonyl groups, possibly altering the $n(O) \rightarrow \pi^*(CO)$ transition characterizing the low-energy band. A scaling factor was proposed to account for these possible intramolecular interactions, leading to the scaled composite cross-section displayed in dark grey in Fig. 5.5. This scaled composite spectrum reaches much higher cross-section values, in less good agreement with our theoretical prediction. It should be noted that the intensity of the first band may also be affected by the level of theory. This can be observed when comparing the photoabsorption cross-section for 2-HPP calculated using SCS-ADC(2) and LR-TDDFT (see Fig 3.4). Both levels of theories appear to indicate

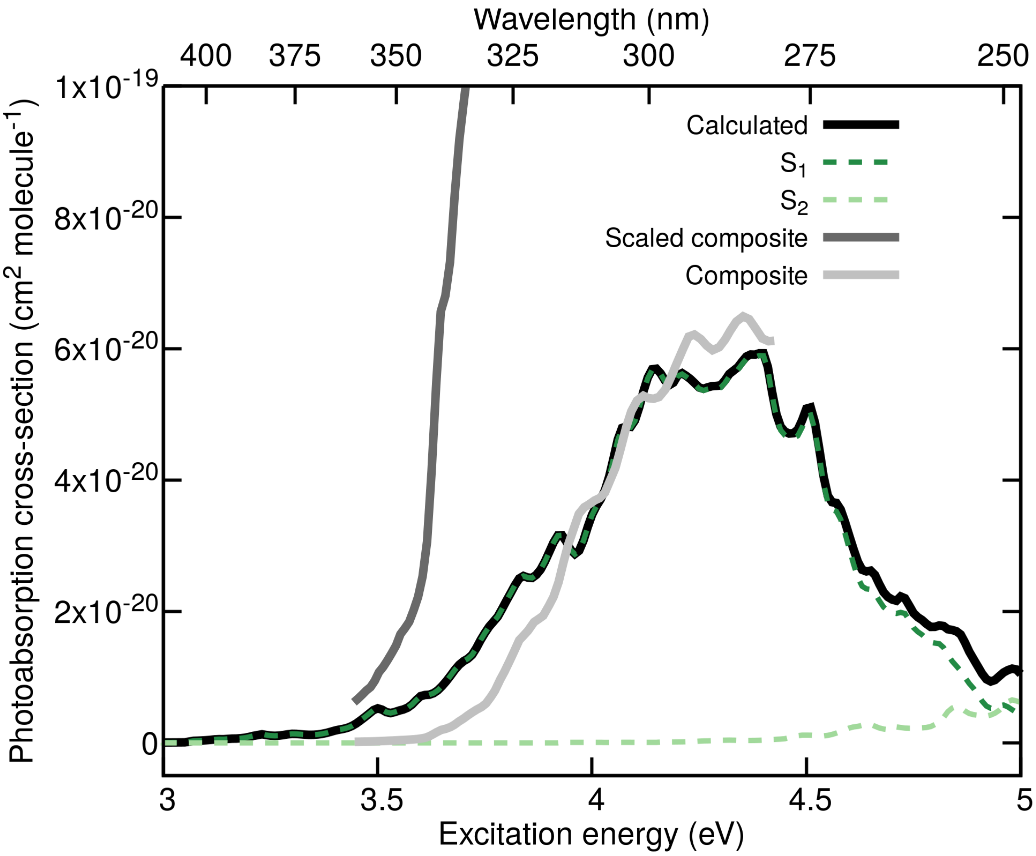

Figure 5.5: Calculated and SARs photoabsorption cross-sections of 2-HPP. The calculated photoabsorption cross-section obtained at the SCS-ADC(2)/def2-SVP level of theory is shown with a black solid line together with the $S_0 \rightarrow S_1$ (dark-green dashed line) and $S_0 \rightarrow S_2$ (light-green dashed line) contributions. The SARs composite photoabsorption cross-section of 2-HPP obtained by combining the experimental cross-sections of methylhydroperoxide and propanal is indicated with a light-grey solid line, while its scaled version is given with a dark-grey solid line. Both cross-sections are reproduced from Ref. 6.

that the 2-HPP photoabsorption cross-section may be slightly altered by intramolecular effects, but perhaps not as much as suggested by the scaling factor employed in the SARs cross-section.

Overall, the photoabsorption cross-section of 2-HPP calculated indicates that, in the actinic region, 2-HPP is most likely to be photoexcited to the first electronic excited state S_1 with a $n(O) \rightarrow \pi^*(CO)$ character. Based on this result, the next step of our study consists of studying the possible photoproducts formed by photoexciting 2-HPP at different wavelengths within the low-energy band of the calculated photoabsorption cross-section.

5.3.3 Wavelength-dependent quantum yield of 2-HPP and formation of photoproducts

In this Section, we focus on the formation of photoproducts following the photoexcitation of 2-HPP in the actinic region and the determination of wavelength-dependent quantum yields $\phi(\lambda)$. Our analysis here is based on conformer 1a, which exhibits an intramolecular hydrogen bond. We also investigated conformer 1c which does not have an intramolecular H-bond showing similar results to conformer 1a. In fact, the conformers suffer fast interconversion on the excited state in comparison with the photolysis time scale. Fig. 5.6 shows the interconversion of one trajectory that remains in the excited state for the entirety of the molecular simulation (100 ps). The initial condition is sampled from the Wigner distribution of conformer 1a, however, the trajectory visits all the S_1 minima optimized from the 1b-1g conformers.

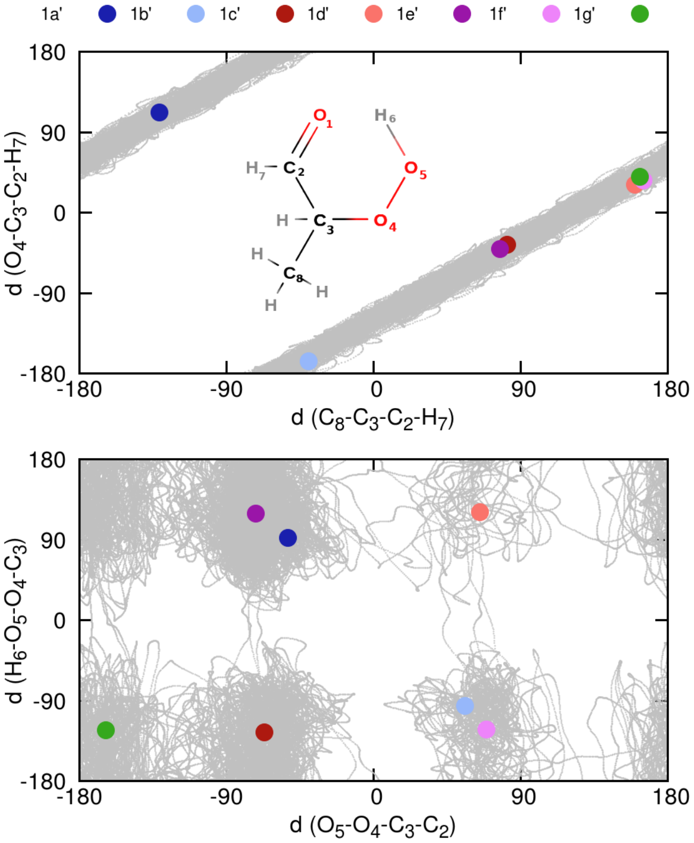

Figure 5.6: Interconversion between different conformers of 2-HPP. The trajectory does not suffer any dissociative pathways during the 100 ps of dynamics. The grey dotted line shows the S_1 trajectory projected on four dihedral angles. The S_1 minima of each conformer are optimized with SCS-ADC(2)/def2-SVP (the corresponding S_0 minima are depicted in Fig. 5.1). The inset shows the atom numbering used in defining the dihedral angle.

We emulated the wavelength-dependent photoexcitation of 2-HPP by defining a series of energy windows in the photoabsorption cross-section of 2-HPP (lower panel of Fig. 5.7).

We sampled a number of initial conditions randomly and grouped them by energy window, that is, we matched their transition energy to S_1 to a given energy window. Each initial condition in each energy window was then used to initialize a TSH trajectory, using SCS-ADC(2) and XMS-CASPT2. Importantly, the TSH dynamics was not stopped as soon as a trajectory reached the ground electronic state S_0 but was continued in S_0 to account for possible athermal effects coming from the non-statistical distribution of the internal energy gained by the photoexcitation.[322] We start our discussion by showing the distribution of the photoproducts observed as a function of the photoexcitation energy, and we comment on the mechanisms leading to their formation in section 5.3.3.1.

The TSH dynamics led to the observation of expected deactivation pathways based on our discussion in section 5.3.1 and Ref. 6, like the dissociation of OH and OOH or the $^1O_2$ release (Fig. 5.7). The release of $^1O_2$ with the formation of prop-1-en-1-ol is one of the main pathways to the photoreactivity of 2-HPP at low excitation energies and occurs for $\sim 45\%$ of all the trajectories undergoing a proton-coupled electron transfer. A significant number of unreactive trajectories were observed; this designation qualifies TSH trajectories that proceeded through a PCET mechanism but returned to the FC region following the nonradiative pathway to S_0.

The OH photodissociation is already present in the low excitation energy windows but gains importance when exciting 2-HPP with higher-energy photons. It is important to note that all dynamics were initiated in S_1 (see Fig. 5.5), meaning that the variation in photoproducts is not caused by the excitation to a different electronic state (with a different electronic character) but by the opening of new reaction channels at higher excitation energies (see also section 5.3.3.1). The photodissociation of OH from 2-HPP in its S_1 excited state is a prime example of such a photochemical process involving a change in electronic character within a given electronic state and its mechanism will be presented in section 5.3.3.1. The photodissociation channel of OOH appears to be a minute contributor to the photochemistry of 2-HPP at all excitation energies sampled.

Two trajectories remained in S_1 for 100 ps without suffering any deactivation pathways. These trajectories are particularly interesting as they could potentially be subjected to processes that are not described explicitly in our simulations, like intersystem crossing or collision with other molecules.[321] Intersystem crossings from S_1 to low-lying triplet states were proposed in Ref. 6 and will be discussed separately in section 5.3.4 below. Our TSH dynamics also highlighted an unexpected (minor) reaction channel involving the formation of a dioxetane moiety following a proton-coupled electron transfer event (see section 5.3.3.1 for the mechanistic details). We finally note that the use of SCS-ADC(2) for our TSH dynamics of 2-HPP implies that some artificial NRCIs might be visited during the dynamics. Such processes are given by white boxes in the lower panel of Fig. 5.5 for transparency but are not included in the determination of the wavelength-dependent quantum yields (upper panel of the same Figure).

In summary, the TSH trajectories appear to indicate that the 2-HPP photochemistry in

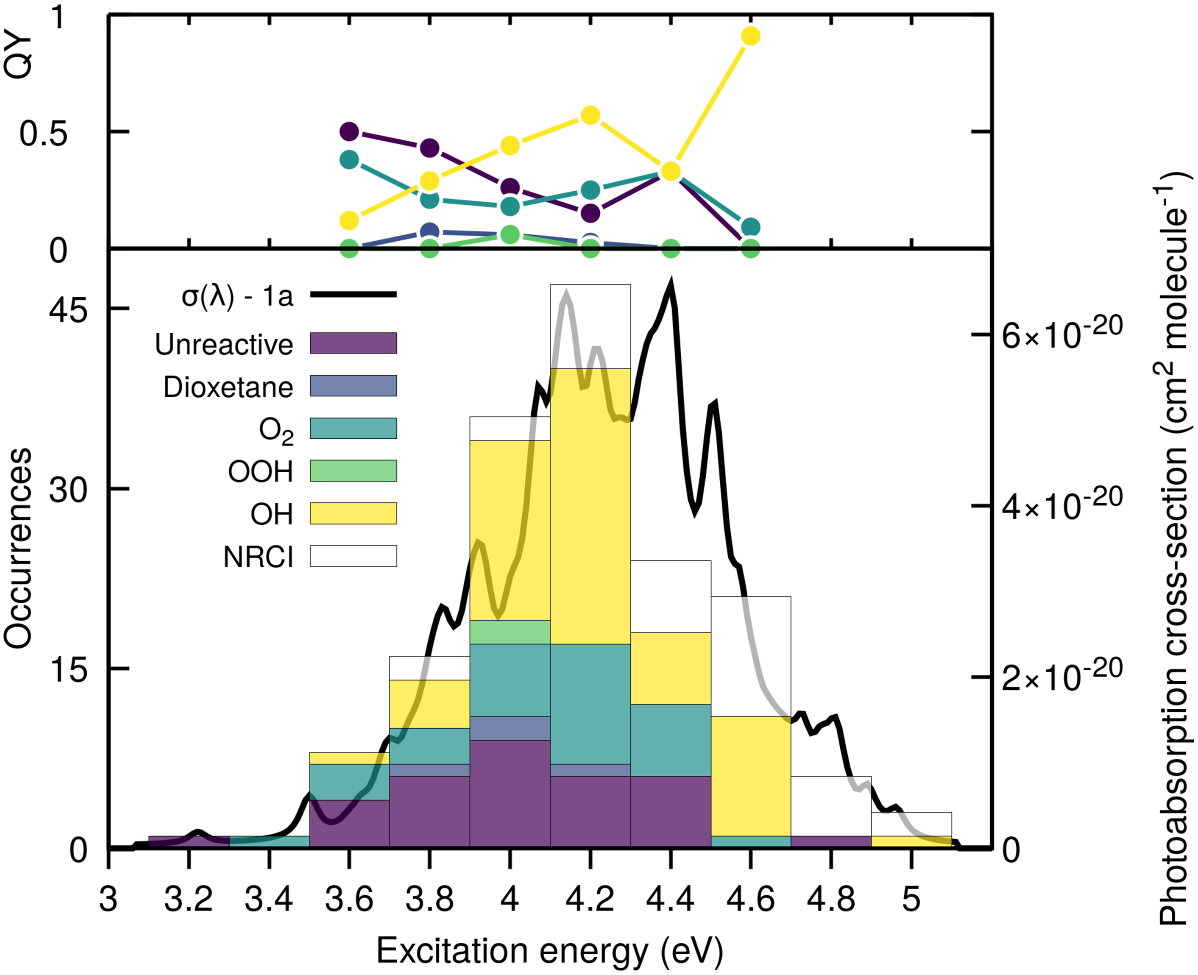

Figure 5.7: Wavelength-dependent photoproducts (lower panel) and quantum yields (upper panel) of 2-HPP. The photoproducts – OH and OOH dissociation, $^1O_2$ release and formation of prop-1-en-1-ol, dioxetane formation, unreactive trajectories, NRCI – were obtained by simulating the excited-state and subsequent athermal ground-state dynamics of 2-HPP (conformer 1a) with TSH/SCS-ADC(2)/def2-SVP and TSH/XMS(3)-CASPT2(12/9)/cc-pVDZ. The occurrences (number of TSH trajectories ending as one of the photoproducts defined) of each reactive pathway are overlaid with the calculated photoabsorption spectra (SCS-ADC(2)/def2-SVP) for S_1 state of the conformer 1a. The trajectories leading to an NRCI pathway were discarded from the quantum yield calculation. The wavelength-dependent quantum yields were calculated only for windows with more than eight successful trajectories.

the actinic region is dominated by a proton-coupled electron transfer process that can lead in half of the cases to the release of $^1O_2$ with the formation of prop-1-en-1-ol, and otherwise to a reformation of the original 2-HPP and, in rare occurrences, to the formation of a dioxetane ring. The photodissociation of OH appears to gain importance with the energy of the photon absorbed, while the dissociation of OOH is only a minor product. A few trajectories could suffer an intersystem crossing process as they remain in S_1 for an extended period of time without any reactions or deactivation to the ground electronic state. The following Section provides more details about the mechanisms of formation for the photoproducts by analyzing exemplary TSH trajectories.

5.3.3.1 Exemplary TSH trajectories illustrating the photochemistry of 2-HPP

This section illustrates the formation of 2-HPP photoproducts by presenting exemplary trajectories from the swarm leading to the overall results shown in Fig. 5.7. Trajectories will be analyzed by plotting the time trace of their electronic energies as well as key distances between atoms.

Let us start by considering the different outcomes following the proton-coupled electron transfer in S_1. As discussed in Sec. 5.3.1, an adequate theoretical description of these photochemical channels requires the use of XMS-CASPT2 as they involve the visit of nonadiabatic coupling regions between S_1 and S_0 and electronic states with a biradical character. The first possible photoproduct of the proton-coupled electron transfer mechanism is the release of $^1O_2$ and formation of prop-1-en-1-ol (panel A in Fig. 5.8). The segment of the trajectory presented starts with 2-HPP in S_1 and the proton-coupled electron transfer taking place, as identified by the shortening of the $O_1{-}H_6$ bond (purple dashed line in Fig. 5.8A). The trajectory approached a region of strong nonadiabaticity with S_0 at around 5695 fs, transferring to the ground electronic state with a biradical character before hopping back to S_1. The proton H_6 remains attached to O_1, and after 20 fs of dynamics the $C_3{-}O_4$ bond (dark green dashed line) begins to elongate, eventually breaking and leading to the dissociation of $^1O_2$ after 5730 fs (see molecular inset for the structure of the photoproduct). As expected from the LIIC pathways discussed earlier (see Fig. 5.2), the dissociation of $^1O_2$ leads to a closing of the S_0/S_1 energy gap.

This process is, however, not the only one possible following the proton-coupled electron transfer mechanism, as illustrated in Fig. 5.8B. In this particular case, the trajectory reaches the S_1/S_0 nonadiabatic region and jumps to S_0, where the proton migrates to O_1 (purple dashed line in Fig. 5.8B). At 145 fs, the proton transfers back to the original O_5 atom reforming the hydroperoxide moiety in S_0 – no dissociation occurs (see $C_3{-}O_4$ bond), the electronic character of the running state changes from biradical to closed-shell and 2-HPP is reformed in the Franck-Condon region. This trajectory exemplifies an overall unreactive trajectory, despite experiencing a proton-coupled electron transfer in S_1 before getting back to a closed shell ground state, *i.e.*, returning towards the Franck-Condon region.

Finally, we highlight a rare example of the formation of a dioxetane group following the PCET (Fig. 5.8C). In this particular case, the dynamics involving a nonadiabatic transition between S_1 and S_0 is similar to what is observed in Fig. 5.8A, with the difference that the trajectory, after briefly oscillating between S_1 and S_0 (4560 to 4575 fs in Fig. 5.8C), stabilizes in S_0 after 4575 fs of dynamics. After 40 fs of dynamics in S_0, the distance between C_2 and O_5 (light green dashed line in Fig. 5.8C) where the two unpaired electrons are located decreases rapidly to form a dioxetane moiety (see molecular structure in the inset of Fig. 5.8C). The

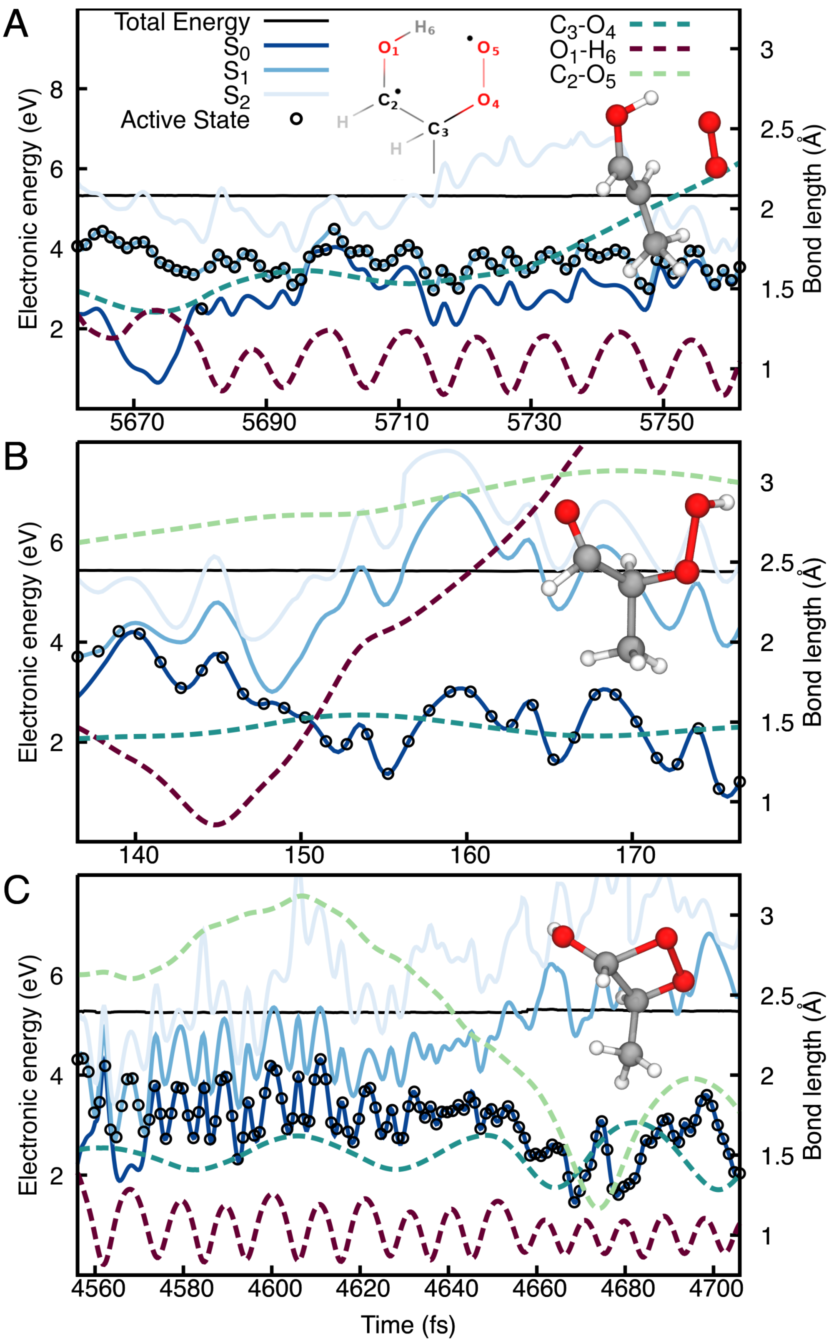

Figure 5.8: Exemplary trajectories for the proton-coupled electron transfer mechanism leading to (A) $^1O_2$ release, (B) return to the Franck-Condon region to reform 2-HPP (unreactive trajectory), and (C) the rare formation of a dioxetane ring. The energy traces (XMS(3)-CASPT2(12/9)/cc-pVDZ) highlight the three lowest electronic states, S_0 (dark blue), S_1 (blue), S_2 (light blue), with the driving state in the TSH dynamics highlighted by a black empty circle (plotted each 5 time steps). The total classical energy is given with a black solid line. The following distances between atoms are also plotted with dashed lines: $O_1{-}H_6$ (purple), $C_3{-}O_4$ (dark green), and $C_2{-}O_5$ (light green, not shown in panel A for clarity), with the atom numbering indicated in panel A for a structure following the proton-coupled electron transfer. Molecular structures illustrating the photoproducts formed are included as insets.

formation of the dioxetane, taking place in the ground electronic state, is correlated with an increased separation in energy between S_0 and S_1/S_2, highlighting the stabilization of this photoproduct.

We move to the analysis of the TSH trajectories leading to an OH photodissociation. As eluded to in Sec. 5.3.1, the dissociation of OH could be obtained by photoexciting directly 2-HPP into its S_2 electronic states, which shows a $n'(OO) \rightarrow \sigma^*(OO)$ character in the Franck-Condon region. This electronic state is, however, higher in energy and it is unlikely – even if not impossible – to be reached in the actinic region (see Fig. 5.5 and discussion in Sec. 5.3.2). The LIIC pathway presented in Fig. 5.3 suggests that the OH photodissociation could also take place from S_1, given that 2-HPP visits a region where the electronic character of this electronic state changes from $n(O) \rightarrow \pi^*(CO)$ to $n'(OO) \rightarrow \sigma^*(OO)$. Considering that the two electronic-state characters discussed here are located on different chromophores (carbonyl for $n(O) \rightarrow \pi^*(CO)$ and hydroperoxide for $n'(OO) \rightarrow \sigma^*(OO)$), one expects that their diabatic coupling should be rather weak. This weak coupling is already visible from the unavoided crossing of the adiabatic states S_1 and S_2 in Fig. 5.3 and reminiscent of a similar behaviour observed in the photochemistry of C_6-HPALD.[321] Such a weak diabatic coupling implies that the process of switching between one electronic character to the other is somehow hampered, and will be revealed in the adiabatic representation by a very localized seam of intersection between S_1 and S_2. When 2-HPP approaches this region of configuration space, the seam of intersections will behave as a trap for the electronic character of the molecule by transferring in a highly efficient manner 2-HPP from S_1 to S_2 – meaning that the molecule preserves its $n(O) \rightarrow \pi^*(CO)$ character in a diabatic picture. This process has been dubbed 'diabatic trapping'[323] or 'upfunnelling'[190] and, in the case of weakly-coupled multichromophoric molecules like 2-HPP or C_6-HPALD, protects them from OH photodissociation. The only way for the molecule to release OH from the S_1 state is to approach the seam in such a way that it remains on S_1 while the electronic character switches from $n(O) \rightarrow \pi^*(CO)$ to $n'(OO) \rightarrow \sigma^*(OO)$.

With this definition in mind, we can now discuss the behaviour of a trajectory exhibiting diabatic trapping (Fig. 5.9A). The segment of the trajectory discussed here starts at 9800 fs in S_1. One can observe that the trajectory reaches the intersection seam with S_2 – a process correlated with an extension of the $O_4{-}O_5$ bond of the hydroperoxide moiety (red dashed line in Fig. 5.9A). The trajectory hops to S_2 and returns back to S_1 within less than 10 fs, but the trajectory on S_1 now sees its $O_4{-}O_5$ bond contracting. The diabatic transfer to S_2 did not result in any OH dissociation. Let us artificially modify this trajectory by enforcing that it has to remain in S_1 (Fig. 5.9B) – all other parameters are strictly identical to those used to propagate the trajectory presented in panel (A). Again, the trajectory approaches the intersection seam, but as the trajectory is now forced to remain in S_1, the $O_4{-}O_5$ bond of the hydroperoxide moiety (red dashed line in Fig. 5.9B) now carries on its extension. As S_1 exhibits a character change to $n'(OO) \rightarrow \sigma^*(OO)$, molecule dissociates to form OH. The change of character from n(O) $\rightarrow \pi^*$(CO) to n$'$(OO) $\rightarrow \sigma^*$(OO) is further confirmed by the contraction of the carbonyl $C_2{=}O_1$ bond when the molecule leaves a n(O) $\rightarrow \pi^*$(CO) character. This comparison of trajectories makes it clear that the transfer to S_2 preserves the n(O) $\rightarrow \pi^*$(CO) character of 2-HPP and somehow protects it from suffering an OH dissociation.

The diabatic trapping illustrated above prevents an efficient OH photodissociation process, but a photoexcited 2-HPP in S_1 will often visit the S_1/S_2 seam and, while being trapped occasionally (one in average), may escape towards the region of configuration space where S_1 acquires a n$'$(OO) $\rightarrow \sigma^*$(OO) character and dissociates OH (explaining the OH quantum yields observed in Fig. 5.7). Figure 5.10 shows an example of a TSH trajectory suffering an OH dissociation. The trajectory avoids in this case the intersection seam, *i.e.*, the energy gap between S_2 and S_1 is not close to zero, allowing it to switch adiabatically character and release OH (red dashed line in Fig. 5.10) with a simultaneous contraction of the carbonyl $C_2{=}O_1$ bond. The increase of OH quantum yield with excitation energies points towards a more efficient process at avoiding the intersection seam, perhaps due to 2-HPP having higher internal energy on S_1.

5.3.4 Intersystem crossing processes

The calculations presented up to this point did not include the possibility for intersystem crossing processes, that is, the transfer of photoexcited 2-HPP from a singlet to a triplet state. ISC is mediated by spin-orbit coupling, which in turn is sensitive to the electronic character of the electronic states considered. If one calculates the spin-orbit coupling matrix element between a singlet and a triplet exhibiting the same electronic character, the resulting magnitude of spin-orbit coupling will be small as a result of the El-Sayed rule. The T_1 electronic state of 2-HPP has the same electronic character as S_1 in the vicinity of the Franck-Condon region, implying that their spin-orbit coupling is weak – for all the sampled occurrences, the mean value for the spin-orbit coupling magnitude between S_1 and T_1 is 1.8 cm^{-1}, with a maximum value of 4.9 cm^{-1}. As our TSH trajectories only account for internal conversion, we analyzed the possible influence of intersystem crossing processes by post-processing our long trajectories evolving in S_1 but remaining unreactive. For a 50ps-long S_1 trajectory, we calculated every 50 fs the electronic-energy difference between S_1 and the low-lying triplet states (T_1, T_2, and T_3) at the SCS-ADC(2)/def2-SVP level of theory and produced a histogram of these energy gaps (Fig. 5.11). A first important observation is that crossings between S_1 and a triplet state are rather infrequent and the low-lying triplet states remain rather far from S_1 during this 50ps-long trajectory. Nevertheless, the calculations presented here are in a spin-diabatic representation, meaning that in this picture one does not need to have crossings between S_1 and a triplet state for an intersystem crossing to take place. To account for this fact, we zoomed in the energy-gap window between -0.5 eV and 0.5 eV and, for each occurrence of a crossing between S_1 and T_2 or T_3 (to account for El-Sayed's rule), we calculated the magnitude of the corresponding spin-orbit

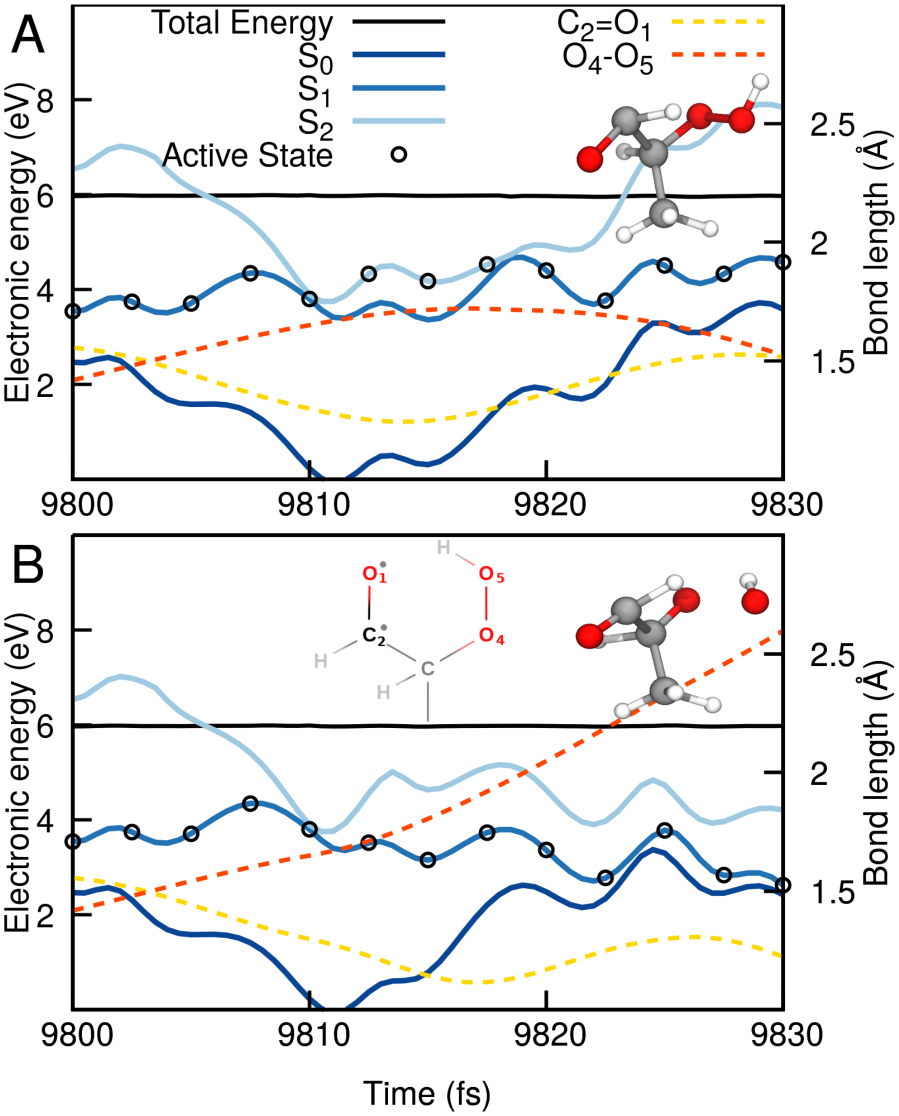

Figure 5.9: Exemplary trajectories illustrating the diabatic trapping mechanism hampering the photodissociation of OH. Panel (A) shows a TSH trajectory exhibiting diabatic trapping. Panel (B) shows the very same trajectory, but this time artificially constrained to remain on the S_1 electronic state. The energy traces (SCS-ADC(2)/def2-SVP) highlight the three lowest electronic states, S_0 (dark blue), S_1 (blue), S_2 (light blue), with the driving state in the TSH dynamics highlighted by a black empty circle (plotted each 5 time steps). The total classical energy is given with a black solid line. The $O_4{-}O_5$ bond of the hydroperoxide moiety is indicated by a red dashed line, while the carbonyl $C_2{=}O_1$ bond is given by a yellow dashed line. The atom numbering is provided in panel B. Molecular structures illustrating the photoproducts formed are included as insets.

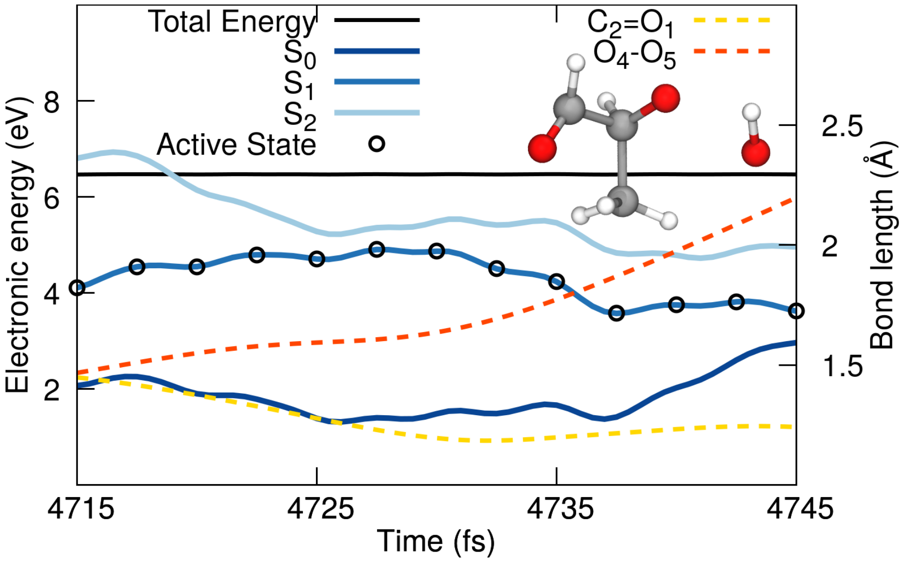

Figure 5.10: Exemplary trajectories illustrating the photodissociation of OH. The energy traces (SCS-ADC(2)/def2-SVP) highlight the three lowest electronic states, S_0 (dark blue), S_1 (blue), S_2 (light blue), with the driving state in the TSH dynamics highlighted by a black empty circle (plotted each 5 time steps). The total classical energy is given with a black solid line. The O_4-O_5 bond of the hydroperoxide moiety is indicated by a red dashed line, while the carbonyl $C_2=O_1$ bond is given by a yellow dashed line. The atom numbering is the same as that employed in Fig. 5.9. A molecular structure illustrating the photoproducts formed is included as inset.

matrix element with SA(3S,3T)-CASSCF(12/9)/cc-pVDZ (circles in the inset of Fig. 5.11). The magnitudes of spin-orbit coupling calculated are all rather small yet sizeable. We further mimicked the effect of an intersystem crossing by restarting, for each occurrence, the trajectory in the corresponding triplet state (mostly in T_2). For 17 out of 18 trajectories launched, we observed an almost immediate OH release, as a result of the dissociative character of T_2. Hence, if the timescale of the molecule in S_1 is long enough to allow for intersystem crossing processes, T_2 appears to be the most likely receiving triple state, leading to an immediate photodissociation of OH. If the molecule can reach T_1 directly from S_1, other decay mechanisms may be expected, as discussed in Ref. 6.

5.3.5 Limitations of the theoretical protocol

We discussed in the previous sections how the photoabsorption cross-section of 2-HPP can be predicted using the nuclear ensemble approach, and how nonadiabatic and ground-state dynamics simulations can be used to approximate quantum yields for photoproducts. As already alluded to in numerous parts of this work, the theoretical strategies used herein have a series of limitations when it comes to the simulation of atmospheric VOCs that we would like to further stress in this Section.

First of all, our work exemplifies the challenges related to the use of an adequate method for

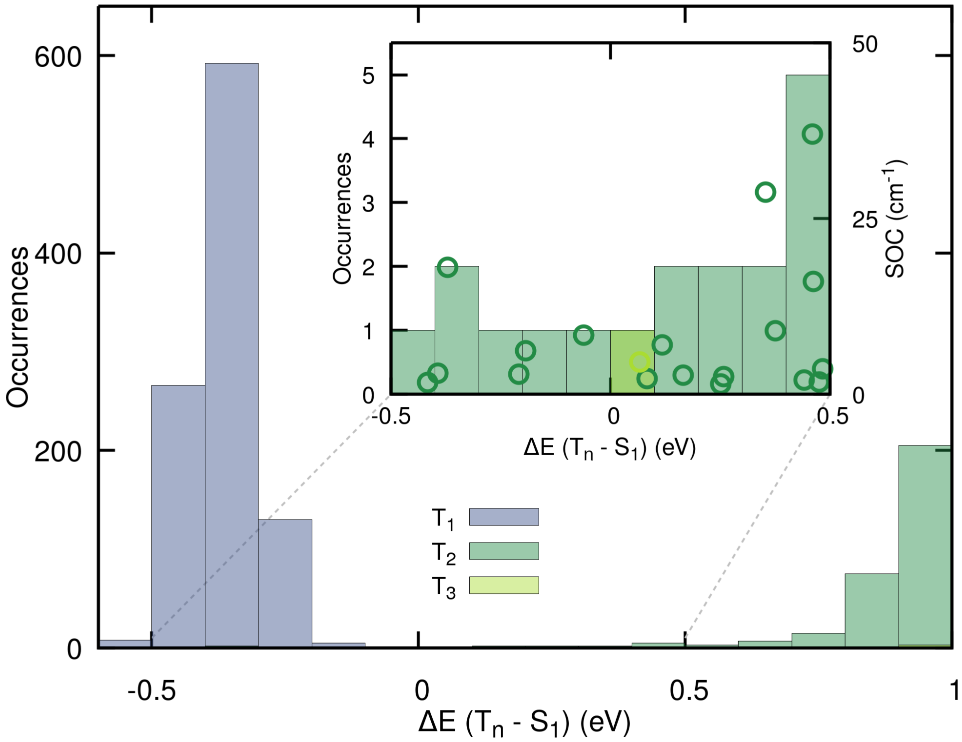

Figure 5.11: Analysis of the energy gaps between an unreactive 50ps-long TSH trajectory evolving in S_1 (SCS-ADC(2)/def2-SVP) and low-lying triplet states. The histograms indicate the energy gap (calculated with SCS-ADC(2)/def2-SVP) between the running S_1 electronic state and the lowest three triplet electronic states sampled each 50fs along the 50ps-long trajectory. The inset provides a zoom on the low-energy gaps (between -0.5 and 0.5 eV), highlighting the interaction between S_1 and the triplet states T_2 and T_3. For each occurrence, the absolute value of the spin-orbit coupling between S_1 and the respective triplet state was calculated at the SA(3S,3T)-CASSCF(12/9)/cc-pVDZ level of theory (empty circles).

the electronic structure. Methods like ADC(2) or even LR-TDDFT can provide a reasonable description of electronic transitions for organic molecules. Care has to be taken though when looking at atmospheric VOCs as some molecules may possess excited electronic states with a significant doubly-excited state character. LR-TDDFT cannot describe such electronic states and ADC(2) can only account for them at zeroth order. The same is true for molecules with a zwitterionic character like Criegee's intermediates, which are notorious for their complex electronic structure.[324] Higher-level methods based on the ADC or CC formalism like ADC(3), CC3, or CC4 would provide more accurate transition energies but at a much higher computational cost.[325–328] More importantly, an electronic structure method can provide a proper description of the excited electronic states of interest at the ground-state optimized geometry but may fail miserably as soon as the molecule leaves this region. Such inhomogeneity of the quality of potential energy surfaces has been exemplified greatly in the past with the charge-transfer issue in LR-TDDFT (see for example the case of DMABN in Ref. [329]) or with the shortcomings of ADC(2) when describing carbonyl-containing molecules. In this work, one of the challenges for the electronic structure was to describe in a balanced way electronic states with different characters – sometimes an issue for SA-CASSCF – and to account for the biradical nature of some photoproducts formed. XMS-CASPT2 appeared to be a good compromise in these regions. However, the multichromophoric nature of 2-HPP makes the active space required for XMS-CASPT2 rather large and therefore computationally expensive. The computational cost explains why XMS-CASPT2 could not be used as an electronic structure method for our TSH dynamics with a largely prolonged timescale. As mentioned in the text, some of our simulations were run for up to 100 ps, which is a considerable computational effort for excited-state dynamics and would simply not be possible with XMS-CASPT2 – in particular if one considers that we ran here a total of 246 trajectories to ensure a modest swarm of TSH trajectories. While we have validated the protocol of switching from SCS-ADC(2) to XMS-CASPT2, this strategy is far from ideal. Recent developments related on XMS-CASPT2 open new perspectives for future application of this method.[330] However, the photochemistry of atmospheric VOCs can also be challenging for XMS-CASPT2. For example, dissociative pathways may imply that more electronic states become important at some point in the dynamics. Gaining more flexibility in the number of electronic states considered in the state-averaging and multi-state process would be highly beneficial, as proposed by recent developments in dynamically-weighted SA-CASSCF.[331]

Obtaining absolute photoabsorption cross-sections implies that one also accounts for the quantum nature of the nuclei in the ground electronic states. The NEA employed in this work offers an efficient way to approximate the photoabsorption cross-section. The underlying sampling of the ground-state probability density for the lowest vibrational level uses a Wigner distribution within a harmonic approximation. The flexibility of some atmospheric VOCs means that a harmonic Wigner distribution may not always lead to a satisfactory representation of the ground-state probability density and other alternatives like *ab initio* molecular dynamics with a quantum thermostat are sometimes required – such effects appear negligible for 2-HPP (see chapter 3).

Last but not least, the excited-state dynamics simulations have some implicit limitations and rely on significant approximations. A first limitation may come from the use of the mixed quantum/classical method TSH. This method treats the nuclei in a classical way and therefore does not allow for tunneling processes. The method also may suffer from its approximation when multiple crossings between the same pair of excited electronic states take place – like the diabatic trapping observed here – but for molecular systems using a decoherence correction (as done here) is usually sufficient to fix this potential issue.[171] The simulations conducted here do not account for intersystem crossing processes. Different strategies have been proposed to account for both internal conversion and intersystem crossing processes in nonadiabatic molecular dynamics,[165, 332, 333] but the challenge is often related to the timescale of these events as well as the added challenge for the electronic-structure method to describe both triplets and singlets. As discussed earlier, the timescale of the TSH trajectories for 2-HPP in this work was up to 100 ps. However, the use of current nonadiabatic molecular dynamics strategies for such long-timescale simulations raises a series of questions, as recently illustrated in Ref. 334. The role of spin-orbit coupling and possibly collisions for long timescale processes could be performed with reduced-dimensionality models like the energy-grained master equation extended to nonadiabatic processes, even if the construction of the model is often informed by all-atom dynamics.[321] Last but not least, the excited-state dynamics presented were directly initiated in the excited-state by selecting initial conditions from the photoabsorption cross-section within a series of energy windows. While this offers a first approximation to wavelength-dependent processes like quantum yields, more involved strategies would be required to simulate the timescales of photoinduced processes for an atmospheric molecule under incoherent sunlight irradiation.[269, 335, 336]

5.3.6 Photolysis rate constants

Armed with a calculated photoabsorption cross-section (Fig. 5.5) and the different wavelength-dependent photolysis quantum yields (Fig. 5.7), we can attempt to predict *in silico* the photolysis rate constants for the main photoproducts of 2-HPP. We adopt here an actinic flux $F(\lambda)$ for a 30° solar zenith angle and 300 DU ozone, obtained from the Tropospheric Ultraviolet and Visible (TUV 5.4) radiation model[247], and we integrate Eq. (3.2) in an interval from 280 to 360 nm. Note that the wavelength-dependent quantum yields are estimated for the dominant 2-HPP conformer (1a). J values for the two main photolysis channels, namely the formation of $^1O_2$ and OH, amount to $J_{^1O_2} = 2.9 \times 10^{-5}$ s^{-1} and $J_{OH} = 3.2 \times 10^{-5}$ s^{-1}, while the cumulative J for all photolysis channels is calculated to be 6.7×10^{-5} s^{-1}. In comparison, Liu et al.[6] determine a J for the 1,5-H shift process (followed by O_2 release) to be 6.8×10^{-4} s^{-1},[1] using the same actinic flux as above and a unity quantum yield. The latter J value is more than 25 times larger than our best estimate for the rate of the O_2 release, while it is still 10 times larger than our total J (including all photolysis processes). Using the scaled photoabsorption cross-section of Liu et al. (scaled composite spectrum in Fig. 5.5) and our calculated $\phi_{^1O_2}(\lambda)$ for the release of $^1O_2$, we obtain a J value of 1.8×10^{-4} s^{-1}. Alternatively, combining our calculated $\sigma(\lambda)$ (Fig. 5.5) with ϕ=1 (used by Liu et al.) gives a J value of 1.1×10^{-4} s^{-1}. Therefore, it is clear that both the reduced $\phi(\lambda)$ and $\sigma(\lambda)$ from the present work, in comparison with Ref. 6, significantly affect the J estimates. In the context of atmospheric chemistry, our new estimate for the cumulative photolysis rate constant is smaller than the rate constant for the reaction of 2-HPP with OH radicals (estimated to be 1.3×10^{-4} s^{-1} based on MCM model [6]), meaning that photolysis may not be a dominating pathway for the removal of 2-HPP.

---

[1] We note that the same authors obtained slightly smaller J of 3.9×10^{-5} s^{-1} with the TUV code, as shown in Table 2 of Ref. 6.

Comparable data for other important α-hydroperoxycarbonyls and their impact on atmospheric species concentration balance remains to be evaluated.

5.4 Conclusions

The theoretical determination of photolysis properties for atmospheric VOCs is a challenging yet rewarding task, as photolysis rates for many atmospherically-relevant, transient VOCs are hardly available based on experiments alone. While using SARs often provides valuable insights on unknown molecules, fully *in silico* investigations provide a more robust and reliable way of investigating the photolysis of various VOC species. In this work, we used a large set of computational strategies to investigate the photochemistry of a complex multifunctional molecule from the family of α-hydroperoxycarbonyls. We presented a series of sensible approximations to calculate the photoabsorption cross-section and wavelength-dependent photolysis quantum yields, the key ingredients to evaluate sought-for photolysis rate constants. Following our earlier work on the photolysis of hydroperoxides,[246] we employed the nuclear ensemble approach to calculate the photoabsorption cross-section of 2-HPP, highlighting a discrepancy with previous estimates based on SARs considerations. A combination of nonadiabatic and ground-state molecular dynamics simulations allowed us to determine wavelength-dependent quantum yields for various photoproducts formed upon photoexcitation of 2-HPP. Nonadiabatic molecular dynamics is expected to provide an unbiased and automated way to explore complex potential energy surfaces and unravel the most relevant dissociation pathways and their corresponding yields, accounting for athermal effects that may elude regular transition-state theory. Using our *in silico* quantum yields and photoabsorption cross-section, we estimated the rate constants of the most important photolysis channels, showing that photolysis processes may not be dominant in atmospheric conditions to explain the removal of 2-HPP – reaction with OH being faster. While our own protocol is subject to limitations (many of which are identified in Sec. 5.3.5), we believe that it represents a reliable framework to explore the photochemistry of various transient VOCs and calculate their photolysis rate constants when these are unavailable experimentally.

Chapter 6

On the photochemistry of Lewis adducts

6.1 Introduction

In the previous chapters, I have shown that theoretical and computational chemistry is a powerful tool to access a wealth of information on the photochemistry of a molecule that is not easily obtained experimentally. In this chapter, we will build upon the protocols we developed for atmospheric VOCs to investigate the photochemistry of Lewis acid-base adducts.

The versatility of Lewis acid-base adducts, characterized by a dative bond between a Lewis acid and Lewis base, have been extensively used in recent years in various applications including functional materials,[106, 337, 338] sensors,[339] and optoelectronic devices.[7, 110, 340] In particular, polycyclic aromatic hydrocarbons (PAH) incorporating heteroatoms into their molecular framework have been an appealing choice to develop organic solar cells or light-emitting diodes thank the simple tuning of their electronic properties their light absorption and emission characteristics.[7, 110, 340] In particular, boron-doped PAHs lead to electron-deficient π systems due to the empty p orbital of the boron atom and they have recently been employed in optoelectronic materials and as organocatalysts.[341–343] The boron center, exhibiting a trigonal planar coordination, acts as a relatively strong Lewis acid, meaning that the molecule can form Lewis adducts with weak Lewis bases such as pyridine (Py).[7, 344, 345] The complexation of boron-doped PAHs with an appropriate Lewis base can be used to produce molecules with a specific functionality such as thermochromism,[346] chemisorption,[339] and dual emission upon photodissociation.[7, 110]

An intriguing example of Lewis adduct photodissociation was reported by Matsuo et and coworkers.[7] In this work, the authors investigated the synthesis of a planarized trinaphthyl-borane showing a remarkable stability towards water and oxygen, as well as a sufficient Lewis acidity to form a stable complex with Py. The resulting trinaphthyl-borane−Py Lewis adduct

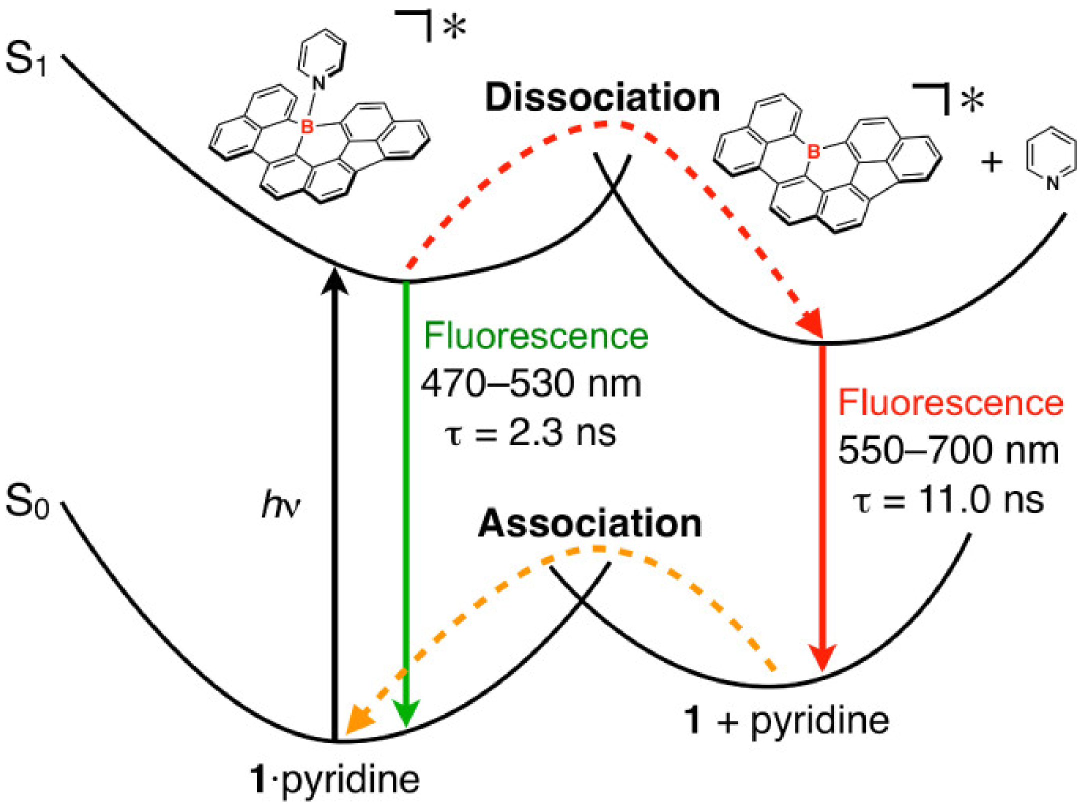

Figure 6.1: Schematic representation of the PESs for the photodissociation of the trinaphthyl-borane−Py adduct. The dual fluorescence is originated from the photodissociation of the Lewis adduct occurring on the excited state. Reproduced from Ref. 7.

(see structure in Fig. 6.1) was investigated with steady-state absorption and fluorescence spectroscopies, revealing an unexpected dual fluorescence. The dual fluorescence was explained by assuming the photodissociation of the adduct on the excited state via the B−N bond cleavage (Fig. 6.1). When photoexcited, the trinaphthyl-borane−Py complex can either (i) decay to the ground state via fluorescence or (ii) photodissociate to yield an electronically excited and uncoordinated trinaphthyl-borane and a Py molecule. The excited trinaphthyl-borane can finally relax via radiative emission – red-shifted with respect to the emission of the parent Lewis adduct – giving rise to the observed dual emission.

The B−N photodissociation was suppressed at low temperatures, indicating the presence of an activation barrier in the first excited electronic state S_1 to break the B−N bond. The authors also investigated the photophysical behavior of the trinaphthyl-borane using a stronger and weaker Lewis base than pyridine. With a stronger Lewis base, the photodissociation was suppressed and only one fluorescence emission – from the parent adduct – was observed. In contrast, with a weaker Lewis base, only the fluorescence from the trinaphthyl-borane was detected, suggesting that the photodissociation was occurring promptly upon photoexcitation. Finally, a computational investigation revealed that the optimized S_1 minimum of the adduct had a shorter B−N bond length – an observation somewhat inconsistent with the photodissociation behavior.

This light-induced reactivity is not unique to trinaphthyl-borane−Py but was also observed in the photochemistry of boron-doped antiaromatic PAH in presence of exceptionally weak Lewis base as phosphorus-containing polycyclic π-systems.[110] The antiaromatic character of the PAH reinforces the Lewis acidity of the boron. A photodissociable adduct can then be formed with a very weak Lewis base like phosphorus, while such photodissociation was not occurring with stronger Lewis bases like Py. Photodissociation was also observed with a constrained boron unit paired with a relatively weak donor embedded in the same molecule,[338, 347–349] and even using the π system of olefinic moiety as a donor.[350]

Interestingly though, the photochemistry and photophysics of B−N Lewis adducts are far from well understood, despite the large number of experimental studies using these properties for functional molecules. In particular, the relation between the strength of the B−N bond in the ground state and its lability upon photoexcitation is still unclear, in part because the mechanistic details that drive the B−N photodissociation are to date unknown. I propose in this chapter a detailed theoretical study of the excited electronic states and the photochemistry of B−N Lewis adducts, starting from the simple ammonia borane H_3N-BH_3 and moving towards more complex systems with pyridine-borane Py−BH_3 and pyridine-boric acid Py−$B(OH)_3$. The photochemistry of these molecules appears richer than anticipated, with multiple channels leading to the photodissociation of H atoms and H_2. The observation of a B−N dissociation channel requires either a high-energy excitation or a specific substitution around the B−N bond, in line with the experimental observations discussed above.

6.2 Computational details

6.2.1 Electronic structure

The photochemistry of B−N Lewis adducts is particularly rich and an adequate choice of the electronic structure method is critical to correctly capture the different photodissociation pathways. Following an extensive benchmark (discussed in the main text), we opted for a combination of MP2[226] and ADC(2).[225, 228, 229] All calculations were performed with Turbomole 7.3.[296] using the frozen core and the RI approximation.[299]

The accuracy of MP2 and ADC(2) at the minimum-energy structure in S_0 was validated against EOM-CCSD (performed with Gaussian09[270]), the multiconfigurational method SA-CASSCF[209–211], and multireference technique XMS-CASPT2.[213, 215] For all calculation we used the correlation-consistent polarized (cc-pVDZ, cc-pVTZ, cc-pVQZ, and the respective augmented sets)[319] and the Karlsruhe (def2-SVPD)[300–302] basis sets. BAGEL 1.2 was used for SA-CASSCF and XMS-CASPT2.[297] SA-CASSCF and XMS-CASPT2 calculations were employed to assess the reliability of ADC(2) along the photodissociation pathways of H_3N-BH_3, where the ground state may acquire a substantial multireference character. Calculations using BAGEL employed DF and frozen cores. For all XMS-CASPT2 calculations, we employed a real vertical shift of 0.5 Hartree and the SS-SR contraction scheme.

6.2.1.1 Benchmark of $H_3N{-}BH_3$

The photochemistry of $H_3N{-}BH_3$ is characterized by four dissociation pathways, namely (a) the B−N dissociation, (b) the B−H dissociation, (c) the concerted dissociation of H_2 via two B−H bonds breaking and (d) the N−H elongation (see scheme 6.4). The S_0/S_1 MECIs, required for the analysis of (b) and (c), have been optimized at XMS-CASPT2. Relaxed scans on the ground state – for (a) and (b) – and first excited state – for (d) – have been optimized with MP2/aug-cc-pVDZ and ADC(2)/aug-cc-pVDZ, respectively. LIICs have been used to connect critical geometries in pathways (b) and (c). Two different active space and state averages have been used throughout this work. The first one, used for pathways (a), involves a SA of 13 singlet states and an active space of eight electrons and nine orbitals. The pictorial representation of the nine natural orbitals computed at SA(13)-CASSCF(8/9)/aug-cc-pVDZ and the corresponding labeling is shown in Fig. 6.2. The second one, used for pathways (b), (c), and (d) is composed of a SA of 5 singlet states and an active space of four electrons and eight orbitals. The pictorial representation of the eight natural orbitals computed at SA(5)-CASSCF(4/8)/aug-cc-pVDZ and the corresponding labeling is presented in Fig. 6.3.

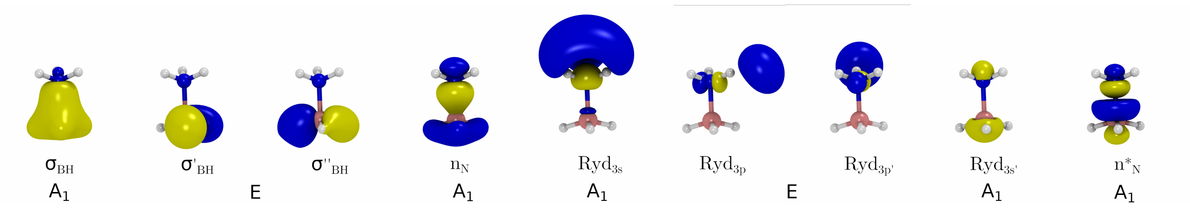

Figure 6.2: Pictorial representation of the nine natural orbitals computed at SA(13)-CASSCF(8/9)/aug-cc-pVDZ level of theory. The symmetry labels are assigned following the C_{3v} point group.

Since the dissociation pathways described for $H_3N{-}BH_3$ are found also in $Py{-}BH_3$ and $Py{-}B(OH)_3$, we consider the benchmark performed on $H_3N{-}BH_3$ to be valid for those molecules as well.

6.2.2 Photoabsorption cross-section and initial conditions

A set of 500 initial conditions for each molecule studied – ammonia borane, pyridine-borane, and pyridine-boric acid – were sampled from an *ab initio* molecular dynamics run (geometries sampled each 2000 a.u.) using MP2/aug-cc-pVDZ for the electronic-structure theory and a QT thermostat, performed with the ABIN code[276] coupled to the Turbomole 7.3.[296] Parameters for the quantum thermostat were taken from the GLE4MD webpage,[279], using a target

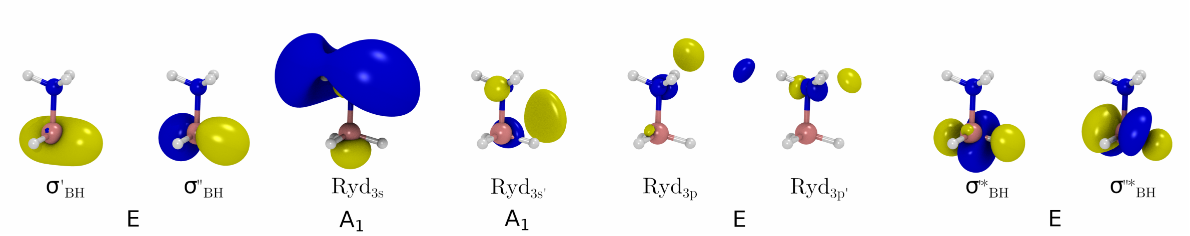

Figure 6.3: Pictorial representation of the eight natural orbitals computed at SA(5)-CASSCF(4/8)/aug-cc-pVDZ level of theory. The symmetry labels are assigned following the C_{3v} point group.

temperature T = 296 K and the following parameters: Ns = 6, $\hbar\omega/kT = 20$, strong coupling. The time step for the *ab initio* molecular dynamics was ∼ 0.5 fs. The equilibration time was determined by monitoring the convergence of the average kinetic energy temperature.

The initial conditions were used to compute the photoabsorption cross-section for the three different molecules at ADC(2)/aug-cc-pVDZ and ADC(2)/cc-pVDZ level of theory.[319] The augmented basis set is mandatory to properly describe the Rydberg character of the $H_3N{-}BH_3$ excited states. In contrast, the use of an augmented basis is less important for the $Py{-}BH_3$ and $Py{-}B(OH)_3$ adducts, characterized by only low-lying valence excited states. All spectral transitions were broadened with Lorentzians using a phenomenological broadening of 0.05 eV. The resulting photoabsorption cross-section for each molecule was obtained by averaging the contribution of all 500 geometries using the NEA. The NEA and the spectrum were calculated with Newton-X version 2.4.[166]

6.2.3 Excited-state dynamics and quantum yields

The nonadiabatic excited-state dynamics simulations were performed with the TSH algorithm.[117] TSH dynamics were carried out using ADC(2)/aug-cc-pVDZ for $H_3N{-}BH_3$ and ADC(2)/cc-pVDZ for $Py{-}BH_3$ and $Py{-}B(OH)_3$, with a time step of 0.5 fs and using Newton-X coupled with Turbomole.[234] The nonadiabatic couplings were obtained by using the overlap-based time-derivative couplings computed using the orbital derivative scheme,[175] and the kinetic energy was adjusted by rescaling the nuclear velocity vector isotropically following a successful hop. The electronic populations were corrected to prevent overcoherence using the energy-based decoherence correction of Granucci and Persico.[177]

The TSH dynamics were started from the same initial conditions used for the NEA (see above), grouped into different energy windows based on the calculated photoabsorption cross-section of $H_3N{-}BH_3$, $Py{-}BH_3$, and $Py{-}B(OH)_3$. Three energy windows with a width of 1.0 eV were selected for $H_3N{-}BH_3$ and $Py{-}BH_3$. For $H_3N{-}BH_3$, the windows were centered at 6.0, 7.0, and 8.0 eV, while for $Py{-}BH_3$ the three windows were centered at 4.0, 5.0, and 6.0 eV. Two windows instead were selected for $Py{-}B(OH)_3$, centered at 4.75 and 5.25 eV and with a width of 0.5 eV. The choice of the width is somewhat arbitrary and guided by the balance between computational cost and the interplay between excited-states observed from the photoabsorption cross-section. The initial conditions chosen were selected randomly (*i.e.*, not based on the oscillator strength) and their statistics are reported in Tab. 6.1. All TSH trajectories were stopped when the S_0/S_1 energy gap becomes smaller than 0.05 eV and the last point of the dynamics is used to assess the type of nonradiative process. The standard deviations of the fraction of trajectories per photodissociation channel were estimated following the method of Persico and Granucci.[281]

Table 6.1: Number of initial conditions chosen for each energy window for the three Lewis adducts reported in this work.

$NH_3{-}BH_3$		Py$-BH_3$		Py$-B(OH)_3$	
Energy windows	n. traj	Energy windows	n. traj	Energy windows	n. traj
6.0 eV	50	4.0 eV	27	4.75 eV	35
7.0 eV	55	5.0 eV	33	5.25 eV	43
8.0 eV	52	6.0 eV	39		

6.3 Results and discussion

6.3.1 Photochemistry of ammonia borane

The first molecule that will investigate is ammonia borane, $H_3N{-}BH_3$. $H_3N{-}BH_3$ is the simplest B$-$N Lewis adduct and was used as a minimal model to study and understand the physical and chemical properties of this class of compounds. $H_3N{-}BH_3$ has received increasing attention in the last few years as a potential hydrogen-storage material. Consequently, $H_3N{-}BH_3$ has been analyzed by several spectroscopic techniques such as microwave,[351] NMR,[352] IR,[353] Raman,[354] single-photon ionization,[355] photoelectron spectroscopy,[356, 357] X-ray crystallography,[358] neutron powder diffraction,[359] and inelastic neutron scattering.[360] The properties of ammonia borane were also analyzed by inelastic neutron scattering spectroscopy[361] and dipole measurements.[362, 363] Finally, the dehydrogenation pathways of $H_3N{-}BH_3$ were investigated with and without catalysts[364–368]. All these experimental studies, though, focused exclusively on the ground electronic state of ammonia borane.

Numerous computational works were proposed to understand the experimental results listed in the previous paragraph. The geometrical parameters at the ground-state equilibrium geometries were studied using HF,[369] MPPT,[369] and DFT.[370] Theory was used to calculated vibrational frequencies and the zero-point energy of ammonia borane,[369–371], as well as its charge transfer characteristics[372] and ground-state dissociation.[373] A (simple) theoretical absorption cross-section of $H_3N{-}BH_3$ was reported[374] in the UV region, but as stated above, there is – to the best of our knowledge – no computational or experimental study focusing on the photochemistry of ammonia borane. Hence, our theoretical work has to start by unraveling the photochemistry of the simplest B$-$N Lewis adduct $H_3N{-}BH_3$, before proceeding

$$\begin{aligned}
\mathrm{H_3N{-}BH_3} + h\nu &\xrightarrow{\text{(a)}} [\mathrm{NH_3}]^* + \mathrm{BH_3} \\
&\xrightarrow{\text{(b)}} [\mathrm{H_3N{-}BH_2}]^* + \mathrm{H} \xrightarrow{\mathrm{CI}_{\mathrm{BH}}^{\mathrm{S_0/S_1}}} \mathrm{H_2N{=}BH_2} + 2\,\mathrm{H}\ ? \\
&\xrightarrow{\text{(c)}} [\mathrm{H_3N{-}BH}]^* + \mathrm{H_2} \xrightarrow{\mathrm{CI}_{\mathrm{H_2}}^{\mathrm{S_0/S_1}}} \mathrm{HN{\equiv}BH} + 2\,\mathrm{H_2}\ ? \\
&\xrightarrow{\text{(d)}} [\mathrm{H{\cdots}H_2N{-}BH_3}]^* \xrightarrow{\mathrm{CI}_{\mathrm{NH}}^{\mathrm{S_0/S_1}}} \mathrm{NH_3} + \mathrm{BH_3}\ ?
\end{aligned}$$

Figure 6.4: Scheme of the possible photodissociation channels for $H_3N{-}BH_3$. The asterisk denotes that the resulting molecular fragment is created in an excited electronic state. The addition of a question mark indicates that although some data suggest these photoproducts may be likely candidates for the ground state dynamics, further investigation is needed to confirm this.

with more complex molecules. The hypothesized photodissociation channels of $H_3N{-}BH_3$ are presented in Fig. 6.4. Our work will aim to (i) confirm the existence of photodissociation (a)-(d) and (ii) provide the wavelength dependence for each channel. A careful benchmark of the electronic-structure methods is first conducted to assess the level of theory required to describe the excited electronic states of this family of molecules at and beyond the FC region.

6.3.1.1 Vertical excitation energies of ammonia borane

The description of the low-lying excited electronic states of $H_3N{-}BH_3$ is a challenge for theoretical methods. Most of these states are characterized by a strong Rydberg character, which is usually poorly described by LR-TDDFT methods.[375] The high density of electronic states in the UV-VUV regime means that the use of multireference methods like XMS-CASPT2 is arduous due to state-averaging. Cornered by the underlined difficulties, ADC(2) appears to be a potential alternative, being in general more reliable than LR-TDDFT but also overcoming the underlined limitations of multireference methods. As observed in chapter 4, ADC(2) suffers from shortcomings that may not have been highlighted in the literature, and its validity needs to be confirmed by performing a detailed benchmark against higher levels of electronic-structure theory, in the FC region and beyond. Such validation is absolutely key before moving the determination of the photoabsorption cross-section and the nonadiabatic excited-state dynamics of ammonia borane, in particular considering the current lack of experimental data on this molecule.

We start by comparing the excitation energies obtained with ADC(2), EOM-CCSD, and XMS-CASPT2 (using different basis sets) to confirm that ADC(2) is able to provide an adequate description of the Rydberg excited electronic states of $H_3N{-}BH_3$ (see Tab. 6.2). The combination of ADC(2) with the aug-cc-pVDZ basis set yields vertical transitions and oscillator strengths in excellent agreement with EOM-CCSD/aug-cc-pVQZ for the lowest nine excited

Table 6.2: Excitation energies (eV) and oscillator strengths (a.u.) of $NH_3{-}BH_3$ computed at the FC point optimized at SCS-MP2/def2-SVPD. The excited states are labeled according to the C_{3v} point group.

	S_1/S_2 (E)	S_3/S_4 (E)	S_5 (A_2)	S_6 (A_1)	S_7/S_8 (E)	S_9 (A_1)
ADC(2)						
aug-cc-pVDZ	6.96	8.24	8.27	8.33	8.45	8.65
	(0.013)	(0.029)	(0.0)	(0.005)	(0.069)	(0.126)
aug-cc-pVTZ	7.07	8.34	8.39	8.42	8.55	8.82
	(0.014)	(0.036)	(0.0)	(0.005)	(0.062)	(0.129)
SCS-ADC(2)						
aug-cc-pVDZ	7.18	8.40	8.45	8.53	8.63	8.86
	(0.017)	(0.043)	(0.0)	(0.004)	(0.055)	(0.135)
aug-cc-pVTZ	7.31	8.52	8.59	8.64	8.75	9.04
	(0.017)	(0.051)	(0.0)	(0.004)	(0.048)	(0.138)
EOM-CCSD						
aug-cc-pVTZ	6.99	8.26	8.31	8.33	8.49	8.87
	(0.014)	(0.033)	(0.0)	(0.005)	(0.063)	(0.132)
aug-cc-pVQZ	7.02	8.31	8.35	8.39	8.51	8.91
	(0.014)	(0.033)	(0.0)	(0.005)	(0.060)	(0.130)
XMS(13)-CASPT2(8/9)						
aug-cc-pVDZ	6.81	8.14	8.16	8.20	8.40	8.71
	(0.010)	(0.004)	(0.0)	(0.0)	(0.060)	(0.140)

states reported. As already suggested by the oscillator strength, a visual inspection of the excited state NTOs confirms the overall agreement, in terms of electronic character, between ADC(2) and EOM-CCSD. These results further agree with XMS-CASPT2, although some oscillator strengths appear weaker with this method.

Based on this first validation of ADC(2)/aug-cc-pVDZ in the FC region, we can now extend our benchmark to the investigation of the photodissociation pathways expected for $H_3N{-}BH_3$. All calculations presented from this point on will make use of an aug-cc-pVDZ basis set, except if stated otherwise.

6.3.1.2 Pathway (a): photodissociation of the B−N bond in ammonia borane

Let us first focus on the dissociation of the B−N bond. In the ground state, the B−N dissociation follows a heterolytic cleavage such that the Lewis acid and base are released as neutral species. How does such dissociation take place in the excited electronic states?

To answer this question, we performed a relaxed scan along the B−N bond length at the MP2 level of theory in the ground electronic state and use the obtained geometries to compute the electronic energies at the ADC(2) level of theory. The resulting electronic energies for the first nine electronic states are represented in Fig. 6.5. At the FC – indicated by the gray dashed line – the two degenerate lowest electronic states (E) have a $\sigma_{\mathrm{BH}} \rightarrow \mathrm{Ryd}_{3s}$ character.

The σ_{BH} is a linear combination of the σ orbitals constituting the B−H bonds, while Ryd_{3s} is the Rydberg-like $3s$ virtual orbital centred on the nitrogen (see NTOs in Fig. 6.5). The other higher excited states have a similar nature and they are all characterized by the same hole (donating) orbital (σ_{BH}). However, the particle (accepting) orbital is either a Rydberg-like $3p$ orbitals of the nitrogen (Ryd_{3p}) or a more complex orbital involving the $3s$ orbital on the boron (see Fig. 6.2). The trend changes when we look at the ninth electronic state (A_1) which, at the FC point, is a $\mathrm{n}_N \rightarrow \mathrm{Ryd}_{3s}$ excitation, where the n_N is the lone pair of the nitrogen (see NTOs in Fig. 6.5).

Now that the character of the electronic states is defined at the FC point, let us follow the evolution of the electronic states along the B−N coordinate (Fig. 6.5). Upon elongation of this bond, we notice that the $\sigma_{\mathrm{BH}} \rightarrow \mathrm{Ryd}_{3s}$ states are strongly destabilized, in stark contrast with the $\mathrm{n}_N \rightarrow \mathrm{Ryd}_{3s}$ state that becomes the first excited state for a B−N bond longer than 2Å. The transfer of electronic character between electronic states is validated by observation of the NTOs for the first excited state at the last point of the relaxed scan (see inset in Fig. 6.5 at ~ 3.6 Å), which confirms the local excitation of ammonia from its lone pair to the Ryd_{3s} orbital.

While the scan along the B−N bond offers an interesting picture of the interplay between electronic states, this picture does not inform us about the accuracy of ADC(2) in describing the excited-state B−N dissociation. The D_1 diagnostic for the MP2 ground state remains well below the recommended limit value of 0.04[304] along the whole relaxed scan. This observation suggests that the ground state is still well described as a (closed-shell) single configuration, consistent with the suggested heterolytic dissociation in the ground state. Furthermore, we compared the electronic energies obtained with ADC(2) to those calculated with SA(13)-CASSCF(8/9) and XMS(13)-CASPT2(8/9) along the very same set of geometries, see Fig. 6.6. The state-averaging includes the first nine electronic states (showed in Fig. 6.5) at the FC point, augmented by 4 additional electronic states arising from excitations originating from the n_N orbital. Disentangling all the electronic states in the FC region is challenging by visual inspection, but we wish to note the overall agreement between SA(13)-CASSCF(8/9) and ADC(2). In particular, we can easily isolate the electronic states arising from the n_N excitation, since they decrease in energy upon elongation of the B−N bond. The agreement is even better between the ADC(2) and XMS(13)-CASPT2(8/9) profile, further validating the use of ADC(2) in this dissociation limit. We note in passing that the ground-state electronic-energy profile along the scan is surprisingly flat at the SA-CASSCF level of theory, but adding dynamic correlation (XMS-CASPT2) recovers the shape observed with MP2 (Fig. 6.5).

The presence of a $\mathrm{n}_N \rightarrow \mathrm{Ryd}_{3s}$ electronic state, leading to the weakening of the B−N bond by removing an electron from the nitrogen lone pair, could offer an explanation for the photodissociation process observed by Matsuo and coworkers.[7] First of all, the lowest electronic states with E symmetry (S_1 and S_2 in the FC region) are clearly stabilized upon

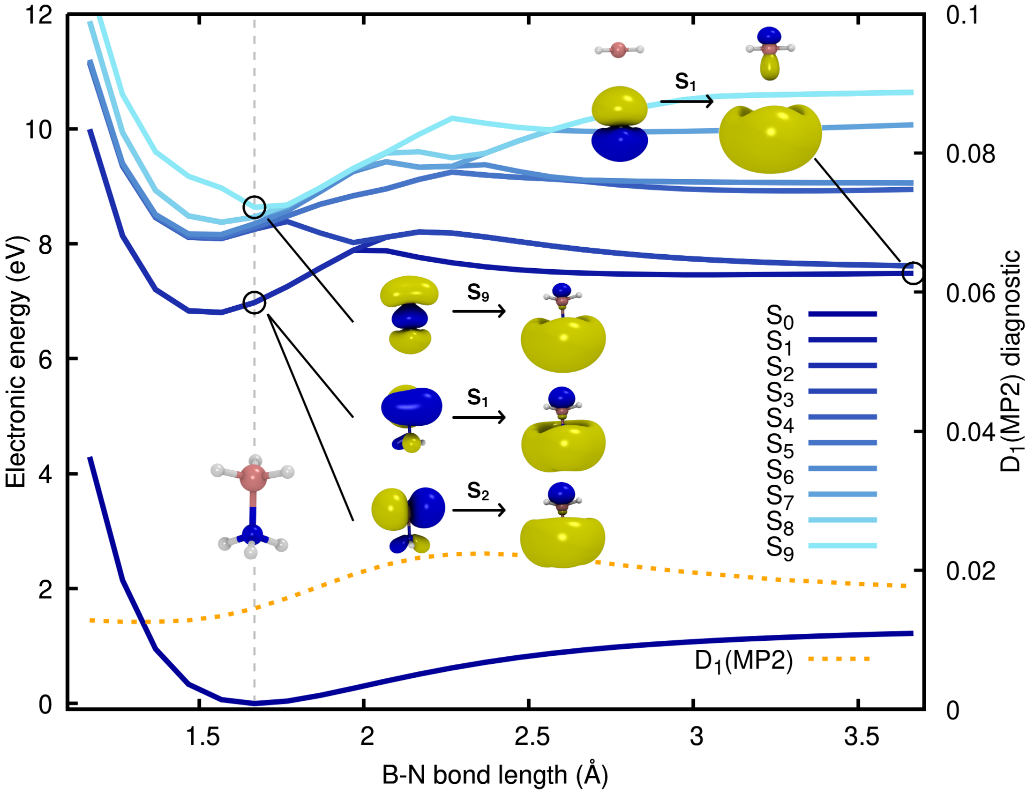

Figure 6.5: Relaxed scan along the B−N bond length of $H_3N{-}BH_3$ obtained for the ground electronic state with MP2. Excited electronic energies were obtained with ADC(2). The FC point is indicated by the gray vertical dashed line with the corresponding geometry as inset. The lowest nine electronic states are depicted in shades of blue – from S_0 in dark blue to S_9 in light blue. The D_1 diagnostic for the MP2 ground state is reported as a dotted orange line. The NTOs of the S_1/S_2 (E) and S_9 (A_1) electronic states at the FC and the S_1 (A_1) state at the last point of the relaxed scan are depicted as insets.

the shortening of the B−N bond, consistent with the computational results obtained for the trinaphthyl-borane−Py adduct.[7] Accessing the $n_N \rightarrow Ryd_{3s}$ state requires overcoming an activation barrier along the B−N bond stretch. If the ammonia borane molecule is photoexcited in the lowest E states (S_1 and S_2 in the FC region), an elongation of the B−N could result in an adiabatic transfer to a $n_N \rightarrow Ryd_{3s}$ character occurring at ∼2 Å (see Fig. 6.5). Once the character of the molecule evolves to this dissociative state, the $H_3N{-}BH_3$ should spontaneously dissociate, resulting in the formation of an electronically excited ammonia molecule and a borane in its ground state, consistently with the reaction channel (a). This behaviour at the dissociation limit for ammonia borane is apparently inconsistent with the one observed for the trinaphthyl-borane−Py, where the trinaphthyl-borane remains electronically excited upon dissociation while the pyridine is in its ground electronic state. This discrepancy can be attributed to the nature of the Lewis acid and base considered and their respective electronic energies. Due to the highly conjugated PAH system, the lowest excited electronic state in the

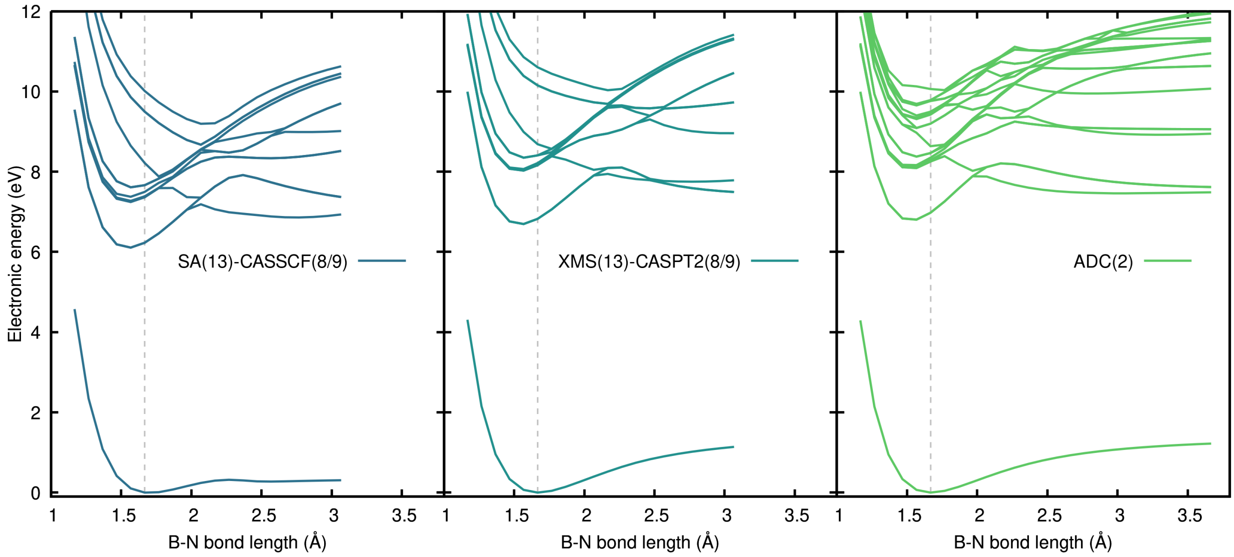

Figure 6.6: Comparison of SA(13)-CASSCF(8/9)/aug-cc-pVDZ (dark blue), XMS(13)-CASPT2(8/9)/aug-cc-pVDZ (blue-green), and ADC(2)/aug-cc-pVDZ (green) electronic energies obtained for the ground-state (MP2) relaxed scan along the B−N bond length of $NH_3{-}BH_3$. The last points of scan are not reported for SA(13)-CASSCF(8/9)/aug-cc-pVDZ and XMS(13)-CASPT2(8/9)/aug-cc-pVDZ due to convergence issues. The FC point is indicated by a gray vertical dashed line.

dissociation limit is expected to be located on the trinaphthyl-borane, as the lowest electronic state of Py is higher in energy. The situation is clearly different in $H_3N{-}BH_3$, where the lowest excited state is imputed to the $n_N \rightarrow Ryd_{3s}$ excitation on ammonia.

We have offered here a detailed investigation of the electronic states of ammonia borane along the B−N bond coordinate, and should now move on to other possible dissociation channels.

6.3.1.3 Pathway (b): H photodissociation from the BH_3 moiety

Inspired by the VUV photodissociation of ethane[376] – structurally and electronically similar to $H_3N{-}BH_3$ – we move to an investigation of the performance of ADC(2) in describing the H and H_2 photodissociation channels of ammonia borane. As observed in the previous section, $H_3N{-}BH_3$ has a dense manifold of excited electronic states, and we propose here to investigate the relaxation processes taking place from the lowest excited state. In comparison to ethane,[376] the introduction of the B and N atoms in ammonia borane produces a strong asymmetry in the electronic structure of the excited electronic state and different behaviour should be expected when H photodissociation is triggered from the BH_3 or the NH_3 moiety. Here, we start the investigation by focusing on the H photodissociation occurring from the BH_3 moiety, which we expect to be more favourable given the character of the first excited electronic state (see above). We note in passing that, in contrast with the B−H stretching, the B−H and N−H stretching modes are not totally symmetric and they lift the degeneracy of the E states. In the following, we will not use spatial symmetry.

The B−H bond cleavage is illustrated in Fig. 6.7, where a profile combining a relaxed scan (ground-state, MP2) is combined with a LIIC towards an optimized MECI for the B−H dissociation obtained at the XMS(5)-CASPT2(4/8) level of theory. The S_1 electronic state is stabilized upon B−H elongation, in agreement with its $\sigma_{\mathrm{BH}} \rightarrow \mathrm{Ryd}_{3s}$ character (see NTOs in Fig. 6.5), and a B−H dissociation can proceed with almost no barrier, suggesting a fast photodissociation of the H atom from the BH_3 moiety. Up to the last point of the scan (indicated with a dashed vertical grey line in Fig. 6.7), the MP2/ADC(2) and XMS-CASPT2 electronic energies are in excellent agreement. At the last point of the scan, the B−H length is 2.7 Å (the sum of the van der Waals radii of H and B is $\sim$ 3Å) but the S_0/S_1 energy gap is still >2 eV. This observation suggests that the B−H bond is fully broken in the excited electronic state and that the B−H elongation is perhaps not the only coordinate that brings the molecule to the CI region.

How does the molecule reach the S_1/S_0 intersection after photodissociation of H from the BH_3 moiety? The answer can be found by inspecting the LIIC connecting the relaxed scan to the $\mathrm{CI}_{\mathrm{BH}}^{\mathrm{S_0/S_1}}$ (Fig. 6.7, right side of the vertical dashed grey line). The $\mathrm{CI}_{\mathrm{BH}}^{\mathrm{S_0/S_1}}$ geometry is characterized by $NH_3{-}BH_2$ and an H atom completely dissociated (B−H distance is $\sim$ 9 Å). The $NH_3{-}BH_2$ molecule exhibits a longer N−H bond ($\sim$ 0.3 Å more with respect to the last point of the relaxed scan, see green dotted line in Fig. 6.7). This distortion of the $NH_3{-}BH_2$ moiety appears to take the molecule toward the $\mathrm{CI}_{\mathrm{BH}}^{\mathrm{S_0/S_1}}$ once the B−H bond is cleaved in the excited state. The N−H elongation process is somewhat captured by ADC(2), which shows a point of degeneracy between the S_1 and S_0 electronic energies, but care needs to be taken. The S_1/S_0 crossing point occurs at a much shorter N−H bond length when compared to XMS-CASPT2, due to the artificial destabilization of the MP2 ground state that takes place too rapidly along the LIIC. This conclusion is reinforced by the sharp increase of the D_1 diagnostic at the beginning of the LIIC, suggesting that the ground electronic state cannot be described adequately by a single closed-shell configuration. Hence, the B−H photodissociation of ammonia borane is well described by ADC(2), but the subsequent processes taking the molecule towards the S_1/S_0 intersection region via N−H elongation pushes the method beyond its limits.

It is worth noticing that the N−H elongation does not necessarily imply the N−H bond rupture but it acts as a simple distortion mode to access the CI region. Another photodissociation channel involves an S_1/S_0 crossing mediated by an N−H dissociation occurring *readily* after the B−H dissociation. This process works along a similar pathway to what is depicted in Fig. 6.7, but it most likely leads to the release of H_2 and $H_2N{=}BH_2$ (as observed in the photodissociation of ethane[376]).

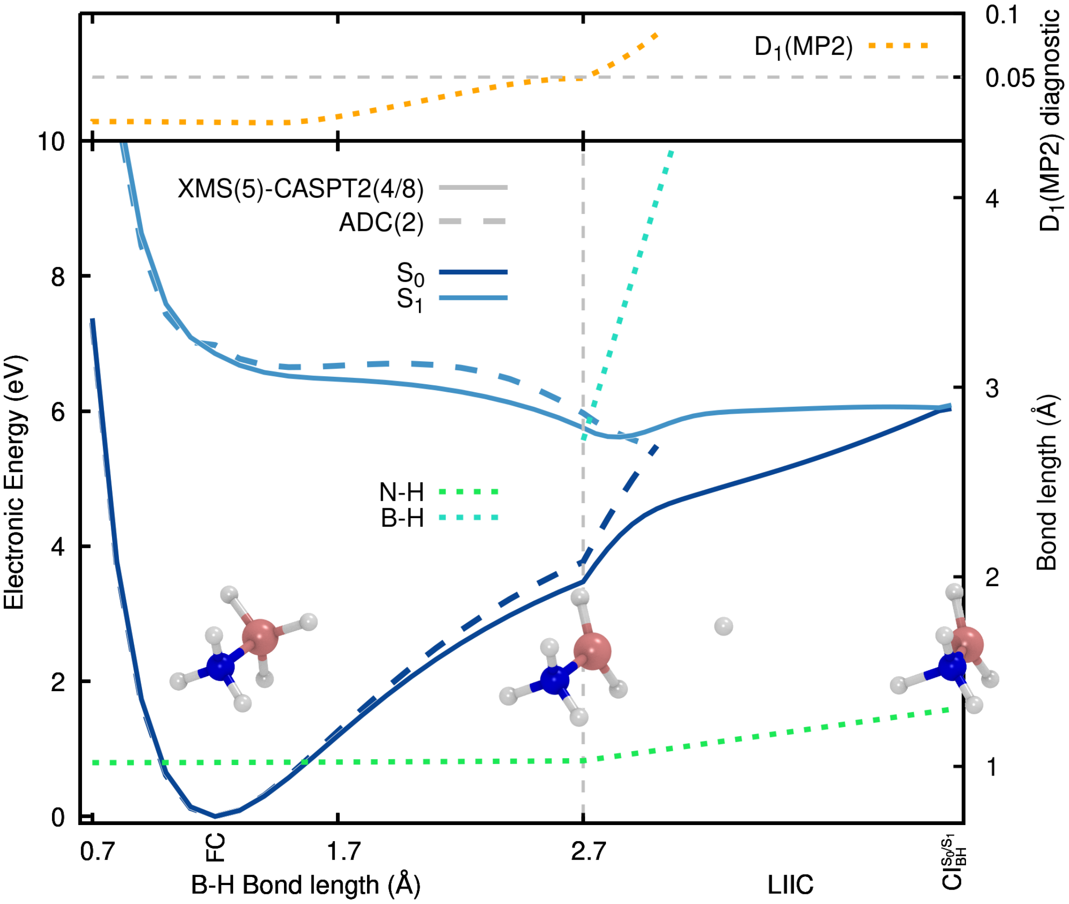

Figure 6.7: Profile showing the electronic energies along an H photodissociation from the BH_3 moiety. The profile is composed of a relaxed scan along the H dissociation coordinate (performed in the ground electronic state), combined with a LIIC that connects the last point of the relaxed scan to the $CI_{BH}^{S_0/S_1}$. The separation between the scan and the LIIC is indicated by a vertical dashed grey line. The two lowest electronic states are depicted in dark and light blue, respectively. ADC(2) and XMS(5)-CASPT2(4/8) profiles are indicated by dashed and solid lines, respectively. The relevant B-H and the N-H bond lengths are shown in blue-green and green dotted lines along the profile. The D_1 diagnostic for the MP2 ground state is reported as a dotted orange line in the upper panel. In the inset, we report three critical structures, namely the FC geometry, an intermediate geometry (the connection between the relaxed scan and the LIIC), and the $CI_{BH}^{S_0/S_1}$ geometry. In the latter structure the H atoms in not visible since it already moved far from the $NH_3{-}BH_2$ molecule.

6.3.1.4 Pathway (c): H_2 dissociation from the BH_3 moiety

The release of H_2 can occur via the simultaneous dissociation of two H atoms from the BH_3 moiety. To investigate this process, we perform a LIIC between the FC point optimized with MP2, the S_1min optimized with ADC(2), and the MECI for the H_2 release ($CI_{H_2}^{S_0/S_1}$) optimized with XMS(5)-CASPT2(4/8). The electronic energies calculated with MP2/ADC(2) and XMS(5)-CASPT2(4/8) along the LIIC are shown in Fig. 6.8.

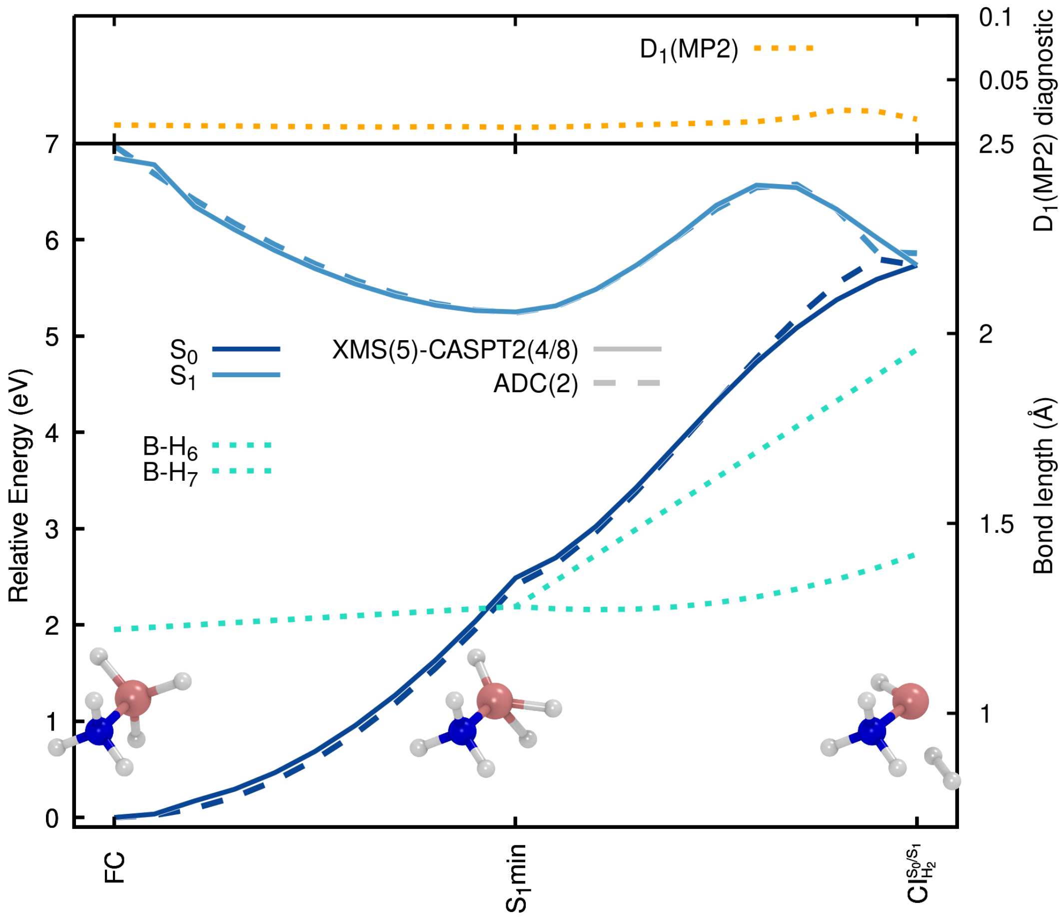

Figure 6.8: LIIC between the FC, S_1min and $CI_{H_2}^{S_0/S_1}$. The two lowest electronic states are depicted in dark and light blue. ADC(2) and XMS(5)-CASPT2(4/8) electronic energies are reported in dashed and solid lines, respectively. The two relevant B−H bonds are shown in blue-green dotted lines. The D_1 diagnostic for the MP2 ground state is reported as a dotted orange line in the upper panel. In the inset, we report the three critical structures of the LIIC, namely the FC point, the S_1min, and the $CI_{H_2}^{S_0/S_1}$.

The first part of the LIIC – connecting the FC point with the S_1min – is characterized by a Jahn–Teller distortion of the molecule along which two out of the three B−H bonds elongate and distort. The elongation can be followed by the B−H_6 and B−H_7 bond lengths displayed as dotted blue-green lines in Fig. 6.8, while the distortion can be seen in the depicted S_1min structure. Through this first section of the LIIC, the S_1 electronic state is stabilized by $\sim$ 1.7 eV.

The second part of the LIIC – connecting the S_1min to the $CI_{H_2}^{S_0/S_1}$ – shows the concerted photodissociation of the two B−H bonds and the release of H_2, forming NH_3−BH. The $CI_{H_2}^{S_0/S_1}$ geometry indicates that the H−H bond is already formed when the S_0/S_1 electronic states cross. While one of the B−H distances is still lower than 1.5 Åat the $CI_{H_2}^{S_0/S_1}$ geometry, the interaction between the boron atom and the H_2 molecule is presumably weak enough to allow the departure of the hydrogen molecule after return to S_0. In other words, it is unlikely that the two B−H bonds would reform when the molecule is in the ground state. Upon inspection of the S_1 energy along the LIIC, we can expect that this process is accessible since the observed energy barrier along the LIIC is lower than the S_1 energy at the FC point.

Comparing the ADC(2) and XMS-CASPT2 electronic energies along this LIIC reveals an excellent agreement between the two methods. This accuracy is also retained close to the CI region where the D_1 diagnostic remains surprisingly low, probably due to the very weak coupling between the ground and the first excited state. We can conclude that ADC(2) should be able to describe adequately the excited-state dynamics leading to the H_2 release via the concerted breaking of two B−H bonds but also to perform well in the direct proximity of the S_1/S_0 intersection region.

6.3.1.5 Pathway (d): H dissociation from the NH_3 moiety

The last photodissociation channel to investigate is the direct N−H bond breaking. To evaluate the likelihood of direct N−H photodissociation, we performed a relaxed scan for the S_1 excited electronic state (with ADC(2)) along the N−H bond of $H_3N{-}BH_3$. The N−H bond length at the S_1min geometry (optimized with ADC(2), see Fig. 6.8), is indicated by the grey vertical dashed line in Fig. 6.9. The electronic energies obtained with ADC(2) and XMS-CASPT2 are in close agreement throughout the entire relaxed scan. The D_1 diagnostic remains safely below the recommended value, indicating that the ground state can be described by a (single) closed-shell configuration. Once again, ADC(2) appears to accurately reproduce the electronic energies for this photodissociation channel, even near the S_1/S_0 intersection region leading to a nonradiative relaxation via N−H elongation.

Given the energy gained from the relaxation to the S_1min from the FC point (see Fig. 6.8), it appears plausible that the CI region can easily be reached by ammonia borane upon photoexcitation.

6.3.1.6 Photoabsorption cross-section and nonadiabatic dynamics

Since all the photodissociation channels described in the previous sections could be accessible upon photoexcitation of ammonia borane, the likelihood of reaching a given S_1/S_0 region is dictated by the initial excitation wavelength and coupled electron-nuclear dynamics between the excited electronic states. Considering the good agreement observed between ADC(2) and XMS-CASPT2 for the different photodissociation pathways (and keeping in mind its potential limitations), we decided to employ the ADC(2)/aug-cc-pVDZ combination to calculate the photoabsorption cross-section of $H_3N{-}BH_3$ and explore its nonadiabatic molecular dynamics with TSH.

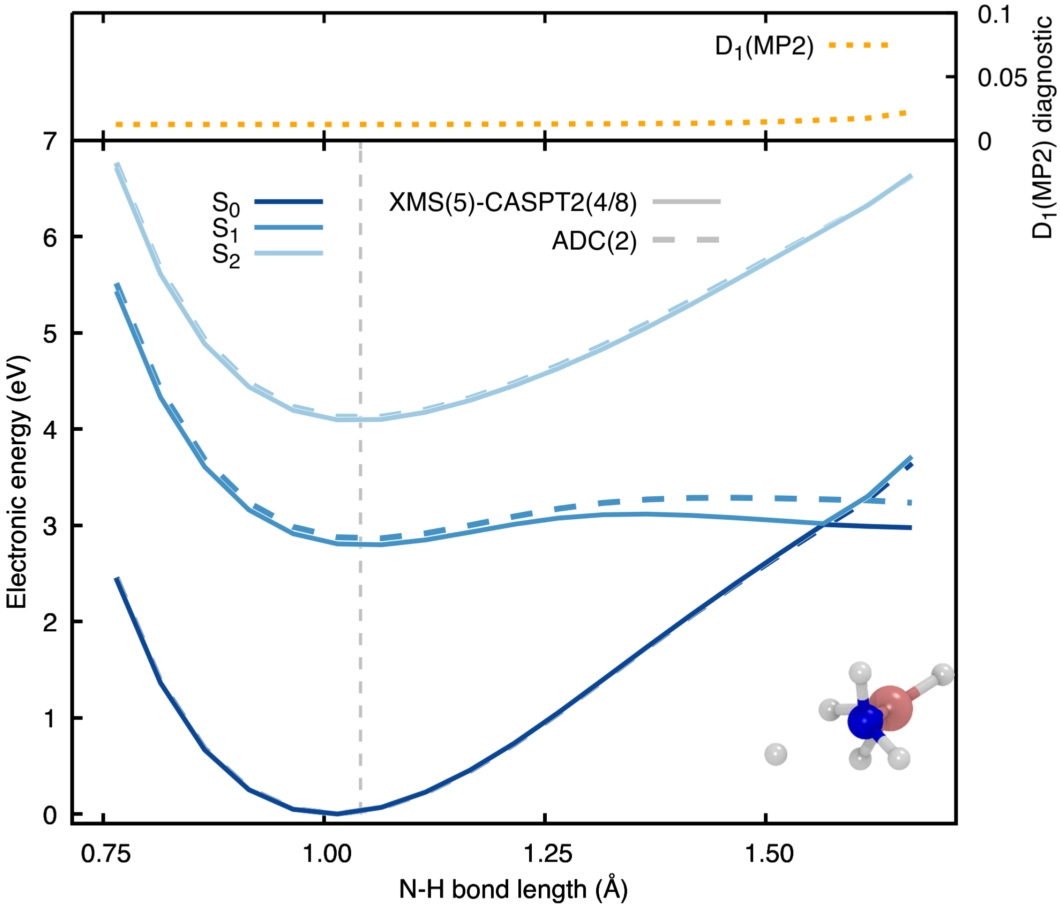

Figure 6.9: Relaxed scan along the N−H bond of H_3N-BH_3 for the the S_1 excited electronic state obtained with ADC(2). The N−H bond length at the S_1min geometry is indicated by the grey vertical dashed line. The three lowest excited states are depicted from dark (S_0) to light (S_2) blue, while the ADC(2) and XMS(5)-CASPT2(4/8) energies are reported in dashed and solid lines, respectively. The D_1 diagnostic for the MP2 ground state is reported as a dotted orange line in the upper panel. In the inset, we report the last structure of the relaxed scan.

The photoabsorption cross-section of H_3N-BH_3 is shown in the upper panel in Fig. 6.10 with a black solid line and is further decomposed into its different electronic-state contributions in the lower panel. The first electronic transition ($S_0 \rightarrow S_1$) spans the 6 to 7 eV energy range and, together with a small contribution from $S_0 \rightarrow S_2$ excitation, is the main transition present in the first selected energy window (shaded green area). The second and third energy windows (light-green and yellow areas) are more congested and contain electronic excitations to different electronic states. The intensity of the photoabsorption cross-section absorption grows across the three windows, with $S_0 \rightarrow S_6$ excitation and $S_0 \rightarrow S_9$ excitations being particularly intense.

Armed with the photoabsorption cross-section, we can proceed with the nonadiabatic dynamics by initiating a swarm of TSH trajectories in each of the three energy windows (green, light green, and yellow areas in Fig. 6.10). Around 50 TSH trajectories were launched in each

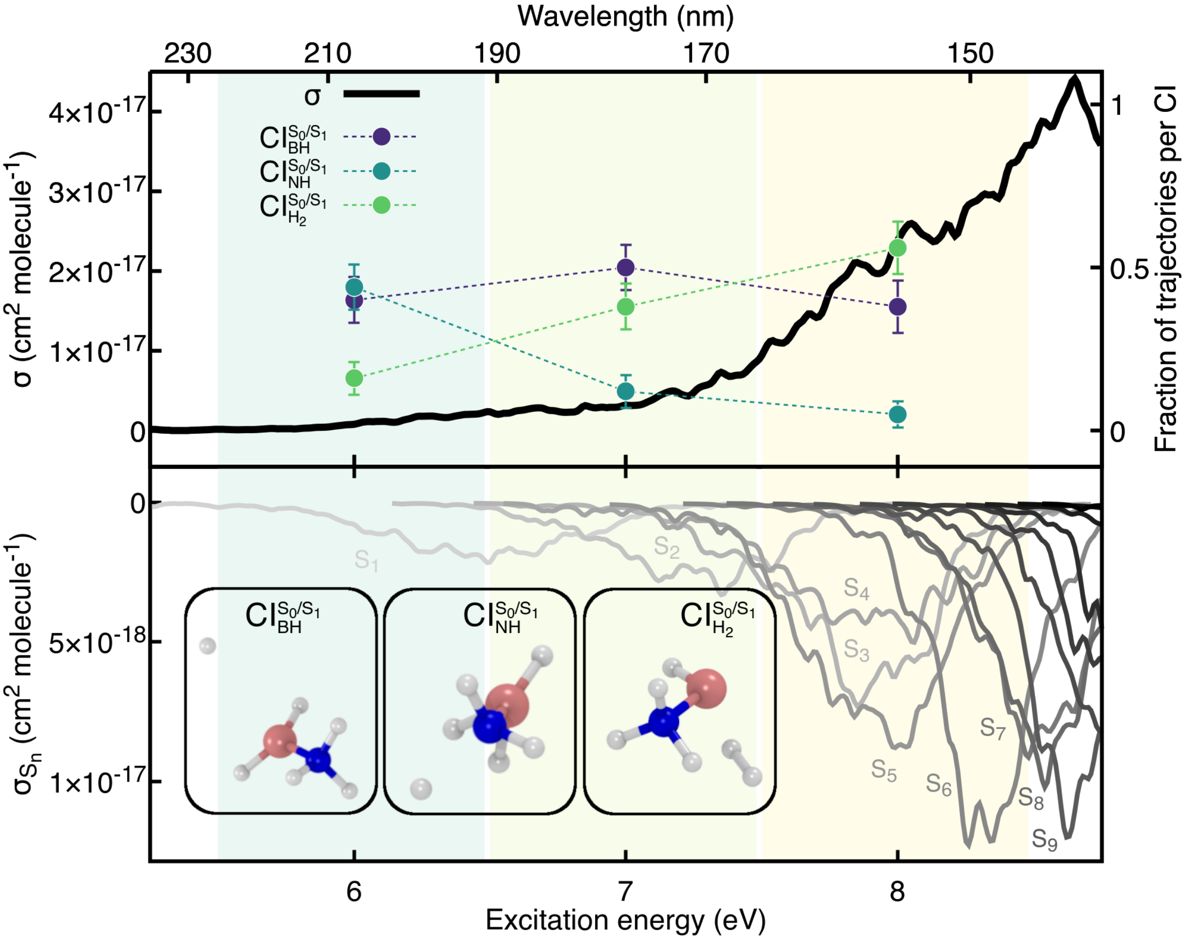

Figure 6.10: Photoabsorption cross-section and CI quantum yields for $H_3N{-}BH_3$. Upper panel: full photoabsorption cross-section (black solid line). The spectral range is partitioned into three energy windows shown as green, light green, and yellow areas. The fraction of trajectories undergoing B−H dissociation ($CI_{BH}^{S_0/S_1}$ purple), N−H dissociation ($CI_{NH}^{S_0/S_1}$ blue-green) and H_2 release from the cleavage of two B−H bonds ($CI_{H_2}^{S_0/S_1}$ light green) is determined for each energy window and reported with filled circles. Lower panel: individual excited-state contributions to the full photoabsorption cross-section depicted with solid lines from light grey ($S_0 \rightarrow S_1$) to black ($S_0 \rightarrow S_{15}$). Exemplary molecular structures for the three photodissociation pathways are shown as inset.

energy window (see Tab. 6.1 for the exact values). The fraction of trajectories reaching a particular CI can be associated with a specific photodissociation pathway (upper panel of Fig. 6.10). Three of the four expected channels discussed above were observed in the TSH dynamics: the B−H dissociation ($\mathrm{CI}_{\mathrm{BH}}^{\mathrm{S_0/S_1}}$), N−H dissociation ($\mathrm{CI}_{\mathrm{NH}}^{\mathrm{S_0/S_1}}$), and the H_2 release from the concerted cleavage of two B−H bonds ($\mathrm{CI}_{\mathrm{H_2}}^{\mathrm{S_0/S_1}}$). Comparing the fraction of trajectories reaching each of these three CIs shows that the B−H dissociation pathway appears to be largely independent of the excitation energy. In contrast, the concerted cleavage of two B−H bonds becomes more favourable at higher excitation energies, at the expense of the N−H elongation nonradiative relaxation. No direct B−N bond photodissociation in the excited electronic states was observed in the TSH dynamics.

Since ADC(2) shows an adequate behaviour in the N−H elongation close to the CIs region, we restarted five trajectories that reached the $\mathrm{CI}_{\mathrm{NH}}^{\mathrm{S_0/S_1}}$ in S_0 and carried on 500 fs of adiabatic dynamics at the MP2/aug-cc-pVDZ level of theory. We observed a fast reformation of the N−H bond on S_0 for all five trajectories, followed by an unexpected B−N dissociation in S_0 due to the vibrationally hot $H_3N{-}BH_3$ adduct. This B−N dissociation should not be confused with the photodissociation described in Sec. 6.3.1.2 – or the one reported by Matsuo and coworkers – where the B−N bond breaking takes place in an excited electronic state and leads to the formation of an electronically excited Lewis acid or base.

Despite the surprisingly rich photochemistry of $H_3N{-}BH_3$, the photodissociation of the adducts still remains elusive. Given the nature of the low-lying electronic states in $H_3N{-}BH_3$, it appears clear that substitution is required on the NH_3 of BH_3 moiety. In the following, we propose to replace NH_3 with Py – an aromatic and relatively weak Lewis base.

6.3.2 Photochemistry of pyridine borane

Due to the similarity between the Lewis adducts we will leverage the excellent result of ADC(2) to investigate using the same methodology the photochemistry and photophysics of $Py{-}BH_3$.

Pyridine borane, $Py{-}BH_3$, represents our first step to develop our simple model of the photochemistry of $H_3N{-}BH_3$ towards understanding the photodissociation of the B−N bond in Lewis adducts. The goal of our 'design' is to (i) lower the energy of the electronic transitions such that they can be accessible experimentally and (ii) reproduce the excited photodissociation observed for the trinaphthyl-borane−Py molecule.[7] From a theoretical perspective, MP2 and ADC(2) will be used given their good performance for ammonia borane and the increase in computational cost resulting from the substitution of NH_3 by pyridine.

The B−N bond length of $Py{-}BH_3$ is slightly shorter than that of $H_3N{-}BH_3$ at the optimized ground-state geometry (obtained with MP2/aug-cc-pVDZ, see Tab. 6.3). This slight shortening of the B−N bond, connected to the sp^2 hybridization of the nitrogen in Py, confirms that the interaction between the Lewis acid and base remains substantial (this finding is further confirmed by the gas-phase binding energies reported by Potter et al.[377])

Table 6.3: B-N bond length (Å) calculated at the optimized S_0 geometry obtained with MP2/aug-cc-pVDZ for NH_3-BH_3, $Py-BH_3$, and $Py-B(OH)_3$ Lewis adducts.

	NH_3-BH_3	$Py-BH_3$	$Py-B(OH)_3$
B-N	1.66	1.64	1.73

6.3.2.1 Photodissociation of the B−N bond in pyridine borane

As done for H_3N-BH_3, we performed a relaxed scan along the B−N bond length with MP2 and used these structures to calculate electronic energies with ADC(2) (Fig. 6.11). Focusing our attention on the FC point, we notice that the first excited state – located at 5 eV above S_0 – can be described by two pairs of NTOs with the following character: $\pi \rightarrow \pi^*$ (upper NTO pair in Fig. 6.11) with a smaller contribution of the type $\pi' + \sigma_{BH} \rightarrow \pi'^*$ (lower NTO pair in Fig. 6.11). The σ_{BH} contribution to the S_1 state is similar to the contribution observed from the particle orbital of the first excited states of H_3N-BH_3. However, the first excited state of $Py-BH_3$ is 2 eV lower than the first excited state of H_3N-BH_3 thanks to the π system of Py, meaning that no contribution from Rydberg-like orbitals is observed in the low-lying states of $Py-BH_3$.

Looking at the NTOs describing the fifth excited state of $Py-BH_3$, we notice that the hole orbital exhibits a clear signature of the pyridine lone pair (n_N, see inset of Fig. 6.11). Following the $n_N \rightarrow \pi^*$ character along the relaxed scan, we observe a stabilization of this state character until it becomes the dominant character of S_1 for B−N distances longer than 2.6 Å. Therefore, if $Py-BH_3$ can access this dissociative state – via photoexcitation or during the subsequent nonadiabatic excited-state dynamics – and follow it diabatically to S_1, the photoexcited adduct is likely to show a B−N bond cleavage.

6.3.2.2 Photoabsorption cross-section and nonadiabatic dynamics

Due to the reduced presence of Rydberg states in the low-lying excited states, we used the smaller basis set cc-pVDZ in place of aug-cc-pVDZ. Vertical transition energies obtained with ADC(2)/cc-pVDZ are in good agreement with those calculated with ADC(2)/aug-cc-pVDZ (see Tab. 6.4).

Table 6.4: Excitation energies (eV) and oscillator strengths (a.u.) of $Py-BH_3$ computed at the FC point optimized at MP2/aug-cc-pVDZ. The excited states are labelled following the C_s point group.

	S_1 (A”)	S_2 (A”)	S_3 (A’)	S_4 (A”)	S_5 (A’)	S_6 (A”)
ADC(2)						
cc-pVDZ	5.16	5.82	6.34	6.71	6.75	6.96
	(0.026)	(0.150)	(0.003)	(0.198)	(0.003)	(0.108)
aug-cc-pVDZ	5.07	5.62	6.15	6.44	6.58	6.76
	(0.031)	(0.146)	(0.003)	(0.202)	(0.004)	(0.133)

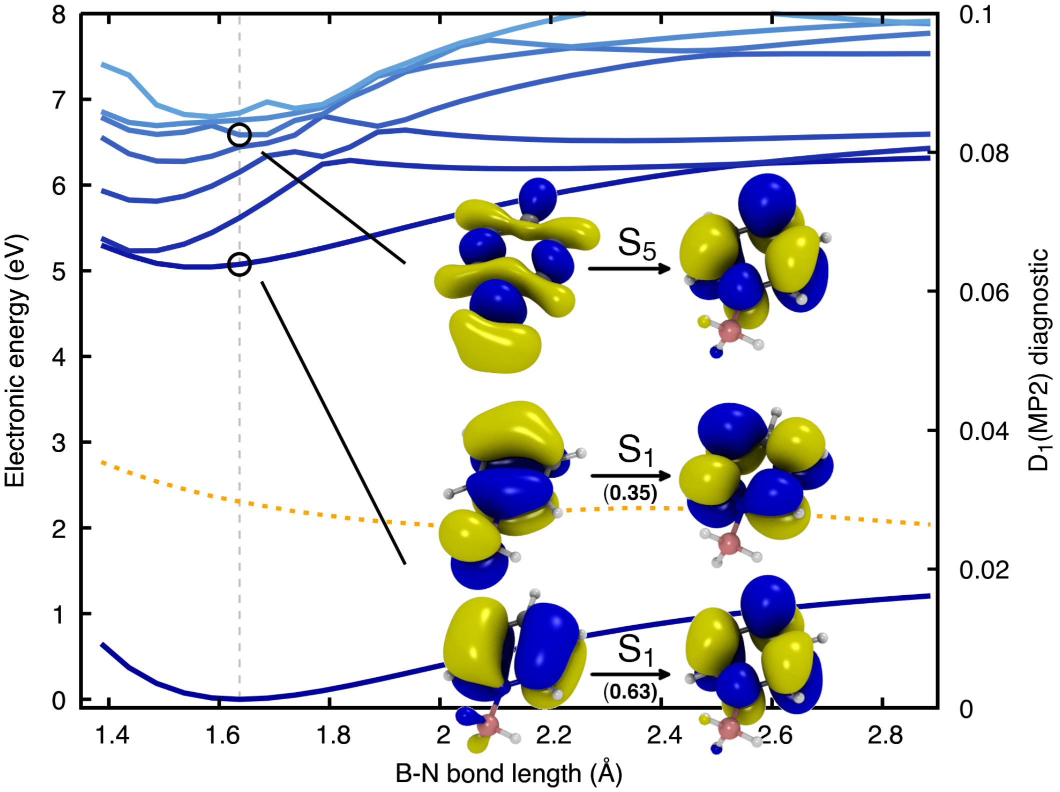

Figure 6.11: Relaxed scan along the B−N bond length of Py−BH$_3$ obtained for the ground electronic state with MP2. Excited electronic energies were obtained with ADC(2). The FC point is indicated by the grey vertical dashed line. The lowest eight electronic states are calculated along the scan and depicted by lines in shades of blue – from S$_0$ in dark blue to S$_7$ in light blue. The D$_1$ diagnostic for the MP2 ground state is reported as a dotted orange line. NTOs for the S$_1$ (A") (two pairs of NTOs are required to describe the first excited state) and S$_5$ (A') electronic state at the FC point are given as insets.

To further confirm the validity of removing the diffuse functions in the basis set used, we calculated the photoabsorption cross-section using ADC(2)/cc-pVDZ and ADC(2)/aug-cc-pVDZ (solid and dashed black lines in the top panel of Fig. 6.12). Once again, the two cross-sections show a good overlap, in particular for excitation energies lower than 6.5 eV. The ADC(2)/aug-cc-pVDZ is only slightly red-shifted with respect to the ADC(2)/cc-pVDZ spectra. The first energy window (green area in Fig. 6.12) contains only a small contribution from the first excited state, with energies that extend up to 4 eV. The second and third windows (light-green and yellow areas in Fig. 6.12, respectively) cover more electronic transitions – the second window in particular contains transitions towards S$_1$, S$_2$ and S$_3$.

The nonadiabatic dynamics simulation of Py−BH$_3$ reveals two dominant nonradiative pathways. The first one involves the cleavage of a B−H bond, consistent with the character of the electronic state discussed in Sec. 6.3.2.1 and in line with the $\mathrm{CI}_{\mathrm{BH}}^{\mathrm{S_0/S_1}}$ observed for H$_3$N−BH$_3$. The second nonradiative pathway, characterized by the $\mathrm{CI}_{\mathrm{puckering}}^{\mathrm{S_0/S_1}}$ in Fig. 6.12, corresponds to

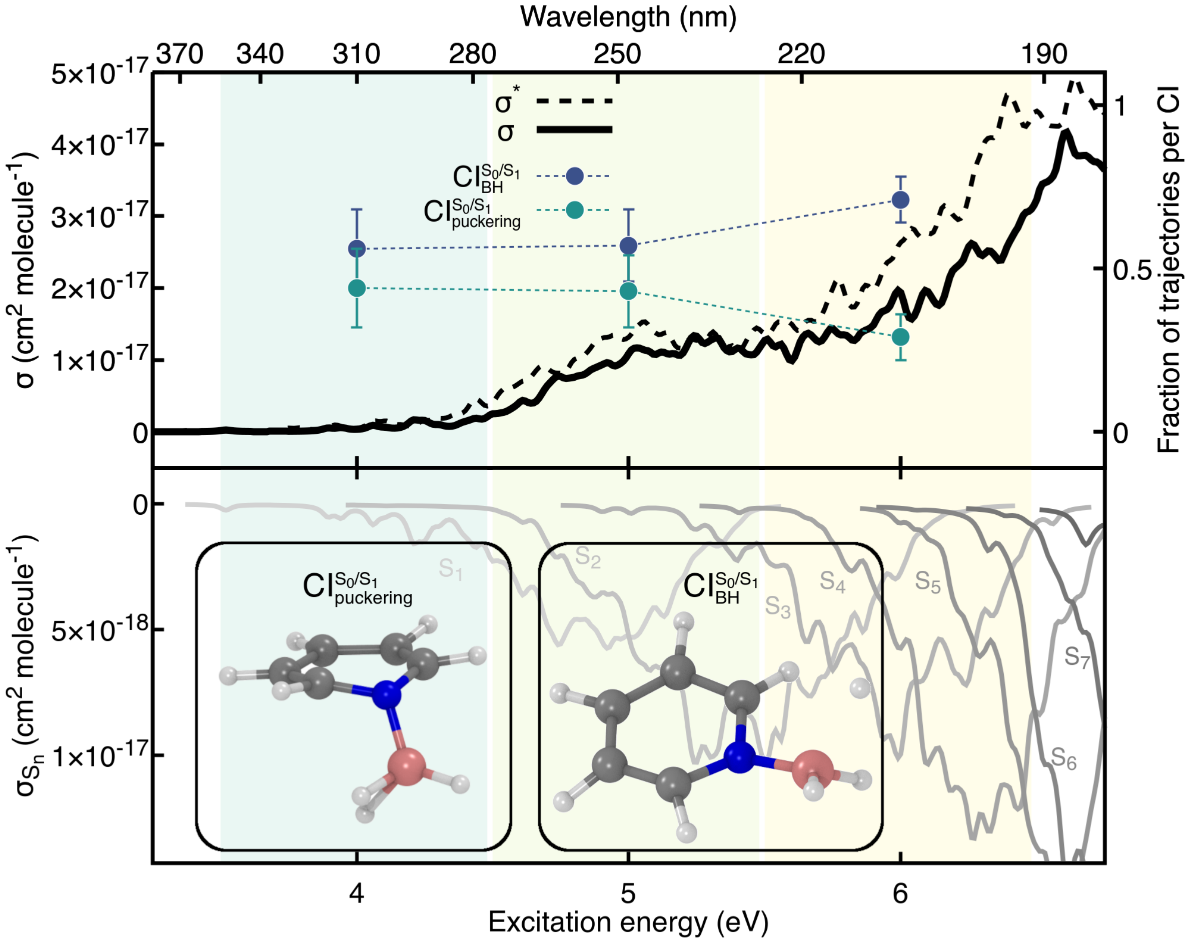

Figure 6.12: Photoabsorption cross-section and CI quantum yields for Py−BH$_3$. Upper panel: full photoabsorption cross-section obtained with ADC(2)/cc-pVDZ (solid black line) and ADC(2)/aug-cc-pVDZ (dashed black line). The spectral range is partitioned into three energy windows shown as green, light green, and yellow areas. The fraction of trajectories undergoing B−H dissociation ($CI_{BH}^{S_0/S_1}$, purple) or ring puckering dissociation ($CI_{puckering}^{S_0/S_1}$, blue-green) is determined for each energy window and reported with filled circles. Lower panel: individual excited-state contributions to the full photoabsorption cross-section depicted with solid lines from light grey ($S_0 \rightarrow S_1$) to dark grey ($S_0 \rightarrow S_8$). Exemplary molecular structures for the three photodissociation pathways are shown as inset.

the puckering of the pyridine ring. Interestingly, the puckering motion either involves the nitrogen atom (shown in the inset of Fig. 6.12) provoking an out-of-plane motion of the BH_3 moiety, or the distortions of one or more carbon atoms of the ring. This nonradiative process closely resembles the usual relaxation mechanism of Py, discussed in detail in the literature.[378, 379] The concerted dissociation of two B−H bonds is not observed in the excited-state dynamics conducted for $Py-BH_3$. We cannot rule out the release of H_2 upon relaxation of $Py-BH_3$ to the ground state or following photoexcitation at higher energies.

Analysis of the wavelength dependence of the two deactivation channels reveals that the fraction of trajectories suffering B−H dissociation or puckering is about the same for the first and second energy windows. However, the fraction of trajectories reaching the $\mathrm{CI}_{\mathrm{BH}}^{\mathrm{S}_0/\mathrm{S}_1}$ increases substantially at higher excitation energies at the expense of the puckering relaxation process.

The substitution of NH_3 with Py has dramatically changed the electronic structure and the underlying photochemistry of the B−N Lewis adducts. However, yet again a B−N photodissociation pathway remains elusive for this molecule at the excitation wavelength probed. We further altered our model of a B−N Lewis adduct by tuning its B−N bond strength. By weakening the strength of the B−N bond, one would expect the excited state with a n_N character to decrease in energy. To achieve this goal, we decided to use a weaker Lewis acid, namely boric acid $B(OH)_3$.

6.3.3 Photochemistry of pyridine-boric acid

The last B−N model studied here is pyridine–boric acid, $Py-B(OH)_3$. $Py-B(OH)_3$ possesses a longer B−N bond at the FC point than that of H_3N-BH_3 and $Py-BH_3$ (see Tab. 6.3), in line with the expected weaker B−N bond for this molecule. To explore whether the weaker nature of the B−N bond in the ground electronic state has implications for the excited electronic properties of the molecule, we performed the same series of calculations as done for the other B−N adducts, starting by monitoring the electronic energies along a B−N relaxed scan.

6.3.3.1 Photodissociation of the B−N bond in pyridine-boric acid

The relaxed scan obtained at the MP2 level of theory along the B−N bond of $Py-B(OH)_3$ is shown in Fig. 6.13. Following the S_0 electronic energy along the B−N relax scan highlights the weak nature of the B−N bond. The S_0 electronic energy curve shows a very shallow minimum in comparison to H_3N-BH_3 and $Py-BH_3$. Focusing now on the excited electronic states at the FC point, we identify that the S_2 electronic state exhibits a $\mathrm{n}_N \rightarrow \pi^*$ state (see NTOs, inset of Fig. 6.13). This observation is in line with a weaker B−N bond and an expected lowering of an electronic state with a $\mathrm{n}_N \rightarrow \pi^*$ character. The character of S_2 is similar to the $\mathrm{n}_N \rightarrow \pi^*$ states of $Py-BH_3$, with an additional contribution coming from the lone pairs of the oxygen atoms on the boric acid moiety and a weaker contribution from the σ C−C and C−H bonds of the pyridine ring.

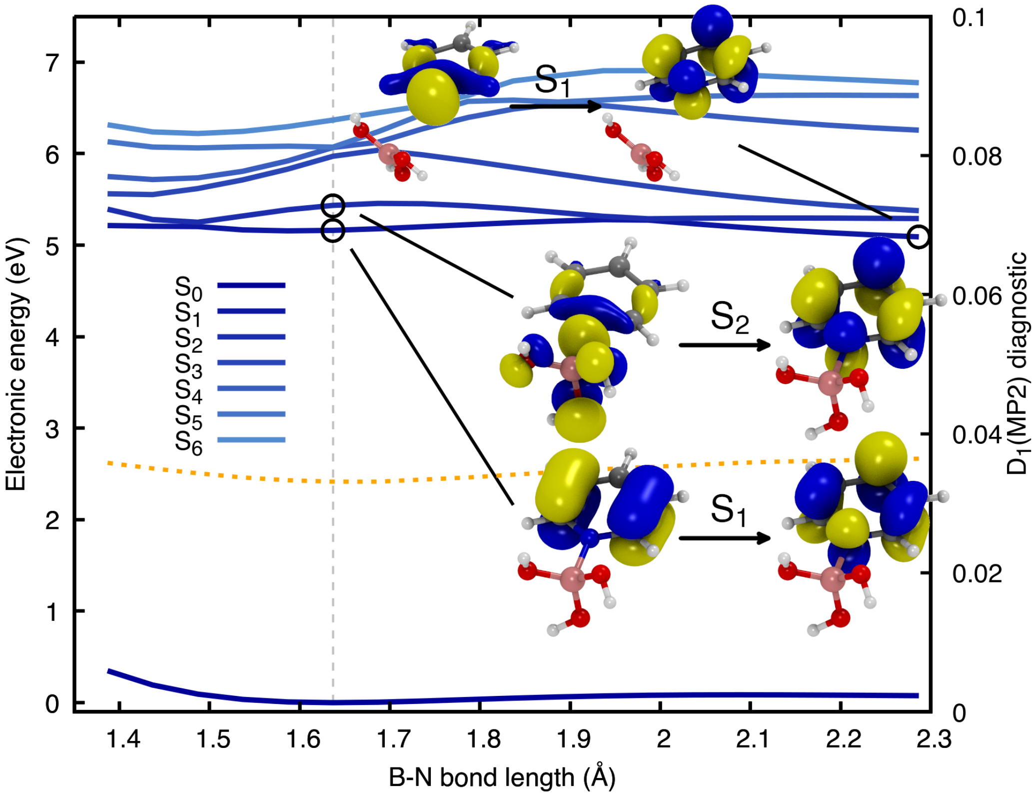

Figure 6.13: Relaxed scan along the B−N bond length of Py−B(OH)$_3$ obtained for the ground electronic state with MP2. Excited electronic energies were obtained with ADC(2). The FC point is indicated by the grey vertical dashed line. The lowest eight electronic states are calculated along the scan and depicted by lines in shades of blue – from S$_0$ in dark blue to S$_7$ in light blue. The D$_1$ diagnostic for the MP2 ground state is reported as a dotted orange line. NTOs for the S$_1$ and S$_2$ excitations at the FC point are given as insets.

Following the n$_N$ → π^* character along the B−N relaxed scan confirms its stabilization upon a B−N bond elongation, in line with our earlier observation for Py−BH$_3$. In contrast with Py−BH$_3$, the diabatic crossing between the n$_N$ → π^* and the $\pi \rightarrow \pi^*$ states occurs fairly close to the FC point (∼1.9 Å). This observation may imply that the n$_N$ → π^* state can be populated more easily in Py−B(OH)$_3$ than in Py−BH$_3$ during the nonadiabatic dynamics.

6.3.3.2 Photoabsorption cross-section and nonadiabatic dynamics

We calculated the photoabsorption cross-section of Py−B(OH)$_3$ and split it into two energy windows for the subsequent TSH nonadiabatic dynamics simulations (Fig. 6.14). The first window aims to include the photochemistry of the molecules excited in the S$_1$ electronic state, with only minor contributions from excitation to the second excited electronic state S$_2$. The higher excitation window is instead more complex as it incorporates multiple contributions from broad transitions (see lower panel of Fig. 6.14). These broad electronic transitions are

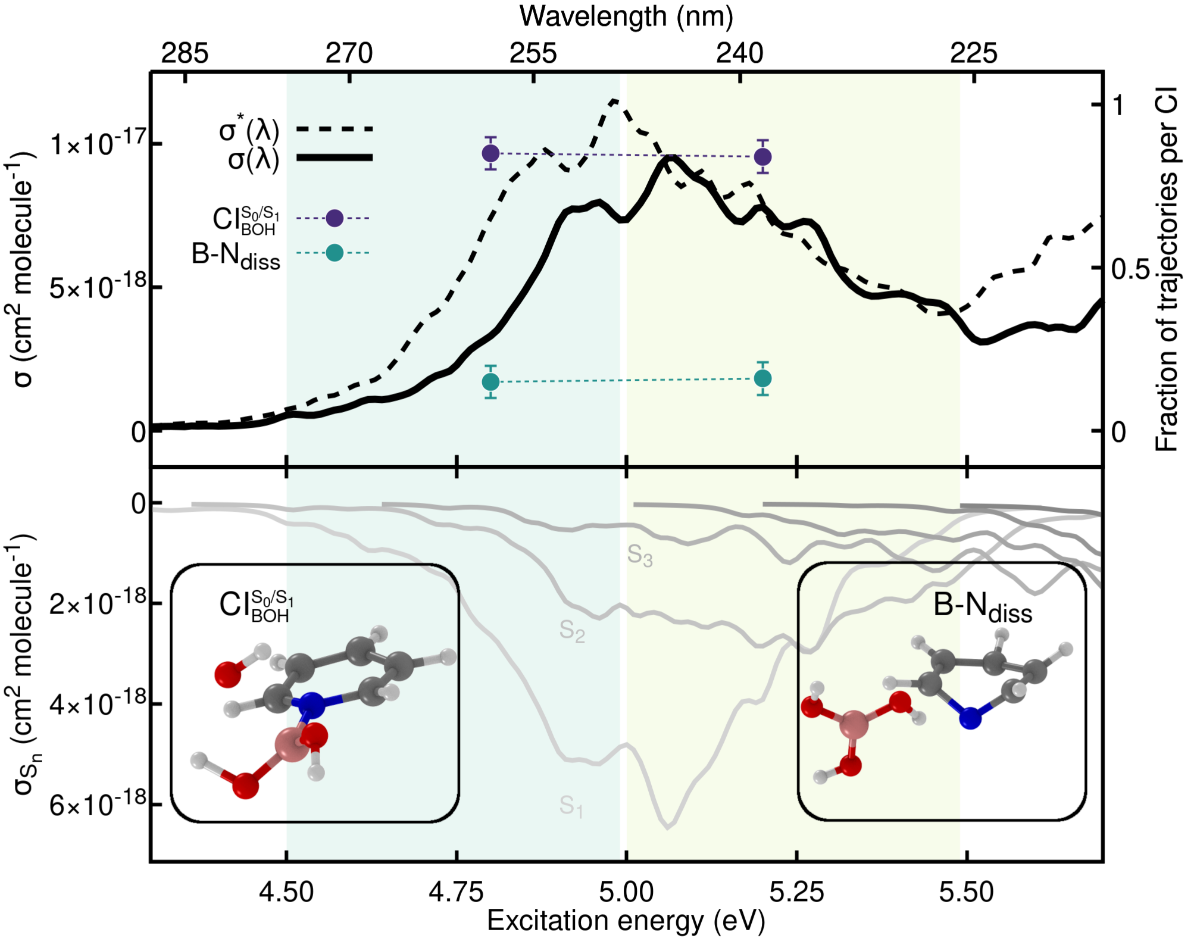

Figure 6.14: Photoabsorption cross-section and CI quantum yields for Py−B(OH)$_3$. Upper panel: full photoabsorption cross-section obtained with ADC(2)/cc-pVDZ (solid black line) and ADC(2)/aug-cc-pVDZ (dashed black line). The spectral range is partitioned into two energy windows shown as green and light green areas. The fraction of trajectories showing a B-OH dissociation ($CI_{BOH}^{S_0/S_1}$, purple) or a B−N dissociation (B−N$_{diss}$ green) is determined for each energy window and reported with filled circles. Lower panel: individual excited-state contributions to the full photoabsorption cross-section depicted with solid lines from light grey ($S_0 \rightarrow S_1$) to dark grey ($S_0 \rightarrow S_8$). Exemplary molecular structures for the two photodissociation pathways are shown as inset.

linked to the weak B−N bond and, consequently, to the spread of the B−N distance in the sampled geometries used to calculate the photoabsorption cross-section (see Fig. 6.15).

For both energy windows, the TSH simulations reveal a nonradiative pathway involving a B−OH cleavage (purple circles in Fig. 6.14) – analogous to the B−H dissociation observed in the nonadiabatic dynamics of Py−BH$_3$. In addition, photoexcitation of Py−B(OH)$_3$ resulted in B−N photodissociation (green circles in Fig. 6.14). The B−N dissociation occurs in a few tens of femtoseconds and the BH$_3$ is released in its ground electronic state while the Py remains photoexcited – in line with the results obtained in the relaxed scan presented above (Fig. 6.13).

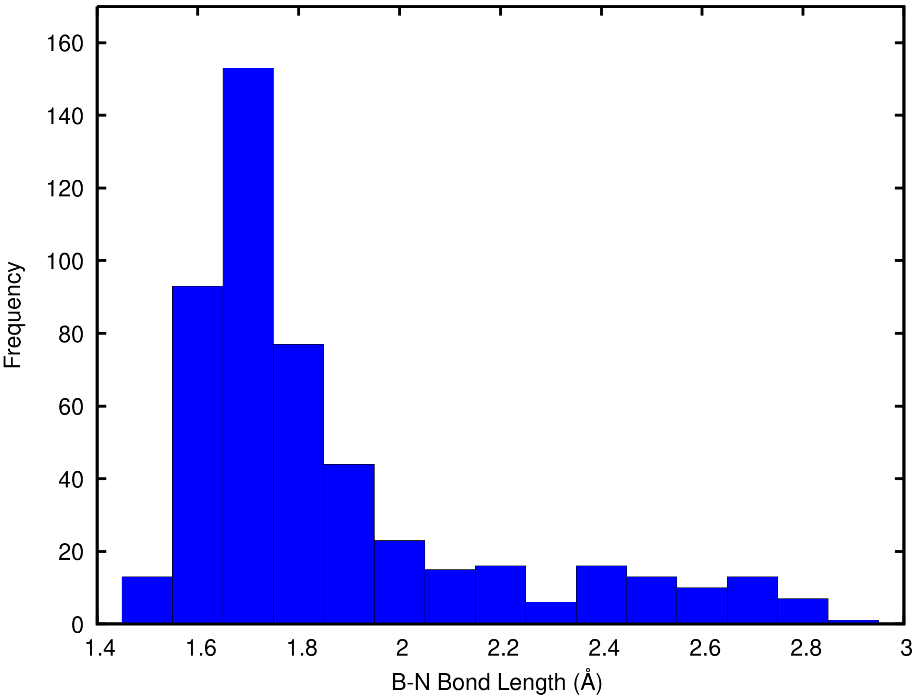

Figure 6.15: Distribution of the B−N bond lengths for the 500 geometries used to calculate the photoabsorption cross-section and initiate the excited-state dynamics of Py−B(OH)$_3$.

The subsequent excited-state dynamics observed for pyridine is in line with earlier studies, where the molecule relaxes towards the ground state by a puckering motion. The puckering of pyridine occurring following a Py−B(OH)$_3$ photodissociation should not be mistaken with the puckering mechanism observed in the excited-state dynamics of Py−BH$_3$, where the B−N bond was still intact (see Fig. 6.12).

The presence of the puckering motion of the pyridine after the B−N photodissociation would suppress any sizable fluorescence signal. The trinaphthyl-borane studied by Matsuo and coworkers (and formed upon dissociation of pyridine) presumably does not possess an accessible S$_0$/S$_1$ CI, meaning that the upon B−N photodissociation the molecule remains in the excited electronic state for long enough to exhibit fluorescence. An important difference between Py−B(OH)$_3$ and trinaphthyl-borane−Py is the presence of an efficient nonradiative decay in the former with the B−OH bond-breaking channel (or the B−H photodissociation in H$_3$N−BH$_3$ and Py−BH$_3$). The photodissociation of the B−OH bond is competitive with the B−N one, even though the B−N bond is extremely weak in Py−B(OH)$_3$. When these additional photodissociative channels are suppressed, like in trinaphthyl-borane, one may expect the B−N photodissociation to occur even for stronger B−N bonds. Our simulations clearly confirm that the stronger the B−N bond the less probable the photodissociation of the Lewis adduct, consistent with the conclusions drawn by Matsuo and coworkers.

6.4 Conclusions

Lewis adducts are an extremely fascinating class of molecules and the synthesis of Lewis adducts that can selectively photodissociate on the excited state and may re-associate upon relaxation to the ground state represents an exciting opportunity to introduce a photoreversible 'click chemistry' where the dative bond can be broken by light and reformed selectively. Excited by such prospectives, in this chapter, we have investigated the photochemistry of three models of Lewis adducts, namely H_3N-BH_3, $Py-BH_3$, $Py-B(OH)_3$.

Using the theoretical protocol developed in chapter 3 we compute the absorption cross-sections and the CI wavelength-dependent quantum yields that lead to the different photodissociation pathways for the three Lewis adducts. In doing so, we first investigate the photochemistry of H_3N-BH_3 which shows some similarities with the VUV photochemistry of ethane. In particular, we observed the B−H bond cleavage and the concerted bond breaking of two B−H bonds as excited-state dissociative pathways, flanked by nonradiative decay through N−H bond extension. A similar B−H bond cleavage on the excited state has also been observed for $Py-BH_3$ together with the puckering distortions that characterize the photochemistry of Py. However, the excited-state dynamics simulations for H_3N-BH_3 and $Py-BH_3$ do not predict the photodissociation of the B−N bond — a process that we observed in the photodynamics of Py–B(OH)3. $Py-B(OH)_3$ presents a very weak B−N bond and its photodissociation competes with the B−OH cleavage, in analogy with the B−H bond breaking mechanism of H_3N-BH_3 and $Py-BH_3$.

We conclude by giving a novel set of qualitative rules to design photodissociable Lewis adducts. The photodissociation of the B−N bond arises from a fine-tuning of the B−N bond strength, which in turn is defined by the acidity and basicity of the pair used to form the adducts. A weaker B−N interaction favors the photodissociation while a stronger Lewis pair can photodissociate only if other nonradiative processes are suppressed. An easy way to suppress nonradiative processes (such as B−H or B−OH photodissociation) is to constrain the boron atom within a molecular framework to enhance its stability. However, a more thoughtful case-by-case study must be performed for molecular systems exhibiting nonradiative decays involving for example puckering motions, typical of small aromatic cyclic compounds. In such cases, the photodissociation behaviour can be easily tweaked by removing or increasing the electron density on the nitrogen (*i.e.*, decreasing or increasing its Lewis basicity) or on the boron (*i.e.*, increasing or decreasing its Lewis acidity).[111, 347, 348] These two ingredients allow for the development and synthesis of photodissociable Lewis adducts that can selectively dissociate on the excited state and reform the dative bond on the ground state.

CHAPTER 7

Conclusions and Outlook

7.1 Conclusions

The fields of theoretical and computational chemistry have proven to be valuable in understanding the reactivity of molecules. They have helped scientists to explain unresolved issues in diverse areas of chemistry, predict the properties and behaviour of new molecules, and explore new research avenues in fields such as biology, materials science, and environmental chemistry. These methods are particularly useful when combined with experimental data, allowing researchers to gain a more in-depth understanding of the fundamental principles that govern molecular reactivity.

Despite the significant progress made in theoretical chemistry, there are still areas where its applications are in their infancy, such as in atmospheric chemistry. To develop predictive models, able to forecast the time evolution of chemicals in atmospheric chemicals, it is crucial to understand the rates of both ground-state and photochemical reactions that take place in the atmosphere. Of particular importance in this regard are the VOCs, which are emitted from both natural and anthropogenic sources. Because some VOCs are transient and challenging to study experimentally, their photochemical reactions are often not included in atmospheric models, leading to discrepancies between predicted and observed atmospheric chemical behaviour.

This thesis presents a detailed protocol for the *in silico* calculation of the photolysis rate constant of VOCs. This protocol is particularly useful for studying transient VOCs, which are challenging to study experimentally and whose reactivity is often deduced based on SARs. To calculate the photolysis rate constant of VOCs using computational methods, two quantities are needed: the photoabsorption cross-section and the wavelength-dependent photolysis quantum yield. On the one hand, the photoabsorption cross-section can be calculated using various methods, but for VOCs, the NEA combined with quantum thermostat sampling has been found to be the most effective. The NEA method accurately determines the positions, heights, and widths of absorption bands, which are sufficient to calculate the photolysis quantum yield. While Wigner sampling can also be used as a substitute for the quantum thermostat, it carries the risk of providing a ground-state distribution that leads to a poor-quality absorption cross-section. On the other hand, the wavelength-dependent photolysis quantum yield can be determined using nonadiabatic dynamics simulation such as trajectory surface hopping.

Because VOCs have a complex electronic structure, it is important to carefully choose the appropriate electronic structure methods for the simulation. Nonadiabatic dynamics simulation often requires the use of expensive multiconfigurational methods to properly describe a region of the configuration space where the ground state becomes dominated by more than one configuration, such as during homolytic bond breaking. However, for transient VOCs with a multichromophoric nature and relatively long excited-state dynamics, such methods are not feasible. One potential alternative is a single-reference method called ADC(2), which has become increasingly popular in the nonadiabatic dynamics community. ADC(2) has been used successfully to study the photochemistry and photophysics of large organic molecules where multiconfigurational methodologies are too expensive, while still providing an accuracy that is superior to LR-TDDFT. Although the ADC(2) is a promising method, there are some previously undisclosed pitfalls to be aware of. Specifically, when studying carbonyl-containing compounds, the low-lying $n\pi^*$ state can present challenges. When the carbon-oxygen bond (C=O) is elongated, there are often artificial S_1/S_0 crossings that occur, predicting nonradiative decay channels in molecular dynamics that are unphysical. This finding is particularly important in the field of atmospheric chemistry, where carbonyl functional groups are common in many VOCs.

An atmospherically-relevant class of carbonyl-containing VOCs is the α-hydroperoxycarbonyls. Due to their transient nature, it is challenging to study these compounds experimentally, and there is currently no available experimental data for their photolysis rate constant. To overcome this, I used a protocol to calculate the photoabsorption cross-section and the wavelength-dependent quantum yields using two electronic structures, ADC(2) and XMS-CASPT(2). By utilizing the strengths of both methods, I were able to simulate the entirety of 2-hydroperoxypropanal photochemistry – a specific α-hydroperoxycarbonyl. The nonadiabatic simulations reveal the major photolytic channel is the release of O_2, as previously suggested in the literature. The study showed that direct OH photolysis could be a significant competitor, despite being previously regarded as a minor channel. This finding has important implications for atmospheric chemistry in determining the oxidation balance of the troposphere and further highlights the importance of including photochemical reactions in atmospheric models.

Finally, I leveraged the theoretical protocol developed for VOCs to investigate the photochemistry, and in particular the photodissociation of three Lewis adducts. The photodissociation has been observed experimentally for several Lewis adducts but a mechanistic investigation is still elusive in the literature. Firstly, we focus on the photochemistry of ammonia borane, the simplest Lewis adduct we took into consideration. The first part of our work is to investigate the photochemistry of this compound which has been surprisingly overlooked in literature from experimental and theoretical points of view. Inspired by the photodissociation of ethane, we reveal some peculiarities in the photolysis of $H_3N{-}BH_3$ – occurring via H and H_2 release – due to the intriguing electronic features introduced by the dative bond. Similar photodissociation pathways are also observed for the other two adducts, $Py{-}BH_3$ and $Py{-}B(OH)_3$. However, the study finds that the sought-after photodissociation only occurs in $Py{-}B(OH)_3$. We also provide a set of qualitative rules to design photodissociable Lewis adducts which mainly rely on the fine-tuning of the B−N bond strength. The study highlights the exciting opportunity to introduce photoreversible "click chemistry" by selectively breaking and reforming the dative bond of Lewis adducts using light.

7.2 Outlook

The fields of theoretical and computational chemistry have shown great potential in advancing our understanding of molecular reactivity, and have already proven valuable in various areas of chemistry. This thesis has provided the stepping stone for the studies of VOC *in silico*, by presenting difficult examples featuring multiple chromophoric groups with intricate electronic structures. The intricate nature of these molecules poses a challenge to automating the calculation of the wavelength-dependent quantum yield. As a result, each molecule requires individualized attention with customized solutions, hindering the process of automation. Nevertheless, my group is presently working on automating the calculation of the photoabsorption cross-section of VOCs. I am of the opinion that an automated and comprehensive tool for providing an initial estimation of the photolysis rate of VOCs, even if rudimentary, would prove to be exceedingly advantageous in the creation of atmospheric models.

My research on Lewis adducts is just the beginning of our attempt to comprehend the photochemistry, specifically the photodissociation, of these fascinating molecules. Despite their experimental synthesis and characterization is possible, there is limited theoretical work available to provide a framework for studying these complexes. The presence of a unique dative bond in the excited state offers an excellent opportunity for various areas of chemistry and biology. Hence, a more comprehensive analysis that considers more extensive complexes with specific functionalization to tune the properties of the adducts is essential. This investigation is already underway in my group, also in collaboration with experimentalists.

Bibliography

[1] Roland Lindh and Leticia González. *Quantum Chemistry and Dynamics of Excited States: Methods and Applications*. John Wiley & Sons, 2020.

[2] Antonio Prlj, Emanuele Marsili, Lewis Hutton, Daniel Hollas, Darya Shchepanovska, David R Glowacki, Petr Slavíček, and Basile FE Curchod. Calculating photoabsorption cross-sections for atmospheric volatile organic compounds. *ACS Earth and Space Chemistry*, 6(1):207–217, 2021.

[3] Jamie Matthews, Amitabha Sinha, and Joseph S Francisco. The importance of weak absorption features in promoting tropospheric radical production. *Proceedings of the National Academy of Sciences*, 102(21):7449–7452, 2005.

[4] Ghanshyam L Vaghjiani and Akkihebbal R Ravishankara. Absorption cross sections of CH_3OOH, H_2O_2, and D_2O_2 vapors between 210 and 365 nm at 297 K. *Journal of Geophysical Research: Atmospheres*, 94(D3):3487–3492, 1989.

[5] Hannelore Keller-Rudek, Geert K Moortgat, Rolf Sander, and Rüdiger Sörensen. The MPI-Mainz UV/VIS spectral atlas of gaseous molecules of atmospheric interest. *Earth System Science Data*, 5(2):365–373, 2013. URL `http://satellite.mpic.de/spectral_atlas`.

[6] Zhen Liu, Vinh Son Nguyen, Jeremy Harvey, Jean-François Müller, and Jozef Peeters. The photolysis of α-hydroperoxycarbonyls. *Physical Chemistry Chemical Physics*, 20(10):6970–6979, 2018.

[7] Kyohei Matsuo, Shohei Saito, and Shigehiro Yamaguchi. Photodissociation of B−N lewis adducts: a partially fused trinaphthylborane with dual fluorescence. *Journal of the American Chemical Society*, 136(36):12580–12583, 2014.

[8] Albert Einstein and Leopold Infeld. *The Evolution of Physics: The Growth of Ideas From Early Concepts to Relativity and Quanta*. Cambridge University Press, 1938.

[9] Max Planck. Zur theorie des gesetzes der energieverteilung im normalspektrum. *Verhandlungen der Deutschen Physikalischen*, 2(17):237–245, 1900.

[10] Niels Bohr. I. On the constitution of atoms and molecules. *The London, Edinburgh, and Dublin Philosophical Magazine and Journal of Science*, 26(151):1–25, 1913.

[11] Louis De Broglie. Waves and quanta. *Nature*, 112(2815):540–540, 1923.

[12] Erwin Schrödinger. An undulatory theory of the mechanics of atoms and molecules. *Physical Review*, 28(6):1049, 1926.

[13] Louis De Broglie. La mécanique ondulatoire et la structure atomique de la matière et du rayonnement. *Journal de Physique et le Radium*, 8(5):225–241, 1927.

[14] David Bohm. A suggested interpretation of the quantum theory in terms of "hidden" variables. *Physical Review*, 85(2):166, 1952.

[15] David Bohm and Basil J Hiley. *The undivided universe: An ontological interpretation of quantum theory.* Routledge, 2006.

[16] Sheldon Goldstein, Roderich Tumulka, and Nino Zanghì. Bohmian trajectories as the foundation of quantum mechanics. *Quantum Trajectories*, pages 1–15, 2011.

[17] Richard P Feynman. Space-time approach to non-relativistic quantum mechanics. *Reviews of Modern Physics*, 20(2):367, 1948.

[18] Enrico Fermi. Quantum theory of radiation. *Reviews of Modern Physics*, 4(1):87, 1932.

[19] Richard P Feynman. Mathematical formulation of the quantum theory of electromagnetic interaction. *Physical Review*, 80(3):440, 1950.

[20] Paul AM Dirac. Quantum mechanics of many-electron systems. *Proceedings of the Royal Society of London A*, 123(792):714–733, 1929.

[21] Max Born and Robert Oppenheimer. Zur quantentheorie der molekeln. *Annalen der Physik*, 84, 1927.

[22] Douglas R Hartree. The wave mechanics of an atom with a non-coulomb central field. part II. Some results and discussion. *Mathematical Proceedings of the Cambridge Philosophical Society*, 24(1):111–132, 1928.

[23] Vladimir Fock. Näherungsmethode zur lösung des quantenmechanischen mehrkörperproblems. *Zeitschrift für Physik*, 61(1):126–148, 1930.

[24] Valérie Blanchet, Marek Z Zgierski, Tamar Seideman, and Albert Stolow. Discerning vibronic molecular dynamics using time-resolved photoelectron spectroscopy. *Nature*, 401 (6748):52–54, 1999.

[25] Patrick Nuernberger, Stefan Ruetzel, and Tobias Brixner. Multidimensional electronic spectroscopy of photochemical reactions. *Angewandte Chemie International Edition*, 54 (39):11368–11386, 2015.

[26] Nicolas Blouin, Alexandre Michaud, David Gendron, Salem Wakim, Emily Blair, Rodica Neagu-Plesu, Michel Belletete, Gilles Durocher, Ye Tao, and Mario Leclerc. Toward a rational design of poly (2,7-carbazole) derivatives for solar cells. *Journal of the American Chemical Society*, 130(2):732–742, 2008.

[27] Hailong Chen, Geoffroy Hautier, and Gerbrand Ceder. Synthesis, computed stability, and crystal structure of a new family of inorganic compounds: carbonophosphates. *Journal of the American Chemical Society*, 134(48):19619–19627, 2012.

[28] Alfred Ludwig. Discovery of new materials using combinatorial synthesis and high-throughput characterization of thin-film materials libraries combined with computational methods. *NPJ Computational Materials*, 5(1):1–7, 2019.

[29] Anubhav Jain, Yongwoo Shin, and Kristin A Persson. Computational predictions of energy materials using density functional theory. *Nature Reviews Materials*, 1(1):1–13, 2016.

[30] Ibrahim Kholil and Tofajjol H Bhuiyan. Electronic, elastic, vibrational and superconducting properties of a ternary superconductors LaIrP (P=P, As): Insights from dft. *Solid State Communications*, 322:114053, 2020.

[31] Richard J Orton, Oliver E Sturm, Vladislav Vyshemirsky, Muffy Calder, David R Gilbert, and Walter Kolch. Computational modelling of the receptor-tyrosine-kinase-activated MAPK pathway. *Biochemical Journal*, 392(2):249–261, 2005.

[32] Luciana Esposito, Akos Banyasz, Thierry Douki, Marion Perron, Dimitra Markovitsi, and Roberto Improta. Effect of C_5-methylation of cytosine on the photoreactivity of DNA: a joint experimental and computational study of TCG trinucleotides. *Journal of the American Chemical Society*, 136(31):10838–10841, 2014.

[33] Chey M Jones, Nanna H List, and Todd J Martínez. Steric and electronic origins of fluorescence in GFP and GFP-like proteins. *Journal of the American Chemical Society*, 144(28):12732–12746, 2022.

[34] Henry W Kreiman, Mackenzie E Batali, Cooper S Jamieson, Molly A Lyon, and James A Duncan. CASSCF calculations reveal competitive chair (pericyclic) and boat (pseudopericyclic) transition states for the [3,3] sigmatropic rearrangement of allyl esters. *The Journal of Organic Chemistry*, 83(4):1717–1726, 2018.

[35] Yun-Xuan Tan, Fang Zhang, Pei-Pei Xie, Shuo-Qing Zhang, Yi-Fan Wang, Qing-Hua Li, Ping Tian, Xin Hong, and Guo-Qiang Lin. Rhodium (III)-catalyzed asymmetric borylative cyclization of cyclohexadienone-containing 1,6-dienes: an experimental and DFT study. *Journal of the American Chemical Society*, 141(32):12770–12779, 2019.

[36] Chendan Zhu, Francesca Mandrelli, Hui Zhou, Rajat Maji, and Benjamin List. Catalytic asymmetric synthesis of unprotected β2-amino acids. *Journal of the American Chemical Society*, 143(9):3312–3317, 2021.

[37] Pablo Garrido-Barros, Dooshaye Moonshiram, Marcos Gil-Sepulcre, Primavera Pelosin, Carolina Gimbert-Suriñach, Jordi Benet-Buchholz, and Antoni Llobet. Redox metal-ligand cooperativity enables robust and efficient water oxidation catalysis at neutral pH with macrocyclic copper complexes. *Journal of the American Chemical Society*, 142(41): 17434–17446, 2020.

[38] Xunhua Zhao and Yuanyue Liu. Unveiling the active structure of single nickel atom catalysis: critical roles of charge capacity and hydrogen bonding. *Journal of the American Chemical Society*, 142(12):5773–5777, 2020.

[39] Niels Hammer, Mette Louise Christensen, Yu Chen, Daniel Naharro, Fang Liu, Karl Anker Jørgensen, and Kendall N Houk. An experimental stereoselective photochemical [1s,3s]-sigmatropic silyl shift and the existence of silyl/allyl conical intersections. *Journal of the American Chemical Society*, 142(13):6030–6035, 2020.

[40] Javier Carmona-García, Tarek Trabelsi, Antonio Francés-Monerris, Carlos A Cuevas, Alfonso Saiz-Lopez, Daniel Roca-Sanjuán, and Joseph S Francisco. Photochemistry of $HOSO_2$ and SO_3 and implications for the production of sulfuric acid. *Journal of the American Chemical Society*, 143(44):18794–18802, 2021.

[41] Jimmy K Yu, Christoph Bannwarth, Ruibin Liang, Edward G Hohenstein, and Todd J Martínez. Nonadiabatic dynamics simulation of the wavelength-dependent photochemistry of azobenzene excited to the nπ^* and $\pi\pi^*$ excited states. *Journal of the American Chemical Society*, 142(49):20680–20690, 2020.

[42] Ruibin Liang, Jimmy K Yu, Jan Meisner, Fang Liu, and Todd J Martinez. Electrostatic control of photoisomerization in channelrhodopsin 2. *Journal of the American Chemical Society*, 143(14):5425–5437, 2021.

[43] Russell S Shapiro. Stromatolites: A 3.5-billion-year ichnologic record. In *Trace Fossils*, pages 382–390. Elsevier, 2007.

[44] Malcolm R Walter. Interpreting stromatolites: these fossils can tell us much about past organisms and environments if we can learn to decode their message. *American Scientist*, 65(5):563–571, 1977.

[45] Brendan P Burns, Falicia Goh, Michelle Allen, and Brett A Neilan. Microbial diversity of extant stromatolites in the hypersaline marine environment of Shark Bay, Australia. *Environmental Microbiology*, 6(10):1096–1101, 2004.

[46] Lucas J Stal. Cyanobacterial mats and stromatolites. In *Ecology of cyanobacteria II*, pages 65–125. Springer, 2012.

[47] Hans-Wilhelm Trissl and Christian Wilhelm. Why do thylakoid membranes from higher plants form grana stacks? *Trends in Biochemical Sciences*, 18(11):415–419, 1993.

[48] Nathan Nelson and Adam Ben-Shem. The complex architecture of oxygenic photosynthesis. *Nature Reviews Molecular Cell Biology*, 5(12):971–982, 2004.

[49] Lars JC Jeuken. *Biophotoelectrochemistry: from bioelectrochemistry to biophotovoltaics*, volume 158. Springer, 2017.

[50] Jenny Z Zhang and Erwin Reisner. Advancing photosystem II photoelectrochemistry for semi-artificial photosynthesis. *Nature Reviews Chemistry*, 4(1):6–21, 2020.

[51] Carles Curutchet and Benedetta Mennucci. Quantum chemical studies of light harvesting. *Chemical Reviews*, 117(2):294–343, 2017.

[52] Seogjoo J Jang and Benedetta Mennucci. Delocalized excitons in natural light-harvesting complexes. *Reviews of Modern Physics*, 90(3):035003, 2018.

[53] Francesco Segatta, Lorenzo Cupellini, Marco Garavelli, and Benedetta Mennucci. Quantum chemical modeling of the photoinduced activity of multichromophoric biosystems: Focus review. *Chemical Reviews*, 119(16):9361–9380, 2019.

[54] Nicoletta Liguori, Roberta Croce, Siewert J Marrink, and Sebastian Thallmair. Molecular dynamics simulations in photosynthesis. *Photosynthesis Research*, 144(2):273–295, 2020.

[55] Dong Ryeol Whang and Dogukan Hazar Apaydin. Artificial photosynthesis: Learning from nature. *ChemPhotoChem*, 2(3):148–160, 2018.

[56] Silvio Osella. Artificial photosynthesis: Is computation ready for the challenge ahead? *Nanomaterials*, 11(2):299, 2021.

[57] Akira Fujishima and Kenichi Honda. Electrochemical photolysis of water at a semiconductor electrode. *Nature*, 238(5358):37–38, 1972.

[58] Samuel S Mao and Shaohua Shen. Catalysing artificial photosynthesis. *Nature Photonics*, 7(12):944–946, 2013.

[59] Man Qiao, Jie Liu, Yu Wang, Yafei Li, and Zhongfang Chen. $PdSeO_3$ monolayer: promising inorganic 2D photocatalyst for direct overall water splitting without using sacrificial reagents and cocatalysts. *Journal of the American Chemical Society*, 140(38):12256–12262, 2018.

[60] Cheng Cheng, Wei-Hai Fang, Run Long, and Oleg V Prezhdo. Water splitting with a single-atom Cu/TiO_2 photocatalyst: atomistic origin of high efficiency and proposed enhancement by spin selection. *JACS Au*, 1(5):550–559, 2021.

[61] Penglin Xu, Ting Zhou, Nadia N Intan, Shaojin Hu, and Xiao Zheng. Rational ligand design for an efficient biomimetic water splitting complex. *The Journal of Physical Chemistry A*, 120(50):10033–10042, 2016.

[62] Guangxu Lan, Yingjie Fan, Wenjie Shi, Eric You, Samuel S Veroneau, and Wenbin Lin. Biomimetic active sites on monolayered metal-organic frameworks for artificial photosynthesis. *Nature Catalysis*, pages 1–13, 2022.

[63] Philipp Gotico, Bernard Boitrel, Régis Guillot, Marie Sircoglou, Annamaria Quaranta, Zakaria Halime, Winfried Leibl, and Ally Aukauloo. Second-sphere biomimetic multipoint hydrogen-bonding patterns to boost CO_2 reduction of iron porphyrins. *Angewandte Chemie International Edition*, 58(14):4504–4509, 2019.

[64] Chern-Hooi Lim, Aaron M Holder, James T Hynes, and Charles B Musgrave. Reduction of CO_2 to methanol catalyzed by a biomimetic organo-hydride produced from pyridine. *Journal of the American Chemical Society*, 136(45):16081–16095, 2014.

[65] Atsushi Urakawa, Fabian Jutz, Gábor Laurenczy, and Alfons Baiker. Carbon dioxide hydrogenation catalyzed by a ruthenium dihydride: A DFT and high-pressure spectroscopic investigation. *Chemistry–A European Journal*, 13(14):3886–3899, 2007.

[66] Jeremy Nathans. Rhodopsin: structure, function, and genetics. *Biochemistry*, 31(21): 4923–4931, 1992.

[67] Krzysztof Palczewski. G protein–coupled receptor rhodopsin. *Annual Review of Biochemistry*, 75:743–767, 2006.

[68] Arieh Warshel. Bicycle-pedal model for the first step in the vision process. *Nature*, 260 (5553):679–683, 1976.

[69] Robert W Schoenlein, Linda A Peteanu, Richard A Mathies, and Charles V Shank. The first step in vision: femtosecond isomerization of rhodopsin. *Science*, 254(5030):412–415, 1991.

[70] Oliver P Ernst, David T Lodowski, Marcus Elstner, Peter Hegemann, Leonid S Brown, and Hideki Kandori. Microbial and animal rhodopsins: structures, functions, and molecular mechanisms. *Chemical reviews*, 114(1):126–163, 2014.

[71] Dieter Oesterhelt and Walther Stoeckenius. Rhodopsin-like protein from the purple membrane of halobacterium halobium. *Nature New Biology*, 233(39):149–152, 1971.

[72] Feng Zhang, Li-Ping Wang, Martin Brauner, Jana F Liewald, Kenneth Kay, Natalie Watzke, Phillip G Wood, Ernst Bamberg, Georg Nagel, Alexander Gottschalk, and Karl Deisseroth. Multimodal fast optical interrogation of neural circuitry. *Nature*, 446(7136): 633–639, 2007.

[73] Germano Giuliani, Federico Melaccio, Samer Gozem, Andrea Cappelli, and Massimo Olivucci. QM/MM investigation of the spectroscopic properties of the fluorophore of bacterial luciferase. *Journal of Chemical Theory and Computation*, 17(2):605–613, 2021.

[74] Keiichi Inoue, María del Carmen Marín, Sahoko Tomida, Ryoko Nakamura, Yuta Nakajima, Massimo Olivucci, and Hideki Kandori. Red-shifting mutation of light-driven sodium-pump rhodopsin. *Nature Communications*, 10(1):1–11, 2019.

[75] María del Carmen Marín, Damianos Agathangelou, Yoelvis Orozco-Gonzalez, Alessio Valentini, Yoshitaka Kato, Rei Abe-Yoshizumi, Hideki Kandori, Ahreum Choi, Kwang-Hwan Jung, Stefan Haacke, et al. Fluorescence enhancement of a microbial rhodopsin via electronic reprogramming. *Journal of the American Chemical Society*, 141(1):262–271, 2018.

[76] Madushanka Manathunga, Adam J Jenkins, Yoelvis Orozco-Gonzalez, Alireza Ghanbarpour, Babak Borhan, James H Geiger, Delmar S Larsen, and Massimo Olivucci. Computational and spectroscopic characterization of the photocycle of an artificial rhodopsin. *The Journal of Physical Chemistry Letters*, 11(11):4245–4252, 2020.

[77] Hannah Ritchie, Max Roser, and Pablo Rosado. Energy production and consumption, Oct 2022. URL `https://ourworldindata.org/energy-production-consumption`.

[78] Arie J Haagen-Smit. Chemistry and physiology of Los Angeles smog. *Industrial & Engineering Chemistry*, 44(6):1342–1346, 1952.

[79] Arie J Haagen-Smit, CE Bradley, and MM Fox. Ozone formation in photochemical oxidation of organic substances. *Industrial & Engineering Chemistry*, 45(9):2086–2089, 1953.

[80] John B Mudd. Peroxyacyl nitrates. In *Responses of plants to air pollution*, pages 97–119. Academic Press New York, 1975.

[81] O Clifton Taylor. Importance of peroxyacetyl nitrate (PAN) as a phytotoxic air pollutant. *Journal of the Air Pollution Control Association*, 19(5):347–351, 1969.

[82] O Clifton Taylor. Effect of air-borne oxidants on leaves of pinto bean and petunia. In *Proceedings. American Society for Horticultural Science*, volume 75, pages 435–44, 1960.

[83] Adolf Vyskocil, Claude Viau, and Serge Lamy. Peroxyacetyl nitrate: review of toxicity. *Human & Experimental Toxicology*, 17(4):212–220, 1998.

[84] Allison H Steiner and Allen L Goldstein. Biogenic VOCs. In *Volatile organic compounds in the atmosphere*, pages 82–128. Wiley-Blackwell, 2007.

[85] Sandra M Saunders, Michael E Jenkin, Richard G Derwent, and Mike J Pilling. Protocol for the development of the master chemical mechanism, MCM v3 (part A): tropospheric degradation of non-aromatic volatile organic compounds. *Atmospheric Chemistry and Physics*, 3(1):161–180, 2003.

[86] Michael E Jenkin, Sandra M Saunders, Volker Wagner, and Mike J Pilling. Protocol for the development of the master chemical mechanism, MCM v3 (part B): tropospheric degradation of aromatic volatile organic compounds. *Atmospheric Chemistry and Physics*, 3(1):181–193, 2003.

[87] Glenn M Wolfe, John D Crounse, Jonathan D Parrish, Jason M St Clair, Melinda R Beaver, Fabien Paulot, Tehshik P Yoon, Paul O Wennberg, and Frank N Keutsch. Photolysis, OH reactivity and ozone reactivity of a proxy for isoprene-derived hydroperoxyenals (HPALDs). *Physical Chemistry Chemical Physics*, 14(20):7276–7286, 2012.

[88] Zhen Liu, Vinh Son Nguyen, Jeremy Harvey, Jean-François Müller, and Jozef Peeters. Theoretically derived mechanisms of HPALD photolysis in isoprene oxidation. *Physical Chemistry Chemical Physics*, 19(13):9096–9106, 2017.

[89] Keiran Rowell. *Structure-Activity Relationships for Carbonyl Photolysis*. PhD thesis, The University of New South Wales, 2020.

[90] Luc Vereecken, Bernard Aumont, Ian Barnes, Joseph W Bozzelli, Mark J Goldman, William H Green, Sasha Madronich, Max R Mcgillen, Abdelwahid Mellouki, John J Orlando, Benedicte Picquet-Varrault, Andrew R Rickard, William R Stockwell, Timothy J Wallington, and William PL Carter. Perspective on mechanism development and structure-activity relationships for gas-phase atmospheric chemistry. *International Journal of Chemical Kinetics*, 50(6):435–469, 2018.

[91] Gilbert N Lewis. *Valence and the Structure of Atoms and Molecules*. Number 14. Chemical Catalog Company, Incorporated, 1923.

[92] Johann N Brönsted. Einige bemerkungen über den begriff der säuren und basen. *Recueil des Travaux Chimiques des Pays-Bas*, 42(8):718–728, 1923.

[93] Thomas Lowry. Strength of acids and bases. *Chemistry and Industry*, 42:43–51, 1923.

[94] Gilbert N Lewis. Acids and bases. *Journal of the Franklin Institute*, 226(3):293–313, 1938.

[95] William B Jensen. The lewis acid-base definitions: a status report. *Chemical Reviews*, 78 (1):1–22, 1978.

[96] John K Ruff. Lewis adducts of the $Fe(CO)_4^{2-}$ and $Co(CO)_4^{-}$ ions. *Inorganic Chemistry*, 7 (8):1499–1503, 1968.

[97] Robert S Mulliken and Willis B Person. *Molecular complexes: a lecture and reprint volume*. Wiley-Interscience, 1969.

[98] Henry A Bent. Structural chemistry of donor-acceptor interactions. *Chemical Reviews*, 68(5):587–648, 1968.

[99] Jenny SJ McCahill, Gregory C Welch, and Douglas W Stephan. Reactivity of "frustrated Lewis pairs": Three-component reactions of phosphines, a borane, and olefins. *Angewandte Chemie*, 119(26):5056–5059, 2007.

[100] Meghan A Dureen and Douglas W Stephan. Terminal alkyne activation by frustrated and classical Lewis acid/phosphine pairs. *Journal of the American Chemical Society*, 131 (24):8396–8397, 2009.

[101] Tieqi Xu and Eugene Y-X Chen. Probing site cooperativity of frustrated phosphine/borane Lewis pairs by a polymerization study. *Journal of the American Chemical Society*, 136 (5):1774–1777, 2014.

[102] Kulbir K Ghuman, Laura B Hoch, Paul Szymanski, Joel YY Loh, Nazir P Kherani, Mostafa A El-Sayed, Geoffrey A Ozin, and Chandra V Singh. Photoexcited surface frustrated Lewis pairs for heterogeneous photocatalytic CO_2 reduction. *Journal of the American Chemical Society*, 138(4):1206–1214, 2016.

[103] Zhenghua Li, Liang Zhang, Masayoshi Nishiura, Gen Luo, Yi Luo, and Zhaomin Hou. CO_2 activation by lewis pairs generated under copper catalysis enables difunctionalization of imines. *Journal of the American Chemical Society*, 142(4):1966–1974, 2020.

[104] Dinesh Nugegoda, Leigh A Hunt, Anthony Devdass, Hammad Cheema, Ryan C Fortenberry, Jonah W Jurss, Nathan I Hammer, and Jared H Delcamp. Lewis acid–lewis base interactions promote fast interfacial electron transfers with a pyridine-based donor dye in dye-sensitized solar cells. *ACS Applied Energy Materials*, 5(2):1516–1527, 2022.

[105] Utku Yolsal, Thomas AR Horton, Meng Wang, and Michael P Shaver. Cyclic ether triggers for polymeric frustrated Lewis pair gels. *Journal of the American Chemical Society*, 143(33):12980–12984, 2021.

[106] Beatrice Adelizzi, Pongphak Chidchob, Naoki Tanaka, Brigitte AG Lamers, Stefan CJ Meskers, Soichiro Ogi, Anja RA Palmans, Shigehiro Yamaguchi, and Egbert W Meijer.

Long-lived charge-transfer state from B−N frustrated Lewis pairs enchained in supramolecular copolymers. *Journal of the American Chemical Society*, 142(39):16681–16689, 2020.

[107] Kenneth G Hancock and David A Dickinson. Photochemical interconversion of the geometrical isomers of aminoboranes. *Journal of the American Chemical Society*, 94(12): 4396–4398, 1972.

[108] Naokazu Kano, Junro Yoshino, and Takayuki Kawashima. Photoswitching of the Lewis acidity of a catecholborane bearing an azo group based on the change in coordination number of boron. *Organic Letters*, 7(18):3909–3911, 2005.

[109] Ying-Li Rao, Hazem Amarne, Shu-Bin Zhao, Theresa M McCormick, Sanela Martic, Yi Sun, Rui-Yao Wang, and Suning Wang. Reversible intramolecular C−C bond formation/breaking and color switching mediated by a N,C-chelate in (2-ph-py) $BMes_2$ and (5-$BMes_2$-2-ph-py) $BMes_2$. *Journal of the American Chemical Society*, 130(39): 12898–12900, 2008.

[110] Naoki Ando, Takuya Yamada, Hiroki Narita, Niels N Oehlmann, Matthias Wagner, and Shigehiro Yamaguchi. Boron-doped polycyclic π-electron systems with an antiaromatic borole substructure that forms photoresponsive B−P Lewis adducts. *Journal of the American Chemical Society*, 143(26):9944–9951, 2021.

[111] Matthew J Voegtle and Jahan M Dawlaty. Can brønsted photobases act as lewis photobases? *Journal of the American Chemical Society*, 144(18):8178–8184, 2022.

[112] Christopher J Cramer. *Essentials of computational chemistry: theories and models.* John Wiley & Sons, 2013.

[113] Frank Jensen. *Introduction to computational chemistry.* John Wiley & Sons, 2017.

[114] Claude Leforestier. Classical trajectories using the full ab initio potential energy surface $H^- + CH_4 \longrightarrow CH_4 + H^-$. *The Journal of Chemical Physics*, 68(10):4406–4410, 1978.

[115] Roberto Car and Michele Parrinello. Unified approach for molecular dynamics and density-functional theory. *Physical Review Letters*, 55(22):2471–2474, 1985.

[116] John C Tully and Richard K Preston. Trajectory surface hopping approach to nonadiabatic molecular collisions: the reaction of H^+ with D_2. *The Journal of Chemical Physics*, 55(2): 562–572, 1971.

[117] John C Tully. Molecular dynamics with electronic transitions. *The Journal of Chemical Physics*, 93(2):1061–1071, 1990.

[118] Sharon Hammes-Schiffer and John C Tully. Proton transfer in solution: Molecular dynamics with quantum transitions. *The Journal of Chemical Physics*, 101(6):4657–4667, 1994.

[119] John C Tully. Mixed quantum-classical dynamics. *Faraday Discussions*, 110:407–419, 1998.

[120] John C Tully. Nonadiabatic dynamics. In *Modern methods for multidimensional dynamics computations in chemistry*, pages 34–72. World Scientific, 1998.

[121] John B Delos, Walter R Thorson, and Stephen K Knudson. Semiclassical theory of inelastic collisions. I. classical picture and semiclassical formulation. *Physical Review A*, 6 (2):709, 1972.

[122] Xiaosong Li, John C Tully, H Bernhard Schlegel, and Michael J Frisch. Ab initio ehrenfest dynamics. *The Journal of Chemical Physics*, 123(8):084106, 2005.

[123] Federica Agostini, Eberhard KU Gross, and Basile FE Curchod. Electron-nuclear entanglement in the time-dependent molecular wavefunction. *Computational and Theoretical Chemistry*, 1151:99–106, 2019.

[124] Federica Agostini, Seung K Min, Ali Abedi, and Eberhard KU Gross. Quantum-classical nonadiabatic dynamics: coupled-vs independent-trajectory methods. *Journal of Chemical Theory and Computation*, 12(5):2127–2143, 2016.

[125] Graeme H Gossel, Federica Agostini, and Neepa T Maitra. Coupled-trajectory mixed quantum-classical algorithm: A deconstruction. *Journal of Chemical Theory and Computation*, 14(9):4513–4529, 2018.

[126] Francesco Talotta, Sabine Morisset, Nathalie Rougeau, David Lauvergnat, and Federica Agostini. Spin-orbit interactions in ultrafast molecular processes. *Physical Review Letters*, 124(3):033001, 2020.

[127] Todd J Martínez, Michal Ben-Nun, and Raphael D Levine. Multi-electronic-state molecular dynamics: A wave function approach with applications. *The Journal of Physical Chemistry*, 100(19):7884–7895, 1996.

[128] Todd J Martínez, Michal Ben-Nun, and Raphael D Levine. Molecular collision dynamics on several electronic states. *The Journal of Physical Chemistry A*, 101(36):6389–6402, 1997.

[129] Todd J Martínez and Raphael D Levine. Non-adiabatic molecular dynamics: Split-operator multiple spawning with applications to photodissociation. *Journal of the Chemical Society, Faraday Transactions*, 93(5):941–947, 1997.

[130] Dmitrii V Shalashilin. Quantum mechanics with the basis set guided by Ehrenfest trajectories: Theory and application to spin-boson model. *The Journal of chemical physics*, 130(24):244101, 2009.

[131] Kenichiro Saita and Dmitrii V Shalashilin. On-the-fly ab initio molecular dynamics with multiconfigurational ehrenfest method. *The Journal of Chemical Physics*, 137(22):22A506, 2012.

[132] Dmitry V Makhov, Christopher Symonds, Sebastian Fernandez-Alberti, and Dmitrii V Shalashilin. Ab initio quantum direct dynamics simulations of ultrafast photochemistry with multiconfigurational ehrenfest approach. *Chemical Physics*, 493:200–218, 2017.

[133] Graham A Worth, Michael A Robb, and Irene Burghardt. A novel algorithm for non-adiabatic direct dynamics using variational Gaussian wavepackets. *Faraday Discussions*, 127:307–323, 2004.

[134] Benjamin Lasorne, Michael J Bearpark, Michael A Robb, and Graham A Worth. Direct quantum dynamics using variational multi-configuration Gaussian wavepackets. *Chemical Physics Letters*, 432(4-6):604–609, 2006.

[135] Gareth W Richings, Iakov Polyak, Kaite E Spinlove, Graham A Worth, Irene Burghardt, and Benjamin Lasorne. Quantum dynamics simulations using Gaussian wavepackets: the vMCG method. *International Reviews in Physical Chemistry*, 34(2):269–308, 2015.

[136] Hans-Dieter Meyer, Uwe Manthe, and Lorenz S Cederbaum. The multi-configurational time-dependent Hartree approach. *Chemical Physics Letters*, 165(1):73–78, 1990.

[137] Michael H Beck, Andreas Jäckle, Graham A Worth, and Hans-Dieter Meyer. The multiconfiguration time-dependent hartree (MCTDH) method: a highly efficient algorithm for propagating wavepackets. *Physics reports*, 324(1):1–105, 2000.

[138] Hans-Dieter Meyer, Fabien Gatti, and Graham A Worth. *Multidimensional quantum dynamics: MCTDH theory and applications.* John Wiley & Sons, 2009.

[139] Max Born and Kun Huang. *Dynamical Theory of Crystal Lattices.* Oxford University Press, 1954.

[140] Rami Gherib, Ilya G Ryabinkin, and Artur F Izmaylov. Why do mixed quantum-classical methods describe short-time dynamics through conical intersections so well? Analysis of geometric phase effects. *Journal of Chemical Theory and Computation*, 11(4):1375–1382, 2015.

[141] Rami Gherib, Liyuan Ye, Ilya G Ryabinkin, and Artur F Izmaylov. On the inclusion of the diagonal born-oppenheimer correction in surface hopping methods. *The Journal of Chemical Physics*, 144(15):154103, 2016.

[142] Robert E Wyatt. *Quantum dynamics with trajectories: introduction to quantum hydrodynamics*, volume 28. Springer Science & Business Media, 2005.

[143] Felipe Franco De Carvalho, Marine EF Bouduban, Basile FE Curchod, and Ivano Tavernelli. Nonadiabatic molecular dynamics based on trajectories. *Entropy*, 16(1):62–85, 2013.

[144] Herbert Goldstein, Charles Poole, and John Safko. *Classical mechanics.* American Association of Physics Teachers, 2002.

[145] C Alden Mead and Donald G Truhlar. On the determination of Born-Oppenheimer nuclear motion wave functions including complications due to conical intersections and identical nuclei. *The Journal of Chemical Physics*, 70(5):2284–2296, 1979.

[146] Michael V Berry. The quantum phase, five years after. *Geometric Phases in Physics*, pages 7–28, 1989.

[147] C Alden Mead. The geometric phase in molecular systems. *Reviews of modern physics*, 64(1):51, 1992.

[148] David R Yarkony. Diabolical conical intersections. *Reviews of Modern Physics*, 68(4):985, 1996.

[149] Yakir Aharonov and David Bohm. Significance of electromagnetic potentials in the quantum theory. *Physical Review*, 115(3):485, 1959.

[150] Ilya G Ryabinkin, Loïc Joubert-Doriol, and Artur F Izmaylov. Geometric phase effects in nonadiabatic dynamics near conical intersections. *Accounts of Chemical Research*, 50(7): 1785–1793, 2017.

[151] Felix T Smith. Diabatic and adiabatic representations for atomic collision problems. *Physical Review*, 179(1):111, 1969.

[152] C Alden Mead and Donald G Truhlar. Conditions for the definition of a strictly diabatic electronic basis for molecular systems. *The Journal of Chemical Physics*, 77(12):6090–6098, 1982.

[153] Horst Köppel, Wolfgang Domcke, and Lorenz S Cederbaum. Multimode molecular dynamics beyond the Born-Oppenheimer approximation. *Advances in Chemical Physics*, pages 59–246, 1984.

[154] Brian K Kendrick, C Alden Mead, and Donald G Truhlar. On the nonexistence of strictly diabatic molecular electronic bases. *Chemical Physics Letters*, 330(5-6):629–632, 2000.

[155] Wolfgang Domcke, Clemens Woywod, and Martin Stengle. Diabatic CASSCF orbitals and wavefunctions. *Chemical Physics Letters*, 226(3-4):257–262, 1994.

[156] Florent X Gadéa and Michel Pélissier. Approximately diabatic states: A relation between effective Hamiltonian techniques and explicit cancellation of the derivative coupling. *The Journal of Chemical Physics*, 93(1):545–551, 1990.

[157] Paul AM Dirac. The quantum theory of the electron. *Proceedings of the Royal Society of London A*, 117(778):610–624, 1928.

[158] Christel M Marian. Spin-orbit coupling and intersystem crossing in molecules. *Wiley Interdisciplinary Reviews: Computational Molecular Science*, 2(2):187–203, 2012.

[159] Marvin Douglas and Norman M Kroll. Quantum electrodynamical corrections to the fine structure of helium. *Annals of Physics*, 82(1):89–155, 1974.

[160] Georg Jansen and Bernd A Heß. Revision of the Douglas-Kroll transformation. *Physical Review A*, 39(11):6016, 1989.

[161] Bernd A Heß, Christel M Marian, Ulf Wahlgren, and Odd Gropen. A mean-field spin-orbit method applicable to correlated wavefunctions. *Chemical Physics Letters*, 251(5-6):365–371, 1996.

[162] Stefan Grimme, Markus Woeller, Sigrid D Peyerimhoff, David Danovich, and Sason Shaik. Theoretical study of the radiationless decay channels of triplet state norbornene. *Chemical Physics Letters*, 287(5-6):601–607, 1998.

[163] Jeremy N Harvey, Stefan Grimme, Markus Woeller, Sigrid D Peyerimhoff, David Danovich, and Sason Shaik. Computational prediction of the isc rate for triplet norbornene. *Chemical Physics Letters*, 322(5):358–362, 2000.

[164] Jörg Tatchen, Natalie Gilka, and Christel M Marian. Intersystem crossing driven by vibronic spin-orbit coupling: a case study on psoralen. *Physical Chemistry Chemical Physics*, 9(38):5209–5221, 2007.

[165] Sebastian Mai, Philipp Marquetand, and Leticia González. A general method to describe intersystem crossing dynamics in trajectory surface hopping. *International Journal of Quantum Chemistry*, 115(18):1215–1231, 2015.

[166] Mario Barbatti, Matthias Ruckenbauer, Felix Plasser, Jiří Pittner, Giovanni Granucci, Maurizio Persico, and Hans Lischka. Newton-X: a surface-hopping program for nonadiabatic molecular dynamics. *Wiley Interdisciplinary Reviews: Computational Molecular Science*, 4(1):26–33, 2014.

[167] Mario Barbatti, Giovanni Granucci, Matthias Ruckenbauer, Felix Plasser, Rachel Crespo-Otero, Jiří Pittner, Maurizio Persico, and Hans Lischka. Newton-X: A package for newtonian dynamics close to the crossing seam., 2016. URL `www.newtonx.org`.

[168] Sebastian Mai, Philipp Marquetand, and Leticia González. Nonadiabatic dynamics: The SHARC approach. *Wiley Interdisciplinary Reviews: Computational Molecular Science*, 8 (6):e1370, 2018.

[169] Felix Plasser, Giovanni Granucci, Jiří Pittner, Mario Barbatti, Maurizio Persico, and Hans Lischka. Surface hopping dynamics using a locally diabatic formalism: Charge transfer in the ethylene dimer cation and excited state dynamics in the 2-pyridone dimer. *The Journal of Chemical Physics*, 137(22):22A514, 2012.

[170] Joseph E Subotnik, Wenjun Ouyang, and Brian R Landry. Can we derive Tully's surface-hopping algorithm from the semiclassical quantum Liouville equation? Almost, but only with decoherence. *The Journal of Chemical Physics*, 139(21):211101, 2013.

[171] Lea M Ibele and Basile FE Curchod. A molecular perspective on Tully models for nonadiabatic dynamics. *Physical Chemistry Chemical Physics*, 22(27):15183–15196, 2020.

[172] Gaohan Miao and Joseph Subotnik. Revisiting the recoherence problem in the fewest switches surface hopping algorithm. *The Journal of Physical Chemistry A*, 123(26): 5428–5435, 2019.

[173] Michael F Herman. Generalization of the geometric optical series approach for nonadiabatic scattering problems. *The Journal of Chemical Physics*, 76(6):2949–2958, 1982.

[174] Jiří Pittner, Hans Lischka, and Mario Barbatti. Optimization of mixed quantum-classical dynamics: Time-derivative coupling terms and selected couplings. *Chemical Physics*, 356 (1-3):147–152, 2009.

[175] Ilya G Ryabinkin, Jayashree Nagesh, and Artur F Izmaylov. Fast numerical evaluation of time-derivative nonadiabatic couplings for mixed quantum-classical methods. *The Journal of Physical Chemistry Letters*, 6(21):4200–4203, 2015.

[176] Jian-Yun Fang and Sharon Hammes-Schiffer. Improvement of the internal consistency in trajectory surface hopping. *The Journal of Physical Chemistry A*, 103(47):9399–9407, 1999.

[177] Giovanni Granucci and Maurizio Persico. Critical appraisal of the fewest switches algorithm for surface hopping. *The Journal of Chemical Physics*, 126(13):134114, 2007.

[178] Chaoyuan Zhu, Shikha Nangia, Ahren W Jasper, and Donald G Truhlar. Coherent switching with decay of mixing: an improved treatment of electronic coherence for non-Born-Oppenheimer trajectories. *The Journal of Chemical Physics*, 121(16):7658–7670, 2004.

[179] Giovanni Granucci and Maurizio Persico. Excited state dynamics with the direct trajectory surface hopping method: azobenzene and its derivatives as a case study. *Theoretical Chemistry Accounts*, 117:1131–1143, 2007.

[180] Weiwei Xie, Marin Sapunar, Nađa Došlić, Matthieu Sala, and Wolfgang Domcke. Assessing the performance of trajectory surface hopping methods: Ultrafast internal conversion in pyrazine. *The Journal of Chemical Physics*, 150(15):154119, 2019.

[181] Maria S Topaler, Thomas C Allison, David W Schwenke, and Donald G Truhlar. Test of trajectory surface hopping against accurate quantum dynamics for an electronically nonadiabatic chemical reaction. *The Journal of Physical Chemistry A*, 102(10):1666–1673, 1998.

[182] Michal Ben-Nun and Todd J Martínez. Ab initio quantum molecular dynamics. *Advances in Chemical Physics*, 121:439–512, 2002.

[183] Basile FE Curchod and Todd J Martínez. Ab initio nonadiabatic quantum molecular dynamics. *Chemical Reviews*, 118(7):3305–3336, 2018.

[184] Benoit Mignolet and Basile FE Curchod. A walk through the approximations of ab initio multiple spawning. *The Journal of Chemical Physics*, 148(13):134110, 2018.

[185] Lea M Ibele, Angus Nicolson, and Basile FE Curchod. Excited-state dynamics of molecules with classically driven trajectories and Gaussians. *Molecular Physics*, 118(8):e1665199, 2020.

[186] Basile FE Curchod. Full and ab initio multiple spawning. *Quantum Chemistry and Dynamics of Excited States: Methods and Applications*, pages 435–467, 2020.

[187] Michal Ben-Nun, Jason Quenneville, and Todd J Martínez. Ab initio multiple spawning: Photochemistry from first principles quantum molecular dynamics. *The Journal of Physical Chemistry A*, 104(22):5161–5175, 2000.

[188] Basile FE Curchod, Aaron Sisto, and Todd J Martínez. Ab initio multiple spawning photochemical dynamics of DMABN using GPUs. *The Journal of Physical Chemistry A*, 121(1):265–276, 2017.

[189] David M Sanchez, Umberto Raucci, KN Ferreras, and Todd J Martínez. Putting photomechanical switches to work: an ab initio multiple spawning study of donor-acceptor stenhouse adducts. *The Journal of Physical Chemistry Letters*, 11(18):7901–7907, 2020.

[190] Todd J Martínez. Ab initio molecular dynamics around a conical intersection: Li(2p) + H_2. *Chemical Physics Letters*, 272(3-4):139–147, 1997.

[191] Wolfgang Domcke, David Yarkony, and Horst Köppel. *Conical intersections: electronic structure, dynamics & spectroscopy*, volume 15. World Scientific, 2004.

[192] Benjamin G Levine, Joshua D Coe, Aaron M Virshup, and Todd J Martínez. Implementation of ab initio multiple spawning in the Molpro quantum chemistry package. *Chemical Physics*, 347(1-3):3–16, 2008.

[193] Yorick Lassmann and Basile FE Curchod. AIMSWISS — Ab initio multiple spawning with informed stochastic selections. *The Journal of Chemical Physics*, 154(21):211106, 2021.

[194] Shane P McCarthy and Ajit J Thakkar. When does the non-variational nature of second-order møller-plesset energies manifest itself? all-electron correlation energies for open-shell atoms from k to br. *The Journal of chemical physics*, 136(5):054107, 2012.

[195] Wolfgang Pauli. Über den zusammenhang des abschlusses der elektronengruppen im atom mit der komplexstruktur der spektren. *Einführung und Originaltexte*, page 229, 1925.

[196] Paul AM Dirac. On the theory of quantum mechanics. *Proceedings of the Royal Society of London A*, 112(762):661–677, 1926.

[197] Garnet Kin-Lic Chan and Martin Head-Gordon. Exact solution (within a triple-zeta, double polarization basis set) of the electronic Schrödinger equation for water. *The Journal of Chemical Physics*, 118(19):8551–8554, 2003.

[198] Peter J Knowles and Nicholas C Handy. A new determinant-based full configuration interaction method. *Chemical Physics Letters*, 111(4-5):315–321, 1984.

[199] Björn Roos. A new method for large-scale CI calculations. *Chemical Physics Letters*, 15 (2):153–159, 1972.

[200] Gene H Golub and Charles F Van Loan. *Matrix computations.* JHU press, 2013.

[201] Gerard LG Sleijpen and Henk A Van der Vorst. A Jacobi-Davidson iteration method for linear eigenvalue problems. *SIAM Review*, 42(2):267–293, 2000.

[202] Péter R Surján and Péter R Surján. The brillouin theorem. *Second Quantized Approach to Quantum Chemistry: An Elementary Introduction*, pages 87–92, 1989.

[203] Trygve Helgaker, Poul Jørgensen, and Jeppe Olsen. *Molecular electronic-structure theory.* John Wiley & Sons, 2013.

[204] Stephen R Langhoff and Ernest R Davidson. Configuration interaction calculations on the nitrogen molecule. *International Journal of Quantum Chemistry*, 8(1):61–72, 1974.

[205] Jeppe Olsen, Danny L Yeager, and Poul Jørgensen. Optimization and characterization of a multiconfigurational self-consistent field (MCSCF) state. *Advances in Chemical Physics*, 54:1–176, 1983.

[206] Ron Shepard. The multiconfiguration self-consistent field method. *Ab Initio Methods in Quantum Chemistry-II*, page 63, 1987.

[207] Esper Dalgaard and Poul Jørgensen. Optimization of orbitals for multiconfigurational reference states. *The Journal of Chemical Physics*, 69(8):3833–3844, 1978.

[208] Hans-Joachim Werner. Matrix-formulated direct multiconfiguration self-consistent field and multiconfiguration reference configuration-interaction methods. *Advances in Chemical Physics*, 69:1–62, 2009.

[209] Björn O Roos, Peter R Taylor, and Per EM Siegbahn. A complete active space SCF method (CASSCF) using a density matrix formulated super-CI approach. *Chemical Physics*, 48(2):157–173, 1980.

[210] Björn O Roos. The complete active space SCF method in a fock-matrix-based super-CI formulation. *International Journal of Quantum Chemistry*, 18(S14):175–189, 1980.

[211] Per EM Siegbahn, Anders Heiberg, Björn O Roos, and Bernard Levy. A comparison of the super-CI and the Newton-Raphson scheme in the complete active space SCF method. *Physica Scripta*, 21(3-4):323, 1980.

[212] Hans-Joachim Werner and Peter J Knowles. An efficient internally contracted multiconfiguration-reference configuration interaction method. *The Journal of Chemical Physics*, 89(9):5803–5814, 1988.

[213] Toru Shiozaki, Werner Győrffy, Paolo Celani, and Hans-Joachim Werner. Communication: Extended multi-state complete active space second-order perturbation theory: Energy and nuclear gradients. *The Journal of Chemical Physics*, 135(8):081106, 2011.

[214] Bess Vlaisavljevich and Toru Shiozaki. Nuclear energy gradients for internally contracted complete active space second-order perturbation theory: Multistate extensions. *Journal of Chemical Theory and Computation*, 12(8):3781–3787, 2016.

[215] Jae Woo Park and Toru Shiozaki. On-the-fly CASPT2 surface-hopping dynamics. *Journal of Chemical Theory and Computation*, 13(8):3676–3683, 2017.

[216] Hans Lischka, Dana Nachtigallova, Adelia JA Aquino, Peter G Szalay, Felix Plasser, Francisco BC Machado, and Mario Barbatti. Multireference approaches for excited states of molecules. *Chemical Reviews*, 118(15):7293–7361, 2018.

[217] Jae Woo Park, Rachael Al-Saadon, Matthew K MacLeod, Toru Shiozaki, and Bess Vlaisavljevich. Multireference electron correlation methods: Journeys along potential energy surfaces. *Chemical Reviews*, 120(13):5878–5909, 2020.

[218] Jochen Schirmer. Beyond the random-phase approximation: A new approximation scheme for the polarization propagator. *Physical Review A*, 26(5):2395, 1982.

[219] Jochen Schirmer, Lorenz S Cederbaum, and O Walter. New approach to the one-particle Green's function for finite Fermi systems. *Physical Review A*, 28(3):1237, 1983.

[220] Jochen Schirmer. Closed-form intermediate representations of many-body propagators and resolvent matrices. *Physical Review A*, 43(9):4647, 1991.

[221] Alexander B Trofimov, IL Krivdina, J Weller, and Jochen Schirmer. Algebraic-diagrammatic construction propagator approach to molecular response properties. *Chemical Physics*, 329(1-3):1–10, 2006.

[222] Jochen Schirmer. *Many-body methods for atoms, molecules and clusters*. Springer, 2018.

[223] Jens Oddershede. Polarization propagator calculations. In *Advances in Quantum Chemistry*, volume 11, pages 275–352. Elsevier, 1978.

[224] Jochen Schirmer and Alexander B Trofimov. Intermediate state representation approach to physical properties of electronically excited molecules. *The Journal of chemical physics*, 120(24):11449–11464, 2004.

[225] Andreas Dreuw and Michael Wormit. The algebraic diagrammatic construction scheme for the polarization propagator for the calculation of excited states. *Wiley Interdisciplinary Reviews: Computational Molecular Science*, 5(1):82–95, 2015.

[226] Chr Møller and Milton S Plesset. Note on an approximation treatment for many-electron systems. *Physical Review*, 46(7):618, 1934.

[227] Dieter Cremer. Møller–plesset perturbation theory: from small molecule methods to methods for thousands of atoms. *Wiley Interdisciplinary Reviews: Computational Molecular Science*, 1(4):509–530, 2011.

[228] Alexander B Trofimov and Jochen Schirmer. An efficient polarization propagator approach to valence electron excitation spectra. *Journal of Physics B: Atomic, Molecular and Optical Physics*, 28(12):2299, 1995.

[229] Christof Hättig. Structure optimizations for excited states with correlated second-order methods: CC2 and ADC(2). *Advances in Quantum Chemistry*, 50:37–60, 2005.

[230] Richard L Martin. Natural transition orbitals. *The Journal of Chemical Physics*, 118(11): 4775–4777, 2003.

[231] Felix Plasser, Michael Wormit, and Andreas Dreuw. New tools for the systematic analysis and visualization of electronic excitations. I. formalism. *The Journal of Chemical Physics*, 141(2):024106, 2014.

[232] Felix Plasser. TheoDORE: A toolbox for a detailed and automated analysis of electronic excited state computations. *The Journal of Chemical Physics*, 152(8):084108, 2020.

[233] Deniz Tuna, Daniel Lefrancois, Łukasz Wolański, Samer Gozem, Igor Schapiro, Tadeusz Andruniów, Andreas Dreuw, and Massimo Olivucci. Assessment of approximate coupled-cluster and algebraic-diagrammatic-construction methods for ground-and excited-state reaction paths and the conical-intersection seam of a retinal-chromophore model. *Journal of Chemical Theory and Computation*, 11(12):5758–5781, 2015.

[234] Felix Plasser, Rachel Crespo-Otero, Marek Pederzoli, Jiří Pittner, Hans Lischka, and Mario Barbatti. Surface hopping dynamics with correlated single-reference methods: 9H-adenine as a case study. *Journal of Chemical Theory and Computation*, 10(4):1395–1405, 2014.

[235] Farhan Siddique, Mario Barbatti, Zhonghua Cui, Hans Lischka, and Adelia JA Aquino. Nonadiabatic dynamics of charge-transfer states using the anthracene-tetracyanoethylene complex as a prototype. *The Journal of Physical Chemistry A*, 124(17):3347–3357, 2020.

[236] Hans Lischka, Mario Barbatti, Farhan Siddique, Anita Das, and Adelia JA Aquino. The effect of hydrogen bonding on the nonadiabatic dynamics of a thymine-water cluster. *Chemical Physics*, 515:472–479, 2018.

[237] Branislav Milovanović, Jurica Novak, Mihajlo Etinski, Wolfgang Domcke, and Nađa Došlić. Simulation of UV absorption spectra and relaxation dynamics of uracil and uracil-water clusters. *Physical Chemistry Chemical Physics*, 23(4):2594–2604, 2021.

[238] Antonio Prlj, Alberto Fabrizio, and Clemence Corminboeuf. Rationalizing fluorescence quenching in meso-BODIPY dyes. *Physical Chemistry Chemical Physics*, 18(48):32668–32672, 2016.

[239] Jurica Novak, Antonio Prlj, Nikola Basarić, Clémence Corminboeuf, and Nađa Došlić. Photochemistry of 1-and 2-naphthols and their water clusters: The role of $^1\pi\pi^*(\mathrm{L}_a)$ mediated hydrogen transfer to carbon atoms. *Chemistry-A European Journal*, 23(34): 8244–8251, 2017.

[240] Mario Barbatti and Hans Lischka. Why water makes 2-aminopurine fluorescent? *Physical Chemistry Chemical Physics*, 17(23):15452–15459, 2015.

[241] Rafał Szabla, Holger Kruse, Petr Stadlbauer, Jiří Šponer, and Andrzej L Sobolewski. Sequential electron transfer governs the UV-induced self-repair of DNA photolesions. *Chemical Science*, 9(12):3131–3140, 2018.

[242] Antonio Prlj, Laurent Vannay, and Clemence Corminboeuf. Fluorescence quenching in BODIPY dyes: The role of intramolecular interactions and charge transfer. *Helvetica Chimica Acta*, 100(6):e1700093, 2017.

[243] Momir Mališ, Jurica Novak, Goran Zgrablić, Fulvio Parmigiani, and Nadja Došlić. Mechanism of ultrafast non-reactive deactivation of the retinal chromophore in non-polar solvents. *Physical Chemistry Chemical Physics*, 19(38):25970–25978, 2017.

[244] Deniz Tuna, Andrzej L Sobolewski, and Wolfgang Domcke. Mechanisms of ultrafast excited-state deactivation in adenosine. *The Journal of Physical Chemistry A*, 118(1): 122–127, 2014.

[245] Michał A Kochman, Attila Tajti, Carole A Morrison, and RJ Dwayne Miller. Early events in the nonadiabatic relaxation dynamics of 4-(n,n-dimethylamino) benzonitrile. *Journal of Chemical Theory and Computation*, 11(3):1118–1128, 2015.

[246] Antonio Prlj, Lea M Ibele, Emanuele Marsili, and Basile FE Curchod. On the theoretical determination of photolysis properties for atmospheric volatile organic compounds. *The Journal of Physical Chemistry Letters*, 11(14):5418–5425, 2020.

[247] Tropospheric ultraviolet and visible (TUV) radiation model, TUV 5.4 code, 2002. URL `https://www2.acom.ucar.edu/modeling/tuv-download`.

[248] Richard Atkinson, Donald L Baulch, Richard Anthony Cox, John N Crowley, Robert F Hampson, Robert G Hynes, Michael E Jenkin, Michel J Rossi, and Juergen Troe. Evaluated kinetic and photochemical data for atmospheric chemistry: Volume I-gas phase reactions of O_x, HO_x, NO_x and SO_x species. *Atmospheric Chemistry and Physics*, 4(6):1461–1738, 2004.

[249] Eric J Heller. The semiclassical way to molecular spectroscopy. *Accounts of Chemical Research*, 14(12):368–375, 1981.

[250] Fabrizio Santoro, Roberto Improta, Alessandro Lami, Julien Bloino, and Vincenzo Barone. Effective method to compute Franck-Condon integrals for optical spectra of large molecules in solution. *The Journal of Chemical Physics*, 126(8):084509, 2007.

[251] Fabrizio Santoro and Denis Jacquemin. Going beyond the vertical approximation with time-dependent density functional theory. *Wiley Interdisciplinary Reviews: Computational Molecular Science*, 6(5):460–486, 2016.

[252] Rachel Crespo-Otero and Mario Barbatti. Spectrum simulation and decomposition with nuclear ensemble: formal derivation and application to benzene, furan and 2-phenylfuran. *Marco Antonio Chaer Nascimento: A Festschrift From Theoretical Chemistry Accounts*, pages 89–102, 2014.

[253] Rachel Crespo-Otero and Mario Barbatti. Recent advances and perspectives on nonadiabatic mixed quantum-classical dynamics. *Chemical Reviews*, 118(15):7026–7068, 2018.

[254] Fabio Della Sala, Roger Rousseau, Andreas Görling, and Dominik Marx. Quantum and thermal fluctuation effects on the photoabsorption spectra of clusters. *Physical Review Letters*, 92(18):183401, 2004.

[255] Meher K Prakash, Jason D Weibel, and RA Marcus. Isotopomer fractionation in the UV photolysis of N_2O: Comparison of theory and experiment. *Journal of Geophysical Research: Atmospheres*, 110(D21), 2005.

[256] Milan Ončák, Lukáš Šištík, and Petr Slavíček. Can theory quantitatively model stratospheric photolysis? Ab initio estimate of absolute absorption cross sections of ClOOCl. *The Journal of Chemical Physics*, 133(17):174303, 2010.

[257] Štěpán Sršeň, Daniel Hollas, and Petr Slavíček. UV absorption of Criegee intermediates: quantitative cross sections from high-level ab initio theory. *Physical Chemistry Chemical Physics*, 20(9):6421–6430, 2018.

[258] Paulo Cabral do Couto, Daniel Hollas, and Petr Slavíček. On the performance of optimally tuned range-separated hybrid functionals for X-ray absorption modeling. *Journal of Chemical Theory and Computation*, 11(7):3234–3244, 2015.

[259] Weixuan Zeng, Shaolong Gong, Cheng Zhong, and Chuluo Yang. Prediction of oscillator strength and transition dipole moments with the nuclear ensemble approach for thermally activated delayed fluorescence emitters. *The Journal of Physical Chemistry C*, 123(15): 10081–10086, 2019.

[260] Hans Riesen, Christian Wiebeler, and Stefan Schumacher. Optical spectroscopy of graphene quantum dots: the case of C132. *The Journal of Physical Chemistry A*, 118(28): 5189–5195, 2014.

[261] Benjamin N Frandsen, Sara Farahani, Emil Vogt, Joseph R Lane, and Henrik G Kjaergaard. Spectroscopy of OSSO and other sulfur compounds thought to be present in the venus atmosphere. *The Journal of Physical Chemistry A*, 124(35):7047–7059, 2020.

[262] Theo Keane, Thomas W Rees, Etienne Baranoff, and Basile FE Curchod. Capturing the interplay between spin-orbit coupling and non-Condon effects on the photoabsorption spectra of Ru and Os dyes. *Journal of Materials Chemistry C*, 7(22):6564–6570, 2019.

[263] Christian Wiebeler, Felix Plasser, Gordon J Hedley, Arvydas Ruseckas, Ifor DW Samuel, and Stefan Schumacher. Ultrafast electronic energy transfer in an orthogonal molecular dyad. *The Journal of Physical Chemistry Letters*, 8(5):1086–1092, 2017.

[264] Štěpán Sršeň, Jaroslav Sita, Petr Slavíček, Vít Ladányi, and Dominik Heger. Limits of the nuclear ensemble method for electronic spectra simulations: Temperature dependence of the (E)-azobenzene spectrum. *Journal of Chemical Theory and Computation*, 16(10): 6428–6438, 2020.

[265] Štěpán Sršeň and Petr Slavíček. Optimal representation of the nuclear ensemble: Application to electronic spectroscopy. *Journal of Chemical Theory and Computation*, 17(10): 6395–6404, 2021.

[266] Mario Barbatti and Kakali Sen. Effects of different initial condition samplings on photodynamics and spectrum of pyrrole. *International Journal of Quantum Chemistry*, 116(10):762–771, 2016.

[267] Michele Ceriotti, Giovanni Bussi, and Michele Parrinello. Nuclear quantum effects in solids using a colored-noise thermostat. *Physical Review Letters*, 103(3):030603, 2009.

[268] Michele Ceriotti, Giovanni Bussi, and Michele Parrinello. Colored-noise thermostats à la carte. *Journal of Chemical Theory and Computation*, 6(4):1170–1180, 2010.

[269] Jiří Suchan, Daniel Hollas, Basile FE Curchod, and Petr Slavíček. On the importance of initial conditions for excited-state dynamics. *Faraday Discussions*, 212:307–330, 2018.

[270] Michael J Frisch, Gary W Trucks, H Bernhard Schlegel, Gustavo E Scuseria, Mike A Robb, James R Cheeseman, Giovanni Scalmani, Vincenzo Barone, Benedetta Mennucci, George A Petersson, et al. Gaussian 09, revision D.01, Gaussian, Inc., Wallingford CT. *http://www.gaussian.com*, 2009.

[271] Carlo Adamo and Vincenzo Barone. Toward reliable density functional methods without adjustable parameters: The PBE0 model. *The Journal of Chemical Physics*, 110(13): 6158–6170, 1999.

[272] Erich Runge and Eberhard KU Gross. Density-functional theory for time-dependent systems. *Physical Review Letters*, 52(12):997, 1984.

[273] Mark E Casida and DP Chong. Recent advances in density functional methods. *Computational Chemistry: Reviews of Current Trends*, 1995.

[274] Mark E Casida. Time-dependent density functional response theory for molecules. In *Recent Advances In Density Functional Methods: (Part I)*, pages 155–192. World Scientific, 1995.

[275] So Hirata and Martin Head-Gordon. Time-dependent density functional theory within the Tamm-Dancoff approximation. *Chemical Physics Letters*, 314(3-4):291–299, 1999.

[276] Daniel Hollas, Ondřej Svoboda, Milan Ončák, and Petr Slavíček. ABIN: Ab initio molecular dynamics program, 2021. URL `https://github.com/PHOTOX/ABIN`.

[277] Štěpán Sršeň, Christoph Bannwarth, B Scott Fales, Edward G Hohenstein, Sara IL Kokkila-Schumacher, Nathan Luehr, James W Snyder Jr, Chenchen Song, Alexey V Titov, Ivan S Ufimtsev, et al. TeraChem: Accelerating electronic structure and ab initio molecular dynamics with graphical processing units. *The Journal of Chemical Physics*, 152(22):224110, 2020.

[278] Štěpán SSršeň, Christoph Bannwarth, Bryan S Fales, Edward G Hohenstein, Christine M Isborn, Sara IL Kokkila-Schumacher, Xin Li, Fang Liu, Nathan Luehr, James W Snyder Jr, et al. TeraChem: A graphical processing unit-accelerated electronic structure package for large-scale ab initio molecular dynamics. *Wiley Interdisciplinary Reviews: Computational Molecular Science*, 11(2):e1494, 2021.

[279] GLE4MD project homepage: Colored noise thermostats for molecular dynamics, 2013. URL `http://gle4md.org/`.

[280] Anne B McCoy. The role of electrical anharmonicity in the association band in the water spectrum. *The Journal of Physical Chemistry B*, 118(28):8286–8294, 2014.

[281] Maurizio Persico and Giovanni Granucci. An overview of nonadiabatic dynamics simulations methods, with focus on the direct approach versus the fitting of potential energy surfaces. *Theoretical Chemistry Accounts*, 133:1–28, 2014.

[282] Sebastian Mai, Hugo Gattuso, Antonio Monari, and Leticia González. Novel molecular-dynamics-based protocols for phase space sampling in complex systems. *Frontiers in Chemistry*, 6:495, 2018.

[283] Loren Ban, Joel Bowman, Stephen Bradforth, Gilberte Chambaud, Martin Dracinsky, Ingo Fischer, Robert Góra, Majdi Hochlaf, Mikolaj Janicki, Adam Kirrander, et al. Molecules in confinement in liquid solvents: general discussion. *Faraday Discussions*, 212:383–397, 2018.

[284] Jean-François Müller, Jozef Peeters, and Trisevgeni Stavrakou. Fast photolysis of carbonyl nitrates from isoprene. *Atmospheric Chemistry and Physics*, 14(5):2497–2508, 2014.

[285] Emanuele Marsili, Antonio Prlj, and Basile FE Curchod. Caveat when using ADC(2) for studying the photochemistry of carbonyl-containing molecules. *Physical Chemistry Chemical Physics*, 23(23):12945–12949, 2021.

[286] Adele D Laurent and Denis Jacquemin. TD-DFT benchmarks: a review. *International Journal of Quantum Chemistry*, 113(17):2019–2039, 2013.

[287] Attila Tajti, Balázs Kozma, and Péter G Szalay. Improved description of charge-transfer potential energy surfaces via spin-component-scaled CC2 and ADC(2) methods. *Journal of Chemical Theory and Computation*, 17(1):439–449, 2020.

[288] Ljiljana Stojanović, Shuming Bai, Jayashree Nagesh, Artur F Izmaylov, Rachel Crespo-Otero, Hans Lischka, and Mario Barbatti. New insights into the state trapping of UV-excited thymine. *Molecules*, 21(11):1603, 2016.

[289] Michał A Kochman, Martina Pola, and RJ Dwayne Miller. Theoretical study of the photophysics of 8-vinylguanine, an isomorphic fluorescent analogue of guanine. *The Journal of Physical Chemistry A*, 120(31):6200–6215, 2016.

[290] Rafał Szabla, Robert W Góra, and Jiří Šponer. Ultrafast excited-state dynamics of isocytosine. *Physical Chemistry Chemical Physics*, 18(30):20208–20218, 2016.

[291] Gregory Gate, Rafał Szabla, Michael R Haggmark, Jiří Šponer, Andrzej L Sobolewski, and Mattanjah S de Vries. Photodynamics of alternative DNA base isoguanine. *Physical Chemistry Chemical Physics*, 21(25):13474–13485, 2019.

[292] Ove Christiansen, Henrik Koch, and Poul Jørgensen. The second-order approximate coupled cluster singles and doubles model CC2. *Chemical Physics Letters*, 243(5-6): 409–418, 1995.

[293] Arnim Hellweg, Sarah A Grün, and Christof Hättig. Benchmarking the performance of spin-component scaled CC2 in ground and electronically excited states. *Physical Chemistry Chemical Physics*, 10(28):4119–4127, 2008.

[294] Walter Kohn and Lu J Sham. Quantum density oscillations in an inhomogeneous electron gas. *Physical Review*, 137(6A):A1697, 1965.

[295] Robert G Parr and Yang Weitao. *Density-Functional Theory of Atoms and Molecules.* Oxford University Press, 01 1995.

[296] Filipp Furche, Reinhart Ahlrichs, Christof Hättig, Wim Klopper, Marek Sierka, and Florian Weigend. Turbomole. *Wiley Interdisciplinary Reviews: Computational Molecular Science*, 4(2):91–100, 2014.

[297] Toru Shiozaki. BAGEL: brilliantly advanced general electronic-structure library. *Wiley Interdisciplinary Reviews: Computational Molecular Science*, 8(1):e1331, 2018.

[298] Hans-Joachim Werner, Peter J Knowles, Gerald Knizia, Frederick R Manby, and Martin Schütz. Molpro: a general-purpose quantum chemistry program package. *Wiley Interdisciplinary Reviews: Computational Molecular Science*, 2(2):242–253, 2012.

[299] Florian Weigend, Andreas Köhn, and Christof Hättig. Efficient use of the correlation consistent basis sets in resolution of the identity MP2 calculations. *The Journal of Chemical Physics*, 116(8):3175–3183, 2002.

[300] Florian Weigend and Reinhart Ahlrichs. Balanced basis sets of split valence, triple zeta valence and quadruple zeta valence quality for H to Rn: Design and assessment of accuracy. *Physical Chemistry Chemical Physics*, 7(18):3297–3305, 2005.

[301] Florian Weigend. Accurate Coulomb-fitting basis sets for H to Rn. *Physical Chemistry Chemical Physics*, 8(9):1057–1065, 2006.

[302] Dmitrij Rappoport and Filipp Furche. Property-optimized Gaussian basis sets for molecular response calculations. *The Journal of Chemical Physics*, 133(13):134105, 2010.

[303] Benjamin G Levine, Joshua D Coe, and Todd J Martínez. Optimizing conical intersections without derivative coupling vectors: Application to multistate multireference second-order perturbation theory (MS-CASPT2). *The Journal of Physical Chemistry B*, 112(2):405–413, 2008.

[304] Curtis L Janssen and Ida MB Nielsen. New diagnostics for coupled-cluster and Møller-Plesset perturbation theory. *Chemical Physics Letters*, 290(4-6):423–430, 1998.

[305] Andreas Köhn and Christof Hättig. Analytic gradients for excited states in the coupled-cluster model CC2 employing the resolution-of-the-identity approximation. *The Journal of Chemical Physics*, 119(10):5021–5036, 2003.

[306] Šimon Budzák, Giovanni Scalmani, and Denis Jacquemin. Accurate excited-state geometries: A CASPT2 and coupled-cluster reference database for small molecules. *Journal of Chemical Theory and Computation*, 13(12):6237–6252, 2017.

[307] Denis Jacquemin, Ivan Duchemin, and Xavier Blase. 0-0 energies using hybrid schemes: Benchmarks of TD-DFT, CIS(d), ADC(2), CC2, and BSE/GW formalisms for 80 real-life compounds. *Journal of Chemical Theory and Computation*, 11(11):5340–5359, 2015.

[308] Łukasz Kielesiński, Olaf W Morawski, Cristina A Barboza, and Daniel T Gryko. Polarized helical coumarins: [1,5] sigmatropic rearrangement and excited-state intramolecular proton transfer. *The Journal of Organic Chemistry*, 86(9):6148–6159, 2021.

[309] Sebastian Mai, Andrew J Atkins, Felix Plasser, and Leticia González. The influence of the electronic structure method on intersystem crossing dynamics. the case of thioformaldehyde. *Journal of Chemical Theory and Computation*, 15(6):3470–3480, 2019.

[310] Emanuele Marsili, Antonio Prlj, and Basile FE Curchod. A theoretical perspective on the actinic photochemistry of 2-hydroperoxypropanal. *The Journal of Physical Chemistry A*, 126(32):5420–5433, 2022.

[311] John D Crounse, Fabien Paulot, Henrik G Kjaergaard, and Paul O Wennberg. Peroxy radical isomerization in the oxidation of isoprene. *Physical Chemistry Chemical Physics*, 13(30):13607–13613, 2011.

[312] Jozef Peeters, Jean-François Müller, Trissevgeni Stavrakou, and Vinh Son Nguyen. Hydroxyl radical recycling in isoprene oxidation driven by hydrogen bonding and hydrogen tunneling: The upgraded LIM1 mechanism. *The Journal of Physical Chemistry A*, 118 (38):8625–8643, 2014.

[313] Domenico Taraborrelli, Mark G Lawrence, John N Crowley, Terry J Dillon, Sergey Gromov, Christoph BM Groß, Luc Vereecken, and Johannes Lelieveld. Hydroxyl radical buffered by isoprene oxidation over tropical forests. *Nature Geoscience*, 5(3):190–193, 2012.

[314] Johannes Lelieveld, Tim M Butler, John N Crowley, Terry J Dillon, Horst Fischer, Laurens Ganzeveld, Hartwig Harder, Mark G Lawrence, Monica Martinez, Domenico Taraborrelli, and Jonathan Williams. Atmospheric oxidation capacity sustained by a tropical forest. *Nature*, 452(7188):737–740, 2008.

[315] Jason M St. Clair, Jean C Rivera-Rios, John D Crounse, Hasse C Knap, Kelvin H Bates, Alex P Teng, Solvejg Jørgensen, Henrik G Kjaergaard, Frank N Keutsch, and Paul O Wennberg. Kinetics and products of the reaction of the first-generation isoprene hydroxy hydroperoxide (ISOPOOH) with OH. *The Journal of Physical Chemistry A*, 120(9): 1441–1451, 2016.

[316] Alexander P Teng, John D Crounse, and Paul O Wennberg. Isoprene peroxy radical dynamics. *Journal of the American Chemical Society*, 139(15):5367–5377, 2017.

[317] Aric C Rousso, Nils Hansen, Ahren W Jasper, and Yiguang Ju. Low-temperature oxidation of ethylene by ozone in a jet-stirred reactor. *The Journal of Physical Chemistry A*, 122 (43):8674–8685, 2018.

[318] Eric Praske, John D Crounse, Kelvin H Bates, Theo Kurtén, Henrik G Kjaergaard, and Paul O Wennberg. Atmospheric fate of methyl vinyl ketone: Peroxy radical reactions with NO and HO_2. *The Journal of Physical Chemistry A*, 119(19):4562–4572, 2015.

[319] David E Woon and Thom H Dunning Jr. Gaussian basis sets for use in correlated molecular calculations. III. the atoms aluminum through argon. *The Journal of Chemical Physics*, 98(2):1358–1371, 1993.

[320] Martin Richter, Philipp Marquetand, Jesús González-Vázquez, Ignacio Sola, and Leticia González. SHARC: ab initio molecular dynamics with surface hopping in the adiabatic representation including arbitrary couplings. *Journal of Chemical Theory and Computation*, 7(5):1253–1258, 2011.

[321] Darya Shchepanovska, Robin J Shannon, Basile FE Curchod, and David R Glowacki. Nonadiabatic kinetics in the intermediate coupling regime: Comparing molecular dynamics to an energy-grained master equation. *The Journal of Physical Chemistry A*, 125(16): 3473–3488, 2021.

[322] Benoit Mignolet, Basile FE Curchod, and Todd J Martínez. Rich athermal ground-state chemistry triggered by dynamics through a conical intersection. *Angewandte Chemie*, 128 (48):15217–15220, 2016.

[323] Lluís Blancafort, Patricia Hunt, and Michael A Robb. Intramolecular electron transfer in bis (methylene) adamantyl radical cation: A case study of diabatic trapping. *Journal of the American Chemical Society*, 127(10):3391–3399, 2005.

[324] Julia C McCoy, Barbara Marchetti, Mushir Thodika, and Tolga NV Karsili. A simple and efficient method for simulating the electronic absorption spectra of Criegee intermediates: Benchmarking on CH_2OO and CH_3CHOO. *The Journal of Physical Chemistry A*, 125 (19):4089–4097, 2021.

[325] Pierre-François Loos, Anthony Scemama, Aymeric Blondel, Yann Garniron, Michel Caffarel, and Denis Jacquemin. A mountaineering strategy to excited states: Highly accurate reference energies and benchmarks. *Journal of Chemical Theory and Computation*, 14(8): 4360–4379, 2018.

[326] Pierre-François Loos, Filippo Lipparini, Martial Boggio-Pasqua, Anthony Scemama, and Denis Jacquemin. A mountaineering strategy to excited states: Highly accurate energies and benchmarks for medium sized molecules. *Journal of Chemical Theory and Computation*, 16(3):1711–1741, 2020.

[327] Mickaël Veril, Anthony Scemama, Michel Caffarel, Filippo Lipparini, Martial Boggio-Pasqua, Denis Jacquemin, and Pierre-François Loos. QUESTDB: A database of highly accurate excitation energies for the electronic structure community. *Wiley Interdisciplinary Reviews: Computational Molecular Science*, 11(5):e1517, 2021.

[328] Pierre-Francois Loos, Filippo Lipparini, Devin A Matthews, Aymeric Blondel, and Denis Jacquemin. A mountaineering strategy to excited states: Revising reference values with EOM-CC4. *Journal of Chemical Theory and Computation*, 18(7):4418–4427, 2022.

[329] Paul Wiggins, JA Gareth Williams, and David J Tozer. Excited state surfaces in density functional theory: a new twist on an old problem. *The Journal of Chemical Physics*, 131 (9):091101, 2009.

[330] Chenchen Song and Todd J Martínez. Reduced scaling extended multi-state CASPT2 (XMS-CASPT2) using supporting subspaces and tensor hyper-contraction. *The Journal of Chemical Physics*, 152(23):234113, 2020.

[331] William J Glover, Amiel SP Paz, Wutthinan Thongyod, and Chutintorn Punwong. Analytical gradients and derivative couplings for dynamically weighted complete active space self-consistent field. *The Journal of Chemical Physics*, 151(20):201101, 2019.

[332] Lucilla Favero, Giovanni Granucci, and Maurizio Persico. Dynamics of acetone photodissociation: a surface hopping study. *Physical Chemistry Chemical Physics*, 15(47): 20651–20661, 2013.

[333] Basile FE Curchod, Clemens Rauer, Philipp Marquetand, Leticia González, and Todd J Martínez. Communication: GAIMS—generalized ab initio multiple spawning for both internal conversion and intersystem crossing processes. *The Journal of Chemical Physics*, 144(10):101102, 2016.

[334] Saikat Mukherjee, Max Pinheiro Jr, Baptiste Demoulin, and Mario Barbatti. Simulations of molecular photodynamics in long timescales. *Philosophical Transactions of the Royal Society A*, 380(2223):20200382, 2022.

[335] Aurélia Chenu and Paul Brumer. Transform-limited-pulse representation of excitation with natural incoherent light. *The Journal of Chemical Physics*, 144(4):044103, 2016.

[336] Mario Barbatti. Simulation of excitation by sunlight in mixed quantum-classical dynamics. *Journal of Chemical Theory and Computation*, 16(8):4849–4856, 2020.

[337] Chao-Jing Sun, Nan Wang, Tai Peng, Xiaodong Yin, Suning Wang, and Pangkuan Chen. BN-functionalized benzotrithiophene-based azaborines: synthesis, structures, and anion binding properties. *Inorganic Chemistry*, 58(6):3591–3595, 2019.

[338] Yafei Shi, Yi Zeng, Pavel Kucheryavy, Xiaodong Yin, Kai Zhang, Guoyun Meng, Jinfa Chen, Qian Zhu, Nan Wang, Xiaoyan Zheng, et al. Dynamic B/N Lewis pairs: Insights into the structural variations and photochromism via light-induced fluorescence to phosphorescence switching. *Angewandte Chemie International Edition*, page e202213615, 2022.

[339] Shinichiro Osumi, Shohei Saito, Chuandong Dou, Kyohei Matsuo, Keita Kume, Hirofumi Yoshikawa, Kunio Awaga, and Shigehiro Yamaguchi. Boron-doped nanographene: Lewis acidity, redox properties, and battery electrode performance. *Chemical Science*, 7(1): 219–227, 2016.

[340] Mukundam Vanga, Ashutosh Sahoo, Roger A Lalancette, and Frieder Jäkle. Linear extension of anthracene via B−N Lewis pair formation: Effects on optoelectronic properties and singlet O_2 sensitization. *Angewandte Chemie International Edition*, 61(5):e202113075, 2022.

[341] Masato Hirai, Naoki Tanaka, Mika Sakai, and Shigehiro Yamaguchi. Structurally constrained boron-, nitrogen-, silicon-, and phosphorus-centered polycyclic π-conjugated systems. *Chemical Reviews*, 119(14):8291–8331, 2019.

[342] Aude Escande and Michael J Ingleson. Fused polycyclic aromatics incorporating boron in the core: fundamentals and applications. *Chemical Communications*, 51(29):6257–6274, 2015.

[343] Jeffrey M Farrell, Carina Mützel, David Bialas, Maximilian Rudolf, Kaan Menekse, Ana-Maria Krause, Matthias Stolte, and Frank Würthner. Tunable low-LUMO boron-doped polycyclic aromatic hydrocarbons by general one-pot C−H borylations. *Journal of the American Chemical Society*, 141(22):9096–9104, 2019.

[344] Kai Schickedanz, Timo Trageser, Michael Bolte, Hans-Wolfram Lerner, and Matthias Wagner. A boron-doped helicene as a highly soluble, benchtop-stable green emitter. *Chemical Communications*, 51(87):15808–15810, 2015.

[345] Fumiya Miyamoto, Soichiro Nakatsuka, Keitaro Yamada, Ken-ichi Nakayama, and Takuji Hatakeyama. Synthesis of boron-doped polycyclic aromatic hydrocarbons by tandem intramolecular electrophilic arene borylation. *Organic Letters*, 17(24):6158–6161, 2015.

[346] Shohei Saito, Kyohei Matsuo, and Shigehiro Yamaguchi. Polycyclic π-electron system with boron at its center. *Journal of the American Chemical Society*, 134(22):9130–9133, 2012.

[347] Takuya Matsumoto, Kazuo Tanaka, Kazuyoshi Tanaka, and Yoshiki Chujo. Synthesis and characterization of heterofluorenes containing four-coordinated group 13 elements: theoretical and experimental analyses and comparison of structures, optical properties and electronic states. *Dalton Transactions*, 44(18):8697–8707, 2015.

[348] Takuya Matsumoto, Hirofumi Takamine, Kazuo Tanaka, and Yoshiki Chujo. Design of bond-cleavage-induced intramolecular charge transfer emission with dibenzoboroles

and their application to ratiometric sensors for discriminating chain lengths of alkanes. *Materials Chemistry Frontiers*, 1(11):2368–2375, 2017.

[349] Qinggao Hou, Lijie Liu, Soren K Mellerup, Nan Wang, Tai Peng, Pangkuan Chen, and Suning Wang. Stimuli-responsive B/N lewis pairs based on the modulation of B−N bond strength. *Organic Letters*, 20(20):6467–6470, 2018.

[350] Ryo Oshimizu, Naoki Ando, and Shigehiro Yamaguchi. Olefin-borane interactions in donor-π-acceptor fluorophores that undergo frustrated-lewis-pair-type reactions. *Angewandte Chemie*, 134(41):e202209394, 2022.

[351] Lawrence R Thorne, Richard D Suenram, and Frank J Lovas. Microwave spectrum, torsional barrier, and structure of BH_3NH_3. *The Journal of Chemical Physics*, 78(1): 167–171, 1983.

[352] Glenn H Penner, YC Phillis Chang, and Jennifer Hutzal. A deuterium NMR spectroscopic study of solid BH_3NH_3. *Inorganic Chemistry*, 38(12):2868–2873, 1999.

[353] Josef Goubeau and E Ricker. Borinhydrazin und seine pyrolyseprodukte. *Zeitschrift für Anorganische und Allgemeine Chemie*, 310(3):123–142, 1961.

[354] RC Taylor and CL Cluff. Vibrational frequency associated with the boron-nitrogen dative bond in amine boranes. *Nature*, 182(4632):390–391, 1958.

[355] Bing Yuan, Joong-Won Shin, and Elliot R Bernstein. Dynamics and fragmentation of van der Waals and hydrogen bonded cluster cations:$(NH_3)_n$ and $(NH_3BH_3)_n$ ionized at 10.51 eV. *The Journal of Chemical Physics*, 144(14):144315, 2016.

[356] DR Lloyd and N Lynaugh. Photoelectron studies of boron compounds. Part 3.-complexes of borane with Lewis bases. *Journal of the Chemical Society, Faraday Transactions 2*, 68: 947–958, 1972.

[357] Domenik Schleier, Marius Gerlach, Deb Pratim Mukhopadhyay, Emil Karaev, Dorothee Schaffner, Patrick Hemberger, and Ingo Fischer. Ammonia borane, NH_3BH_3: A threshold photoelectron-photoion coincidence study of a potential hydrogen-storage material. *Chemistry–A European Journal*, 28(42):e202201378, 2022.

[358] CF Hoon and Eduard C Reynhardt. Molecular dynamics and structures of amine boranes of the type $R_3N.BH_3$. I. X-Ray investigation of $H_3N.\ BH_3$ at 295K and 110K. *Journal of Physics C: Solid State Physics*, 16(32):6129, 1983.

[359] Nancy J Hess, Gregory K Schenter, Michael R Hartman, Luc L Daemen, Thomas Proffen, Shawn M Kathmann, Christopher J Mundy, Monika Hartl, David J Heldebrant, Ashley C Stowe, et al. Neutron powder diffraction and molecular simulation study of the structural

evolution of ammonia borane from 15 to 340 K. *The Journal of Physical Chemistry A*, 113(19):5723–5735, 2009.

[360] Damian G Allis, Mark E Kosmowski, and Bruce S Hudson. The inelastic neutron scattering spectrum of $H_3B{:}NH_3$ and the reproduction of its solid-state features by periodic DFT. *Journal of the American Chemical Society*, 126(25):7756–7757, 2004.

[361] Annalisa Paolone, Oriele Palumbo, Pasquale Rispoli, Rosario Cantelli, and Tom Autrey. Hydrogen dynamics and characterization of the tetragonal-to-orthorhombic phase transformation in ammonia borane. *The Journal of Physical Chemistry C*, 113(14):5872–5878, 2009.

[362] Anne Staubitz, Alasdair PM Robertson, and Ian Manners. Ammonia-borane and related compounds as dihydrogen sources. *Chemical Reviews*, 110(7):4079–4124, 2010.

[363] Gabriel Merino, Vladimir I Bakhmutov, and Alberto Vela. Do cooperative proton-hydride interactions explain the gas-solid structural difference of BH_3NH_3? *The Journal of Physical Chemistry A*, 106(37):8491–8494, 2002.

[364] Melanie C Denney, Vincent Pons, Travis J Hebden, D Michael Heinekey, and Karen I Goldberg. Efficient catalysis of ammonia borane dehydrogenation. *Journal of the American Chemical Society*, 128(37):12048–12049, 2006.

[365] Xingyue Zhang, Lisa Kam, Ryan Trerise, and Travis J Williams. Ruthenium-catalyzed ammonia borane dehydrogenation: mechanism and utility. *Accounts of Chemical Research*, 50(1):86–95, 2017.

[366] Ahmad Al-Kukhun, Hyun Tae Hwang, and Arvind Varma. Mechanistic studies of ammonia borane dehydrogenation. *International Journal of Hydrogen Energy*, 38(1):169–179, 2013.

[367] Nathan C Smythe and John C Gordon. Ammonia borane as a hydrogen carrier: dehydrogenation and regeneration. *European Journal of Inorganic Chemistry*, 2010(4):509–521, 2010.

[368] Papri Bhattacharya, Jeanette A Krause, and Hairong Guan. Mechanistic studies of ammonia borane dehydrogenation catalyzed by iron pincer complexes. *Journal of the American Chemical Society*, 136(31):11153–11161, 2014.

[369] John S Binkley and Lawrence R Thorne. A theoretical study of the properties of BH_3NH_3. *The Journal of chemical physics*, 79(6):2932–2940, 1983.

[370] Seung Mi Lee, Xiang-Dong Kang, Ping Wang, Hui-Ming Cheng, and Young Hee Lee. A comparative study of the structural, electronic, and vibrational properties of NH_3BH_3 and $LiNH_2BH_3$: Theory and experiment. *ChemPhysChem*, 10(11):1825–1833, 2009.

[371] Robert L Sams, Sotiris S Xantheas, and Thomas A Blake. Vapor phase infrared spectroscopy and ab initio fundamental anharmonic frequencies of ammonia borane. *The Journal of Physical Chemistry A*, 116(12):3124–3136, 2012.

[372] Yirong Mo, Lingchun Song, Wei Wu, and Qianer Zhang. Charge transfer in the electron donor-acceptor complex BH_3NH_3. *Journal of the American Chemical Society*, 126(12): 3974–3982, 2004.

[373] Paul M Zimmerman, Zhiyong Zhang, and Charles B Musgrave. Dynamic mechanisms for ammonia borane thermolysis in solvent: Deviation from gas-phase minimum-energy pathways. *The Journal of Physical Chemistry Letters*, 2(4):276–281, 2011.

[374] Mahadevappa Naganathappa, Tahemina Qureshi, and Ajay Chaudhari. Mono and disubstituted ammonia borane: A computational study. *Journal of Molecular Liquids*, 211: 776–783, 2015.

[375] Alexander S Zyubin and Alexander M Mebel. Performance of time-dependent density functional and Green functions methods for calculations of excitation energies in radicals and for Rydberg electronic states. *Journal of Computational Chemistry*, 24(6):692–700, 2003.

[376] Yao Chang, Jiayue Yang, Zhichao Chen, Zhiguo Zhang, Yong Yu, Qingming Li, Zhigang He, Weiqing Zhang, Guorong Wu, Rebecca A Ingle, et al. Ultraviolet photochemistry of ethane: implications for the atmospheric chemistry of the gas giants. *Chemical Science*, 11(19):5089–5097, 2020.

[377] Robert G Potter, Donald M Camaioni, Monica Vasiliu, and David A Dixon. Thermochemistry of lewis adducts of BH_3 and nucleophilic substitution of triethylamine on NH_3BH_3 in tetrahydrofuran. *Inorganic Chemistry*, 49(22):10512–10521, 2010.

[378] Panayiotis C Varras, Panagiotis S Gritzapis, and Konstantina C Fylaktakidou. An explanation of the very low fluorescence and phosphorescence in pyridine: a CASSCF/CASMP2 study. *Molecular Physics*, 116(2):154–170, 2018.

[379] Panayiotis C Varras and Panagiotis S Gritzapis. Can the symmetrical Dewar pyridine be observed experimentally? a theoretical study. *Molecular Physics*, 118(7):e1662126, 2020.